

AD 607238

AFCRL-64-750

THEORETICAL STUDIES RELATED TO THE  
DETERMINATION OF SEISMIC ENERGY SOURCE DEPTH

T. W. Spencer

W. L. Baker

J. W. C. Sherwood

D. P. Squier

R. D. Tooley

California Research Corporation

La Habra, California

Contract No. AF19(604)-8344

Project 8652

Task 865205

FINAL REPORT

July 15, 1964

COPY	2	OF	2	sent
HARD COPY		\$.	6.00	
MICROFICHE		\$.	1.25	

228p

Prepared for

AIR FORCE CAMBRIDGE RESEARCH LABORATORIES  
OFFICE OF AEROSPACE RESEARCH  
UNITED STATES AIR FORCE  
BEDFORD, MASSACHUSETTS

WORK SPONSORED BY ADVANCED RESEARCH PROJECTS AGENCY

PROJECT VELA-UNIFORM

ARPA Order No. 180-61  
Project Code No. 8100 Task 2

**BEST  
AVAILABLE COPY**

THEORETICAL STUDIES RELATED TO THE  
DETERMINATION OF SEISMIC ENERGY SOURCE DEPTH

T. W. Spencer

W. L. Baker

J. W. C. Sherwood

D. P. Squier

R. D. Tooley

California Research Corporation

La Habra, California

Contract No. AF19(604)-8344

Project 8652

Task 865205

FINAL REPORT

July 15, 1964

Prepared for

AIR FORCE CAMBRIDGE RESEARCH LABORATORIES  
OFFICE OF AEROSPACE RESEARCH  
UNITED STATES AIR FORCE  
BEDFORD, MASSACHUSETTS

WORK SPONSORED BY ADVANCED RESEARCH PROJECTS AGENCY

PROJECT VELA-UNIFORM

ARPA Order No. 180-61  
Project Code No. 8100 Task 2

Request for additional copies by Agencies of the Department of Defense, their contractors, and other government agencies should be directed to the:

DEFENSE DOCUMENTATION CENTER (DDC)  
CAMERON STATION  
Alexandria, Virginia 22314

Department of Defense Contractors must be established for DDC services or have their "need-to-know" certified by the cognizant military agency of their project or contract.

All other persons and organizations should apply to the:

U. S. DEPARTMENT OF COMMERCE  
OFFICE OF TECHNICAL SERVICES  
WASHINGTON, D. C. 20230



**BLANK PAGE**

## ABSTRACT

This report summarizes work on a number of different but related topics, as follows: The effect of seismic source depth on Rayleigh wave spectra is examined for a dissipative half space and for an elastic layer overlying an elastic half space. In the two-layer earth model, the higher-mode amplitude spectra increase relative to the fundamental as the source approaches the base of the crust. The exact ray theory and matrix method are in principle devices for obtaining the response of a layered system over a limited time interval. Both methods prove to be inefficient from the standpoint of automatic computation but useful in analyzing certain general properties of the response functions in multilayered systems. Geometric ray theory is used to study the effects of layer thickness and range on the refracted arrival along a high-speed layer embedded in an infinite medium. When the layer is thick compared with the dominant wavelength, the refracted arrival exhibits range-limited shingling and may consist of two or more events separated by equal time intervals which depend only on the layer thickness. The reflection of a plane compressional wave at a plane interface is analyzed with particular emphasis on the equation for continuity of the instantaneous energy flux. Inside the critical angle, Knott's equation gives continuity of the instantaneous flux, but beyond the critical angle Knott's equation must be replaced by three separate conditions.

The partition of energy among the reflected and transmitted waves and the relative phases are tabulated for over 2000 cases to show the effect of systematically varying the compressional velocity ratio, the Poisson's ratios and the density. Deconvolution techniques are applied to the body wave phases generated by two explosions and an earthquake in an effort to reduce the distortion introduced by the transmission and recording systems.

## CONTENTS

	<u>Page</u>
INTRODUCTION	1
I. SIGNAL-TO-NOISE RATIO AND SPECTRA OF EXPLOSION- GENERATED RAYLEIGH WAVES IN A DISSIPATIVE HALF-SPACE	6
II. THE EFFECT OF SOURCE DEPTH ON RAYLEIGH WAVE SPECTRA IN A LAYERED EARTH	15
III. SEISMIC MODELING	
A. Explosive Sources	37
B. Piezoelectric Sources	54
IV. LONG-TIME RESPONSE PREDICTED BY EXACT ELASTIC RAY THEORY	
A. Introduction	72
B. Long-Time Behavior	75
C. Convergent Groups	80
V. HIGH-FREQUENCY ELASTIC WAVE THEORY	
A. Introduction	87
B. The Source Function	87
C. Generalized Ray Theory	89
D. Singular Behavior of the Generalized Response Functions at Times Associated with Least-Time Paths	102
E. The One-Interface System	103
VI. ANALYSIS OF A PROGRAM FOR COMPUTING THEORETICAL SEISMOGRAMS FOR MULTILAYERED MEDIA	123

CONTENTS (Cont'd.)

	<u>Page</u>
VII. THE REFRACTED ARRIVAL FROM A LAYER	127
VIII. REFLECTION AND TRANSMISSION OF PLANE COMPRESSIONAL WAVES	155
IX. SOME EXPERIMENTS ON INVERSE FILTERING OF SEISMIC RECORDS	161
REFERENCES	181

## INTRODUCTION

This report summarizes research carried out at the California Research Corporation during the contract period, February 15, 1961 through June 14, 1964. The primary purpose of this research was to investigate theoretically the feasibility of improving our ability to determine seismic energy source depth.

In the past source depth determinations have been based exclusively on the use of body waves. However, a large part of the energy emitted by a source in the crust is trapped in the crust and goes into surface waves. Surface waves attenuate less rapidly than body waves because they spread in two dimensions rather than in three. These facts suggest that at the stations closest to an underground explosion (say 500 km), most of the energy may be in the form of surface waves. At great distances the surface waves produced by a low-yield explosion are weak compared to the body waves probably because most of the surface wave energy is concentrated at higher frequencies which are scattered by lateral inhomogeneities in the crust. We have studied the effect of source depth on the Rayleigh wave spectra for a dissipative half space and for an elastic surface layer overlying an elastic half space. Some of the theoretical predictions have been compared with results from two-dimensional seismic model studies.

Two methods were considered for computing the total response of a layered system: (a) the exact ray theory and (b) the matrix method. In the exact ray theory the total response is expanded in an infinite series. Each term in the series describes the response produced by energy which reaches the receiver by a certain generalized transmission path. The response over a finite time interval is determined by a finite number of terms in the expansion. For the axially symmetric case, each term is given by a contour integral. The time (and consequently the cost) required to perform the numerical integrations was found to be prohibitive even on a machine like the IBM 7094.

The theoretical analysis of the general term in the exact ray theory expansion revealed that the response function for each path diverges in the long-time limit and that the rate of divergence increases as the number of reflections increases. This suggests that if the individual response functions are added together in an indiscriminate way it is quite possible for the magnitude of the result at an intermediate stage of computation (before all the terms are computed) to exceed the magnitude of the correct total result by a number which exceeds the number of significant figures retained by the machine. A prescription is given for grouping the ray paths together in such a way that each group response function converges in the long-time limit.

The first and second terms are derived in a high-frequency asymptotic expansion of the general term in the exact ray theory expansion for the multi-layer system. The high-

frequency terms describe rays which traverse least-time reflection and refraction paths. The factors which describe the attenuation produced by geometrical spreading can be used in any system in which the radiation field is axially symmetric. All the information required to construct a high-frequency theoretical seismogram for a layered system is given.

The matrix method was used to attack the multilayer problem along different lines. The matrix method gives the kernel in a double integral transform for the response of a layered system. The kernel is a function of frequency and phase velocity. We restrict our attention to phase velocities which exceed the highest phase velocity for unattenuated normal mode propagation. In this restricted domain the kernel is non-singular. The truncated integral describes in an approximate way the response in the time interval preceding the arrival of the normal modes and in this respect determines a theoretical refraction seismogram. The feasibility of performing the double integration numerically is considered. The formal expression for the kernel is analyzed to demonstrate the existence or absence of unattenuated normal modes in different models.

An accurate knowledge of the velocity structure in the crust is required in the determination of epicentral position and focal depth, in the use of equalization techniques to remove from surface waves the phase distortion introduced by the transmission path, and to remove from body waves the distortion introduced by



reverberation in the crust. For these and other reasons, the Branch of Crustal Studies of the U. S. Geological Survey has undertaken an extensive refraction program to delineate the velocity structure in the crust. One difficulty with the refraction method is that it cannot detect the presence of low-velocity layers. This problem could be circumvented if it were possible to determine the base (or thickness) of the high velocity zones. The effect of layer thickness on the refracted arrival from a layer embedded in an infinite medium is investigated in detail. The two-dimensional seismic model was used to study the refracted arrivals in two- and four-layer models.

The subject of the reflection and transmission of a plane compressional wave at a plane interface is an old one. Even so some new results are presented in this report. On physical grounds we know that the normal component of the instantaneous energy flux must be continuous across an interface. Inside the critical angle Knott's equation is the correct mathematical statement of continuity. Outside the critical angle Knott's equation requires continuity of the net flux (i.e., the instantaneous flux integrated over a period), but not continuity of the instantaneous flux. The mathematical statement of continuity of the instantaneous flux is derived. The fraction of the incident energy which goes into the reflected and transmitted waves and the relative phases for the vertical component of displacement are tabulated for over two thousand different combinations of the compressional velocity ratio, of Poisson's ratio, and of density ratio.

The earth transmission system and the recording system introduce a certain amount of distortion in the body wave phases which lengthen the phases in time and reduce resolving power. Deconvolution techniques are applied to body wave phases from two explosions and an earthquake in an effort to remove the distortion introduced by the transmission path.

Each section of this report is complete in itself and is independent of the preceding and following sections. The figures for each section are placed either at the end of the section or appear on the page(s) following first mention. All the references are grouped together at the end of the report. Except for the sections on seismic modeling and inverse filtering, the material is covered in greater detail in the scientific reports which have been issued during the course of the contract.

# I. SIGNAL-TO-NOISE RATIO AND SPECTRA OF EXPLOSION-GENERATED RAYLEIGH WAVES IN A DISSIPATIVE HALF SPACE

This preliminary theoretical study is basically concerned with the estimation of the depth of an explosive source from a knowledge of the radiated Rayleigh wave. The differentiation between artificial and natural sources on the basis of source depth requires a precise determination of source depth. Present techniques for determining source depth at short ranges rely exclusively on the use of body wave phases. These methods presuppose good control at short ranges. This may be difficult to obtain. It is reasonable to inquire whether accurate source depth information can be extracted from surface waves at moderate ranges, say, of the order of 500 kms. At great distances the surface waves generated by low-yield nuclear explosions are generally not detected probably because most of the energy goes into the higher frequency components which are scattered by lateral inhomogeneities in the upper crust.

To investigate the effect of source depth on the surface wave spectrum and the factors which govern our ability to recover that spectrum, we consider the Rayleigh wave generated by an explosion in a homogeneous and isotropic half space. This is the simplest medium which permits the propagation of Rayleigh waves. The explosive charge is assumed to be situated at the center of a spherical cavity of radius  $a$ . In what follows, decoupling (Latter, Le Levier, Martinelli, and McMillan, 1961) is assumed throughout.

The Laplace transform of the radial stress in a spherically symmetric compressional wave is

$$\overline{\tau}_{rr} = -\frac{\sigma e^{-sr/\alpha}}{r} \overline{\chi}(s) \left( 1 + 4\frac{\beta^2}{\alpha^2} \left( \frac{\alpha}{sr} \right) + 4\frac{\beta^2}{\alpha^2} \left( \frac{\alpha}{sr} \right)^2 \right), \quad (1)$$

where  $r$  is the radial distance from the center of the shot cavity,  $s$  is the Laplace transform variable,  $\sigma$  is the density,  $\beta$  is the shear velocity, and  $\alpha$  is the compressional velocity. Following Latter, we approximate the stress at the cavity wall by a step. This requirement determines  $\overline{\chi}(s)$  in the form:

$$\overline{\chi}(s) = \frac{Pa}{\sigma} \frac{e^{sa/\alpha}}{s} \left( 1 + 4\frac{\beta^2}{\alpha^2} \left( \frac{\alpha}{sa} \right) + 4\frac{\beta^2}{\alpha^2} \left( \frac{\alpha}{sa} \right)^2 \right)^{-1}, \quad (2)$$

where  $P$  is the magnitude of the step in stress. Because of preferential absorption of the higher frequencies, only the wavelength components which are large compared to the cavity radius are important at distance. The assumption  $|\alpha/sa| \gg 1$ , reduces (2) to

$$\overline{\chi}(s) = \frac{Pa^3}{4\sigma\beta^2} s. \quad (3)$$

To determine whether (3) is valid, we must compare the shortest wavelengths in the Rayleigh wave train at 500 km with the minimum cavity radius required to achieve decoupling. The quantity  $Pa^3$  determines the strength of the source and is related to the yield,  $W$ , by

$$Pa^3 = \frac{3}{4\pi} (\gamma - 1) W, \quad (4)$$

where  $\gamma$  is the ratio of the specific heats of the gases in the cavity.

Sherwood and Spencer (1962) have derived an expression for the spectrum of the vertical component of the particle velocity in the Rayleigh wave at the free surface. The phase spectrum is

$$\phi(f) = -\left(\frac{2\pi f \rho}{c} + \frac{\pi}{4}\right), \quad (5)$$

where  $f$  is the frequency,  $\rho$  is the range, and  $c$  is the Rayleigh wave velocity. It is to be noted that the phase spectrum is independent of the source depth,  $H$ . The amplitude spectrum is

$$A_0(f) = \frac{\chi M}{\rho^{1/2}} f^{3/2} e^{-\frac{2\pi}{c} H f (1 - c^2/\alpha^2)^{1/2}} \quad (6)$$

where  $M$  is the TNT mass equivalent in kilotons and

$$\chi = \frac{(0.6) 10^{12} B c^{1/2}}{\sigma \beta^4}.$$

$B$  is a complicated function of Poisson's ratio which decreases monotonically from about 1.2 to 0.2 as the Poisson's ratio increases from zero to one-half. It is evident from (6) that the higher frequency components decay more rapidly with source depth than the lower frequencies. Hence, the amplitude spectrum of the Rayleigh wave becomes relatively richer in high frequencies as the source depth  $H$  is diminished.

Unfortunately, the absorptive properties of the medium have an effect similar to source depth in diminishing the relative content of the higher frequency components. It seems that the loss properties of a solid medium can often be approximately represented by a mechanical quality factor,  $Q$ , which does not vary much with frequency (see O'Brien (1961) for bibliography).

Hueter and Bolt (1955) state that the absorption of progressive waves is approximately expressible as

$$\Gamma = e^{-\pi f \rho / Q c}. \quad (7)$$

An interpolation of measurements in the vicinity of .01 to 10 cps (see O'Brien (1961) and Press (1954)) indicates that in the frequency range of interest (1 to .1 cps), the  $Q$  for Rayleigh waves should be very approximately 100. It does seem, however, that lower frequency Rayleigh waves have a higher  $Q$  value. Also, the higher frequencies generally experience considerable scattering in the inhomogeneous near-surface region which should result in a decrease in the effective  $Q$  value. Hence, the effective  $Q$  for a surface wave mode should tend to decrease with increasing frequency, but we are not presently in a position to give precise quantitative values. This is important, for we see from (6) and (7) that the source depth and dissipation have a similar frequency-dependent effect on the amplitude spectrum of the Rayleigh wave. It is thereby apparent that an error in our knowledge of  $Q$  will limit our ability to estimate the source depth accurately.

The combined effects of source depth and dissipation determine the amplitude spectrum in the form

$$A(f) = A_0(f) \Gamma(f) = \frac{\chi M}{\rho^{1/2}} f^{3/2} e^{-kf} \quad (8)$$

where

$$k = \frac{2\pi}{c} \left\{ \frac{\rho}{2Q} + H \left( 1 - \frac{c^2}{\alpha^2} \right)^{1/2} \right\}. \quad (9)$$

Assuming that the velocities  $c$  and  $\alpha$  are known accurately, we see that the incremental changes in the other parameters are related by

$$\delta k = \frac{2\pi}{c} \left\{ \frac{(\delta \rho)}{2Q} - \frac{\rho(\delta Q)}{2Q^2} + (\delta H) \left(1 - \frac{c^2}{\alpha^2}\right)^{1/2} \right\},$$

where  $(\delta X)$  represents a small increment in  $X$ . Even under the assumption that  $k$  can be accurately estimated from the amplitude spectrum of the Rayleigh wave train, and even if the range  $\rho$  is known accurately, it is evident that there is an error in source depth,  $(\delta H)$ , given by

$$\delta H = \frac{\rho}{2Q^2} \left(1 - \frac{c^2}{\alpha^2}\right)^{-1/2} (\delta Q). \quad (10)$$

To appreciate the magnitude of this error, let us enter plausible values into (10). For a reasonable value of  $c/\alpha$ , a range  $\rho$  of 500km, and an error  $(\delta Q)$  of 10 in a  $Q$  of about 100, we have

$$(\delta H) \approx 0.3 \text{ km}.$$

This is about the resolution in source depth that we are seeking, but it seems that it will take considerable effort to attain it.

The normalized Rayleigh spectra defined by

$$U(f) = \rho^{1/2} A(f) / M$$

are plotted in Figure 1.

Our ability to extract information from the Rayleigh wave signal is limited by the microseism or noise background. We assume that, at the time and place of detection, the characteristics of the background noise  $N(f)$  are similar to those of

the minimum noise curve depicted by Brune and Oliver (1959) and reproduced in Figure 1. Accordingly, our final estimates refer to approximately the maximum signal-to-noise ratio that we can expect for a decoupled shot.

Actual seismograms are the result of subjecting the true ground motion to some composite filter system. This filter system is usually a reasonably simple combination of a conventional seismometer and galvanometer. However, it could in principle be a far more sophisticated filter which one might obtain by means of analog or digital operations on the output of a seismometer. The importance of recording a wide range of seismic frequencies with good accuracy in conjunction with adequate filtering operations cannot be overemphasized. Sherwood and Spencer (1962) consider two filter systems: (1) the Benioff short period system installed at Wichita\* and (2) a more nearly optimum system in which the filter characteristic is a function of the spectral content of both the Rayleigh signal and the ambient ground motion.

As our definition of signal-to-noise ratio, we adopt the following form:

---

\*The transmission curve for particle velocity for the Wichita instrument is given in the article by Gudzin and Hamilton (1961).



$$\left(\frac{S}{N}\right) = \frac{\text{Average level of signal amplitude spectrum}}{\text{Average level of conflicting noise amplitude spectrum}}$$

Recording the signal and noise through the short period Benioff system gives a signal-to-noise ratio per kiloton of TNT  $\left[(S/N)/M\right]$  which varies with range as shown in Figure 2.

It must be emphasized that our results are valid only for the decoupled source, step function in pressure input, constant  $Q$  dissipation, half-space model, and noise structure which we have assumed. A coupled shot is far more efficient in generating seismic waves than a decoupled shot, and its spectrum may be different. It is particularly important to compare the long wave length content of the two spectra in situations where the free surface or some other major impedance discontinuity lies within the nonlinear zone. In a layered earth the Rayleigh waves propagate in more than one mode, and each mode exhibits dispersion. Dispersion causes the Rayleigh wave to spread out over a relatively long time interval with a subsequent decrease in the signal-to-noise ratio. When the phase velocity variation with frequency is known, it is possible partially to compensate for the deleterious effect of dispersion by a technique such as that due to Aki (1960). The variation of absorption with depth and the lateral inhomogeneity of the wave guide probably cause the  $Q$  to decrease with increasing frequency. These factors must be considered in comparing our results with observed signal-to-noise ratios.

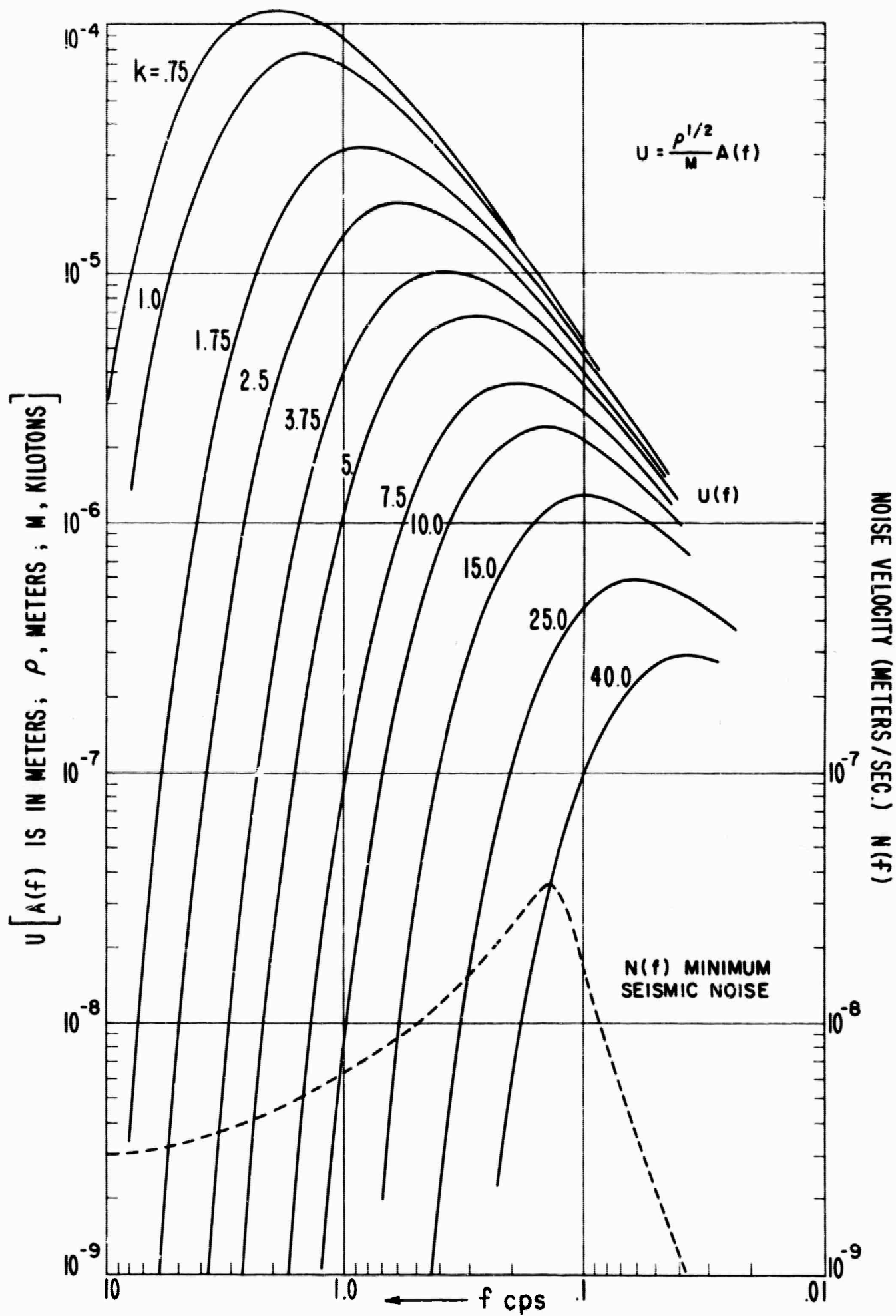


FIGURE 1  
 NORMALIZED RAYLEIGH WAVE AND  
 NOISE AMPLITUDE SPECTRA

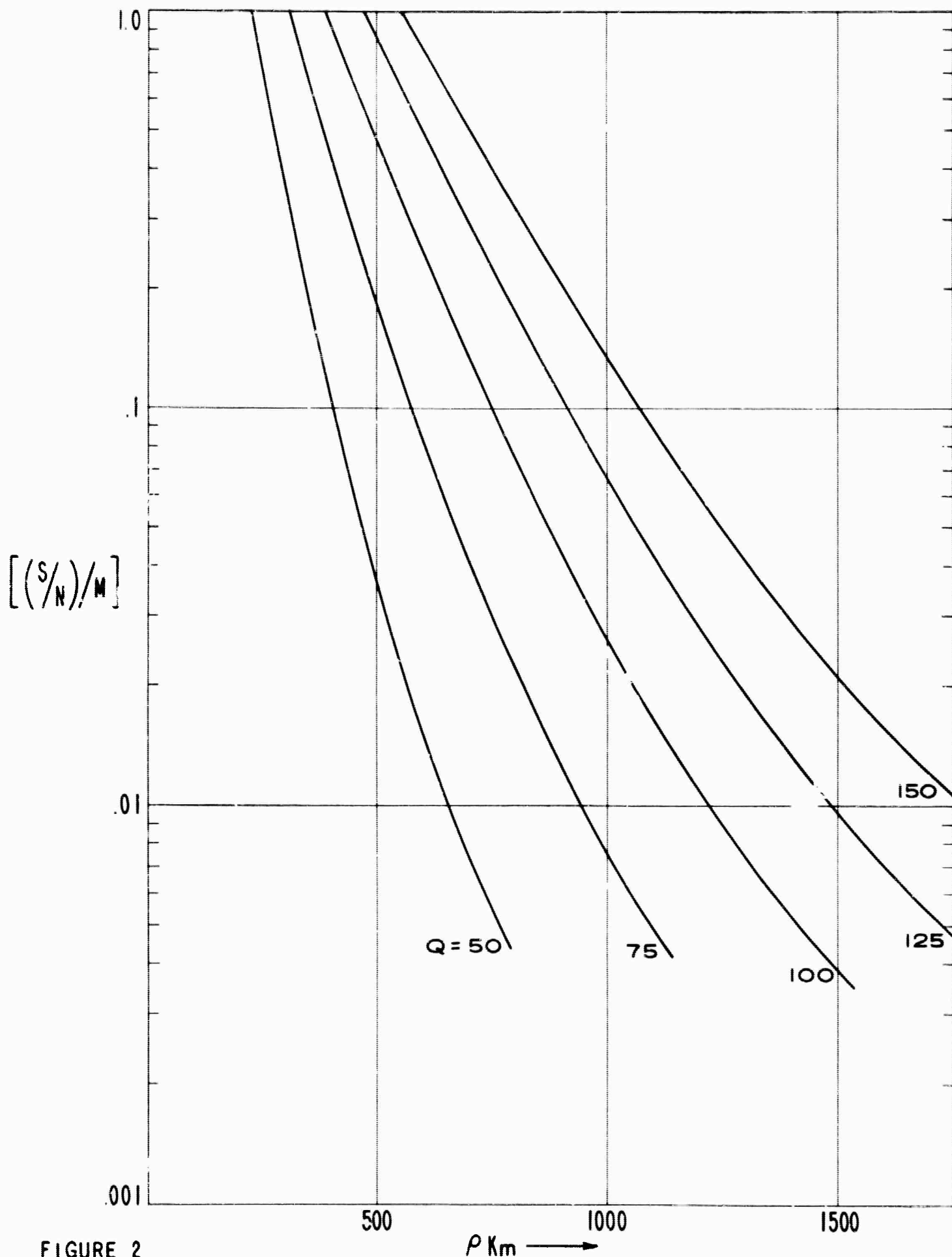


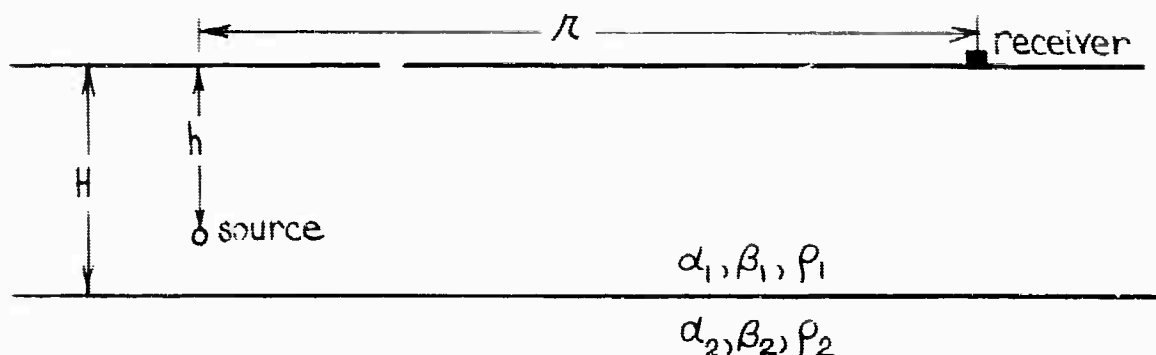
FIGURE 2  
APPROXIMATE SIGNAL TO NOISE RATIO  
PER KILOTON OF TNT AS A FUNCTION  
OF RANGE. DETECTOR IS A SHORT  
PERIOD BENIOFF INSTRUMENT.  $H=0$ .

## 11. THE EFFECT OF SOURCE DEPTH ON RAYLEIGH WAVE MOTION IN A LAYERED EARTH

In comparison with the more conventional use of the body-wave phases, the use of surface waves for source depth determination has both advantages and disadvantages. A prominent disadvantage of surface waves for source depth work is their longer periods. It is evident that the effect of small changes in source depth will be reflected only in the higher frequency portions of the wave train. The results of our Rayleigh wave work substantiate this point. For the case of an earth model consisting of a 30 kilometer crust overlying a half-space of mantle material, the effect of a change in depth for a source within the crust is apparent only at periods less than 10 seconds.

A possible advantage of surface waves in seismic studies is that they undergo less attenuation due to geometrical spreading than body waves. In addition, surface waves are less affected by small changes in velocity structure than body-wave phases. The use of body-wave arrivals for source depth determination requires an accurate knowledge of the velocity structure in the region between the source and the receiver. The recognition of source depth effects on surface wave motion does not require as detailed a knowledge of the velocity structure.

The general method of solution was as follows:



A point impulsive source is located at a depth,  $h$ , within a surface layer of thickness  $H$  overlying a semi-infinite half-space. The motion is recorded at a horizontal offset  $R$  from the source.  $\alpha$ ,  $\beta$ , and  $\rho$  are, respectively, compressional wave speed, shear wave speed, and density. The problem is to obtain an expression, capable of being evaluated, for the motion at a receiver at distance  $R$ . It develops that we cannot obtain a closed algebraic expression for the total motion recorded from the point source. The best we can do is to obtain an integral solution for the motion. It is of the form

$$M = \int_0^{\infty} \int_0^{\infty} J_0(KR) e^{i\omega t} \left\{ \frac{f(Z, \omega, h, H, K)}{\Delta(\omega, K, H)} \right\} d\omega dK.$$

It is not possible to evaluate this integral exactly, but various approaches have been used to obtain certain parts of the solution. One approach (Pekeris, 1948; Spencer, 1960) is to expand the integrand in an infinite series, each term of which represents the contribution from energy that has traveled a particular path to the receiver. Each of these new integrals can be evaluated by Cagniard's method. A second approach, and the one used in the

Rayleigh work, is to attempt a direct evaluation of the integral by means of contour integration. In such an approach the Rayleigh wave, or normal mode motion, arises from the contributions of the residues at the real poles of the integrand. The contributions of these residues were evaluated numerically for the present work. The solutions obtained gave the spectrum of the normal mode motion for both the horizontal and vertical components of displacement resulting from a buried point source.

For the case in which the model consists of a half-space of uniform material, the effect of placing the source deeper beneath the free surface is well known (Rayleigh 1885). The effect of source depth,  $Z$ , upon the spectrum is given by a term  $e^{-\phi f Z}$ , where  $f$  is frequency and  $\phi$  is a term independent of source depth. From this it is evident that a deeper source results in longer period motion. For the case of a source within a layered elastic medium, the effect of source depth upon the normal mode motion is not so simple. In such a system, an infinite number of different modes of propagation are theoretically possible, and the total observed motion is the sum of an infinite number of these modes. The frequency spectra and the relative excitation of the modes are functions of source depth. Hence the total observed motion will also be a function of source depth. The aim of our work on normal mode motion was to determine explicitly just how the source depth does affect the total motion, at least for the first few modes.

The first case considered was that of a liquid layer overlying a liquid half-space. This case, which is algebraically much simpler than the solid case considered later, served as an illustration of the method and, in addition, gave a partial check on the answers, since the case had been previously considered by Pekeris (1948) and certain of his solutions can be applied. The expression for the horizontal and vertical components of displacement,  $q$  and  $W$  respectively, are given by

$$q = 2 \int_0^{\infty} \frac{K}{\epsilon_1} \frac{\Delta_A}{\Delta} (\sin \bar{\nu}_1 Z) J_1(Kr) dK,$$

$$W = -2 \int_0^{\infty} K \frac{\Delta_A}{\Delta} (\cos \bar{\nu}_1 Z) J_0(Kr) dK.$$

$\Delta$  is the Rayleigh determinant,  $K$  is the wave number,  $\epsilon_1 = (\frac{c^2}{\alpha_1^2} - 1)^{1/2}$  and  $\bar{\nu}_1 = K\epsilon_1$ .  $\Delta_A$  is a 3 by 3 determinant involving various parameters of the system. Evaluation of these integrals in the complex zeta plane,  $\zeta = K + i\tau$ , yields the following expressions for the normal mode portions of the solution:

$$W = 2\sqrt{2\pi} \sum_{\text{Res}} K(K/r)^{1/2} (\Delta_A/\Delta') (\cos \bar{\nu}_1 Z) e^{i(\omega\tau - Kr - \pi/4)},$$

$$q = 2\sqrt{2\pi} \sum_{\text{Res}} K(K/r)^{1/2} (\Delta_A/\epsilon_1 \Delta') (\sin \bar{\nu}_1 Z) e^{i(\omega\tau - Kr - 3\pi/4)}.$$

$\Delta'$  represents  $d\Delta/dK$ . The summation is over the real poles of the integrand.

The expressions for  $q$  and  $W$  were evaluated numerically on an IBM 7090 digital computer. The programs were written for variable values of  $r, z, h, H, \alpha, \beta$ , and  $\rho$ . Figures 1 through 6 show examples for the effect of source depth on the vertical component of particle displacement. Figure 1 is a plot of the individual amplitude spectra for the first six normal modes for a source depth of  $1/6$  the layer thickness. Figure 2 shows the amplitude spectra for a source depth of  $29/30$  the layer thickness. Figures 3 through 6 show the amplitude spectra for the motion consisting of the sum of the first six normal modes as a function of source depth. The receiver offset is 18.3 times the layer thickness, and four values of source depth are used.

The general conclusions for the liquid case are that the higher modes are important and give significant contributions to normal mode motion in a liquid system. The amplitude spectra of the individual normal modes are broad and contribute motion over a large range of  $H$  above the cut-off frequency. The spectra for the total summed motion in the liquid-liquid case are quite complicated because of the contribution of the many modes that are required to describe the total motion. The effect of source depth on the finer structure of the spectra for the total normal mode motion in the liquid-liquid case most probably will not be observed because of the complicated nature of the summed spectra. The most important feature seems to be a broadening of the spectrum as the source is placed deeper within the layer. Longer period components are relatively stronger for deeper sources.



For the case of a solid elastic layer overlying a solid half-space, equations similar to those for the liquid case were obtained. The solid case equations are, however, quite lengthy and will not be written down here. It was found that the higher normal modes are not nearly so important in the solid case as they are for the liquid case. Three modes are sufficient to describe the total Rayleigh wave motion with reasonable accuracy. The spectra of the individual normal modes are more sharply peaked than in the liquid case. Figures 7 through 9 show examples of the amplitude spectra for the horizontal component of displacement of the first three Rayleigh modes. Examples are taken for source depths of  $1/30$  the layer thickness,  $1/3$  the layer thickness, and  $2/3$  the layer thickness. Figures 10 through 15 show the spectrum of the total motion resulting from the sum of the first three normal modes. This again is for the horizontal component of displacement, and the source depths are taken from near the free surface at  $1/30$  the layer thickness to near the layer-half space interface at  $29/30$  the layer thickness. The effect of source depth on the spectrum is apparent only where the contribution of the second mode begins to be significant. This is at a value of  $fH/\alpha_1 = .5$  for a 30-kilometer crust, and for this case corresponds to a period of 10 seconds. An appreciable difference in the spectra as a function of source depth appears only for periods of 7 seconds or less. The peak of the Rayleigh wave motion for a source within a 30-kilometer crust is at a period of 20 seconds. A source near

the free surface generates predominantly first mode motion. As the source is placed deeper within the layer, the higher modes, and higher frequencies, become relatively more important.

In summary, there are theoretically predicted differences in the amplitude spectrum of Rayleigh wave motion as a function of source depth. These differences are evident only in the higher frequency portion of the wave train at periods less than 10 seconds. Whether these effects will be useful in practice in the presence of microseism noise is a question best answered by an analysis of field seismograms.

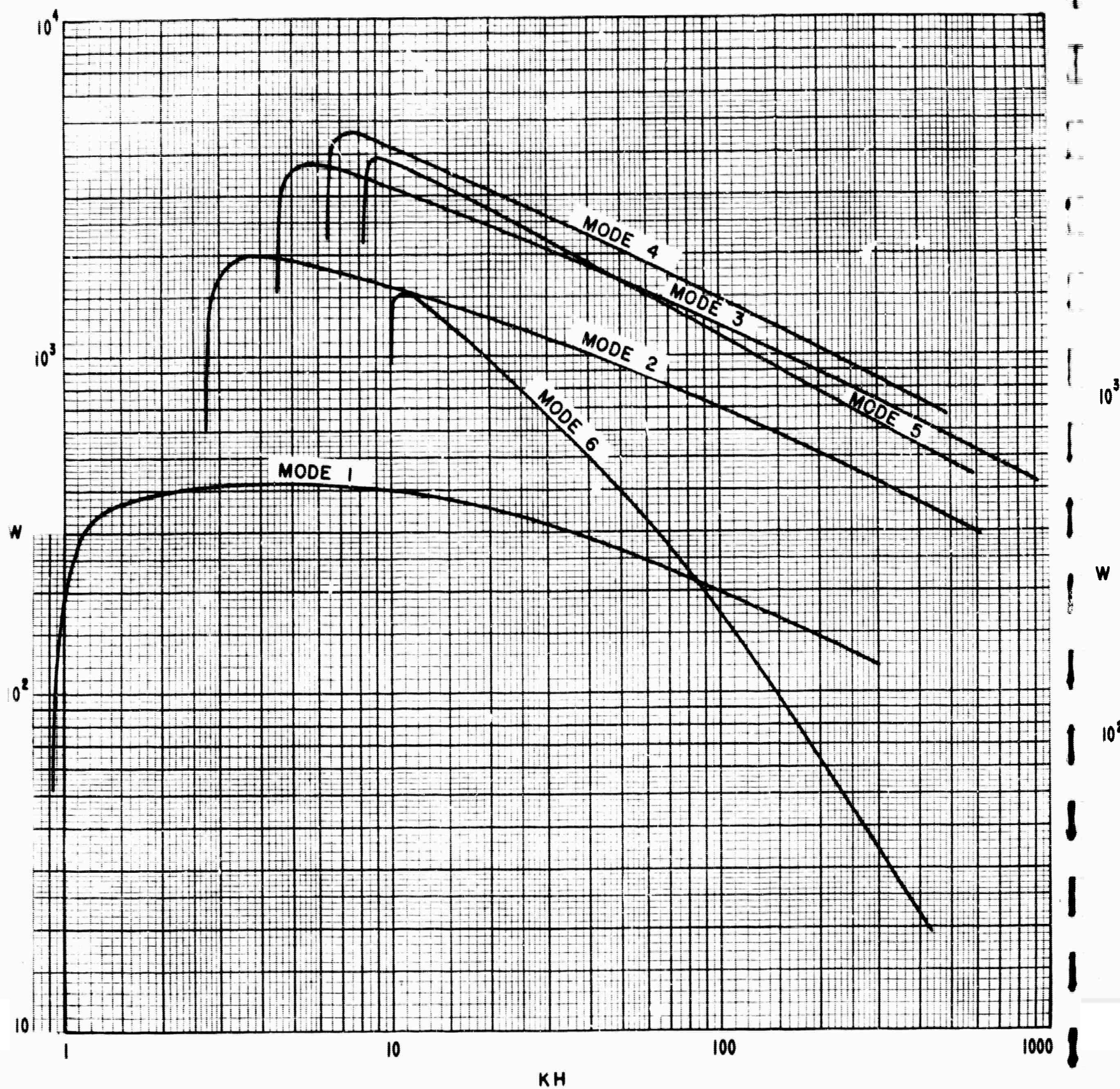


FIGURE 1

SPECTRA OF INDIVIDUAL NORMAL  
MODES FOR LIQUID CASE.

$$\frac{\rho_2}{\rho_1} = 2.0, \quad \frac{\alpha_2}{\alpha_1} = 2.0, \quad h = \frac{H}{6}$$

LE 42-786

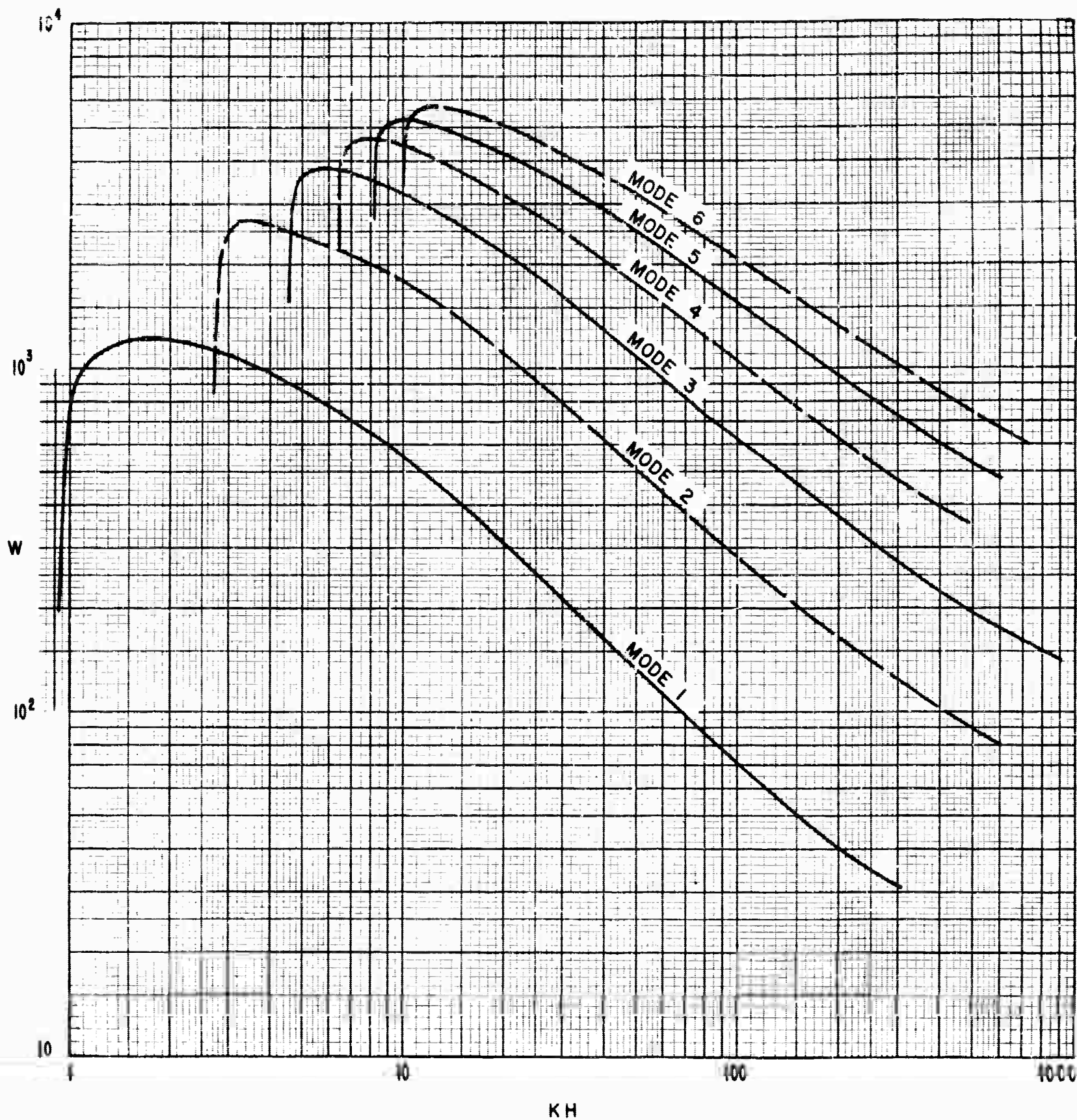


FIGURE 2

SPECTRA OF INDIVIDUAL NORMAL  
MODES FOR LIQUID CASE.

$$\frac{\rho_2}{\rho_1} = 2.0, \quad \frac{\alpha_2}{\alpha_1} = 2.0, \quad h = \frac{29H}{30}$$



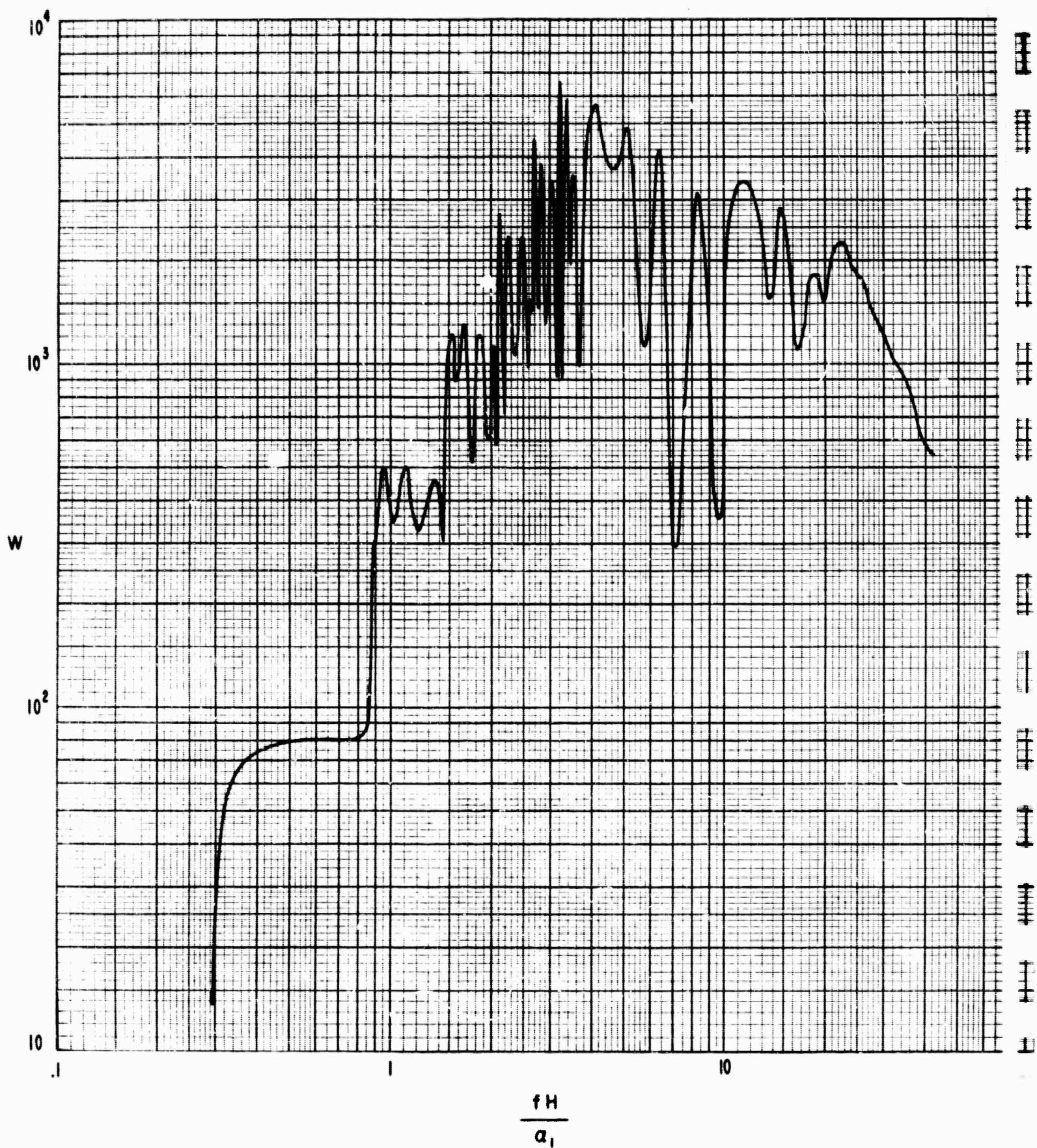


FIGURE 3

SPECTRUM OF SUM OF FIRST  
SIX NORMAL MODES.

$$h = \frac{H}{30}, \quad r = 18.3H$$

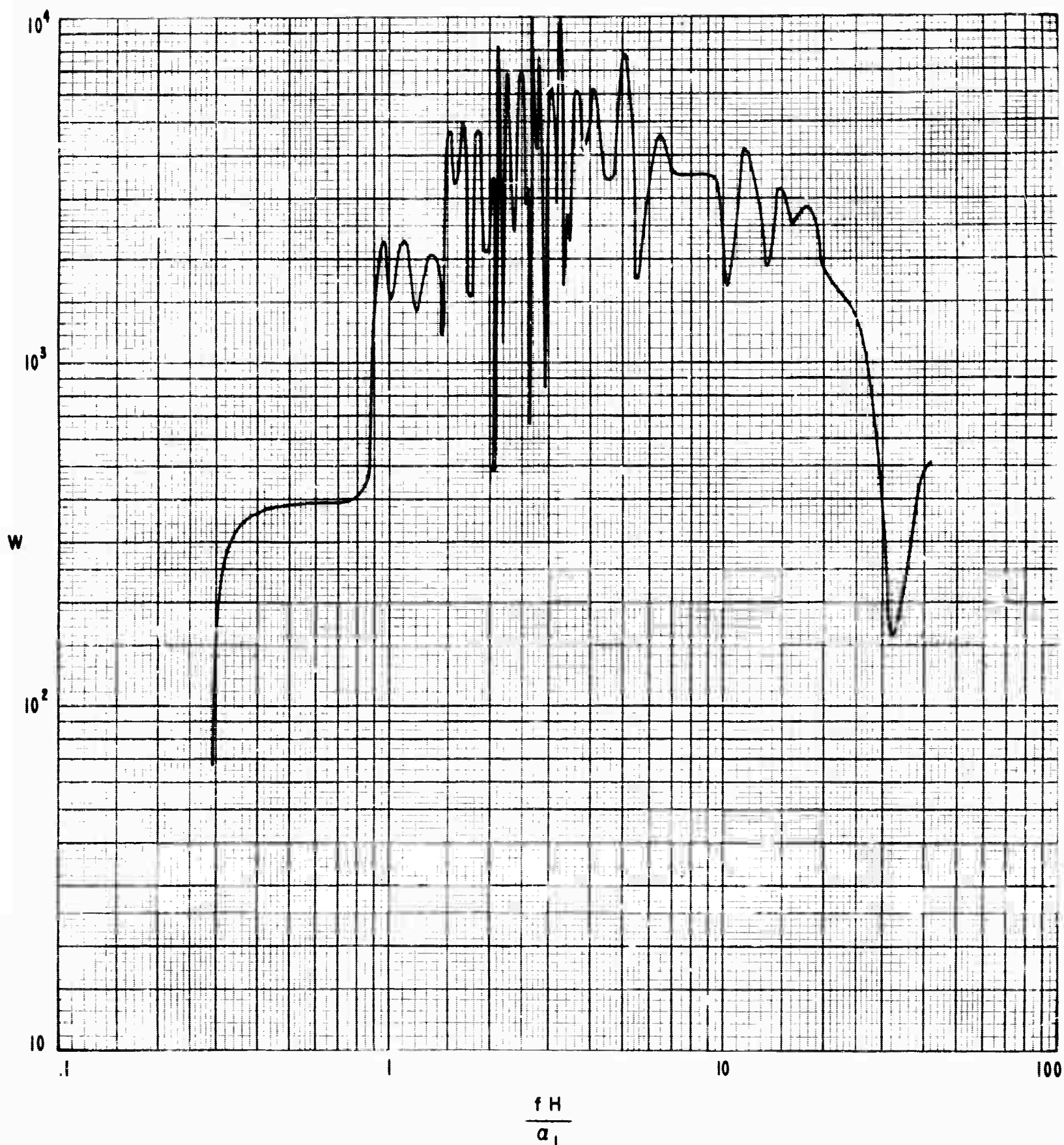


FIGURE 4

SPECTRUM OF SUM OF FIRST  
SIX NORMAL MODES.

$$h = \frac{H}{6}, \quad r = 18.3 H$$

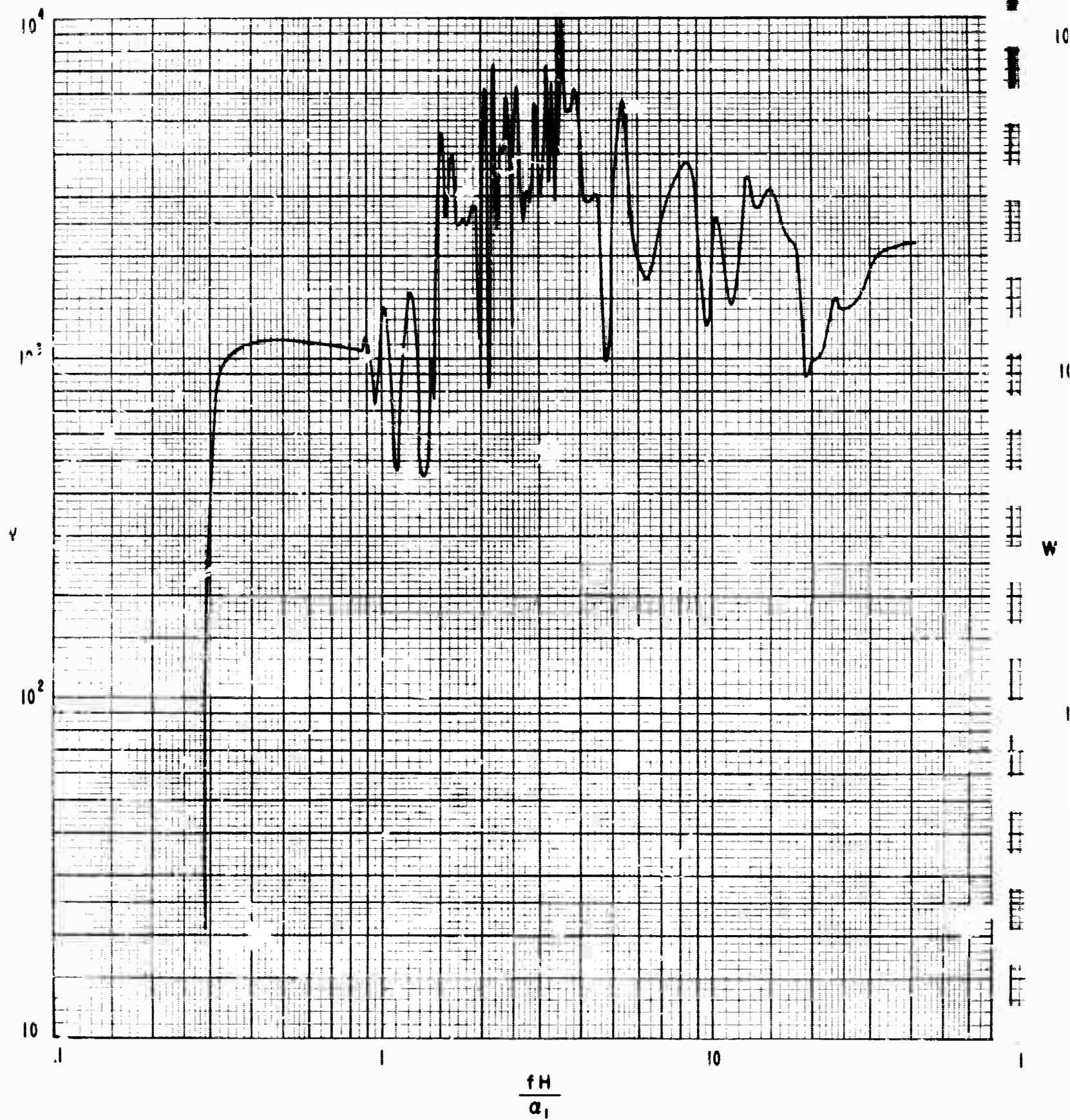


FIGURE 5

SPECTRUM OF SUM OF FIRST  
SIX NORMAL MODES.

$$h = \frac{2H}{3}, \quad r = 18.3H$$



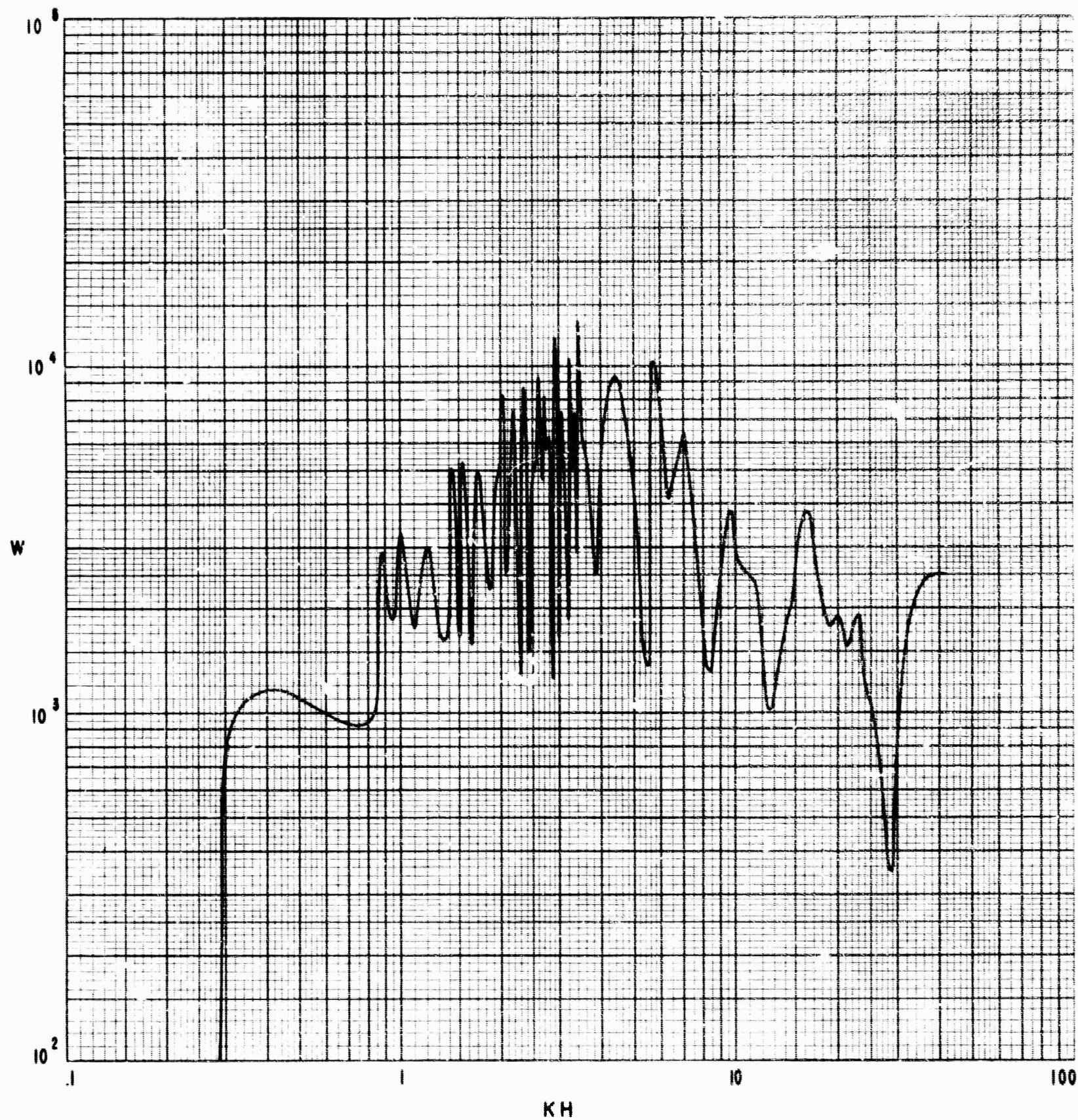


FIGURE 6

SPECTRUM OF SUM OF FIRST  
SIX NORMAL MODES.

$$h = \frac{29H}{30}, \quad r = 18.3 H$$



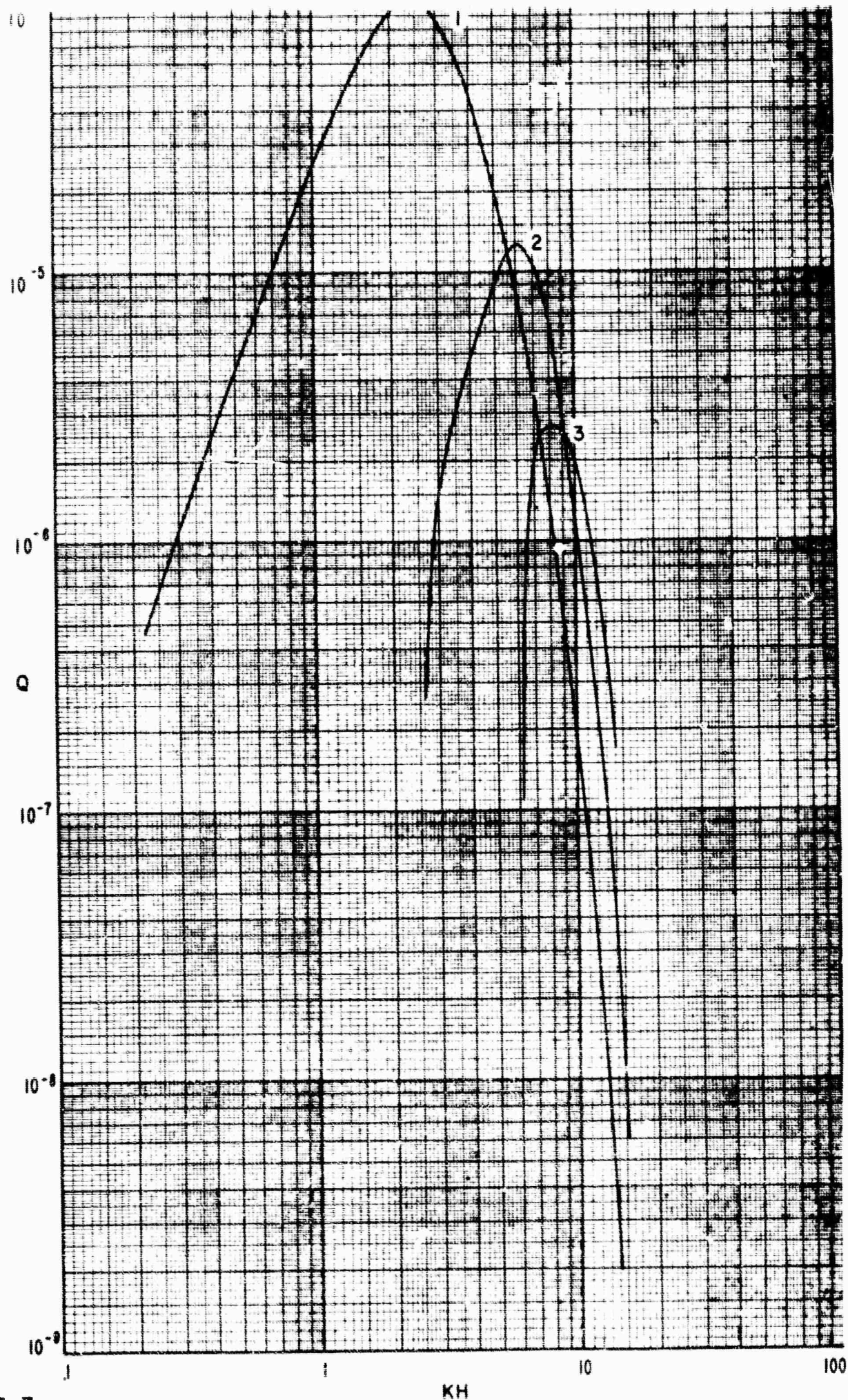


FIGURE 7

INDIVIDUAL SPECTRA FOR HORIZONTAL COMPONENT OF  
DISPLACEMENT FOR FIRST THREE RAYLEIGH MODES.  
SOLID LAYER OVER SOLID HALF SPACE.

$$\alpha_2=8.1, \alpha_1=6.08, \beta_2=4.67, \beta_1=3.51, \frac{\mu_2}{\mu_1}=\frac{20}{9} \quad h=\frac{H}{30}$$



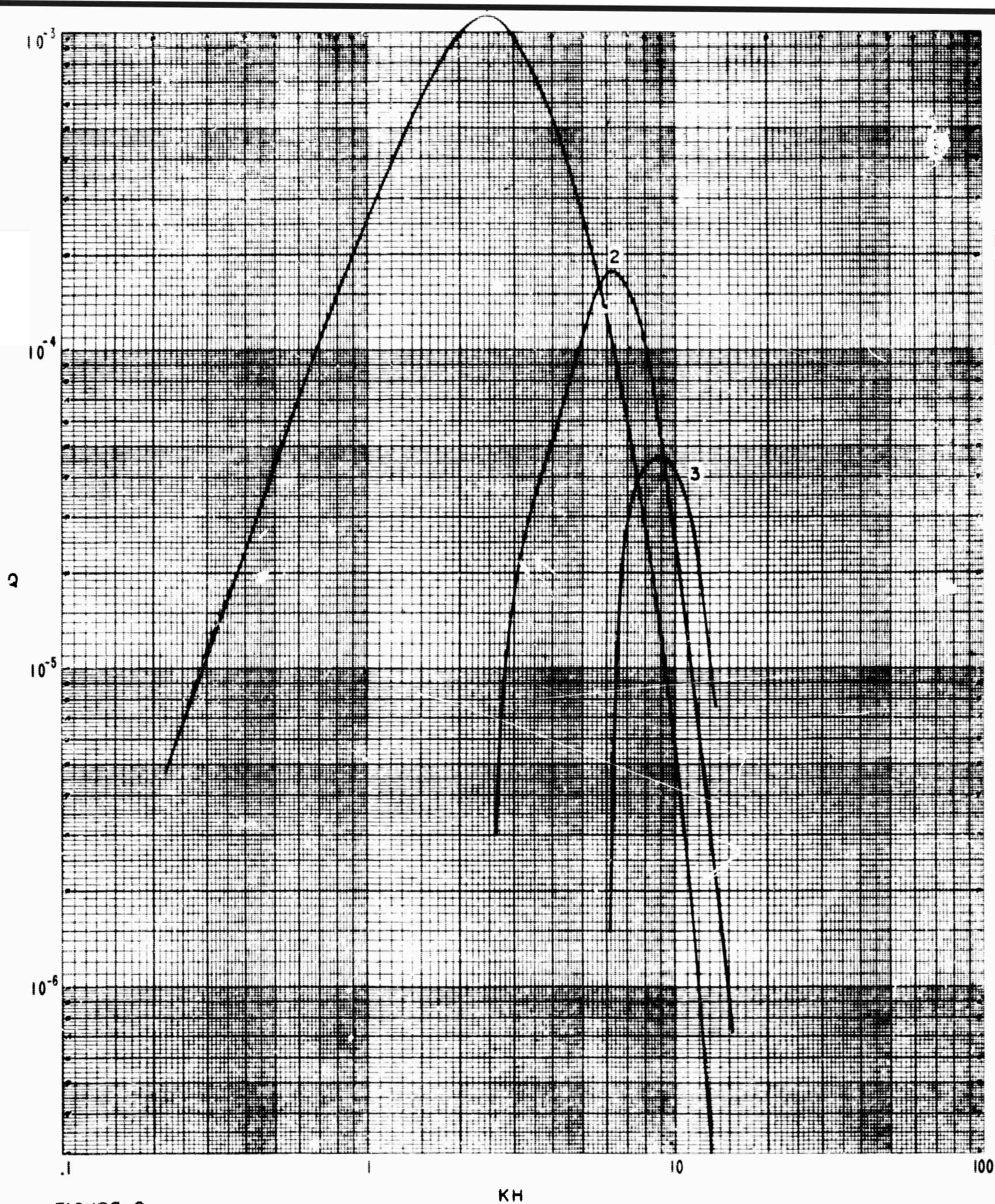


FIGURE 8

INDIVIDUAL SPECTRA FOR HORIZONTAL COMPONENT OF  
DISPLACEMENT FOR FIRST THREE RAYLEIGH MODES.  
SOLID LAYER OVER SOLID HALF SPACE.

$$\alpha_2 = 8.1, \alpha_1 = 6.08, \beta_2 = 4.67, \beta_1 = 3.51, \frac{\mu_2}{\mu_1} = \frac{20}{9} \quad h = \frac{H}{3}$$



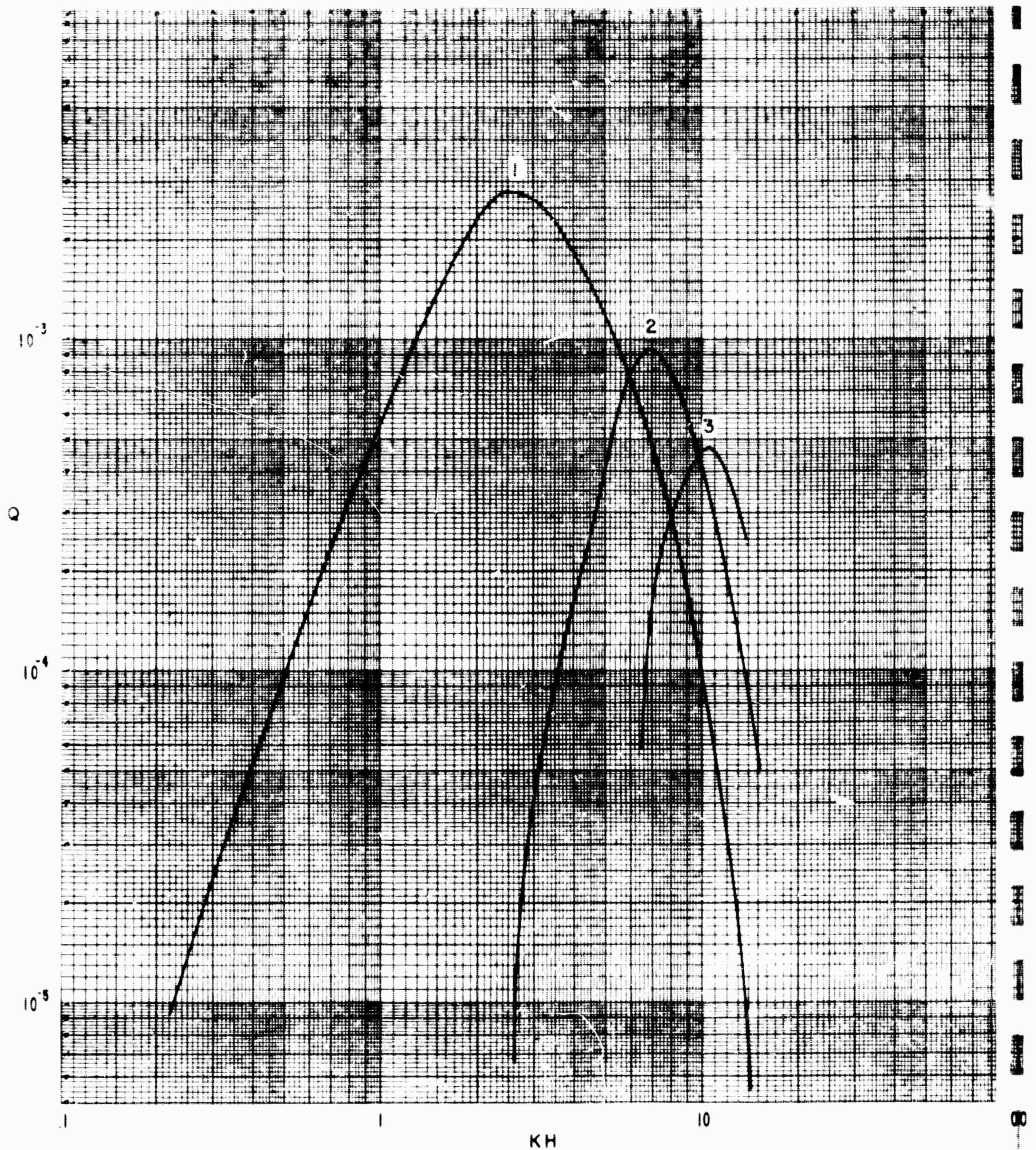
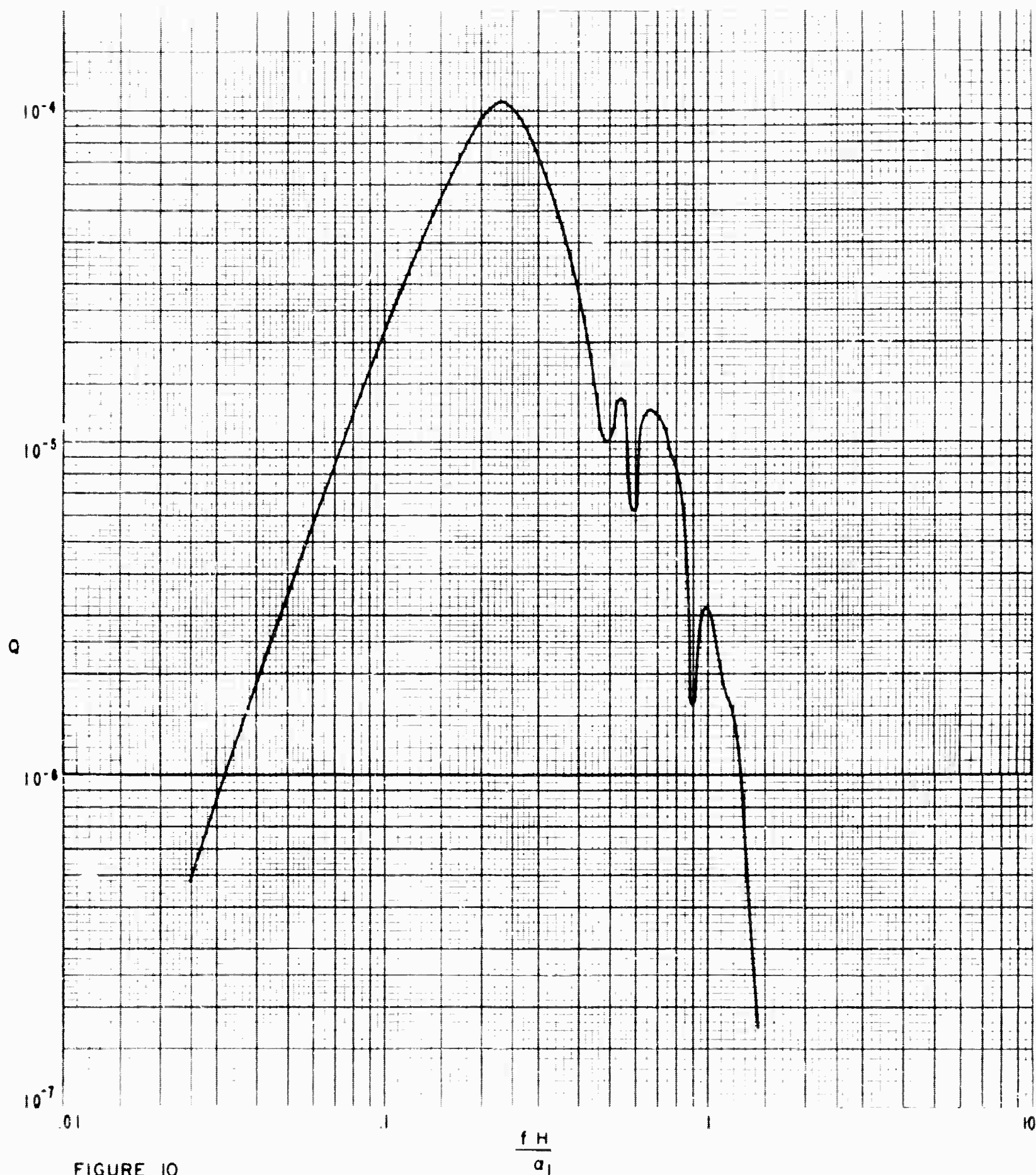


FIGURE 9

INDIVIDUAL SPECTRA FOR HORIZONTAL COMPONENT OF  
DISPLACEMENT FOR FIRST THREE RAYLEIGH MODES.  
SOLID LAYER OVER SOLID HALF SPACE.

$$\alpha_2 = 8.1, \alpha = 6.08, \beta_2 = 4.67, \beta_1 = 3.51, \frac{r_2}{\mu_1} = \frac{20}{9}, h = \frac{2H}{3}$$



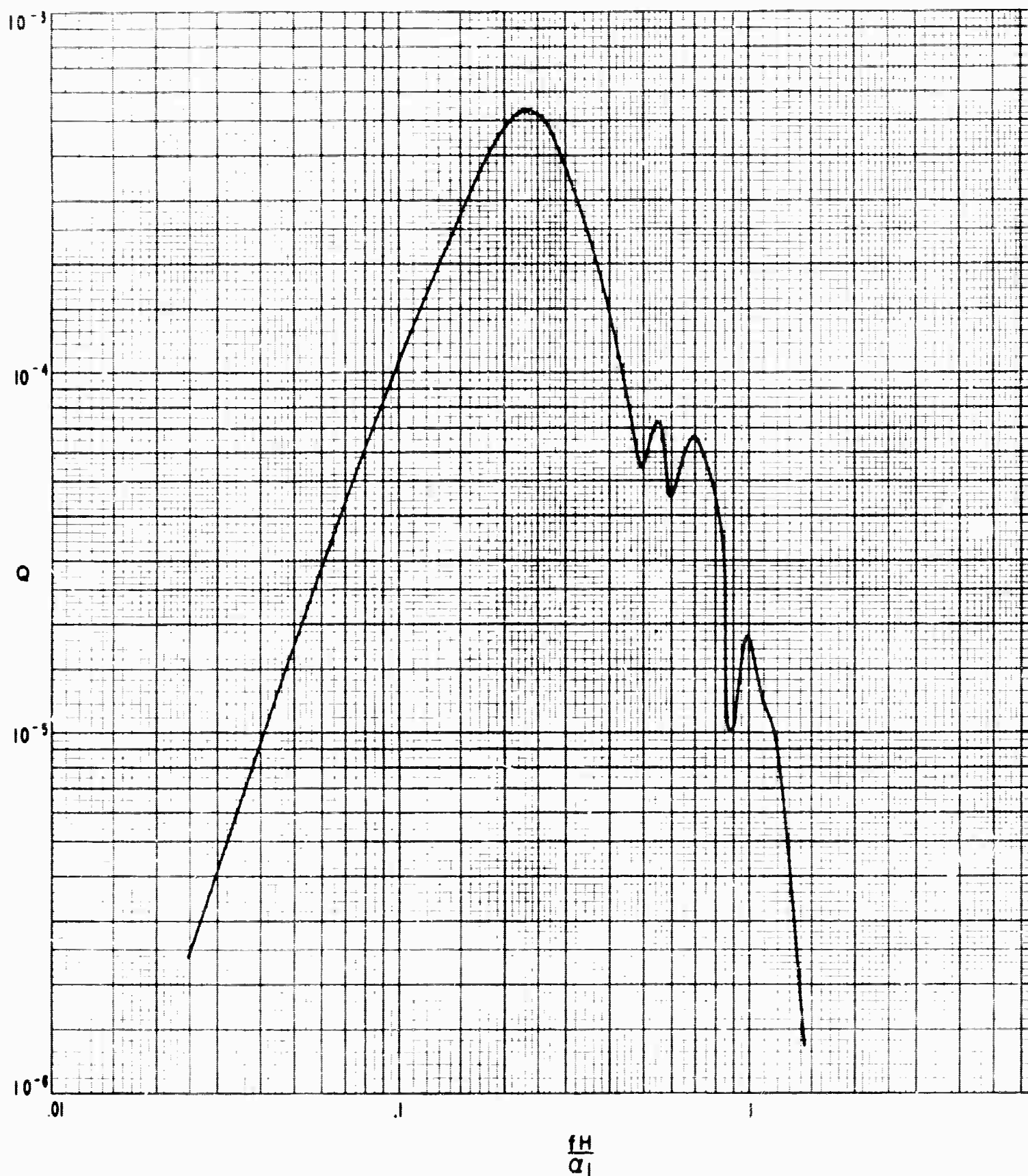


FIGURE II

SPECTRUM OF SUM OF HORIZONTAL DISPLACEMENTS  
FOR FIRST THREE RAYLEIGH MODES.

SOLID - SOLID MODEL.

$$h = \frac{H}{6}, \quad r = 16.7H$$



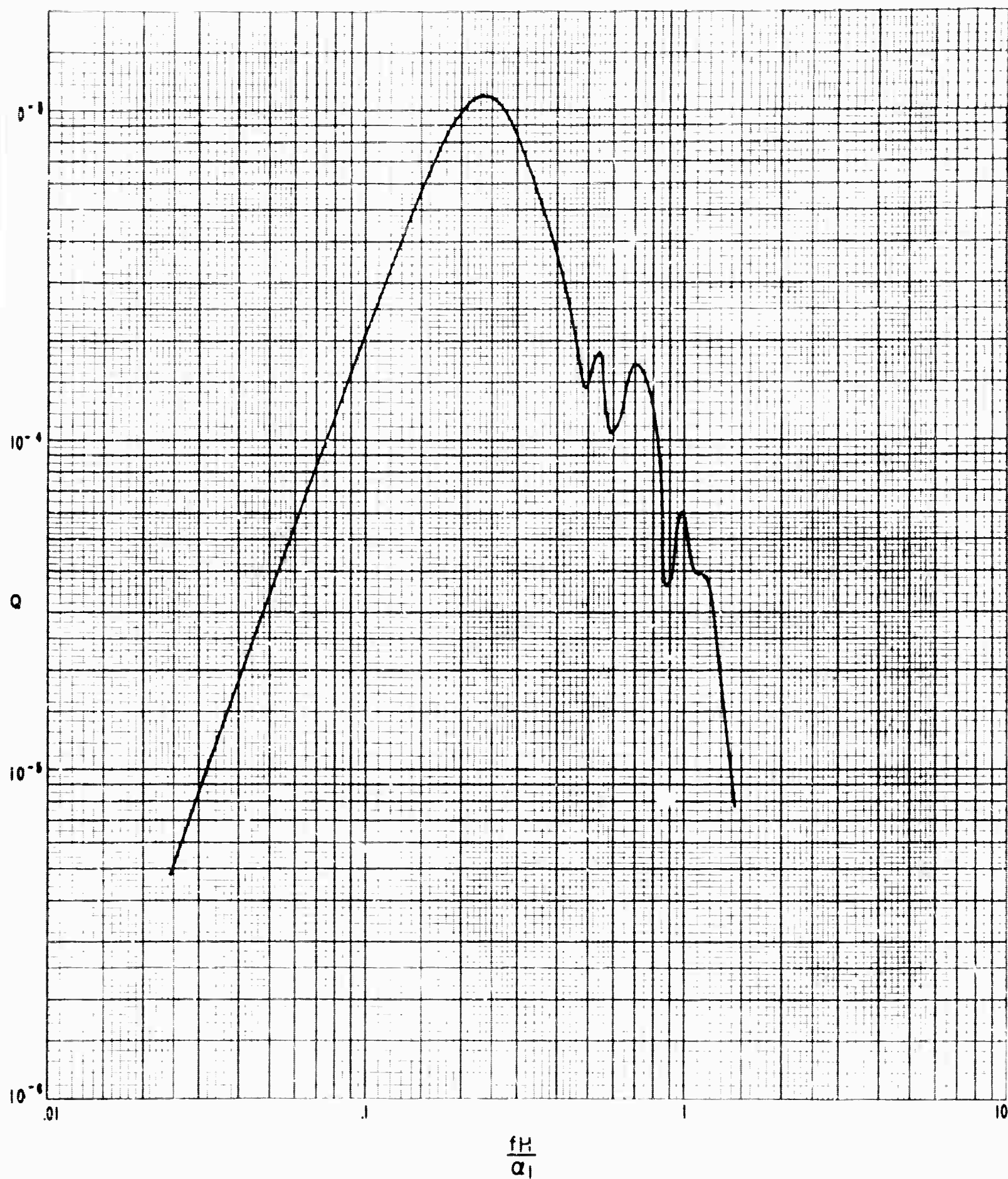


FIGURE 12

SPECTRUM OF SUM OF HORIZONTAL DISPLACEMENTS  
FOR FIRST THREE RAYLEIGH MODES.

SOLID - SOLID MODEL.

$$h = \frac{H}{3}, \quad r = 16.7H$$

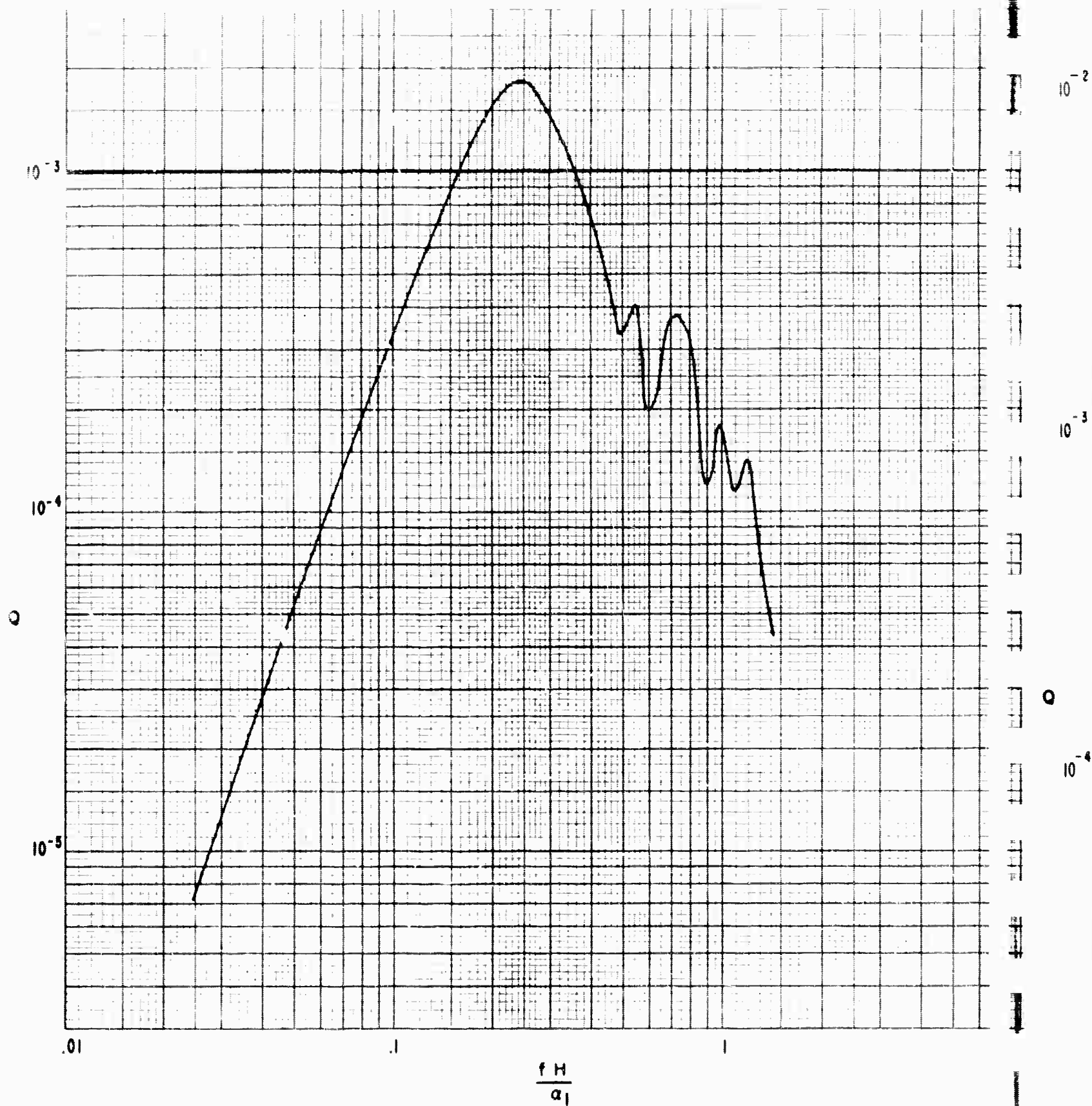


FIGURE 13

SPECTRUM OF SUM OF HORIZONTAL DISPLACEMENTS  
FOR FIRST THREE RAYLEIGH MODES.

SOLID - SOLID MODEL

$$h = \frac{H}{2}, \quad r = 16.7H$$

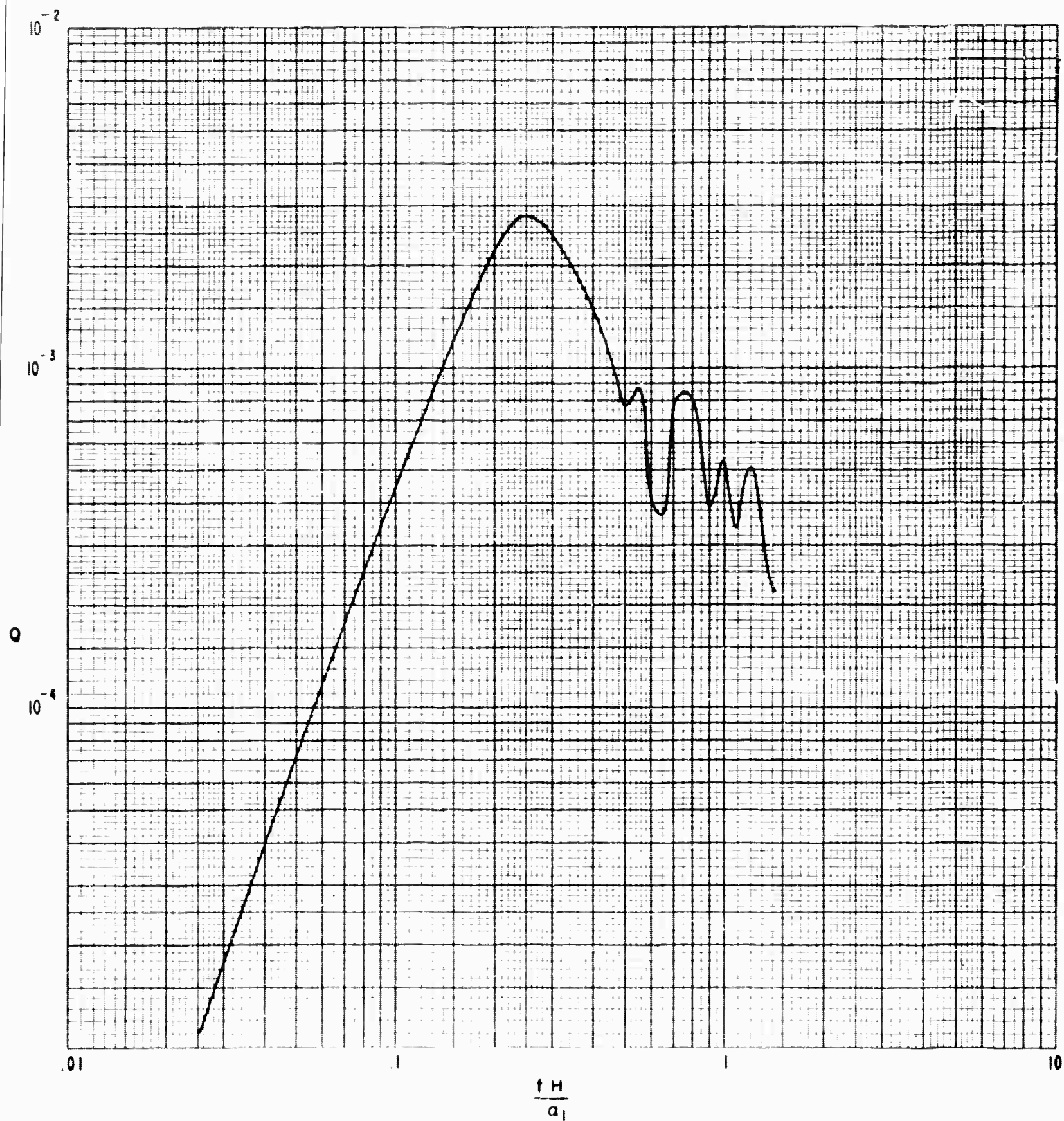


FIGURE 14

SPECTRUM OF SUM OF HORIZONTAL DISPLACEMENTS  
FOR FIRST THREE RAYLEIGH MODES.

SOLID-SOLID MODEL

$$h = \frac{2H}{3}, \quad r = 16.7H$$



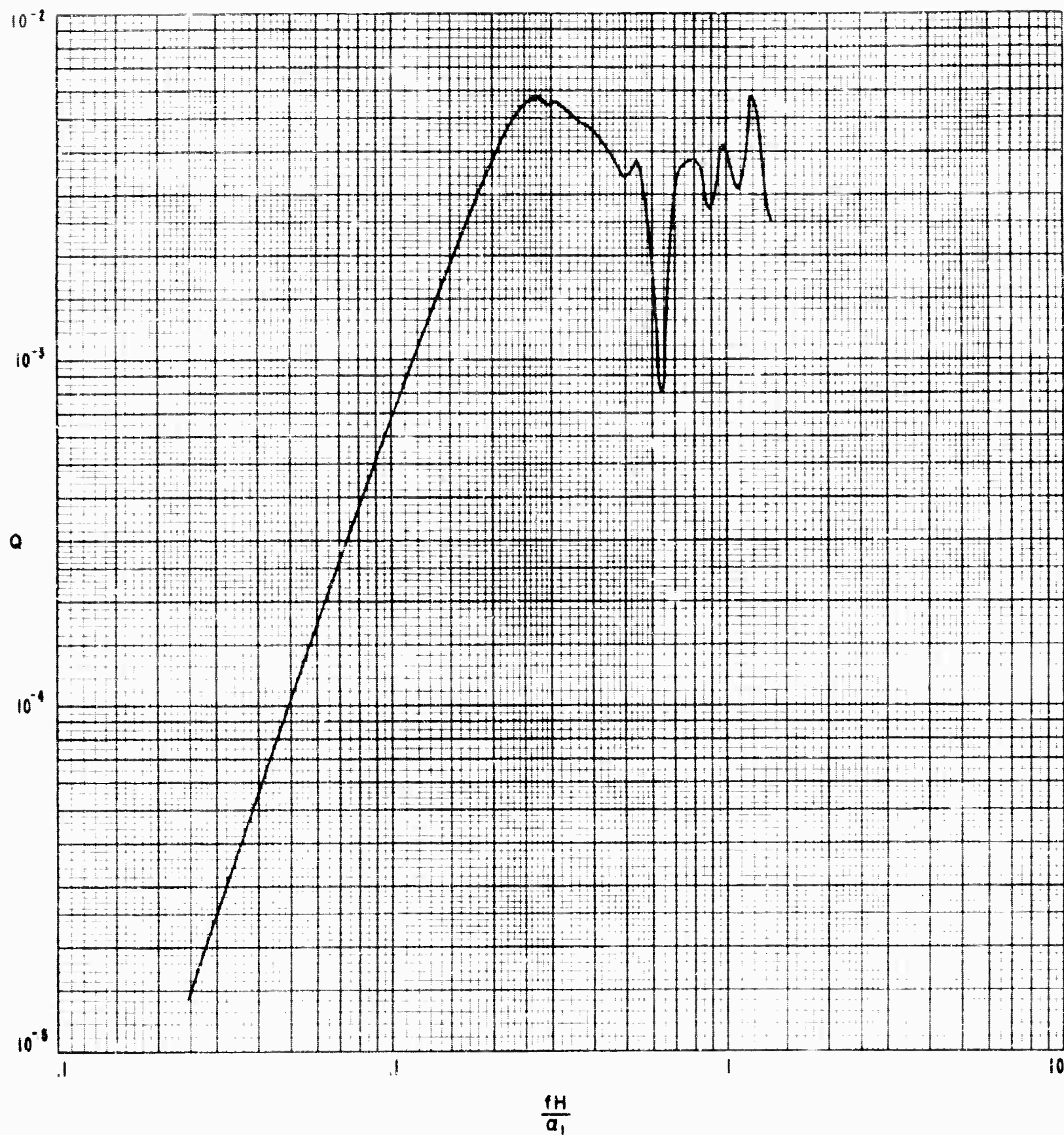


FIGURE 15

SPECTRUM OF SUM OF HORIZONTAL DISPLACEMENTS  
FOR FIRST THREE RAYLEIGH MODES.

SOLID - SOLID MODEL.

$$h = \frac{29H}{30}, \quad r = 16.7 H$$

### III. SEISMIC MODELING

#### A. Explosive Sources

Initially the model work was set up to supply corroborating data for our theoretical work dealing with the effect of source depth upon Rayleigh wave motion. The theoretical solutions give the motion produced by an impulsive, point, compressional source. Because of this we wanted a source with as wide a band as possible and hence began our work using an explosive source. In this section we review the results which were obtained using this source.

Two-dimensional seismic models were used for all the cases which we studied. It is easier to construct and work with two-dimensional models and then extend the results to three-dimensional wave propagation than it is to construct three-dimensional models. The basic model consisted of a sheet of cold-rolled steel, 8 feet long, 4 feet wide, and .060 inch thick. For the wavelengths used in the modeling experiments, the thickness of this sheet is vanishingly small. A layer having elastic properties different from those of the steel was formed along one edge of the sheet by first milling out a groove .030 inch deep, 1 inch wide, and 8 feet long. This milled-out section was then filled with a low velocity material to simulate the case of a low-velocity layer overlying a high-velocity half-space. In the earlier work the groove was filled with a 50-50 lead-tin solder. Unfortunately, it was difficult to hold the thickness of the solder

layer to a proper tolerance without a further milling operation. A different method was employed for later models. This method consisted of cementing a copper strip .030 inch thick, 1 inch wide, and 8 feet long into the milled-out section. This gives good control over the thickness of the composite layer but introduces the problem of obtaining good coupling between the copper and the steel. A semi-rigid epoxy cement, Eccobond 45, was used in constructing the models for the explosive source work. A slightly flexible epoxy was chosen so that the bond between the copper and the steel might withstand a small amount of flexing without breaking and so that the model would be better able to resist the high local stresses resulting from the explosions. This type of epoxy did give a somewhat smaller signal amplitude than a similar model with a rigid epoxy, but this was not a problem since there was always sufficient signal strength from the explosive source.

Figure 1 shows the construction of the two-dimensional seismic models. Wave propagation in two-dimensional seismic models has been discussed by Oliver, et al., (1954). Compressional wave energy propagates with the plate wave velocity of the material. The shear wave energy propagates with the shear velocity in an infinite solid and is unaffected by the two-dimensional nature of the system. Rayleigh waves in two dimensions propagate in a slightly different manner from those in the infinite solid case. The major difference between the infinite solid and the two-dimensional case is that the plate dilatational velocity replaces the bulk P wave velocity in the Rayleigh equation.

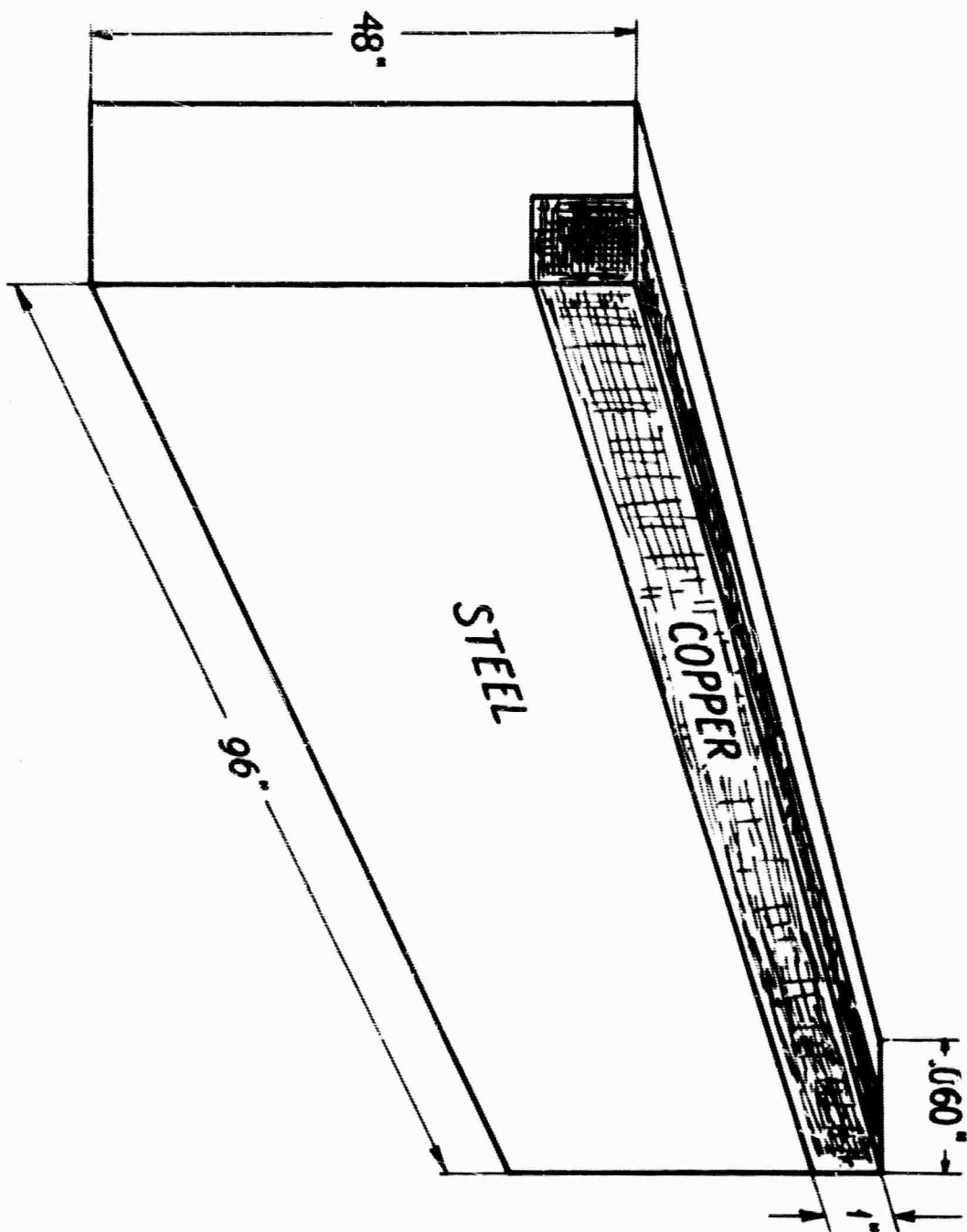


FIGURE 1

CONSTRUCTION OF THE 2 DIMENSIONAL SEISMIC MODELS

The seismic velocities in the composite layer are governed by the relative thicknesses, densities, and elastic parameters of the materials making up the layer. For wavelengths which are long compared to the total thickness of the layer, the body-wave velocities in the composite system are given by Angona (1960) as:

$$C^2 = \frac{\alpha_1 \rho_1 C_1^2 + \alpha_2 \rho_2 C_2^2 + \dots + \alpha_n \rho_n C_n^2}{\alpha_1 \rho_1 + \alpha_2 \rho_2 + \dots + \alpha_n \rho_n}$$

where

$\alpha_n$  is the fraction of material  $n$ ,

$\rho_n$  is the density of material  $n$ ,

$C_n$  is the acoustic wave velocity of material  $n$ .

The phase and group velocities for the first three Rayleigh modes for the model shown in Figure 1 are given in Figure 2. The phase velocities of the higher modes lie between the shear velocity in the steel and that in the composite layer. The first mode phase velocities lie between the Rayleigh velocities in the steel plate and in the composite layer.

The source used in these model experiments was a small charge of silver acetylide. Silver acetylide is formed as a precipitate when acetylene gas is bubbled through an aqueous solution of silver nitrate. When dry this precipitate is a powerful explosive which can be detonated by either heat or shock. A certain amount of care is required in the preparation and use of this explosive.

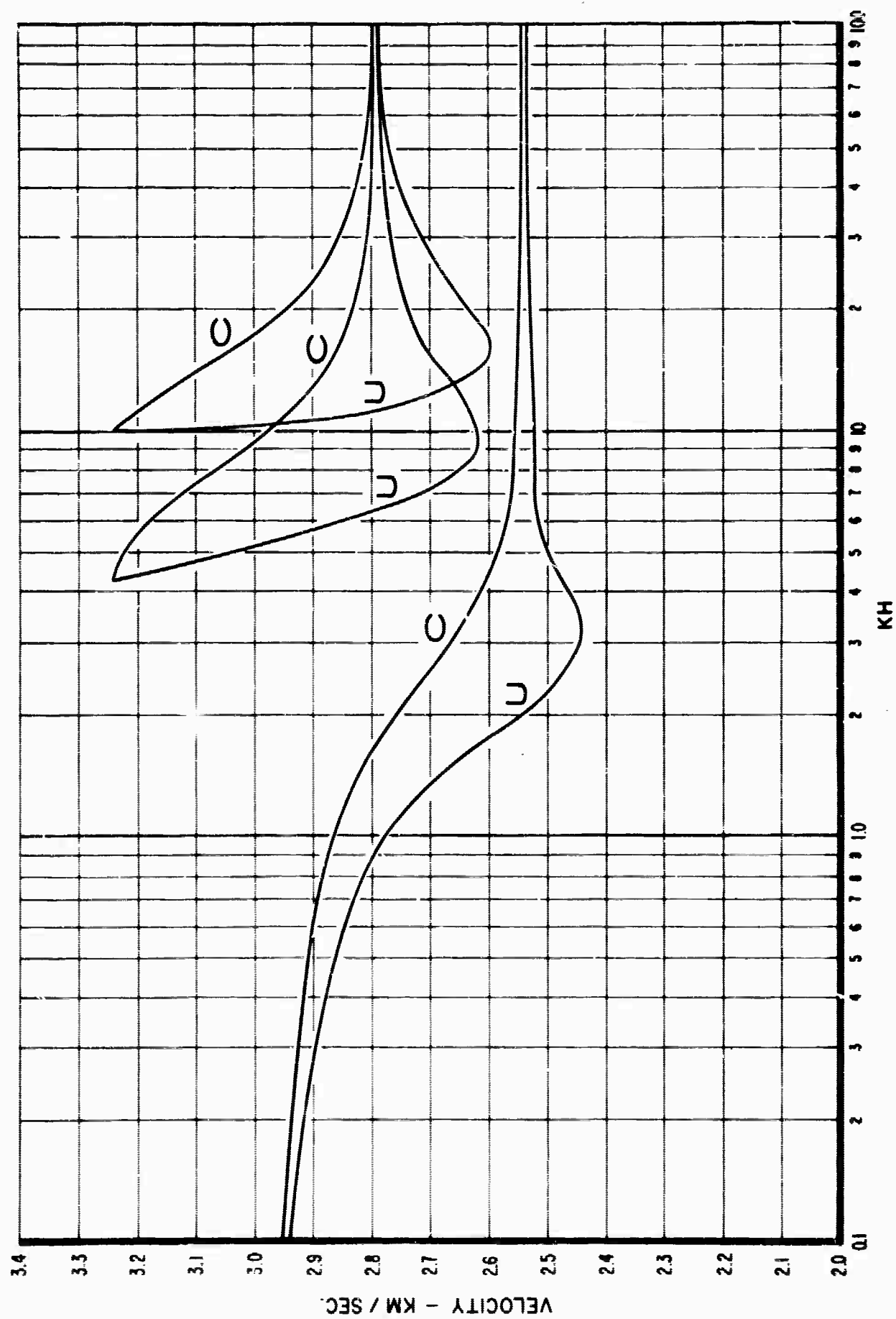


FIGURE 2

PHASE AND GROUP VELOCITY FOR FIRST THREE RAYLEIGH MODES IN 2 DIMENSIONAL SEISMIC MODEL.

Chemically pure silver nitrate, distilled water, and purified acetylene (99.5 per cent minimum purity) are used in making the explosive. The use of tap water can lead to precipitates which are too unstable to be handled safely in model work. Four grams of silver nitrate are dissolved in 150 milliliters of distilled water, and acetylene is bubbled through the mixture until the yellow precipitate is formed (about five minutes). The precipitate is collected on a filter paper and dried by blotting with dry filter papers until it becomes a plastic mass. The silver acetylide charges are then shaped and mounted on a small rod. Figure 3 shows the details of the die in which the charges are made. Figure 4 shows the procedure for making the charges. The charges are .048 inch in diameter, 0.1 inch in length, and are mounted on the end of a steel rod. The charges are detonated by means of an electrically heated wire which is positioned close to the explosive. The flash of the charge is used to trigger the oscilloscope on which the model records are displayed.

The receiver which was first used in this particular model work is essentially a condenser microphone. The surface of the model, or one face of a small square hole cut into the model, forms one plate of the condenser microphone. The other plate is mounted on the end of a shielded lead connecting directly to the grid of a cathode follower. From the cathode follower the

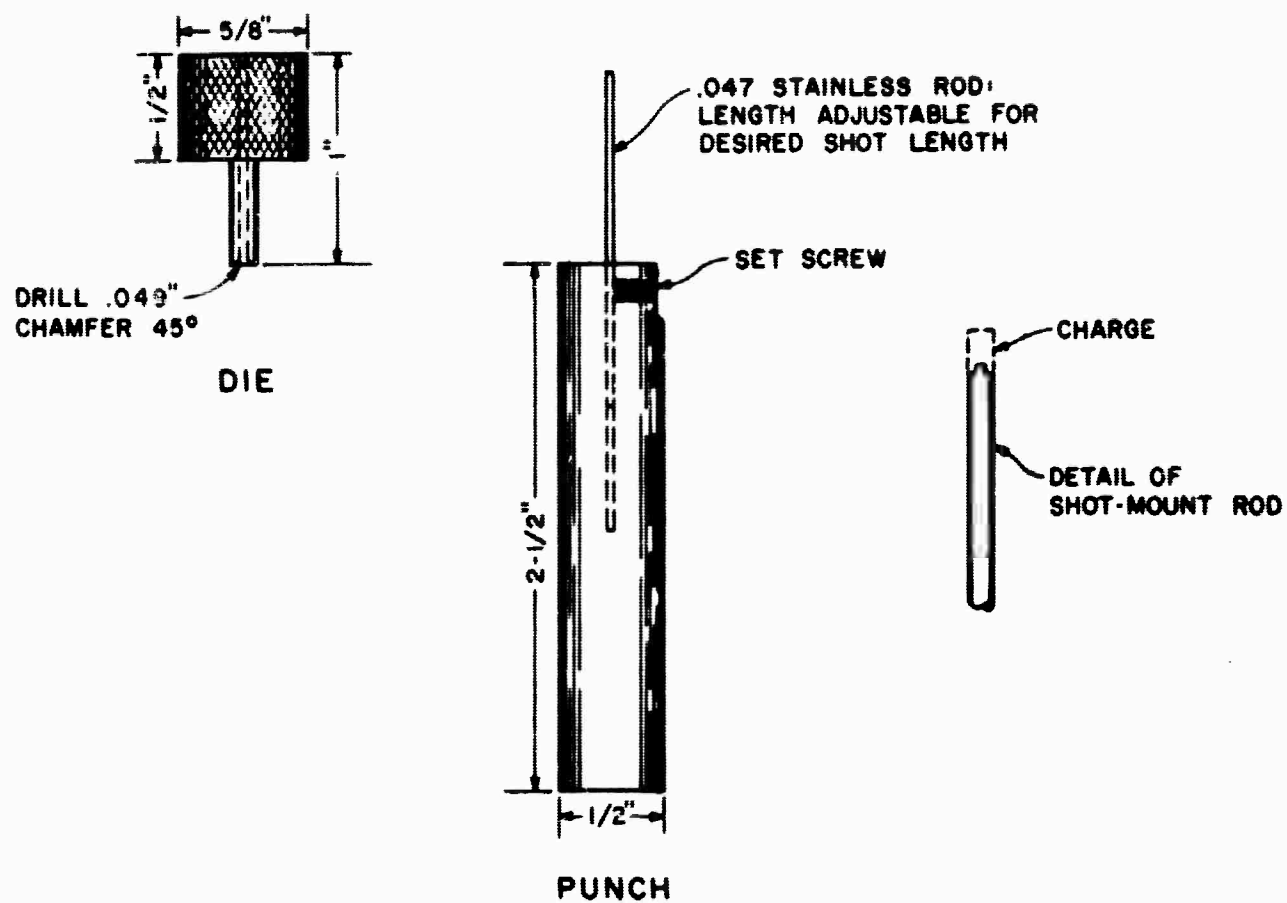
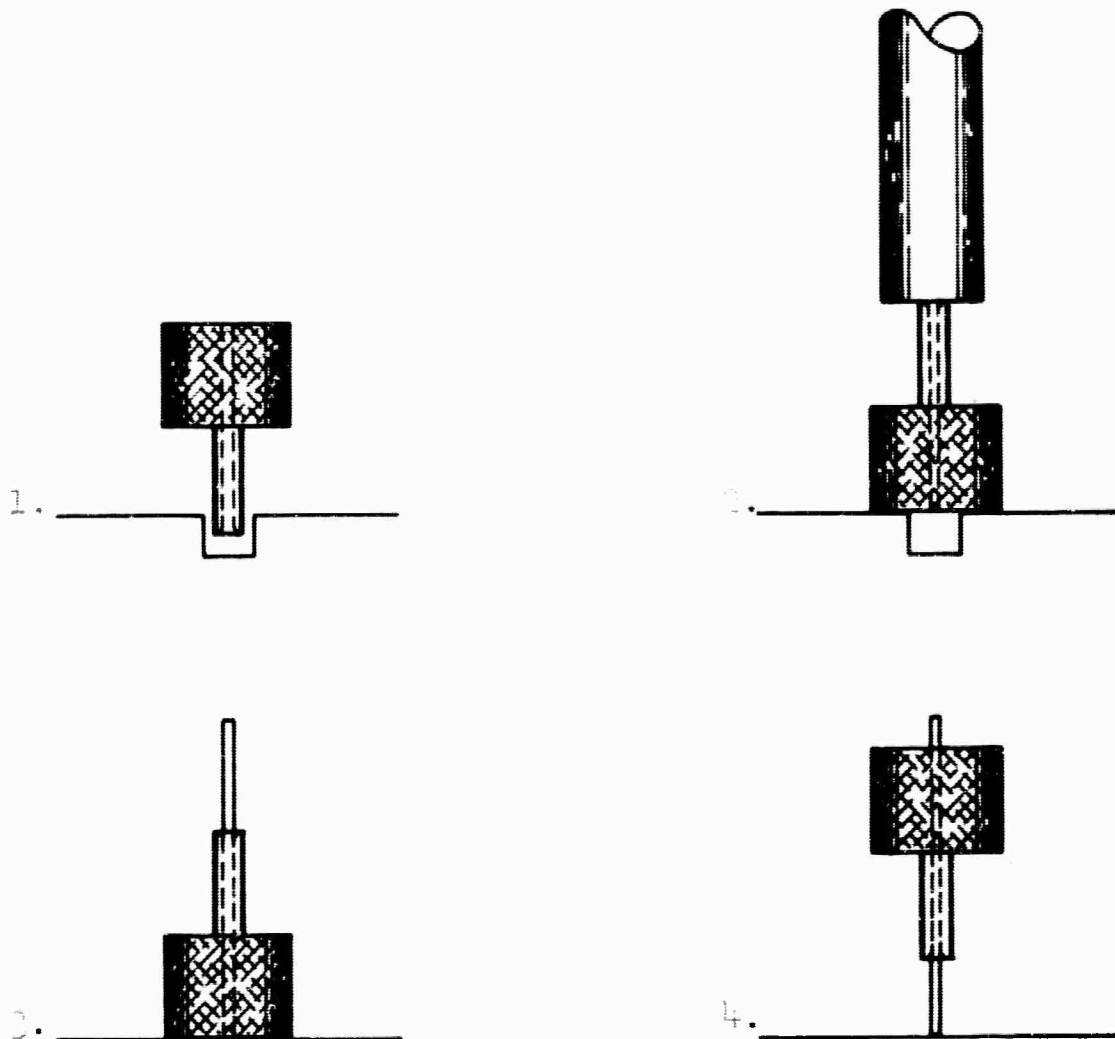


FIGURE 3

SILVER ACETYLIDE MOLDING USED IN SEISMIC MODELING





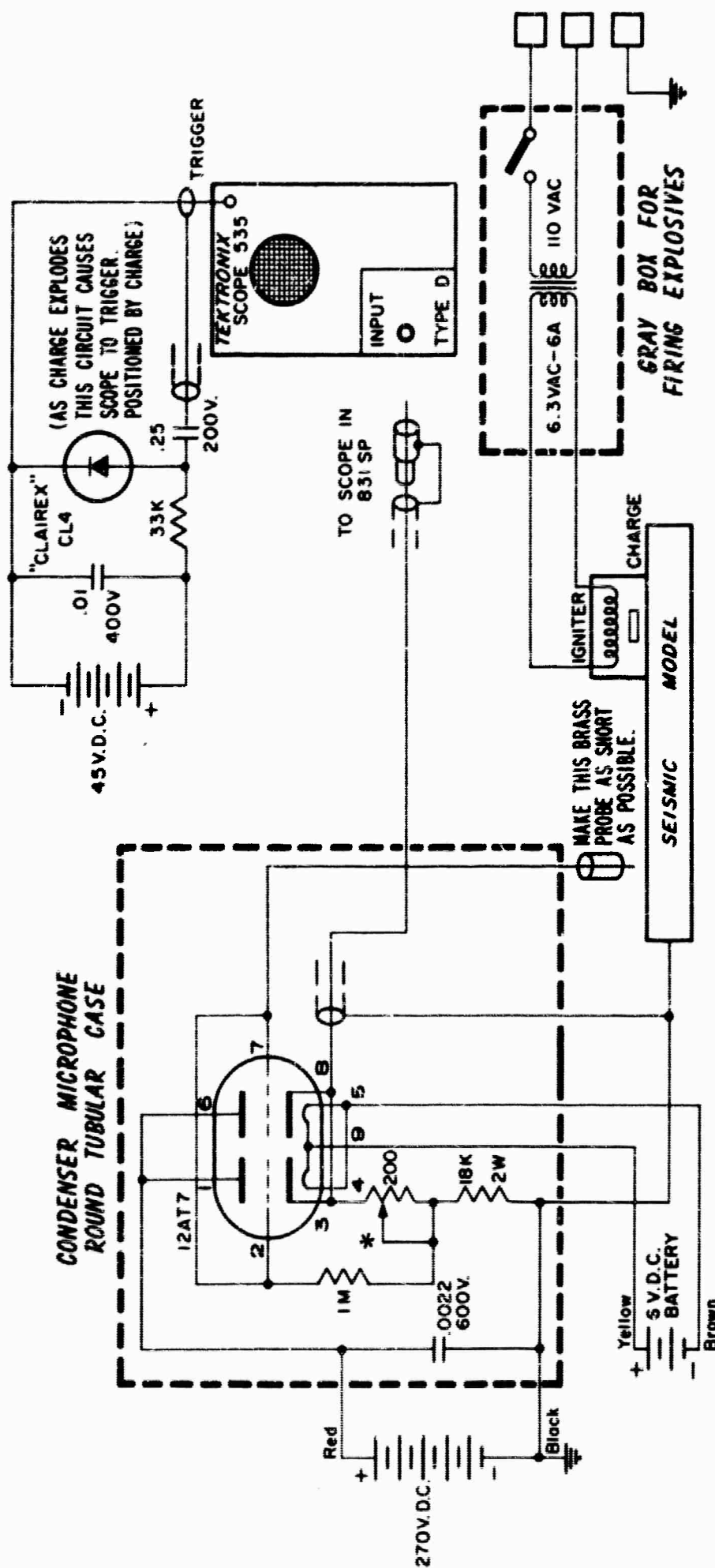
1. Charge die by tapping several times into well filled with damp explosive.
2. Turn die upside down over clean hole and force excess explosive out. If more compaction is required, this may first be done on a smooth surface and then forced out into hole.
- 2A. Cut explosive off even with end of die head.
3. Remove punch, insert mounting rod, place die head on smooth surface and tap mounting rod to seat explosive.
4. Reverse die, tap end of mounting rod and remove.

**FIGURE 4**

**METHOD USED TO MANUFACTURE SILVER ACETYLIDE CHARGES**

output goes directly to an oscilloscope. Figure 5 shows both the circuit for the condenser microphone receiver and the details of the phototube circuit which is used to trigger the sweep of the oscilloscope.

The use of the explosive source with the condenser microphone receiver gives wide band records with clearly defined arrivals. Figure 6 shows four of these records. The source is positioned either at the surface or within a round hole .064 inch in diameter. The receiver is located either on the surface or in a small square hole. The arrivals of all of the various wave types at the receiver are clearly defined and quite sharp. In spite of their apparent good quality, however, these records were not appropriate for our modeling of the effect of source depth upon model seismograms because of the following considerations. We were interested in modeling a mathematical solution that postulated a point compressional source at depth. In order to simulate this source, a small hole was drilled in the model, and an explosive charge was detonated in this hole. No matter how carefully the explosive was centered in the hole, a large shear wave was invariably generated. This made the source inapplicable for our work. An alternative approach to determine the effect of source depth upon the seismic wave form received at the surface is to make use of a reciprocity relationship between the dilatation and the vertical component of displacement (Rayleigh, 1945). For a given separation between source and receiver, the vertical displacement recorded at the surface from



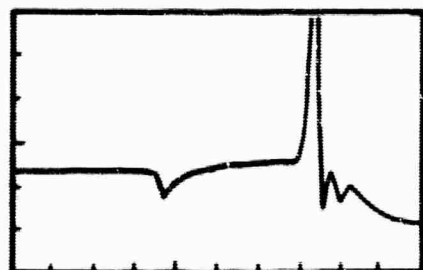
\*ADJUST TO 150 V.D.C.

FIGURE 5

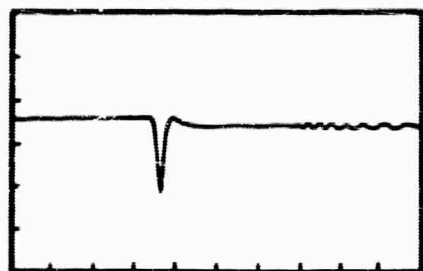
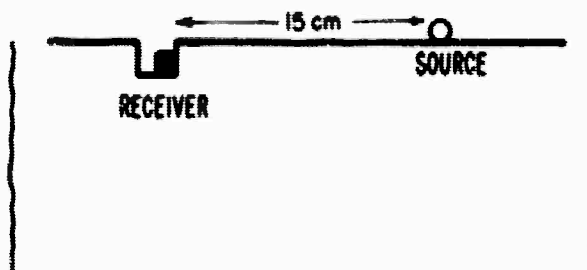
## DIAGRAMS FOR TRIGGER CIRCUIT AND CONDENSER MICROPHONE

# RECORDS

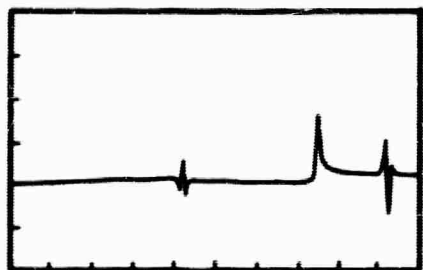
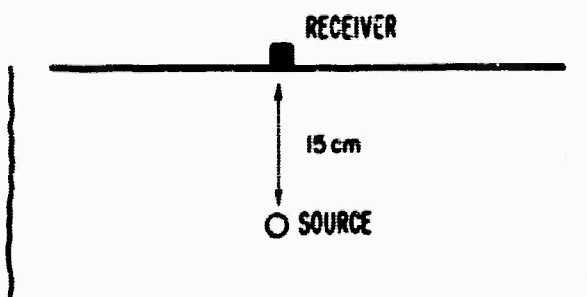
# RECEIVER LOCATIONS



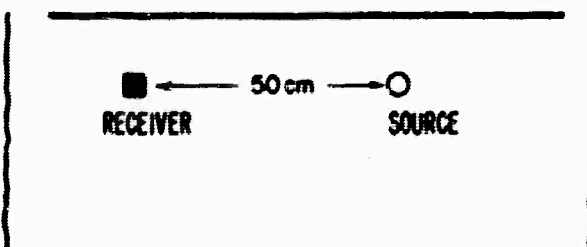
SWEEP =  $10 \mu \text{ sec/cm}$



SWEEP =  $10 \mu \text{ sec/cm}$



SWEEP =  $20 \mu \text{ sec/cm}$



SWEEP =  $10 \mu \text{ sec/cm}$

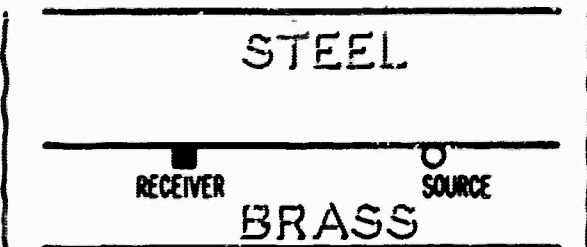


FIGURE 6

RECORDS FROM EXPLOSIVE SOURCE AND CONDENSER MICROPHONE RECEIVER.

a dilatational source at a depth,  $h$ , is the same as the dilatation at the depth,  $h$ , resulting from a vertical force applied at the surface. Thus for the modeling work we could apply a vertical force (by means of an explosive charge) at the surface of the model and record the dilatation at depth. This would be equivalent to the effect of a change in depth of a dilatational (i.e., pure compressional) source on the vertical component of displacement at the surface. The method which was first employed to take advantage of the above-mentioned reciprocity was to place an explosive source at the surface of the model and to locate a condenser microphone in a small hole at a specified depth in the model. Unfortunately, this method failed to give results useful in checking our mathematical solutions because of the difficulty in relating in a precise way the output of the condenser microphone to the dilatation. There was obviously some non-dilatational deformation of the hole as the seismic energy arrived and this was also recorded by the condenser microphone.

The approach which was finally adopted was to use strain gages to record the dilatation at depth in the model. The receivers were heavily-doped silicon semi-conductor strain gages, type P01-05-120 made by Micro Systems, Inc. These gages are .060 inches long, .005 inches wide, and .002 inches thick. At each desired depth location two gages, crossed at right angles to one another, were cemented to the model. One gage then gave the  $\partial u / \partial x$  component of the dilatation while the other gave the  $\partial v / \partial y$  component. The outputs of the two strain gages were

summed in series to give the total dilatation,  $\theta = \partial U / \partial x + \partial V / \partial y$ . The original configuration had four gages mounted at each receiver location, two on each side of the model exactly opposite one another. The purpose of this arrangement was to cancel out flexural waves in the model. It developed, however, that the flexural waves were small and did not interfere with the normal mode motion, so the additional two gages were eliminated. Figure 7 shows the placement of the gages at four different depths on the model. The source is located as shown at the top of the model. This particular position of the source largely eliminated flexural vibrations and gave quite reproducible results. Figure 8 gives an example of two shots recorded at the same location. The shots were at the surface of the model and the receivers were located near the layer-half space interface at an offset of 40 centimeters. As can be seen from the example, there are essentially no differences between the two records.

Figures 9 and 10 show the records and the corresponding amplitude spectra from four different receiver locations. The receivers were located as near as possible to the top of the model, at a depth of  $1/6$  the layer thickness, at a depth  $2/3$  the layer thickness, and as near as possible to the layer-half space boundary. The one-inch layer on the model was assumed to represent the crust of the earth and the modeling results were adjusted to a one-inch-equals-30-kilometer change in scale. The abscissa scale for the period of the spectra is in seconds. The amplitude spectra

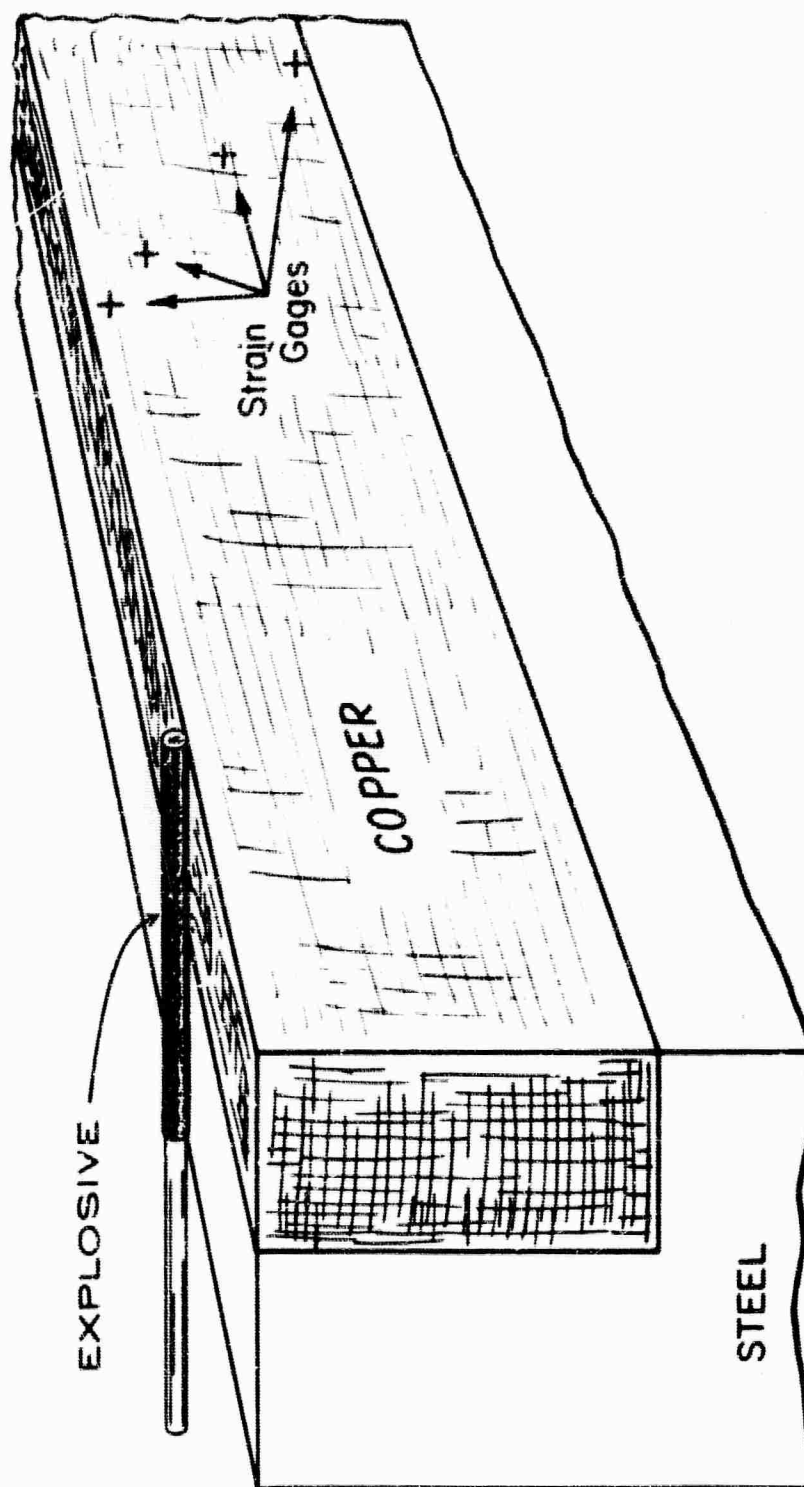
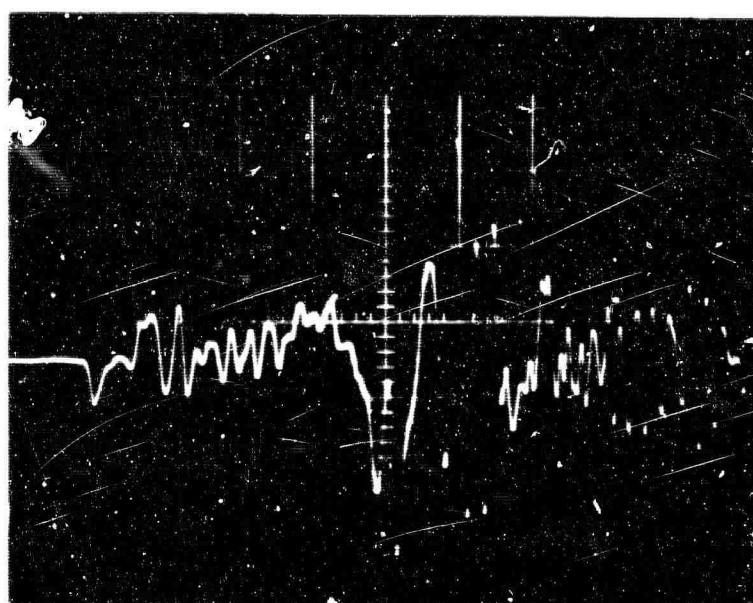
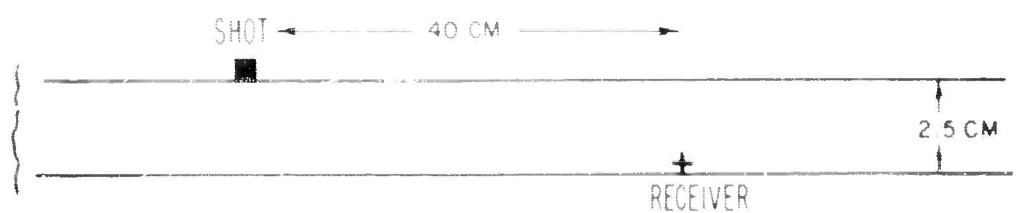
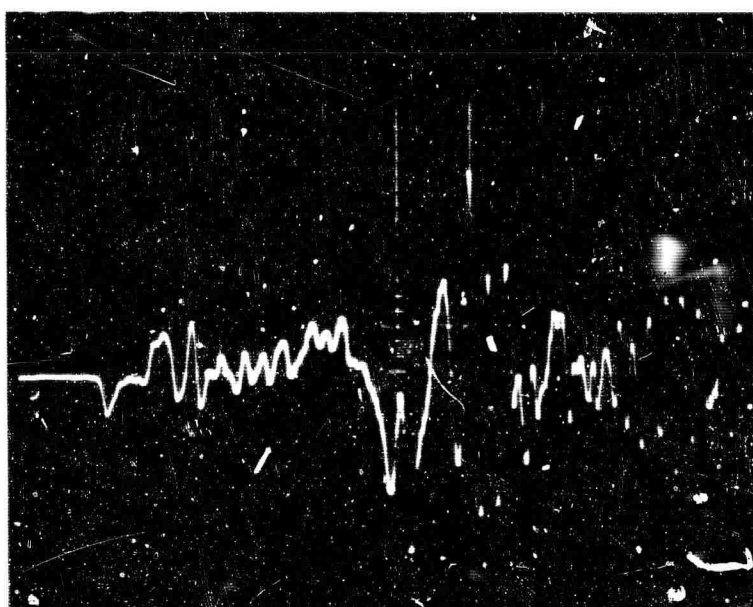


FIGURE 7

PLACEMENT OF STRAIN GAGES ON SEISMIC MODEL



*SHOT 1*

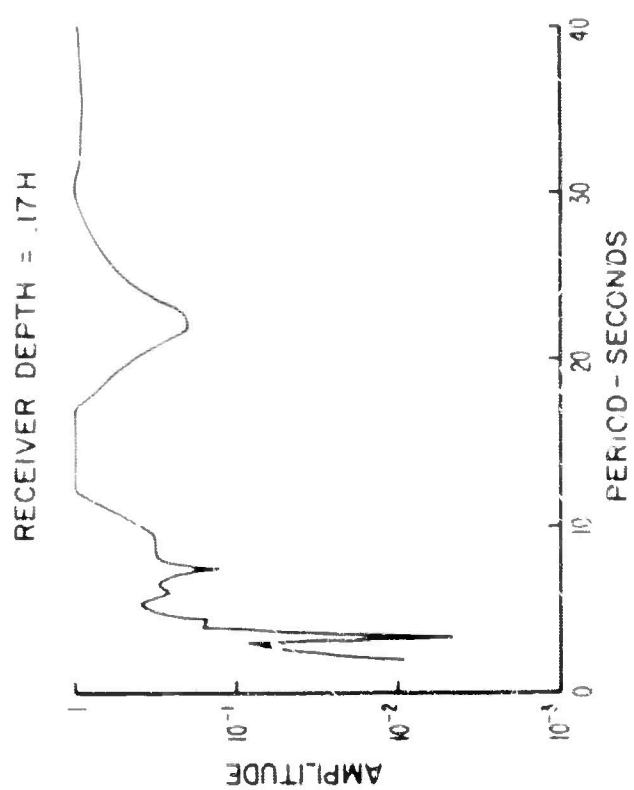
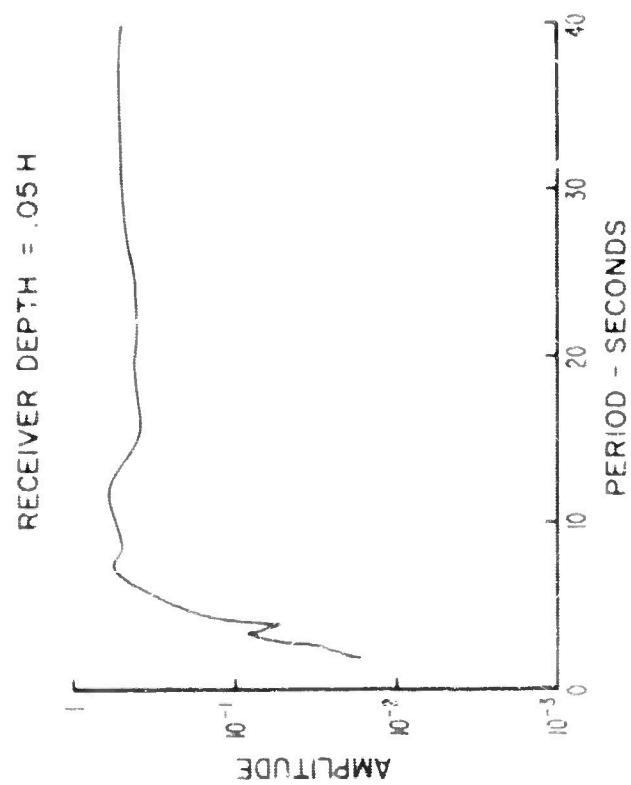


*SHOT 2*

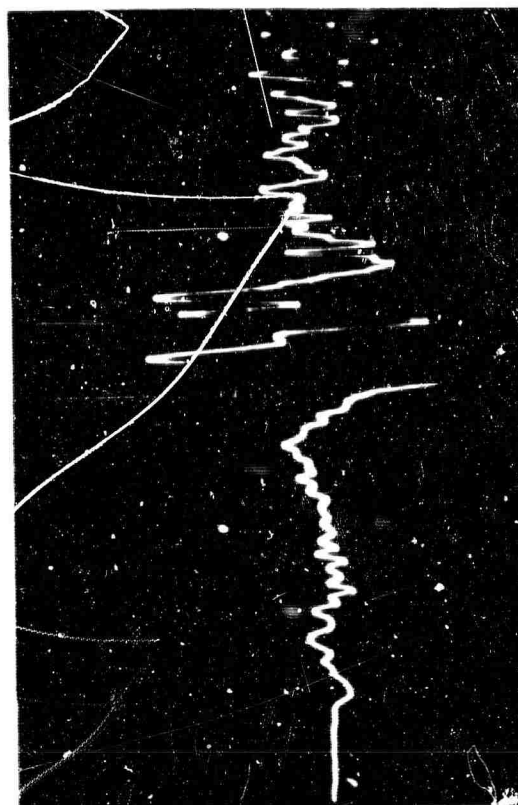
FIGURE 8

REPRODUCIBILITY OF RECORDS WITH EXPLOSIVE SOURCE  
AND STRAIN GAGE RECEIVERS.





SWEEP = 20  $\mu$  sec/cm



SWEEP = 20  $\mu$  sec/cm

SEISMIC TRACE AND AMPLITUDE SPECTRUM FOR DIFFERENT RECEIVER DEPTHS.

FIGURE 9

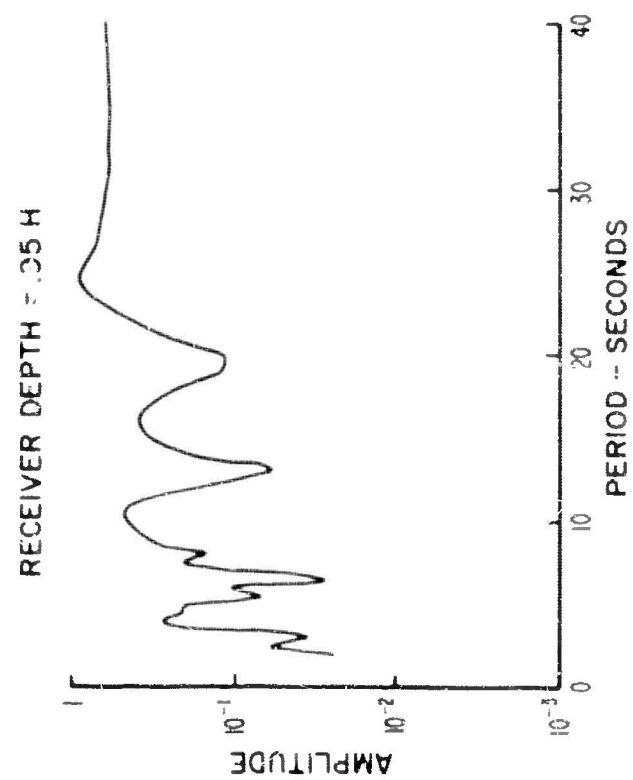
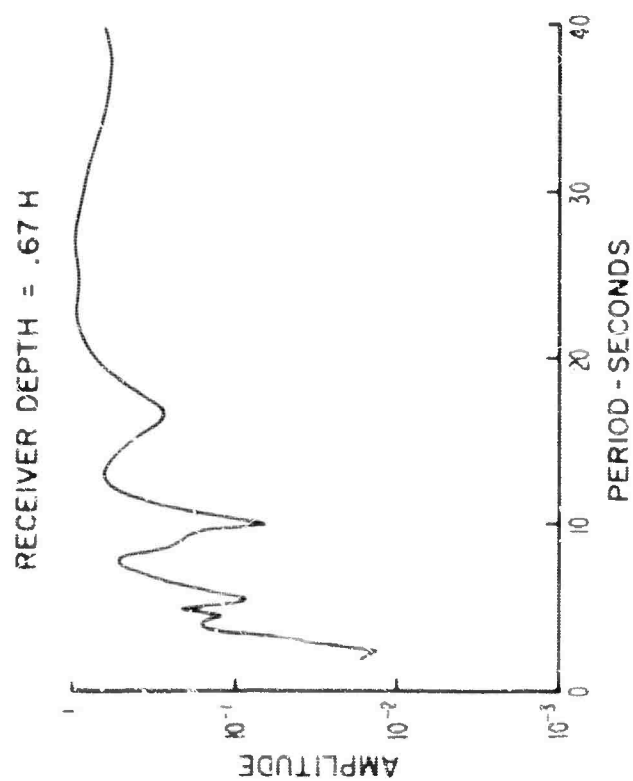


FIGURE 10

SEISMIC TRACE AND AMPLITUDE SPECTRUM FOR DIFFERENT RECEIVER DEPTHS.

can then be compared with the results derived from the theoretical normal mode solutions. The modeling results show that from a period of 7 or 8 seconds out to longer period motion, the spectrum for the surface source is flatter than the spectra for the deeper sources. As the source is placed deeper within the layer, the spectra become slightly more irregular and the high frequency components increase slightly relative to the longer period components. This same effect was apparent in the theoretical solutions.

#### B. Piezoelectric Sources

The use of piezoelectric sources and receivers was motivated by two basic considerations. In the first place, the use of explosive sources limits the choice of materials from which the models can be constructed. Only steel was able to withstand the force of the explosion without deforming, and even it would deform under repeated shots. Copper and lead deform easily and a single shot will cause cracking and spalling in a Plexiglas model. The use of an explosive source essentially requires the use of a steel model, and steel is more difficult to fabricate into models than are softer materials such as Plexiglas, epoxy, etc. Furthermore, it is conceivable that the force of the explosive charge could affect the model in such a way that the elastic properties of the composite layer change as a result of each shot. During the Rayleigh wave work special precautions were taken to minimize destruction of the model by the source. A small metallic shield was placed between the source and the model, but even with this precaution only a limited number of shots could be fired on each model.

The second reason for using piezoelectric devices is to have a repeatable source. With a pulsed source we can directly observe the seismic records on the oscilloscope screen and can have a continuous monitoring of the wave form as the source and detector are moved. An explosive source is not so reproducible as we would like and the seismic records must be photographed on the oscilloscope screen to be observed. In addition, the piezoelectric sources give better amplitude reproducibility than the explosive source. The principal disadvantage of the piezoelectric sources and receivers is that they do not give the sharp wide-band records of the explosive source and that the resulting seismograms require heavier filtering than the explosive records.

Figure 11 shows a block diagram of the seismic modeling equipment using the piezoelectric equipment. The source and receiver are identical rectangular pieces of lead zirconium titanate (PZT<sup>4</sup>) manufactured by the Cleavite Corporation. The source is activated by a voltage pulse from a 1,000 volt pulser. The wave shape from the pulser is variable from a spike of 1 micro-second width to a "fish tail" pulse with a decay time of 5 milliseconds. The voltage pulse most used in our work was a fish tail pulse with a decay time of one millisecond. The basic pulser unit was constructed at Calresearch, and the circuit diagram is shown in Figure 12. We have, in addition, two commercially made pulsing units with an output of 30 volts. These units are useful for records made at small offsets from the source. The onset of the source pulse is put on the seismogram by a Hewlett Packer

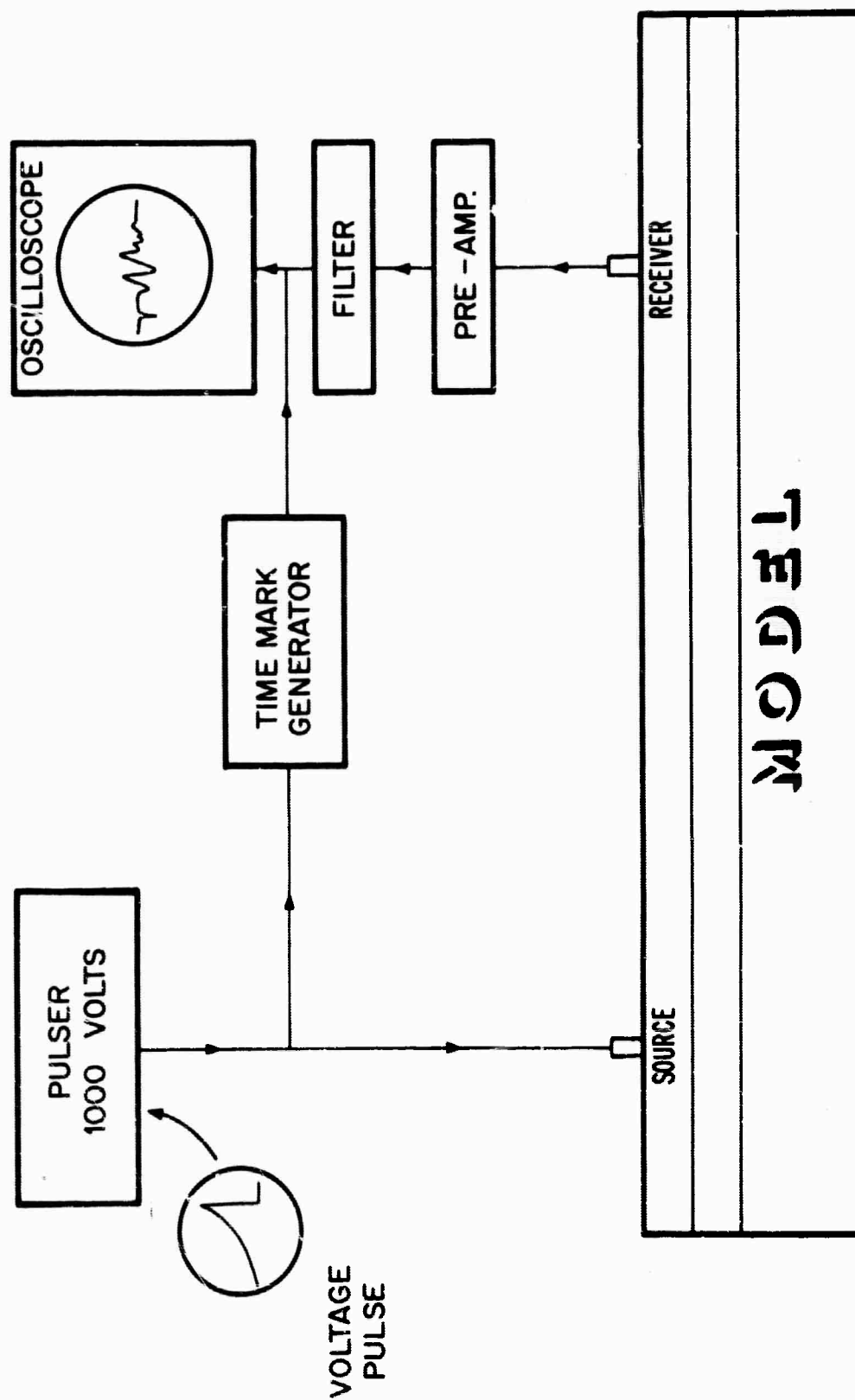


FIGURE 11

SEISMIC MODELING EQUIPMENT

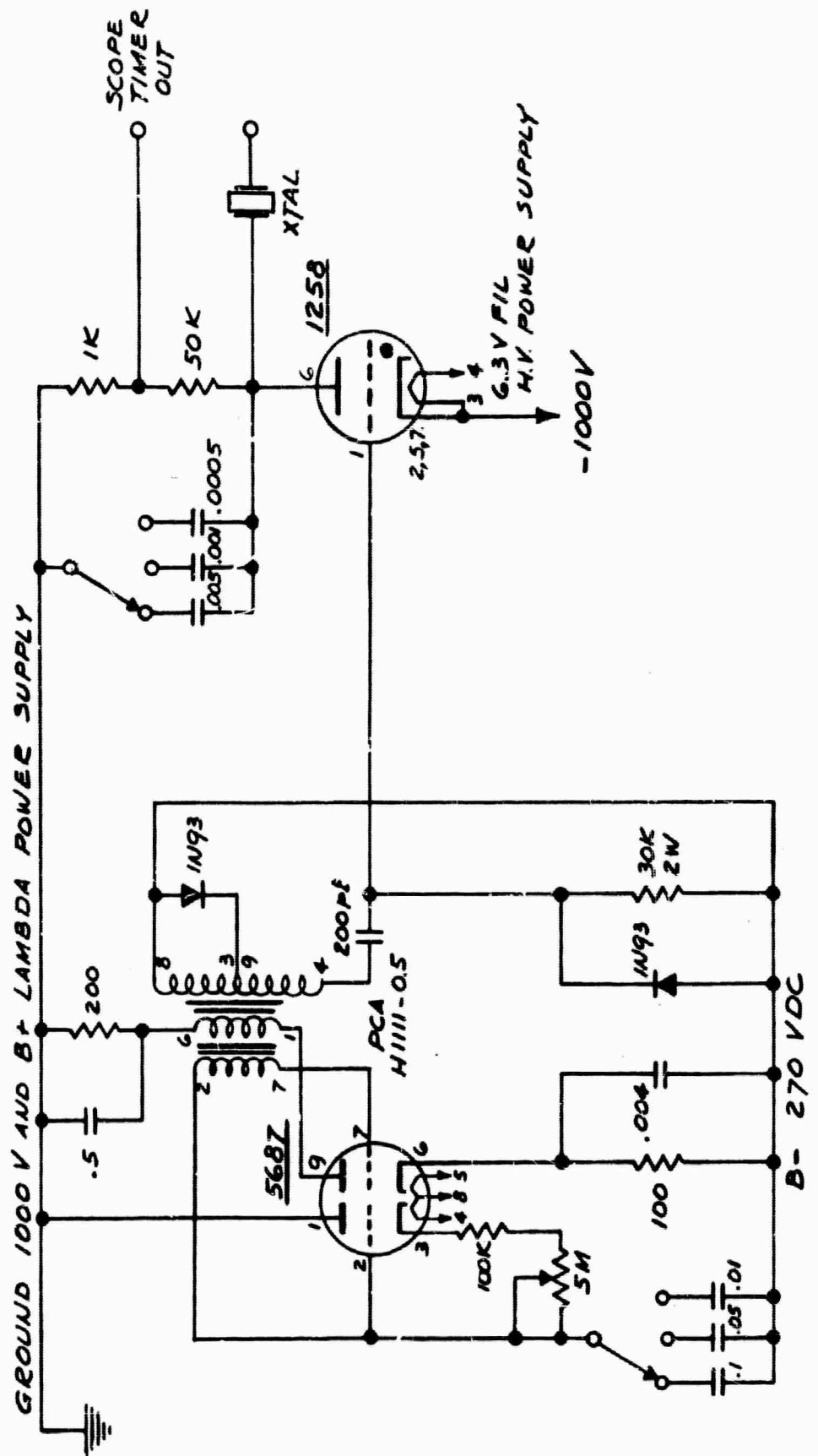
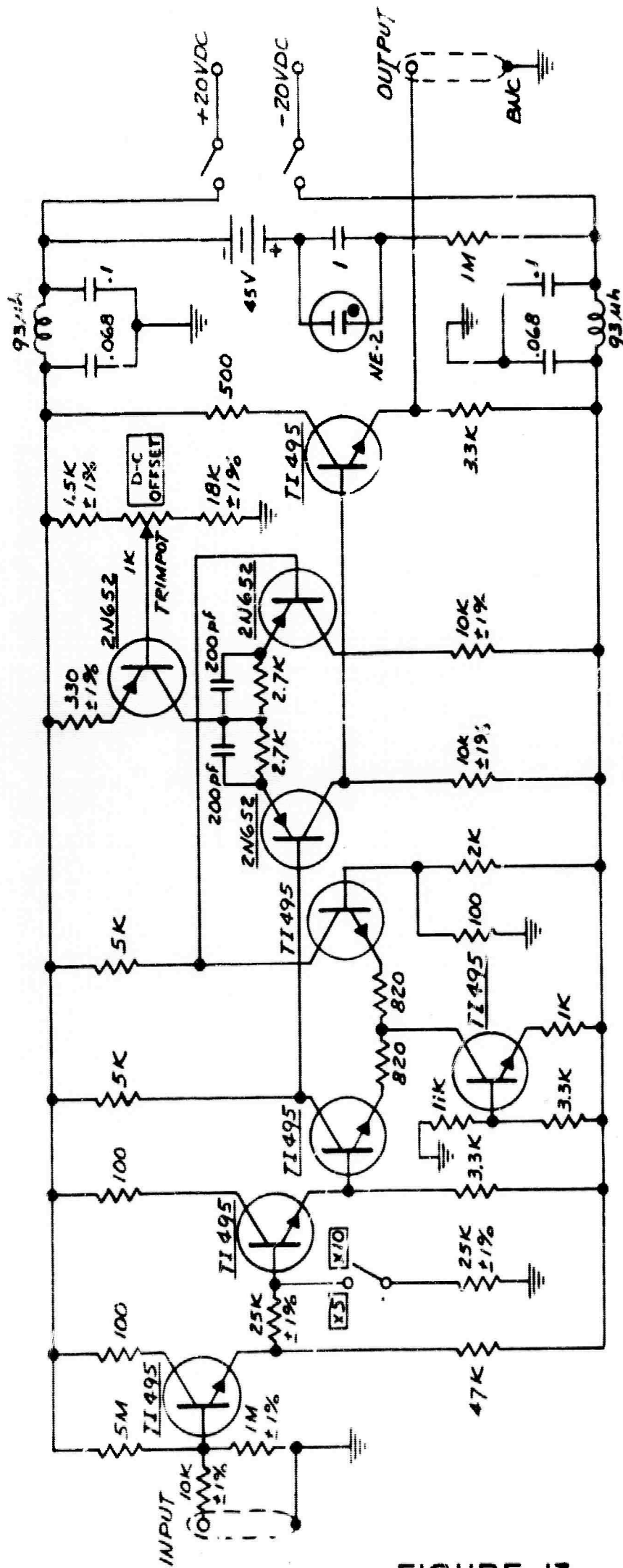


FIGURE 12

Digital Delay Generator, Model 218A. When the pulser fires, a low voltage signal is fed into the digital delay generator. At a specified number of microseconds after receiving the input, the generator puts out a signal which is fed directly to the oscilloscope trace. The sweep of the oscilloscope is triggered by the firing of the pulser, but the onset of the sweep is not reliable enough to be used as a time reference. The signal from the receiver is first put through a buffer amplifier which performs the dual function of matching impedances in the receiver circuit and providing a variable gain of either 5 or 10. The circuit diagram of this amplifier is shown in Figure 13. After amplification the signal is fed into a variable band-pass SKL filter. It then goes directly into a Tektronix 545 oscilloscope. The digital delay generator is adjusted until the oscilloscope trace shows a time mark some 5 microseconds prior to the onset of the wave form recorded by the receiver.

Figure 14 is a photograph of the modeling equipment when in operation. The seismic model is located in the foreground. It lies flat on a large table, whereas the model was vertical in the explosive source work. There is a cushioning layer of polyurethane foam between the model and the table for the purpose of damping out flexural waves in the model. A further modification to the model is that the milling of the steel sheet is no longer used in the construction of the composite layers. It was found that if a copper strip was cemented directly to the steel sheet, a low velocity, composite layer was formed with properties essentially



**NOTE:**

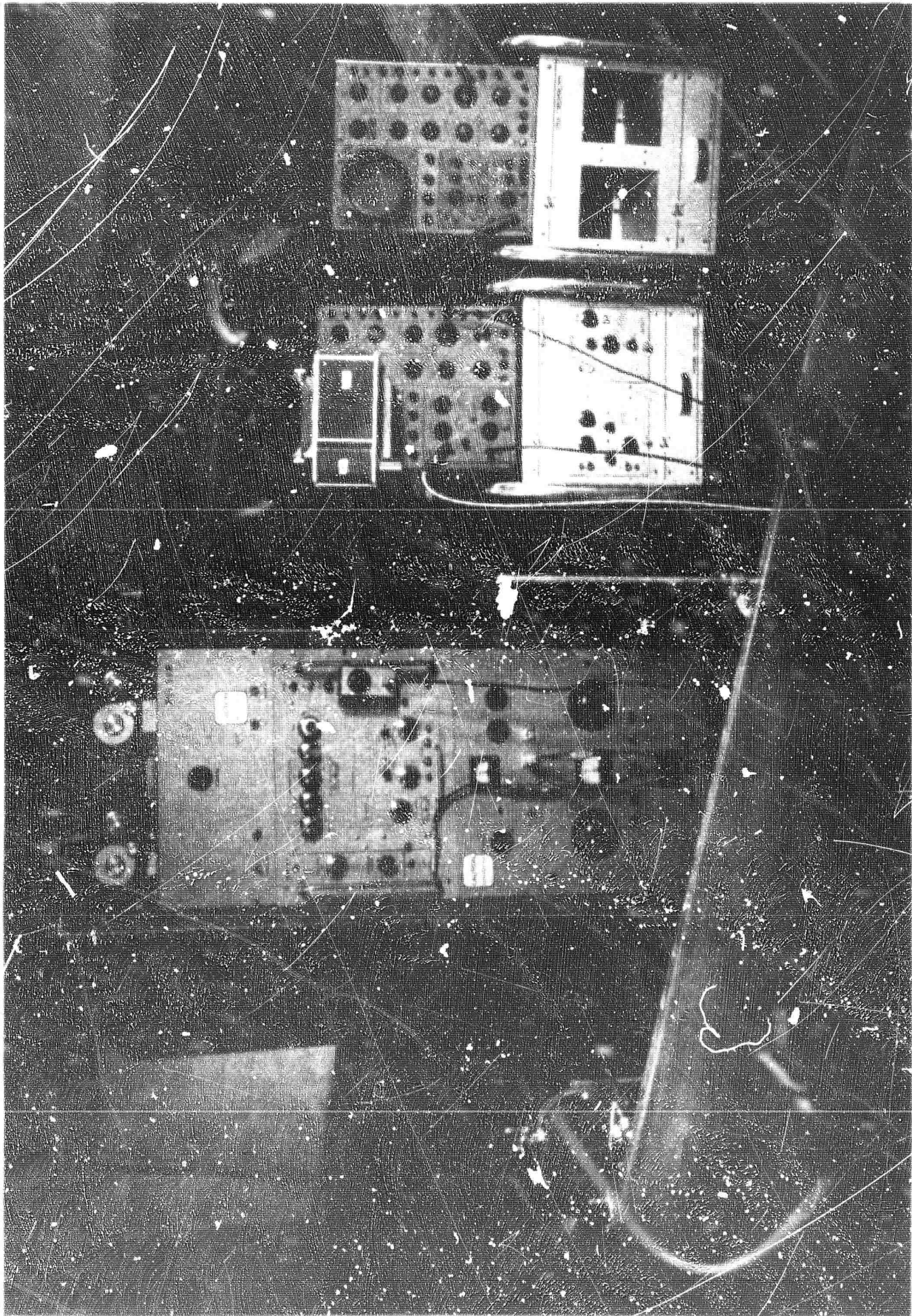
1. ALL COMPONENTS ARE MOUNTED IN SHIELDED CONTAINER
2. BATTERIES ARE MOUNTED IN ADJACENT SHIELDED CONTAINER
3. BATTERIES ARE EVEREADY 738 OR EQUIVALENT
4. ALL PRECISION RESISTORS ARE METAL FILM OR DEPOSITED CARBON
5.  $R_{IN} \approx 500K$ , GAIN 5 OR 10,  $(V_O)_{max} \geq 10 V P-P$

BANDPASS - 0 TO  $> 600 KC \pm 1 db$   
 RESISTANCE IN OHMS, CAPACITANCE IN  $\mu F$

**FIGURE 13**

**SEISMIC MODELING BUFFER AMPLIFIER**



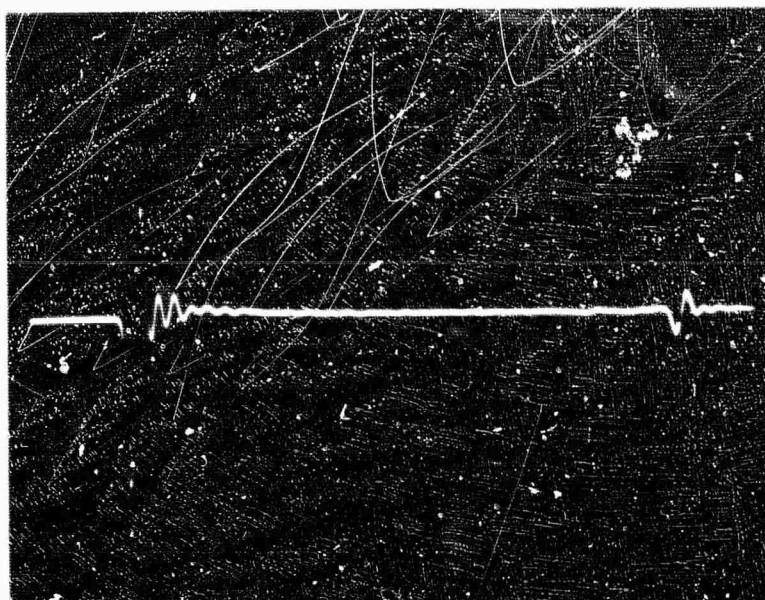


PHOTOGRAPH OF SEISMIC MODELING EQUIPMENT

identical to the layer in which a section of the model was first milled out before the addition of the copper strip. The model shown in the photograph consists of a steel sheet 8 feet long, 4 feet wide, and .030 inches thick. A copper strip 8 feet long, 1 inch wide, and .030 inches thick was attached along one edge. This technique makes it relatively easy to construct either layers or more irregularly shaped regions of different elastic properties for the seismic modeling investigations. A more rigid epoxy than was used in the explosive work was found to be best in the construction of the models for the piezoelectric work. The semi-rigid epoxy used previously caused an undesirable attenuation of energy in the model. The epoxy giving the best results was a rigid Hysol epoxy, base A94899 and hardener H23044.

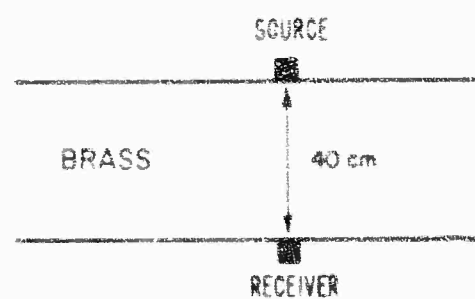
In Figure 14, the rack immediately behind the model contains the filter, the digital delay generator, and two different pulsing units. The recording oscilloscope, with camera attached, is adjacent to the instrument rack. The second oscilloscope is used either as an auxiliary amplifier or to monitor the unfiltered wave form. The source is located in the holder on the left edge of the model, while the receiver is on the long rod which is between the instrument rack and recording oscilloscope in the photograph. The buffer amplifier is located just beneath the receiver.

Figure 15 gives two examples of the wave forms recorded with the equipment shown in the previous photograph. The first illustration shows the direct wave and the first reflected arrival



SWEEP =  $20 \mu \text{ sec/cm}$

# DIRECT ARRIVAL AND REFLECTED WAVE



SWEEP =  $20 \mu \text{ sec/cm}$

# REFRACTION RECORD

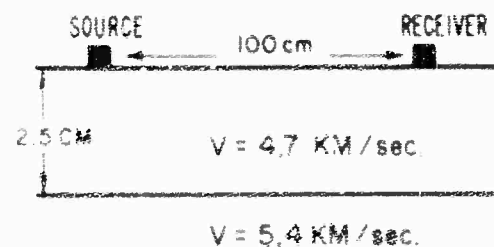


FIGURE 15

EXAMPLES OF RECORDS FROM SEISMIC MODEL

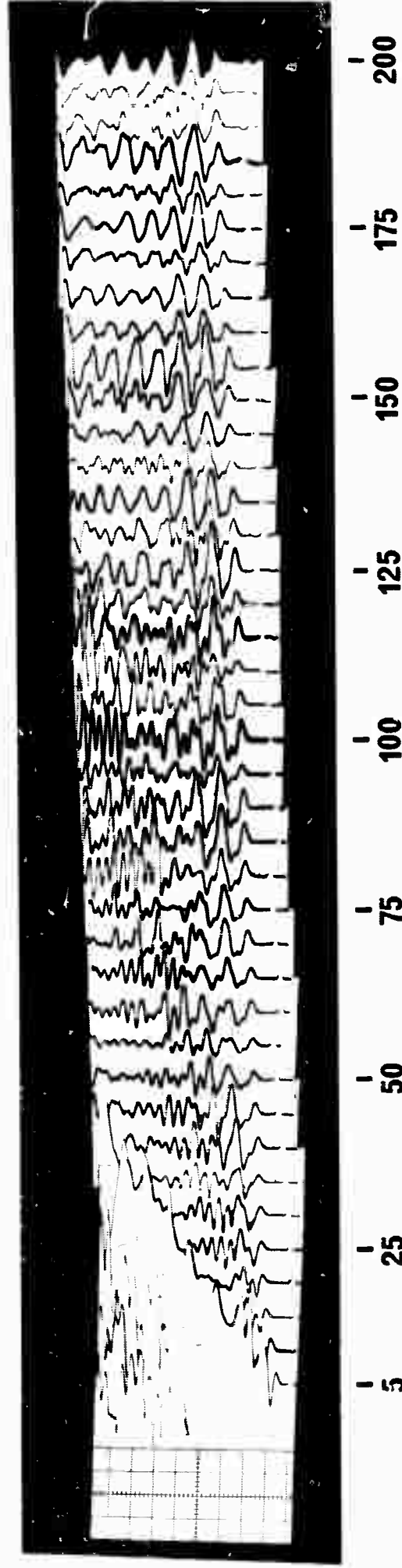
for a path through a brass sheet. The travel path is 30 centimeters long. The second illustration shows a refraction record for a single layer at an offset of 100 centimeters. In both illustrations there is evidence that resonance in the source and receiver contribute to the wave form observed on the seismic record. The source and receiver have a primary resonance of 250 kc. Filtering can be used to reduce the energy at this frequency. Frequency filtering cannot, however, entirely eliminate resonance phenomena, and the wave shapes are never so sharp as in the work done with explosive sources and strain gage receivers.

The primary purpose in setting up refraction modeling with the piezoelectric sources was to investigate the behavior of the refracted arrival through a high-velocity layer in a solid medium. Theoretical work on this problem is summarized in another section of this report. The case we examined by modeling techniques was that of a high-velocity layer lying between two lower velocity layers, with these three layers overlying a high-velocity half-space. We examined the behavior of the refracted arrival through the high-velocity layer as a function of the thicknesses and elastic properties of the adjacent layers. We accordingly began with a study of the propagation through a system consisting of a single low-velocity surface layer overlying a high-velocity half-space. At the conclusion of this work two additional layers were placed immediately beneath the low-velocity layer, and the three-layer profile was compared with that for the single layer.



Figure 16 shows records taken every 5 centimeters for receiver offsets of from 5 to 200 centimeters along the single layer model. The direct arrival through the layer, the refracted arrival through the half-space, and the Rayleigh wave arrival are all clearly defined. Figure 17 gives the travel-time curve for the direct and refracted arrivals. The arrival times of the two phases are particularly well defined. There is very little scatter in the data. The velocities deduced from the travel-time curve are in agreement with the wave velocity measured directly through both the composite surface layer and the steel sheet. The layer thickness inferred from the travel time curves is 23 mm. This is approximately 10 per cent lower than the measured thickness of 25.4 mm.

In addition to a knowledge of the arrival times of the phases, we wish to determine the amplitude behavior of these arrivals. Data on amplitudes are not nearly so reliable as data on arrival times. The principal reason for this uncertainty is the effect of the variable coupling of the receiver to the model. Receiver positioning is all important in modeling work. This results from the relatively large size of the receiver when compared to the other dimensions in the system. Even though our receivers are only two millimeters square, they correspond, when scaled up to the real-earth case, to seismometers 130 feet square. The loading effect of such seismometers is obviously more important than that of a short-period Benioff seismometer in actual earthquake recording. In order to have some knowledge of the relative coupling factor at different receiver locations, an auxiliary calibration source is



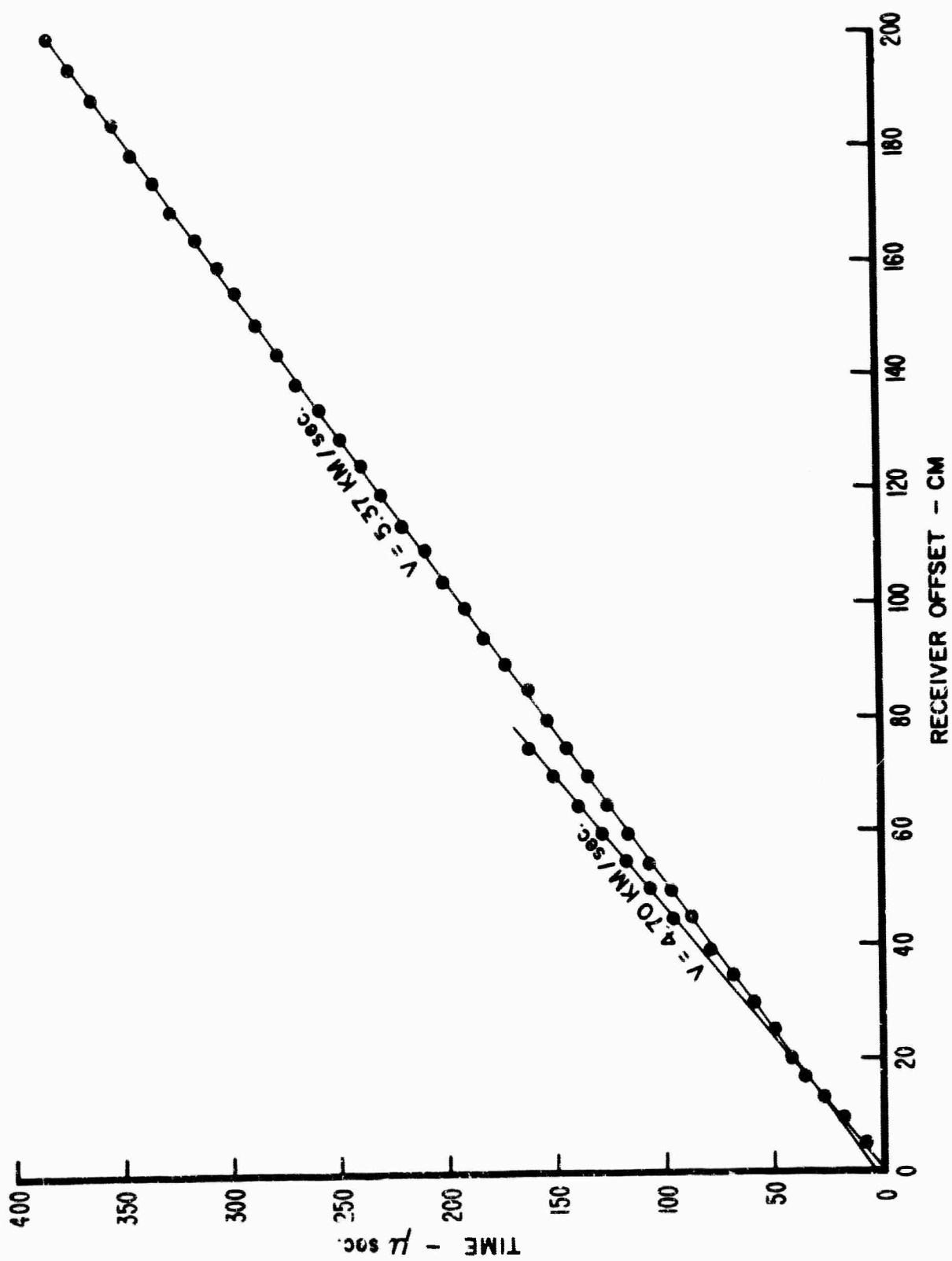
RECEIVER OFFSET - CM

$$V = 4.7 \text{ KM/sec.}$$

$$V = 5.37 \text{ KM/sec.}$$

ONE LAYER MODEL

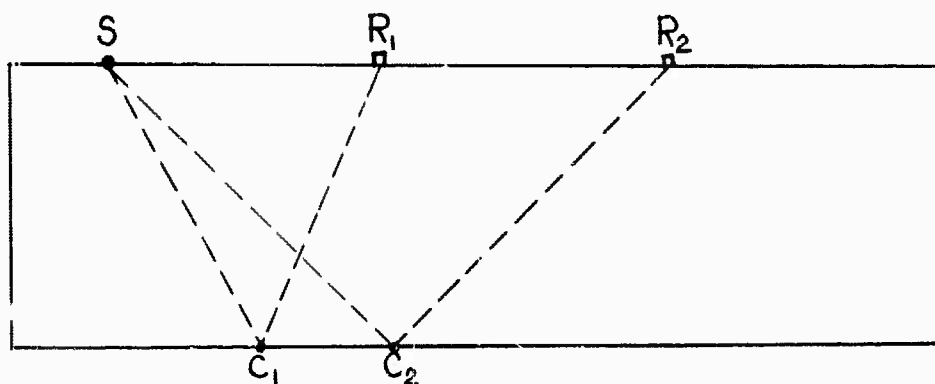
FIGURE 16



ONE LAYER MODEL

FIGURE 17

used in the modeling work. This source is placed on the edge of the model opposite to that along which the refraction profile is made and is located midway between the source and the receiver. Records are then made of the wave form of the calibration source as recorded by the profile receiver and by the profile source used as a receiver. A diagram for the positioning of the calibration source is shown below.



The source used for the seismic profile is fixed at S. The profile receiver is moved along the various positions,  $R_i$ . The calibration source is moved along the opposite side of the model and at each receiver position,  $R_i$ , is located at a position,  $C_i$ , which is equidistant from S and  $R_i$ . The object is to calibrate the receiver at each position along the profile.

At any receiver point,  $R_i$ , the amplitude,  $A_i$ , recorded on the oscilloscope trace is given by  $A_i = M_i W_i$ , where  $W_i$  is the "true" wave amplitude immediately below the receiver position and  $M_i$  is the magnification of this true motion by a combination of



the receiver plus the electronics. The assumption is made that the calibration source is nondirectional so that for any  $C_i$   $W_{S_i}$  and  $W_{R_i}$  are equal.  $W_{S_i}$  is the wave amplitude at S due to a calibration source at  $C_i$ .  $W_{R_i}$  is the wave amplitude at  $R_i$  due to the source at  $C_i$ . We wish to determine the ratio  $M_{R_2}/M_{R_1}$ . We can measure the initial amplitude of the two calibration records recorded at S and  $R_i$  and can form the ratio of these amplitudes

$$X_i = \frac{W_{S_i} M_{S_i}}{W_{R_i} M_{R_i}} .$$

This gives then that  $M_{R_2}/M_{R_1} = X_2/X_1$ , under the assumptions that  $M_{S_1} = M_{S_2}$ , since the source is fixed at S, and that  $W_{S_1} = W_{R_1}$  because the source is nondirectional. Using the records from the calibration source to normalize the refraction profile amplitudes, it is possible to get a reasonably reliable measure of the amplitudes at the various receiver positions.

Figure 18 shows the normalized refracted wave amplitudes for the single layer model. These amplitudes do not fit the theoretical predictions (Heelan, 1954) of an attenuation as the inverse 3/2 power of receiver offset, but show a more rapid attenuation with distance. An attenuation varying as the -1.75 power of receiver offset fits the observed data. Three profiles were run along the single layer model and all gave similar attenuation coefficients for the refracted wave.

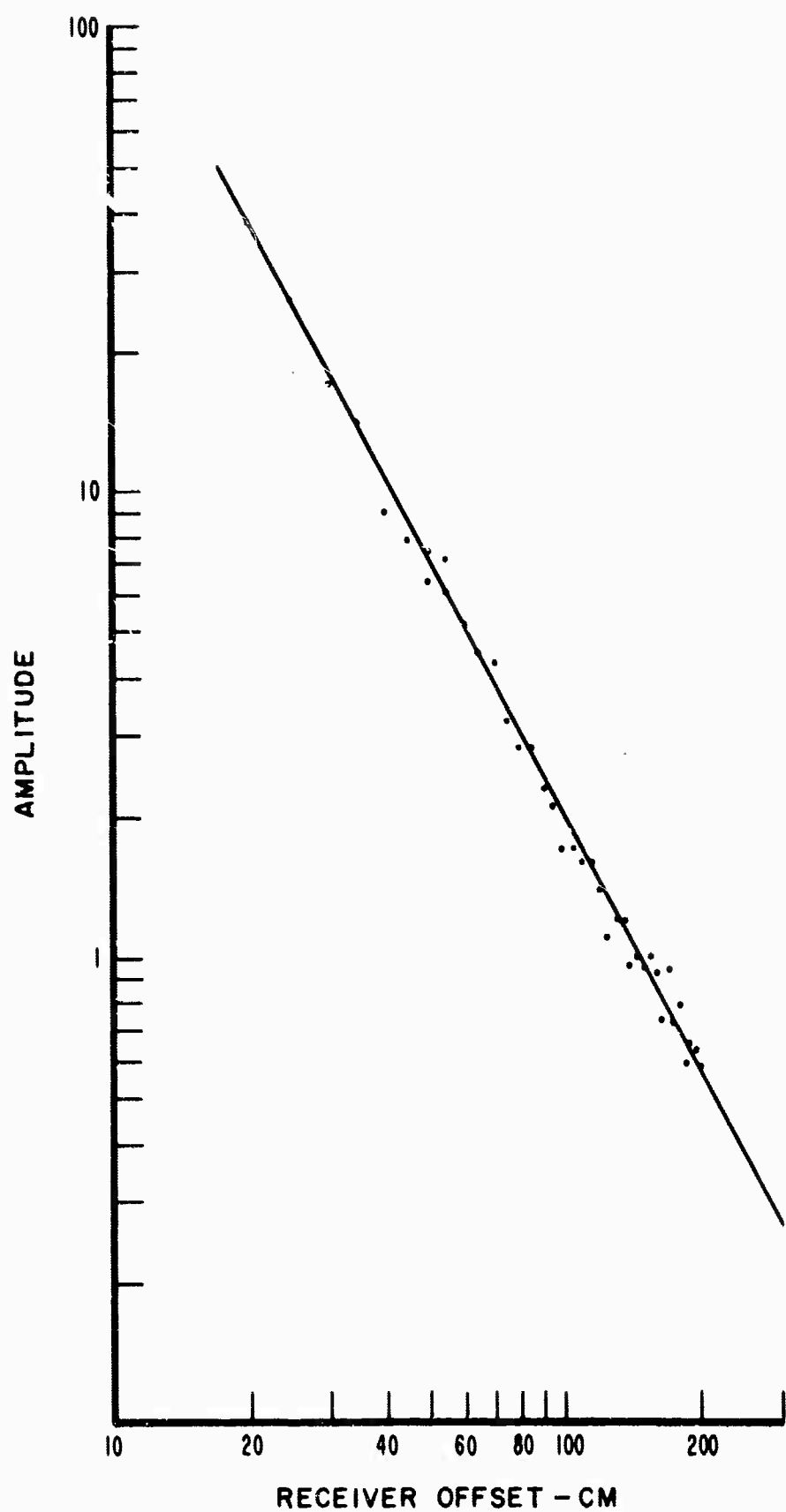


FIGURE 18

REFRACTED WAVE AMPLITUDE-ONE LAYER MODEL

Figure 19 shows the profile along a model consisting of three layers overlying a half-space. The direct and refracted wave velocities are the same as for the single layer case. At the time this profile was taken, the receiver positions unfortunately were not calibrated, and the amplitude data are not sufficiently accurate for comparison with the single layer case.

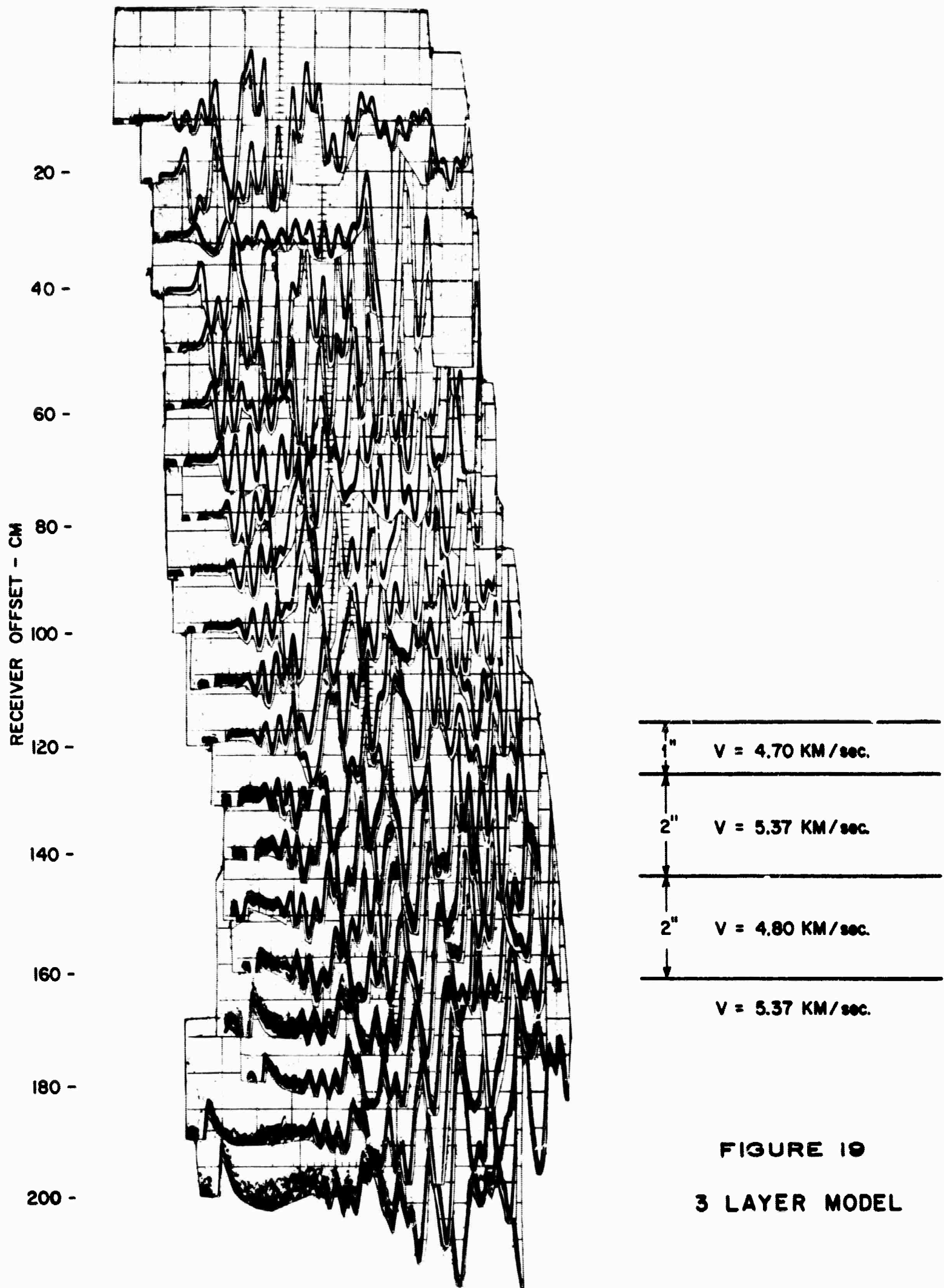


FIGURE 19  
3 LAYER MODEL

#### IV. LONG-TIME RESPONSE PREDICTED BY EXACT ELASTIC RAY THEORY

##### A. Introduction

Cagniard (1939) analyzed in considerable detail the response produced by the reflection of a spherically symmetric compressional wave at a plane interface between two solid half-spaces. The total response is the sum of a compressional component and a shear component. For a step function input in particle velocity, both components diverge in the long-time limit. Each component depends on an integral which goes to zero in the long-time limit and on a polynomial in time which contains a linear term and a cubic term. When the compressional and shear components are added together, the cubic terms cancel one another but the linear terms remain. The linear divergence results from using an input function (a step) which is not permissible on physical grounds. When a physically realizable function is used, the total response goes to zero in the long-time limit even though the component parts of the total response diverge. Cagniard's analysis is here extended to rays which are multiply reflected in a multi-interface system, and a prescription is presented for arranging the rays in groups. Each group response function goes to zero in the long-time limit even though its component parts diverge. The prescription facilitates the computation of the exact response function over an extended time interval in which many rays contribute.

The vertical component of particle velocity in a spherically symmetric compressional wave is

$$U_o = \left( \frac{P_o a}{b_1} \right) \frac{1}{r_o V_1} \left( \frac{Z-H}{r_o} \right) \left\{ \chi(\tau) + \frac{V_1}{r_o} \int_0^\tau \chi(\xi) d\xi \right\}, \quad \tau = t - \frac{r_o}{V_1}. \quad (1)$$

The plane  $Z = 0$  is at a depth  $H$  below the source and at a depth  $Z$  below the receiver (Figure 1).  $r_o$  is the source-receiver separation.  $V$  is the compressional wave velocity and  $b$  is the density. Subscript one refers to medium one.  $a$  is the radius of the spherical cavity and  $P_o$  is the peak pressure applied to the cavity wall. The choice of the source function,  $\chi$ , is not completely arbitrary. It must be chosen so that each point in the medium returns to its original state a finite time after the arrival of the disturbance at that point. This implies that the static component of such quantities as the stress and strain must be finite. The Laplace transform of the radial stress produced by a spherically symmetric compressional wave is

$$\bar{T}_{rr} = -P_o a \bar{\chi} \frac{e^{-sr_o/V_1}}{r_o} \left\{ 1 + 4 \frac{v^2}{V_1^2} \left( \frac{V_1}{sr_o} \right) + 4 \frac{v^2}{V_1^2} \left( \frac{V_1}{sr_o} \right)^2 \right\}.$$

$\bar{\chi}$  is the Laplace transform of  $\chi$ .  $s$  is the Laplace transform variable and  $v$  is the shear velocity. In order for the static component of stress to be finite

$$\lim_{s \rightarrow 0} \bar{\chi} = AS^\lambda, \quad \lambda \geq 2. \quad (2)$$

As a consequence of (2),  $\chi(\tau)$  must have at least two axis crossings and

$$\int_{-\infty}^{\infty} (C_1 + C_2 w) \chi(t-w) dw = 0 \quad (3)$$

for arbitrary  $C_1$  and  $C_2$ .

An axially symmetric radiation field in a layered system can be expanded in an infinite series. Each term can be derived directly from the integral representation for the Laplace transform of the source radiation field by using the method of generalized reflection and transmission coefficients (Spencer, 1960). This method provides a simple prescription for transforming the integral representation for the source radiation field into an integral representation for the response function associated with any generalized transmission path. The quantities which are required to specify a generalized transmission path contain all the information required by the prescription to construct the associated integral representation. A particular generalized path is completely determined by specifying: (a) the total vertical distance ( $E_l$ ) traveled in each layer in each mode (compressional and shear) and (b) the sequence in which the layers are traversed.

The integral representation in cylindrical coordinates of the Laplace transform of (1) is

$$\bar{U}_0 = \left(\frac{P_0 a}{b_1}\right) \frac{\bar{X}}{S} \int_0^\infty \lambda J_0(\lambda \rho) e^{-\alpha_1 |z-H|} d\lambda, \quad \alpha_1 = (\lambda^2 + \frac{S^2}{V^2})^{1/2}.$$

$\rho$  is the radial distance from the axis of symmetry (Z-axis).

$J_0$  is the zero order Bessel function of the first kind. The prescription gives the Laplace transform of the response associated with each generalized path in the form

$$\bar{U} = -\left(\frac{P_0 a}{b_1}\right) \frac{\bar{X}}{S} \int_0^\infty \lambda J_0(\lambda \rho) A(\lambda, S) e^{-K(\lambda, S)} d\lambda \quad (4)$$

where

$$K(\lambda, S) = \sum_{i=1}^M E_i (\lambda^2 + \frac{S^2}{V_i^2})^{1/2}.$$

M is twice the number of layers traversed by the disturbance. The  $y_i$  are the compressional and shear wave velocities in the different layers.  $A(\lambda, S)$  represents the product of the generalized reflection and transmission coefficients.

### B. Long-Time Behavior

Cagniard has developed an elegant method for inverting Laplace transforms of the form given in (4).  $S$  is treated as a positive real variable. This restriction on  $S$  is a distinctive feature of Cagniard's theory. The transformation  $\lambda = S\xi/V_R$  in (4) gives

$$A\left(\frac{S\xi}{V_R}, S\right) = f(\xi), \quad K\left(\frac{S\xi}{V_R}, S\right) = S \frac{H_R}{V_R} \sum_{l=1}^M \frac{E_l}{H_R} (\xi^2 + k_l^2)^{1/2} = S \frac{H_R}{V_R} k(\xi). \quad (5)$$

Because  $S$  is real this transformation is nothing more than a change in scale, yet it serves to vastly simplify the  $S$ -dependence of the integrand and to express that dependence in explicit form.

$\xi$  is dimensionless.  $H_R$  and  $V_R$  refer to a characteristic dimension and velocity respectively.

The branch points of  $f(\xi)$  and  $k(\xi)$  are associated with the square roots  $(\xi^2 + \frac{V_R^2}{y_l^2})^{1/2}$ . The branch points of  $f(\xi)$  are labeled  $\pm i f_l$  ( $l=1, \dots, N$ ), and those of  $k(\xi)$  are labeled  $\pm i k_l$  ( $l=1, \dots, M$ ). The condition  $f_1 \leq k_1 \leq \dots \leq k_M \leq f_N$  is always satisfied. The integrand is made single-valued by cutting the  $\xi$ -plane along the imaginary axis between each branch point and its complex conjugate (Figure 2). We confine our attention to the sheet of the Riemann surface on which all the square roots



are positive real on the positive real  $\xi$ -axis. Cagniard demonstrated that the branch points are the only singularities except in the very special case where an interface can support a Stoneley wave. For each interface which can support a Stoneley wave,  $f(\xi)$  has two pure imaginary conjugate poles ( $iQ_K, -iQ_K$ ). The order of the poles associated with a particular interface is determined by the number of times the disturbance interacts with (is reflected from or transmitted across) that interface.

Applying Cagniard's method to (4) gives

$$\left(\frac{b_1}{p_0 a}\right) H_R V_R \bar{U} = S \bar{X} \int_{t_0}^{\infty} e^{-st} F\left(\frac{t}{H_R/V_R}\right) dt, \quad \tau = \frac{t}{H_R/V_R} \quad (6)$$

$F(\tau)$  is the vertical component of the particle velocity produced by a step variation in the source function. When  $\tau > \tau_0$  (the travel time via the least-time reflection path),  $F(\tau)$  can be expressed in the form

$$F(\tau) = F_B(\tau) + F_I(\tau), \quad \tau > \tau_0,$$

where

$$F_B(\tau) = \frac{1}{\pi} \mathcal{R} \int_B \frac{\xi f(\xi) d\xi}{i \{g(\xi, \tau)\}^{1/2}}, \quad (7)$$

$$F_I(\tau) = \frac{1}{\pi} \mathcal{R} \int_I \frac{\xi f(\xi) d\xi}{i \{g(\xi, \tau)\}^{1/2}}, \quad (8)$$

and

$$g(\xi, \tau) = (\tau - k(\xi))^2 + \xi^2 \left(\frac{p}{H_R}\right)^2.$$

$\mathcal{R}\{\}$  indicates that only the real part of the quantity in parenthesis is required. The contour, B, wraps around the part of the branch cut between  $-if_1$  and  $-if_N$  in a clockwise sense (Figure 2.) Any poles below  $-if_N$  are enclosed in a clockwise sense and are included in B. In the long-time limit  $F_B$  decays like  $\tau^{-1}$ .

The I contour is a semi-circle in the lower half plane with center at the origin. The contour is traversed in a counterclockwise sense. The value approached by the integral in (8) in the limit as the radius of the semi-circle goes to infinity determines  $F_I(\tau)$ .

A careful examination of  $\{g(\xi, \tau)\}^{-1/2}$  reveals that

$$\lim_{\xi \rightarrow \infty} \{g(\xi, \tau)\}^{-1/2} = -\frac{1}{A\xi} \sum_{n=0}^{\infty} \left( \frac{P_{2n}(\tau)}{\xi^{2n}} + \frac{P_{2n+1}(\tau)}{\xi^{2n+1}} \right),$$

where

$$A = \left\{ \left( \frac{p}{H_R} \right)^2 + \left( \sum_{l=1}^M \frac{E_l}{H_R} \right)^2 \right\}^{1/2}$$

and

$$P_{2n}(\tau) = \sum_{l=0}^n a_{nl} \tau^{2l}, \quad P_{2n+1}(\tau) = \sum_{l=0}^n b_{nl} \tau^{2l+1}.$$

$P_{2n}(\tau)$  and  $P_{2n+1}(\tau)$  are polynomials in even and odd powers of  $\tau$ , respectively.

The form of  $f(\xi)$  depends on whether the generalized transmission path is degenerate. Degeneracy occurs when one or more of the layers are traversed in both the compressional and shear modes. Then there are two or more generalized paths for which the  $E_l$  (and consequently the functions  $k(\xi)$ ) are identical but the  $f(\xi)$  are in general different. We can group all degenerate paths together by modifying the form of  $f(\xi)$ . The response functions associated with degenerate paths all have identical onset times. When the path is not degenerate,  $f(\xi)$  is expressed by a

product of the generalized coefficients. When the path is degenerate,  $f(\xi)$  is expressed as a sum of products of the generalized coefficients.

The behavior of  $f(\xi)$  for large  $\xi$  can be derived from the expressions for the generalized reflection and transmission coefficients. Each of the four generalized reflection coefficients has the form

$$\lim_{\xi \rightarrow \infty} R(\xi) = r_2 \xi^2 + r_0 \xi^0 + r_{-2} \xi^{-2} + \dots$$

If the incident wave approaches the interface through a solid ( $v_i \neq 0$ ),  $r_2$  cannot vanish in any of the reflection coefficients.

If the incident wave approaches the interface through a fluid, there is only one reflection coefficient ( $R_{PP}$ )\* and  $r_2 = 0$ . If both media are fluids and there is no density contrast,  $r_0 = 0$ . The four generalized transmission coefficients have the form

$$\lim_{\xi \rightarrow \infty} T(\xi) = w_0 \xi^0 + w_{-2} \xi^{-2} + \dots$$

$w_0$  may vanish under certain conditions.

If the transmission path is not degenerate,  $f(\xi)$  is just the product of the generalized coefficients. In what follows we assume that there are no fluid layers. Let  $m$  be the number of reflection coefficients in the product. If a reflection coefficient is raised to the  $k^{\text{th}}$  power, it is counted  $k$  times in determining  $m$ .

\*The letter subscripts indicate the mode of propagation before and after transmission (P for compressional and S for shear). The number subscripts indicate the layers in which the disturbance propagates (the  $i^{\text{th}}$  layer is above the  $(i+1)^{\text{th}}$  interface).

Let  $p$  be the number of transmission coefficients for which the  $w_0$  term vanishes. If  $w_0 = 0$ , in a transmission coefficient which is raised to the  $k^{\text{th}}$  power, that coefficient is counted  $k$  times in determining  $p$ . If the transmission path is degenerate,  $f(\xi)$  will be given by a sum in which each term consists of a product of the generalized coefficients. Both the number of reflection coefficients and the number of transmission coefficients will be the same for each term in the sum. Consequently, the same value of  $m$  must be associated with each term in the sum. However, even though the number of transmission coefficients is the same in each term, the particular coefficients need not all be the same. Consequently, the value of  $p$  need not be the same for every term. Let  $p_0$  be the smallest of the  $p$  values. Then

$$\lim_{\xi \rightarrow \infty} f(\xi) = \gamma_1 (\xi^2)^{m-p_0} + \gamma_2 (\xi^2)^{m-p_0-1} + \dots + \gamma_k (\xi^2)^{m-p_0-(k-1)} + \dots, \quad (9)$$

regardless of whether the path is degenerate or not. The  $\gamma_k$  are functions of the density and velocity ratios across the interfaces intersected by the generalized transmission path.

For large  $\xi$  the integrand in (8) can be expressed as an infinite series in powers of  $\xi$ . When integrated around the semi-circle, even powers of  $\xi$  give pure imaginary values which contribute nothing to  $F_I(\tau)$ . Except for the  $\xi^{-1}$  term, odd powers of  $\xi$  vanish when integrated around the semi-circle. Integration of the  $\xi^{-1}$  term gives

$$F_I(\tau) = 0, \quad m < p_0,$$

$$= \frac{1}{A} \sum_{k=1}^{m-p_0+1} \gamma_{m-p_0-k+2} P_{2k-1}(\tau), \quad m \geq p_0.$$

When  $m < p_0$ ,  $F_I(\tau)$  vanishes because there is no  $\xi^{-1}$  term.

Each of the  $P_{2k-1}(\tau)$  contain only odd powers of  $\tau$ . There are  $k$  terms in  $P_{2k-1}(\tau)$  and  $\tau^{2k-1}$  is the highest order term. Therefore,  $F_I(\tau)$  can also be expressed in the form

$$F_I(\tau) = \sum_{k=0}^{m-p_0} C_k \tau^{2k+1}, \quad m \geq p_0. \quad (10)$$

The determination of the  $C_k$  is straightforward but tedious even for simple transmission paths.

The long-time response is determined by a polynomial of degree  $2(m-p_0)+1$  in odd powers of  $\tau$ . Suppose  $p_0=0$ . For direct transmission paths,  $m=0$  and  $F_I$  contains only the linear term. For primaries,  $m=1$  and  $F_I$  contains both a linear and a cubic term. For an  $m^{\text{th}}$  order multiple,  $F_I$  contains all the odd powers of  $\tau$  through  $\tau^{2m+1}$ . This divergent behavior is a characteristic feature of the response functions for the individual transmission paths.

### C. Convergent Groups

The existence of the divergent tails can be extremely troublesome in the numerical evaluation of the exact response over an extended time interval in which higher order multiples contribute. For example, in using a digital computer to evaluate and sum the individual response functions, an intermediate stage of calculation may be reached in which the magnitude of the partial sum exceeds the magnitude of the correct total sum by a number which exceeds the number of significant figures carried by the computer. When this occurs the final computed sum is nonsense. Pekeris and Longman (1958) did not encounter this difficulty for the case of

a fluid layer over a fluid half-space because  $r_2=0$  in the expansion for the reflection coefficient. Consequently, the constant term is the leading term in  $\hat{f}(\xi)$  for all paths. It follows that the response produced by an input step diverges linearly and the response produced by an impulse approaches a constant for each path. For the all solid, multi-layer systems, we can circumvent this problem by collecting the ray paths into groups. Equation (6) shows that the long-time response produced by a particular source function is obtained by convolving  $\chi$  with  $dF_I/dt$ . Equation (3) shows that for a physically realizable source function,  $dF_I/dt$  must not diverge more rapidly than  $t$ , otherwise the medium is left with a residual particle velocity. This suggests that the rays can be grouped together in such a way that the cubic and higher order terms vanish in the group response to a step function input.

By analyzing several cases we have found that the generalized transmission paths which belong to a particular group have the following characteristics in common:

- (A) the interfaces at which the reflections take place,
- (B) the sequence in which the reflecting interfaces are encountered,
- (C) the generalized path to the first reflector.

Let  $F_J$  be the step function response associated with the  $J^{th}$  generalized transmission path. The response function obtained by summing all the  $F_J$  which have (A), (B), and (C) in common varies linearly in the long-time limit.

Figure 3 shows four primaries which are reflected from the  $(l+1)^{th}$  interface:  $P_{l-1} S_l P_l P_{l-1}$ ,  $P_{l-1} S_l P_l S_{l-1}$ ,  $P_{l-1} S_l S_l P_{l-1}$  and  $P_{l-1} S_l S_l S_{l-1}$ . These primaries have a common transmission path to the reflector and form a group. When we say that the paths are common down to the reflector, we mean that the mode of transmission across each layer between the source and the reflector is the same. This does not mean that the least-time reflection paths are the same - in fact, they are different. This group does not include all the primaries from the  $(l+1)^{th}$  interface. Actually there are sixteen primaries which can be arranged in four groups of four each. All members of each group have common paths down to the reflector. Each group response function varies linearly in the long-time limit. Consequently, the total primary response function varies linearly in the long-time limit.

Now consider the general case where the paths suffer  $m$  reflections. Let the reflectors be designated by  $R_K (K=1, \dots, m)$  and let the order in which the  $R_K$ 's are arranged indicate the sequence in which the reflectors are encountered. If the disturbance is reflected from the same interface more than once, the designation for that interface will appear more than once in the  $R_K$  sequence. The total number of paths which go through a particular reflection sequence and have a common path to the first reflector is  $2^{N_1+1}$ .  $N_1$  is the number of interfaces which all paths encounter in going from the  $R_1$  reflector to the receiver. The highest order term in the individual  $F_I$  is  $\gamma^{2m+1}$ . The highest order term obtained by summing all the  $F_I$  which have a common



path to the last reflector is  $\tau^{2m-1}$ . The highest order term obtained by summing all the  $F_I$  which have a common path to the next to last reflector is  $\tau^{2m-3}$ . Each time we reduce by one the number of reflectors on the common part of the path, we reduce the exponent of the highest order term in the resultant polynomial by two and increase the number of contributing paths from  $2^{N_k+1}$  to  $2^{N_{k-1}+1}$ . The highest order term in the function obtained by summing all the  $F_I$  which have a common path to  $R_1$  is  $\tau$ .

In computing the response of a layered system we first determine those generalized paths for which  $\tau_0$  lies within the time interval of interest. These paths are arranged in groups according to (A), (B), and (C). In each group we determine the  $\tau_0$  which is largest ( $\tau_{mx}$ ) and evaluate the individual  $F_I$  in the interval  $\tau \leq \tau_{mx} + T/(H_R/V_R)$ , where  $T$  is the duration of the source function. There is no need to calculate the  $F_I$  for larger times because their sum varies linearly and vanishes when convolved with a physically realizable source function. The conditions (A), (B), and (C) determine the minimum number of rays which when added together have the desired long-time behavior. By grouping the individual rays according to (A), (B), and (C), we can construct convergent functions from divergent ones. The total response produced by a physically realizable source function can be expressed in terms of functions which decay in the long-time limit even though the component parts of these functions diverge.

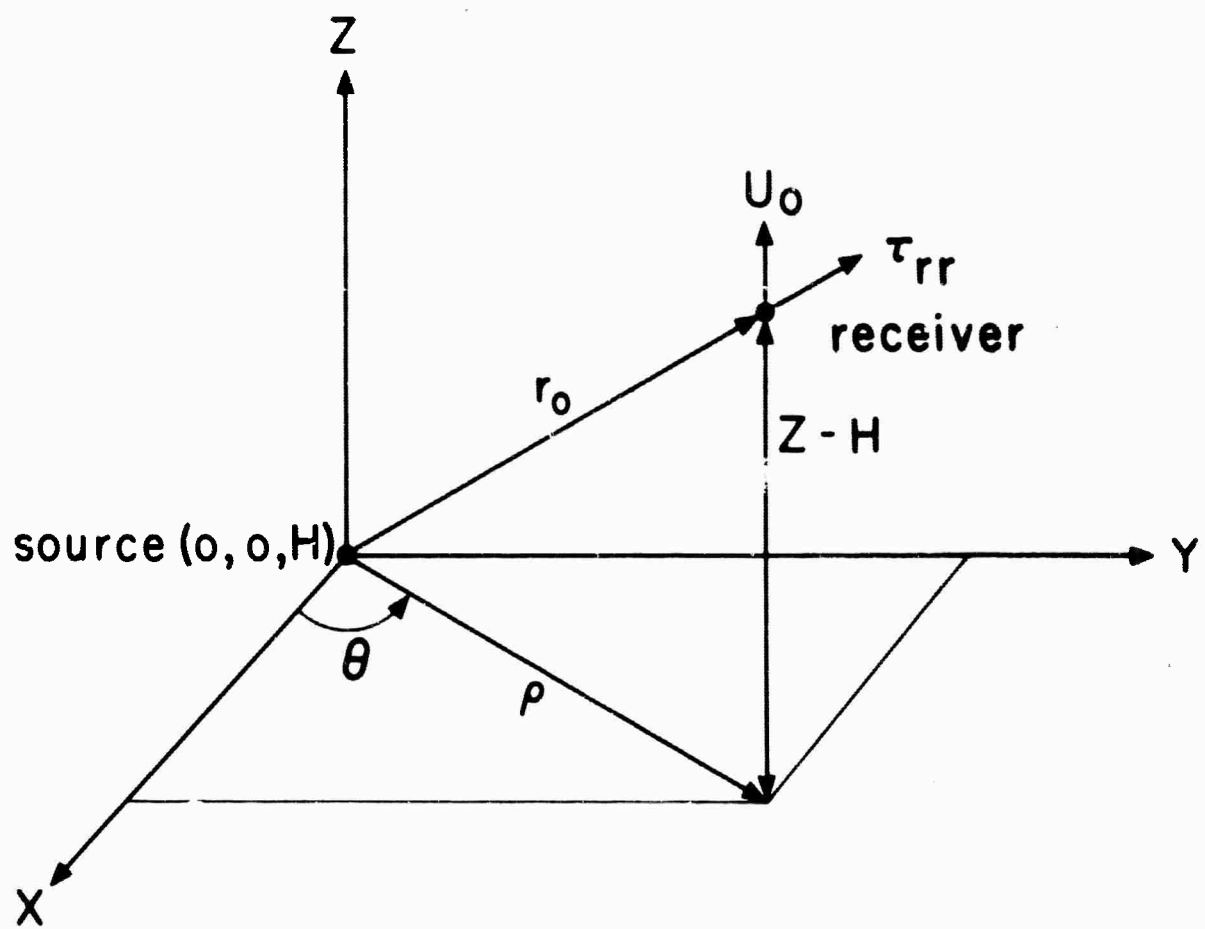


FIGURE I

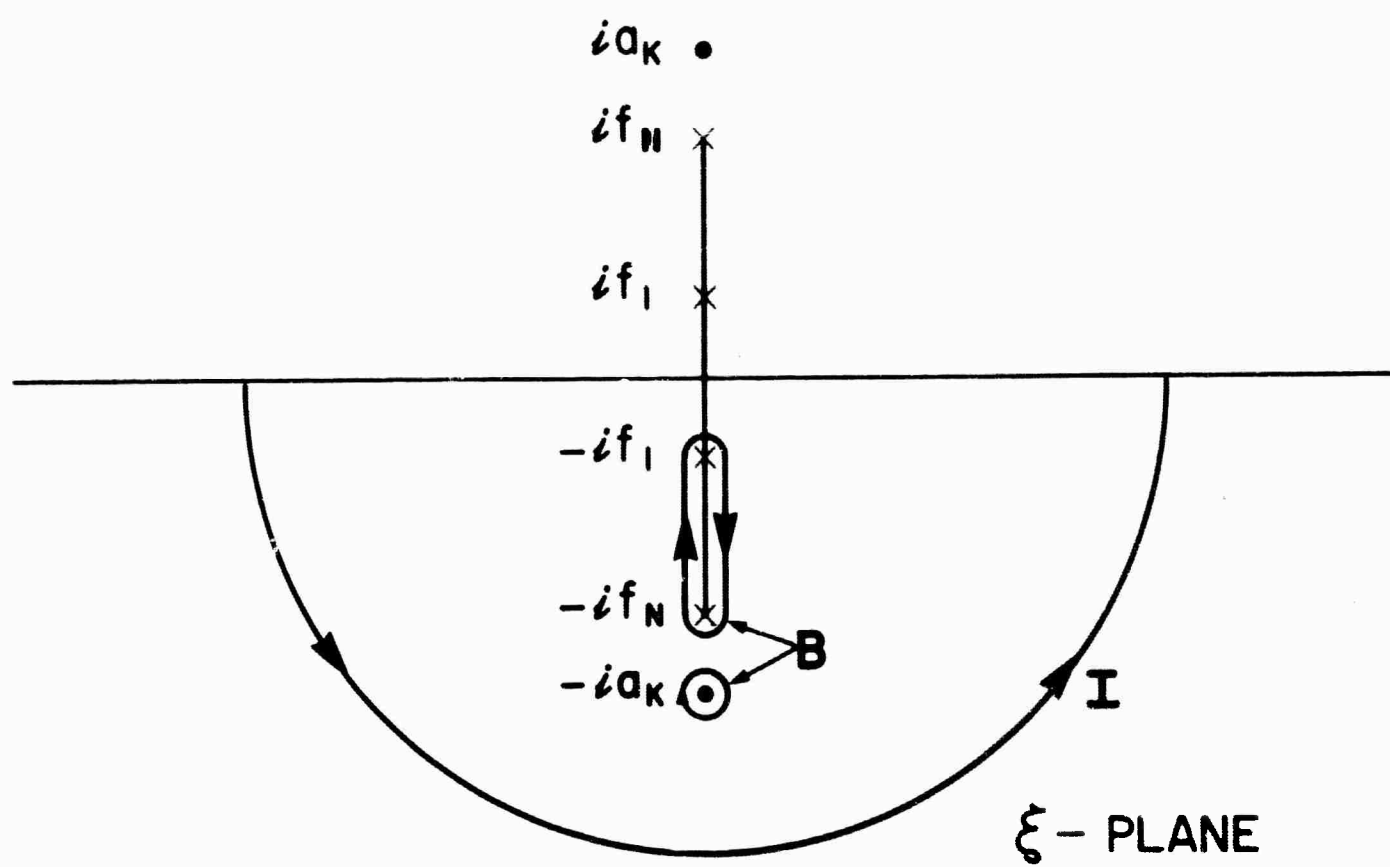


FIGURE 2

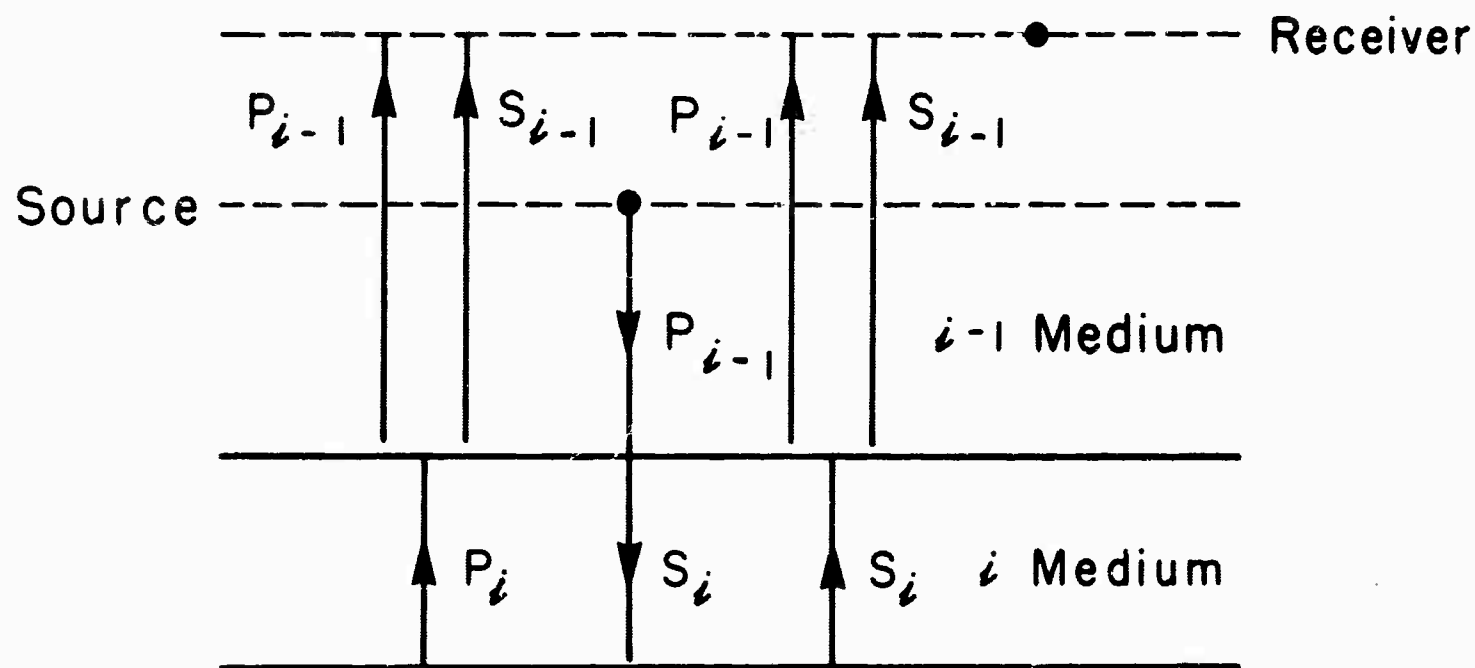


FIGURE 3

## V. HIGH-FREQUENCY ELASTIC WAVE THEORY

### A. Introduction

Because of the mathematical complexity of even the simplest problems in elastic wave theory, considerable work has been directed toward obtaining approximations to the exact theory. Two of the most useful approximations are the normal mode theory (valid at large ranges) and geometric ray theory (valid at high frequencies). In using the approximations we generally do not know what the error is - all we know is that in some limit the error is negligible and that the limit itself depends on how we choose to measure the error. The limit is usually estimated by determining the point at which some prediction of the approximate theory begins to depart from what seems physically reasonable. Our objective is to develop the high frequency theory for a layered medium and to point out some of its shortcomings.

### B. The Source Function

We consider the response produced by a source which radiates a spherically symmetric compressional wave. In an infinite homogeneous medium, the vertical component of the particle velocity is

$$U_o = \left( \frac{P_o a}{b_1} \right) \frac{1}{r V_1} \left( \frac{Z-H}{r} \right) \left\{ \chi(\tau) + \frac{t_o V_1}{r} \int_0^\tau \chi(\xi) d\xi \right\}, \quad (1)$$

where

$$\tau = \frac{t - r/V_1}{t_d}, \quad r = (\rho^2 + (Z-H)^2)^{1/2}.$$

$r$  is the source-receiver separation. The plane  $Z=0$  is at a depth  $H$  below the source and  $Z$  below the receiver.  $P_0$  is the peak pressure applied to the cavity wall and  $Q$  is the radius of the cavity.  $V_1$ ,  $v_1$  and  $b_1$  refer, respectively, to the compressional velocity, shear velocity and density in medium one. The source function,  $\chi$ , merely expands or contracts with  $t_d$  but does not change shape. The amplitude spectrum of  $\chi$  is assumed to peak at a dominant frequency  $f_d = 1/t_d$ . At distances which are large compared with the dominant wavelength, the second term in (1) becomes negligible with respect to the first term, the disturbance propagates without change of shape, and  $\chi(\tau)$  determines the time variation. In effect,  $\chi(\tau)$  is a high-frequency approximation to the response of an infinite medium.

To determine the range of validity of the high-frequency approximation we first demonstrate that  $\chi$  and the integral of  $\chi$  take on non-zero values over the same interval.  $\chi$  must be chosen so that each point returns to its original state a finite time after the arrival of the disturbance at that point. This means that the static component of the stress and strain must be finite. The Laplace transform of the radial stress in a spherically symmetric compressional wave is

$$\overline{T}_{rr} = -P_0 a \overline{\chi} \frac{e^{-sr/V_1}}{r} \left\{ 1 + 4 \frac{v_1^2}{V_1^2} \left( \frac{V_1}{sr} \right) + 4 \frac{v_1^2}{V_1^2} \left( \frac{V_1}{sr} \right)^2 \right\}.$$

In order for the static component to be finite,

$$\lim_{s \rightarrow 0} \overline{\chi} = A s^\lambda, \quad \lambda \geq 2. \quad (2)$$

As a consequence of (2), the static component of  $\chi$  must vanish. This insures that the integral of  $\chi$  is zero outside the interval where  $\chi$  takes on non-zero values. Therefore, the validity of the high-frequency approximation depends only on the relative amplitudes of the first and second terms in (1). If the two time functions had been resolved, their significance would depend not on their relative amplitudes but on the amplitude of the background (signal plus noise) which is coincident in time. If there were no background, neither term could be neglected. For purposes of illustration let

$$\chi(\tau) = \left(\sin^2 \frac{\pi}{K} \tau\right) (\cos 2\pi \tau), \quad 0 \leq \tau \leq K \quad (K \geq 2).$$

The first factor determines the shape of the envelope.  $K$  determines the number of oscillations and the bandwidth. The condition  $K \geq 2$  forces the low frequency behavior to satisfy (2). For  $K = 4$ , the ratio of the maximum amplitudes is  $.16 t_d v_1 / r$ . Therefore, for a dominant wavelength to range ratio of one half, the second term is about eight per cent of the first term. This provides an estimate of the upper limit on the dominant wavelength to dimension ratio for which the high-frequency approximation is valid.

### C. Generalized Ray Theory

An axially symmetric radiation field in a layered system can be expanded in a series. Each term can be derived directly from the integral representation for the source radiation field by using the method of generalized reflection and transmission



coefficients (Spencer, 1960). This method provides a prescription for transforming the integral representation for the source radiation field into an integral representation for the response function associated with any generalized transmission path. The quantities which are required to specify a particular generalized transmission path contain all the information required by the prescription to construct the associated integral representation. A particular generalized path is completely determined by specifying: (a) the total vertical distance traveled in each layer in each mode (compressional and shear) and (b) the sequence in which the layers are traversed.

The integral representation in cylindrical coordinates of the Laplace transform of (1) is

$$\overline{U}_0 = \left( \frac{P_0 \alpha}{b_1} \right) (\text{sign}(z-H)) \frac{\overline{X}}{S} \int_0^\infty \lambda J_0(\lambda \rho) e^{-\alpha_1 |z-H|} d\lambda,$$

where

$$\alpha_1 = \left( \lambda^2 + \frac{S^2}{V^2} \right)^{1/2}.$$

The prescription gives the Laplace transform of the response associated with each generalized path in the form

$$\overline{U} = - \left( \frac{P_0 \alpha}{b_1} \right) \frac{\overline{X}}{S} \int_0^\infty \lambda J_0(\lambda \rho) A(\lambda, S) e^{-K(\lambda, S)} d\lambda \quad (3)$$

where

$$K(\lambda, S) = \sum \left( P_i \left( \lambda^2 + \frac{S^2}{V_i^2} \right)^{1/2} + T_i \left( \lambda^2 + \frac{S^2}{V_i^2} \right)^{1/2} \right).$$

The summation extends over all layers traversed by the disturbance. The  $P_i$  and  $T_i$  are the total vertical distances traveled in the  $i^{\text{th}}$  layer in the compressional and shear modes respectively.  $A(\lambda, S)$  represents the product of the generalized reflection and transmission coefficients.

The functions  $A(\lambda, S)$  and  $K(\lambda, S)$  contain square roots of the form  $(\lambda^2 + S^2/y_i^2)^{1/2}$ .  $y_i$  refers to a body wave velocity. To make the integrand single-valued, we cut the  $\lambda$ -plane along a straight line between the branch points.  $S$  is considered complex of the form  $S = \omega e^{i\phi}$  ( $\omega > 0$ ). The angle which the cut makes with the real axis and the argument of the square root at points on the cut is indicated in Figure 1.

As  $\phi \rightarrow \pi/2$ , the cut approaches the path of integration (along the positive real  $\lambda$ -axis) from below. Let  $S = i\omega$ , then the path of integration lies above the cut. The change of scale  $\lambda = \omega \xi / V_R$  transforms (3) into

$$\bar{U}(i\omega) = -\left(\frac{P_0 a}{b_1}\right) \frac{\bar{\chi}(\omega)}{i H_R V_R} \gamma \int_0^\infty \underset{\text{ABOVE}}{\xi} J_0\left(\gamma \xi \frac{P}{H_R}\right) f(\xi) e^{-\gamma k(\xi)} d\xi, \quad (4)$$

where

$$\gamma = \frac{\omega H_R}{V_R}, \quad f(\xi) = A\left(\frac{\omega \xi}{V_R}, i\omega\right),$$

and

$$k(\xi) = \sum_{i=1}^M \frac{E_i}{H_R} (\xi^2 - k_i^2)^{1/2}, \quad k_i = \frac{V_R}{y_i}. \quad (5)$$

In (5) we have used one expression for both the compressional and shear terms.  $E_i$  may refer to either  $P_i$  or  $T_i$  and  $M$  is twice the number of layers traversed by the disturbance.  $H_R$  and  $V_R$  may be associated with a characteristic dimension and velocity respectively.

As  $\phi \rightarrow -\pi/2$ , the cut approaches the path of integration from above. Let  $S = -i\omega$ , then the path of integration lies below the cut. The change of scale  $\lambda = \omega\xi/V_R$  transforms (3) into

$$\bar{U}(-i\omega) = \left(\frac{P_0 a}{b_1}\right) \frac{\bar{\chi}(-i\omega)}{iH_R V_R} \gamma \int_0^\infty \xi J_0(\gamma \xi \frac{P}{H_R}) f(\xi) e^{-\gamma k(\xi)} d\xi. \quad (6)$$

BELOW

The only difference between the integrals in (4) and (5) is in the position of the cut with respect to the path of integration.

$\bar{U}$  is the transform of a real time function - therefore,  
 $(\bar{U}(i\omega))^* = \bar{U}(-i\omega), \quad \omega > 0.$

The asterisk designates the complex conjugate.  $\chi$  is by definition a real time function, hence

$$(\bar{\chi}(i\omega))^* = \bar{\chi}(-i\omega).$$

The relationship

$$\left(\underset{\text{ABOVE}}{k(\xi)}\right)^* = \left(\underset{\text{BELOW}}{k(\xi)}\right), \quad 0 \leq \xi < \infty,$$

follows directly from (5). Therefore, the condition that  $U$  be real implies

$$\left(\underset{\text{ABOVE}}{f(\xi)}\right)^* = \left(\underset{\text{BELOW}}{f(\xi)}\right), \quad 0 \leq \xi < \infty. \quad (7)$$

This result is one of a group of symmetry relations which relate the values of  $f(\xi)$  above and below the cut and at points reflected in the imaginary axis. The symmetry relations are valid for real  $\xi$  and follow directly from the expressions for the generalized coefficients.

The spectrum for an impulsive source function ( $\bar{\chi}=1$ ) is

$$\left(\frac{b_i}{p_{0i}}\right)(H_R V_R) \bar{U} = iY Y(\gamma), \quad (8)$$

where

$$Y(\gamma) = \int_0^{\infty} \xi J_0(\xi \gamma \frac{p}{H_R}) f(\xi) e^{-\gamma k(\xi)} d\xi, \quad \gamma > 0. \quad (9)$$

ABOVE

A knowledge of the nature and position of the singularities of  $f(\xi)$  and  $k(\xi)$  is necessary for the development of the asymptotic expansion and to a proper understanding of the results. We confine our attention to the sheet of the Riemann surface on which the square roots  $(\xi^2 - V_R^2/U_i^2)^{1/2}$  are positive real on the real axis to the right of the branch points. All the singularities of  $f(\xi)$  and  $k(\xi)$  lie on the real axis. The branch points of  $f(\xi)$  are designated by  $\pm f_i (i = 1, \dots, N)$  and those of  $k(\xi)$  by  $\pm k_i (i = 1, \dots, M)$ .

If the body wave velocities in the layers are all different, the branch points of  $f(\xi)$  form a set which includes all the branch points of  $k(\xi)$  plus additional ones.  $f(\xi)$  contains the four branch points associated with each interface intersected by the generalized transmission path.  $k(\xi)$  contains only branch points which are associated with the particular mode of propagation in the layers. Even when the generalized transmission path traverses every layer in both modes,  $f(\xi)$  contains

four additional branch points associated with the layers immediately above the uppermost reflector and immediately below the lowermost reflector. Note that if there is no reflection at the interfaces between which the transmission path is contained, the generalized transmission path cannot traverse the outermost layers in both modes. Then, even if all the other layers were traversed in both modes,  $f(\xi)$  would still contain two branch points not contained in  $k(\xi)$ . If the body wave velocities are not distinct, special cases can arise where the branch points of  $f(\xi)$  and  $k(\xi)$  are identical. The relation

$$f_1 \leq k_1 \dots k_i \dots, k_M \leq f_N$$

is satisfied in all cases.

The poles of the integrand, when they exist, are associated with zeros of the denominators in the expressions for the generalized coefficients. Cagniard (1939) demonstrated that at an interface between two elastic half-spaces the denominator has no zeros on the permissible sheet of the Riemann surface except in the very special case where the interface can support a Stoneley wave. Then the denominator has the two real zeros  $\pm \xi_i = \pm v_R / w_i$ .  $w_i$  is the Stoneley velocity on the  $i^{\text{th}}$  interface. Spencer (1956) showed that a Stoneley wave is always excited at a liquid-solid interface. A Rayleigh wave is always excited at a solid-vacuum interface. In all three cases the zeros are real and are situated symmetrically with respect to the origin.  $w_i$  is always less than

the smallest body wave velocity in the adjacent media. Therefore, the pole,  $\xi_i$ , cannot lie on any of the four cuts associated with the  $i^{\text{th}}$  interface and

$$\text{minimum } \xi_i = \xi_{\min} > k_1.$$

In deriving the asymptotic expansion of  $Y(\gamma)$ , we find that only the case  $\sum_{i=1}^M E_i/H_R = 0$  can yield terms associated with the poles. This situation arises when the source and receiver are situated in the same horizontal plane and the generalized transmission path is a direct path. If the source and receiver are in the same plane but not on an interface, the direct paths do not interact with any interface. The response function is then just the time variation in the direct wave, a function which is prescribed in the initial statement of the problem. If the source and receiver are on the same interface, the direct paths interact with that interface only and the problem reduces to the one interface case.  $Y(\gamma)$  becomes

$$Y(\gamma) = \int_{\text{ABOVE}}^{\infty} \xi J_0(\gamma \xi \frac{p}{H_R}) f(\xi) d\xi, \quad \sum_{i=1}^M \frac{E_i}{H_R} = 0.$$

Clearly the asymptotic expansions for high frequency and large offset are identical.

By expressing the Bessel function in terms of the Hankel functions of the first and second kinds and using Cauchy's integral theorem, we can demonstrate that

$$Y(\gamma) = \frac{1}{2} \int_{\text{ABOVE}}^{\xi_N} \xi (f(\xi) - f^*(\xi)) H_0^2(\gamma \xi \frac{p}{H_R}) d\xi + \int_{\xi_i}^{\infty} \xi f(\xi) H_0^2(\gamma \xi \frac{p}{H_R}) d\xi, \quad \sum_{i=1}^M \frac{E_i}{H_R} = 0. \quad (10)$$

The asymptotic expansion of the branch line integral can be obtained by using a variation of the method of stationary phase discussed by Erdelyi (1956). The high frequency behavior is determined by the four branch points ( $N = 4$  for the one interface problem). This is to be expected because the path along the interface is a least-time path for four modes of propagation (i.e., the compressional and shear body waves in the adjacent media). The second term in (10) is present only if the interface can support a Rayleigh or Stoneley wave. The purpose in discussing a problem which has been extensively treated in the literature is to point out the very special situation under which the pole and every branch point of  $f(\xi)$  contribute to the high frequency asymptotic expansion.

When  $\sum_{i=1}^M E_i/H_R \neq 0$ , the expression which corresponds to (10), is

$$Y(\gamma) = \frac{1}{2} \int_{f_1}^{\sin \theta} \xi (f(\xi) - f^*(\xi)) H_0^2(\gamma \xi \frac{P}{H_R}) e^{-\gamma k(\xi)} d\xi + \frac{1}{2} \int_{-\sin \theta}^{\sin \theta} \xi f(\xi) H_0'(\gamma \xi \frac{P}{H_R}) e^{-\gamma k(\xi)} d\xi \quad (11)$$

$$+ \frac{1}{2} \int_{\sin \theta}^{\sin \theta} \xi f(\xi) H_0^2(\gamma \xi \frac{P}{H_R}) e^{-\gamma k(\xi)} d\xi.$$

$(C_+)$

$\theta$  is the angle between the vertical and the segment of the least-time reflection or transmission path which is traversed with velocity  $V_R$ .  $\sin \theta$  satisfies

$$\frac{P}{H_R} = \sin \theta \sum_{i=1}^M \frac{E_i/H_R}{(k_i^2 - \sin^2 \theta)^{1/2}}, \quad 0 \leq \sin \theta < k_1. \quad (12)$$



The mathematical significance of  $\sin\theta$  can be seen by replacing the Hankel functions by their asymptotic representations. In the resultant integrands,  $\gamma$  appears only in the exponentials  $e^{-\gamma K_-(\xi)}$  and  $e^{-\gamma K_+(\xi)}$  where

$$K_{\mp}(\xi) = \mp \left( \xi \frac{p}{H_R} + k(\xi) \right).$$

$\xi_- = -\sin\theta$  is the only saddle point on the surface  $|e^{-\gamma K_-(\xi)}|$  in the upper half plane.  $\xi_+ = \sin\theta$  is the only saddle point on the surface  $|e^{-\gamma K_+(\xi)}|$  in the upper half plane. The contours  $C_-$  and  $C_+$  can be continuously deformed into lines slightly above the part of the real axis to the right of the saddle points without enclosing any singularities of the integrand.

When  $\sin\theta > f_1$ , the asymptotic expansion of the first term describes the head waves. The condition for the existence of head waves is that one or more of the  $f_i$  be less than  $k_1$ . The number of head waves which exist at a particular offset is determined by the  $f_j$  which satisfy

$$0 < f_j < \sin\theta, \quad j=1, \dots, I.$$

Associated with each head wave there is a critical cone

$$\theta_j = \sin^{-1} f_j,$$

a critical distance

$$\frac{p}{H_R} = f_j \sum_{i=1}^M \frac{E_i/H_R}{(k_i^2 - f_j^2)^{1/2}} \quad )$$

and a travel time

$$\tau_j = \frac{t_j}{H_R/V_R} = \frac{p}{H_R} f_j + \sum_{i=1}^M \frac{E_i}{H_R} (k_i^2 - f_j^2)^{1/2}.$$

The asymptotic expansion of  $\bar{U}$  can be expressed in the form

$$\left(\frac{b_1}{p_0 a}\right)(H_R V_R) \bar{U} = e^{-i\gamma\tau_0} \Psi + e^{-i\gamma\tau_1} \Phi_1 + 2 \sum_{J=2}^I e^{-i\gamma\tau_J} \Phi_J, \quad \sum_{i=1}^M \frac{E_i}{H_R} \neq 0. \quad (13)$$

The  $\tau_J$  are normalized travel times for the least-time paths.

This result indicates that the response function and all its derivatives are continuous for  $\tau \neq \tau_J$  ( $J = 0, \dots, I$ ). The first term in (13) comes from the saddle points. This term describes the high frequency behavior of waves which travel least-time reflection paths.  $\tau_0$  is give by

$$\tau_0 = \sum_{i=1}^M \frac{E_i}{H_R} \frac{k_i^2}{(k_i^2 - \sin^2 \theta)^{1/2}}$$

The form of  $\Psi$  depends on whether the observation point is off or on a critical cone. At a point which is not on a critical cone

$$\Psi = \sum_{k=1}^{\infty} \frac{\psi_k}{\gamma^{k+1}}, \quad \theta \neq \theta_J (J=1, \dots, I). \quad (14)$$

The leading coefficients are

$$\psi_1 = - \frac{f(\sin \theta)}{(\beta_1 \beta_2)^{1/2}},$$

$$\psi_2 = \frac{i}{2} \frac{1}{\beta_1^{1/2} \beta_2^{3/2}} \left\{ \frac{f(\sin \theta)}{4} \left[ 3 \left( \frac{2\beta_3 + \beta_4}{\beta_2} - 5 \sin^2 \theta \frac{\beta_3^2}{\beta_2^2} \right) - \frac{1}{\sin^2 \theta} \left( \frac{\beta_2}{\beta_1} - 1 \right) \right] \right. \\ \left. + \frac{1}{\sin \theta} \left( 3 \sin^2 \theta \frac{\beta_3}{\beta_1} - 1 \right) \frac{df}{d\zeta} \right|_{\sin \theta} - \frac{d^2 f}{d\zeta^2} \Big|_{\sin \theta} \right\}.$$

The  $\beta_i$  are determined by

$$\beta_1 = \sum_{i=1}^M \frac{E_i}{H_R} \frac{1}{Q_i}, \beta_2 = \sum_{i=1}^M \frac{E_i}{H_R} \frac{k_i^2}{Q_i^3}, \beta_3 = \sum_{i=1}^M \frac{E_i}{H_R} \frac{k_i^2}{Q_i^5}, \beta_4 = \sum_{i=1}^M \frac{E_i}{H_R} \frac{k_i^2(k_i^2 + 4\sin^2\theta)}{Q_i^7},$$

where  $Q_i = (k_i^2 - \sin^2\theta)^{1/2}$ . Each of the coefficients in (14) is continuous as  $\theta$  approaches zero. This is somewhat surprising for in the derivation of (14) the Hankel functions were replaced by their asymptotic expansions for large argument and as  $\theta$  approaches zero, the argument approaches zero.

As the point of observation approaches a critical cone, the derivatives of  $f(\xi)$  diverge. This follows from the fact that  $f(\xi)$  is a function of the square roots,  $(f_J^2 - \xi^2)^{1/2}$  ( $J=1, \dots, I$ ). Differentiation introduces terms which contain  $1/(f_J^2 - \xi^2)^{1/2}$  as a multiplicative coefficient. These quantities are evaluated at  $\xi = \sin\theta$ . As the point of observation approaches the critical cone ( $\theta_J$ ),  $\sin\theta \rightarrow f_J$  and  $1/(f_J^2 - \xi^2)^{1/2}$  diverges. Consequently, the asymptotic expansion is not uniform in  $\sin\theta$ .

The significance of  $\psi_1$  becomes apparent when we note that  $f(\sin\theta)$  is a function of the ordinary plane wave reflection and transmission coefficients for the least-time reflection path. The factor  $1/(\beta_1 \beta_2)^{1/2}$  corrects the plane wave amplitude for geometric spreading. This factor can be used to compute the effect of geometric spreading for any least-time reflection path in an axially-symmetric, stratified system. The asymptotic expansion in (13) is derived on the assumption that the

source radiation field is isotropic. If the source field is axially symmetric but not isotropic,  $\psi_1$  contains an additional factor which specifies the dependence of the source field on the polar angle.

At a point which lies on a critical cone

$$\Psi = \sum_{k=1}^{\infty} \frac{\chi_k(J)}{\gamma^{(k-1)/4}}, \quad \theta = \theta_J. \quad (15)$$

The saddle point,  $\sin \theta$ , coincides with the branch point  $f_J$ . In order to use Laplace's method to obtain the asymptotic expansion of (11),  $f(\xi)$  must be analytic at the saddle point. Analyticity is achieved by introducing the transformation  $\eta = (\xi^2 - f_J^2)^{1/2}$ . A one-to-one correspondence between points in the  $\eta$  and  $\xi$  planes is achieved by cutting the  $\eta$ -plane along the imaginary axis between  $if_J$  and  $-if_J$ . The  $\chi_k(J)$  can be expressed in terms of  $f(\eta)$  and its derivatives evaluated at the origin on the right side of the cut. The leading coefficients are

$$\chi_1(J) = \frac{-f(\eta=0^+)}{(\beta_1 \beta_2)^{1/2}},$$

$$\chi_2(J) = \frac{-2^{1/4} \Gamma(3/4)}{\pi^{1/2}} e^{i3\pi/8} \left( \frac{f_J}{\beta_1 \beta_2^{3/2}} \right)^{1/2} \frac{df}{d\eta} \Big|_{\eta=0^+}.$$

The  $\beta_i$  must be evaluated at  $\sin \theta = f_J$ . It is important to note that on a critical cone  $\psi_1(\sin \theta = f_J) = \chi_1(J)$ . We refer to the leading term as the geometric term and to the difference between the exact spectrum and the geometric term as the perturbation term. On

a critical cone the asymptotic expansion is obtained in powers of  $\gamma^{1/4}$ , elsewhere the expansion is obtained in powers of  $\gamma$ . Consequently the perturbation spectrum must exhibit a sharp peaking of the high frequency components near the critical cones.

The second and third terms in (13) describe the high frequency behavior of the primary head wave and the secondary head waves respectively. Again by introducing the transformation  $\chi = (\xi^2 - f_J^2)^{1/2}$  we make

$$q(\xi) = f(\xi) - f^*(\xi) \quad (16)$$

analytic at the branch point  $\xi = f_J$ . The asymptotic expansions are

$$\Phi_J = \sum_{k=1}^{\infty} \frac{\phi_k(J)}{\gamma^k}, \quad J=1, \dots, I. \quad (17)$$

The leading coefficients are

$$\begin{aligned} \phi_1(J) &= \frac{f_J}{2\left(\frac{\rho}{H_R}\right)^2 \left(1 - \frac{\rho}{f_J}\right)^{3/2}} \left. \frac{dq}{d\chi} \right|_{\chi=0^+}, \\ \phi_2(J) &= \frac{e^{i\pi/2}}{16\left(\frac{\rho}{H_R}\right)^3 \left(1 - \frac{\rho}{f_J}\right)^{7/2}} \left\{ \left. \frac{dq}{d\chi} \right|_{\chi=0^+} \left[ \left(1 - \frac{\rho}{f_J}\right)^2 + 6\left(1 - \frac{\rho}{f_J}\right) + 15 \left(1 + \sum_{i=1}^M \frac{E_i}{\rho} \frac{1}{\left(\frac{k_i^2}{f_J^2} - 1\right)^{3/2}} \right) \right] \right. \\ &\quad \left. - 4f_J^2 \left(1 - \frac{\rho}{f_J}\right) \left. \frac{d^3 q}{d\chi^3} \right|_{\chi=0^+} \right\}. \end{aligned}$$

Because of the terms in  $(1-\rho/\rho)^{-n/2}$ , the  $\phi_k(J)$  diverge as the point of observation approaches the critical cone. The same behavior is exhibited by the  $\psi_k$  (for the least-time reflection path). The geometric factor in  $\phi_k(J)$  is identical with that obtained by Heelan (1953).

D. The Singular Behavior of the Generalized Response Functions at Times Associated with Least-Time Paths

The high-frequency character of the spectrum is completely determined by the non-analytic behavior of the response function at the  $\tau_j$ . If the response function were analytic, the spectrum would exhibit a completely different high-frequency character (an analytic function decays more rapidly with frequency than  $\omega^{-N}$  where  $N$  is any positive integer no matter how large). The  $\tau_j$  are the only non-analytic points, otherwise there would be additional contributions to (13).

To discover the nature of the singularity at  $\tau_j$ , we apply the inverse Fourier transform to the geometric term and to the leading terms in the asymptotic expansion of the perturbation term. Each of these terms can be associated with a whole family of time functions. All members of a family possess spectra which exhibit identical high frequency characteristics. Accordingly, we attach significance only to those characteristics of the time function which are exhibited by all members of the

family. One such characteristic is the highest order singularity. A discontinuity in the function itself is regarded as a higher order singularity than a discontinuity in slope, etc. The highest order singularity associated with each member of a particular family will be identical. For example, if the function is continuous but its first derivative diverges logarithmically at  $\tau_j$ , every member of the family will be continuous and will have a derivative which diverges logarithmically at  $\tau_j$ .

The functions to which we apply the inverse Fourier transform are of the form

$$\overline{R}(\tau_j) = e^{-i\gamma\tau_j} \frac{A_j}{(i\gamma)^q} e^{i\zeta\gamma/|\gamma|}, \quad q \geq 0. \quad (18)$$

If  $\zeta \neq 0$  and  $q \geq 1$ , this function is not Fourier transformable. However, there is a whole family of time functions which in the high frequency limit exhibit the dependence on  $\gamma$  given in (18). To find a member of the family we modify the low frequency behavior to make the result Fourier transformable. We make the modification in such a way that the phase and amplitude spectra are respectively odd and even functions of  $\gamma$ . One way of modifying (18) is to replace  $(i\gamma)^q$  by  $(i\gamma + \alpha)^q$  where  $\alpha$  is positive real. It is important to note that in what follows none of the results depends on  $\alpha$ .



The time function corresponding to the modified  $\bar{R}(\tau_J)$  can be obtained by convolving the time functions corresponding to

$$\bar{L}_e(\gamma) = A_J e^{i\gamma\tau_J}$$

and

$$\bar{P}(\gamma) = \frac{e^{-i\gamma\tau_J}}{(i\gamma + \alpha)^2}.$$

In the process of convolution,

$$L(\tau) = \frac{A_J}{H_R/V_R} \left\{ -\frac{\sin S_J}{\pi\tau} + \delta(\tau) \cos S_J \right\}$$

produces the same results as  $L_e(\tau)$  and may be considered equivalent to it.  $\delta(\tau)$  is the Dirac delta function. The time function which corresponds to  $\bar{P}$  is

$$P(\tau) = 0, \tau < \tau_J, \\ = \frac{1}{2\pi H_R/V_R} \int_{-\infty}^{\infty} \frac{e^{i(\tau-\tau_J)\xi}}{(i\xi + \alpha)^2} d\xi, \tau > \tau_J.$$

Applying the convolution theorem gives

$$R(\tau_J) = -\frac{A_J \sin S_J}{\pi} \int_{-\infty}^{\tau-\tau_J} \frac{P(\tau-\eta)}{\eta} d\eta, \tau < \tau_J, \\ = -\frac{A_J \sin S_J}{\pi} \int_{-\infty}^{\tau-\tau_J} \frac{P(\tau-\eta)}{\eta} d\eta + A_J \cos S_J P(\tau), \tau > \tau_J. \quad (19)$$

The singular character of the response function at each  $\tau_J$  can be obtained by substituting the individual terms from the asymptotic expansion into (18) and (19).

The geometric term for the least-time reflection path is

$$R(\tau_0) = \frac{1}{(H_R/V_R)(\beta_1\beta_2)^{1/2}} \left\{ \frac{df(\sin\theta)}{d(\tau-\tau_0)} - (Rf(\sin\theta)) \delta(\tau-\tau_0) \right\}. \quad (20)$$

The strengths of the delta function and  $(\tau-\tau_0)^{-1}$  terms are determined by the real and imaginary parts of the function of the plane wave coefficients respectively. Inside and on the first critical cone ( $\theta \leq \theta_1$ ),  $f(\sin\theta)$  is pure real and the  $(\tau-\tau_0)^{-1}$  term is absent. Except for the factor which corrects for geometric spreading,  $R(\tau_0)$  is similar to a result derived by Arons and Yennie (1950) by considering the reflection of a plane wave at a liquid-solid interface. Equation (20) shows that their result is also valid for a multiply reflected wave which is initially spherical in shape.

The geometric terms associated with the head waves produce finite discontinuities at the  $\tau_J$  given by

$$\lim_{\epsilon \rightarrow 0} (R(\tau_J + \epsilon) - R(\tau_J - \epsilon)) = G(\tau_J) - (2 - \delta_{1,J}) i \phi(J), \quad J=1, \dots, I. \quad (21)$$

This is a real quantity because  $\phi(J)$  is pure imaginary.

$\delta_{1,J} = 0 (J \neq 1)$ ,  $\delta_{1,1} = 1$ . It may be worth pointing out that (21) does not predict how the head wave amplitude decays with distance but only how the discontinuity decays with distance. Under certain conditions the two are equivalent but not always. Consider the response produced by a source function  $\chi(\tau/(t_d/(H_R/V_R)))$ . We have shown that convolution of a function which varies linearly

with a physically realistic source function (which satisfies (2)) yields zero. Consequently, if on each side of  $T_j$ , the impulse response varies linearly over an interval  $T$  which is equal to the duration of  $\chi$ , then (21) describes how the head wave amplitude decays with distance. Certainly for a source function of finite duration this condition cannot be satisfied in the vicinity of a critical cone but it may be approached as the distance from the critical cone increases.

Convolving  $\chi(T/(t_d/(H_R/V_R)))$  with the step discontinuities associated with the head waves introduces a factor  $t_d/(H_R/V_R)$  in the expression for the head wave amplitude. By dividing the source function by  $(t_d/(H_R/V_R))^{1/2}$  we make the total energy radiated into the system independent of  $t_d$ . It follows that the head wave amplitude is proportional to  $(t_d/(H_R/V_R))^{1/2}$  even though the energy input is independent of  $t_d$ . As the dominant period increases, the energy in the head wave increases. If this behavior were continued to very long periods, the energy in the head wave would exceed the total energy radiated into the system. We conclude that a  $(t_d/(H_R/V_R))^{1/2}$  low-frequency dependence of the head wave amplitude is indicative of the failure of the high-frequency theory.

The singular behavior of the response computed from geometric theory is sketched in Figure 2.

Next we investigate the singular behavior of the perturbation function at the  $\tau_J$ . The singularities are sketched in Figure 3. At a point which is not on a critical cone, the reflected wave is associated with

$$P(\tau_0) = \frac{1}{H_R/V_R} \left\{ (Re \psi_2) 1(\tau - \tau_0) - (Im \psi_2) \frac{\log |\tau - \tau_0|}{\pi} \right\}, \quad \theta \neq \theta_J (J=1, \dots, I). \quad (22)$$

Inside the first critical cone,  $\psi_2$  is pure real and the logarithmic term is absent. On a critical cone the reflected wave is given by

$$P_-(\tau_0) = \left( \frac{\Gamma(3/4)}{2^{1/2} \pi} \right) \frac{1}{H_R/V_R} \frac{A_0 \sin \zeta_0}{\pi} \frac{C_-}{(\tau_0 - \tau)^{3/4}}, \quad \tau < \tau_0, \quad (23)$$

$$P_+(\tau_0) = \left( \frac{\Gamma(3/4)}{2^{1/2} \pi} \right) \frac{1}{H_R/V_R} \left( \frac{A_0 \sin \zeta_0}{\pi} C_+ + A_0 \cos \zeta_0 \right) \frac{1}{(\tau - \tau_0)^{3/4}}, \quad \tau > \tau_0,$$

where

$$A_0 e^{i\zeta_0} = e^{i\pi/8} \chi_2(J) = - \frac{2^{1/4} \Gamma(3/4)}{\pi^{1/2}} \left( \frac{f_J}{\beta_1 \beta_2^{3/2}} \right)^{1/2} e^{i\pi/2} \frac{df}{d\chi} \Big|_{\chi=0^+}$$

$$C_- = \int_1^\infty \frac{d\zeta}{\zeta(\zeta-1)^{3/4}}, \quad C_+ = P \int_{-1}^\infty \frac{d\zeta}{\zeta(\zeta+1)^{3/4}}.$$

P indicates that the Cauchy principal value is required. On the first critical cone ( $J=1$ ),  $e^{i\pi/2} \frac{df}{d\chi} \Big|_{\chi=0^+}$  is pure real. Consequently, the perturbation function vanishes for  $\tau < \tau_0$ . On any critical cone except the first, the perturbation function

diverges from both the left and right. On the critical cones the divergence is not symmetric about  $\tau_0$  while everywhere else it is symmetric.

The head waves are associated with discontinuities in the slope of the perturbation function which are given by

$$\lim_{\epsilon \rightarrow 0} \left\{ \frac{dP}{d\tau} \Big|_{\tau_J + \epsilon} - \frac{dP}{d\tau} \Big|_{\tau_J - \epsilon} \right\} = - \frac{(2 - \delta_{1J})}{H_R/V_R} \phi_2(J). \quad (24)$$

By convolving a physically realistic source function with each of the geometric singularities (e.g., the step, delta function, and  $(\tau - \tau_0)^{-1}$  term), we obtain three primary wavelets. The high-frequency response of a layered system consists of a superposition of the wavelets for all least-time paths. By time delaying the wavelets and multiplying by the proper amplitude factors, we can construct the high-frequency response from three basic waveforms.

#### E. The One-Interface System

For a system which consists of two half-spaces perfectly coupled together along a plane, several interesting characteristics of the spectrum can be inferred directly from (9) without resorting to approximate theory. The geometric parameters are indicated in Figure 4. Let  $V_R = V_1$  and  $H_R = R$  (the distance along the least-time path for the reflected compressional (P) wave). The spectrum of the response function produced by waves which arrive at the receiver in the compressional mode is

$$(RV_1)\overline{U} = i\gamma \int_0^\infty \xi J_0(\gamma \xi \sin \theta_{PP}) f(\xi) e^{-\gamma(\cos \theta_{PP})(\xi^2 - 1)^{1/2}} d\xi, \quad \gamma = \omega \frac{R}{V_1}.$$

ABOVE

The spectrum, considered as a function of  $\gamma$ , has a shape that depends only on the angle of incidence,  $\theta_{PP}$ . Changes in source and receiver positions which do not change  $\theta_{PP}$  have no effect on the spectral shape. The spectrum plotted as a function of  $\omega$  is displaced toward lower frequencies as  $R$  increases and toward higher frequencies as  $R$  decreases. In general, the shear spectrum is more complicated. However, if the source and receiver are situated in the same plane ( $Z=H$ ), both the compressional and shear spectra can be put in the form

$$(HV_1)\overline{U} = i\gamma \int_0^\infty \xi J_0(2\gamma \xi \tan \theta_{PP}) f(\xi) e^{-\gamma\{(1+\delta)(\xi^2-1)^{1/2} + (1-\delta)(\xi^2 V_1^2/V_2^2)^{1/2}\}} d\xi \quad (25)$$

ABOVE

$$\gamma = \omega \frac{H}{V_1},$$

where  $\delta=1$  for the compressional component and  $\delta=0$  for the shear component. From (25), we infer that the shape of the response function (considered as a function of  $t/(H/V_1)$ ) depends only on  $\theta_{PP}$ . This means that the amplitudes of the head, reflected and interface waves bear a fixed relationship to one another which is independent of position on a particular ray.

If we impose certain criteria to determine a cutoff on the usefulness of the high frequency theory, that cutoff must satisfy a relation of the form

$$\frac{H}{V_1} \omega_0 = C(\theta_{PP}). \quad (26)$$

Increasing  $H$  reduces  $\omega_0$  and extends to lower values the frequency range within which the use of high frequency theory is justified. In near zone work whose objective is to delineate the layering, we are not interested in frequencies below a certain value. By using (26) we can find a function,  $H_0(\theta_{PP})$ , which corresponds to the low-frequency cutoff. This function defines a fictitious surface lying above the interface. Above this surface the use of high-frequency theory is justified over the entire frequency band of interest--but between this surface and the interface it is not.

Cagniard's method yields an expression for the exact impulse response. Inside the critical angle the response functions for the compressional and shear components can be easily separated into a geometric term (which is just the delta function) and a perturbation term. The perturbation term is plotted in Figure 5 for  $V_1/V_2=0.5$  ( $\theta_c=30^\circ$ ) and in Figure 6 for  $V_1/V_2=1.5$  (no critical angle).  $\sigma$  is the Poisson's ratio. In each

figure the perturbation function is plotted for several values of  $\theta_{pp}$ . The compressional functions are plotted on the left side under  $P^P$  and the shear functions are plotted on the right side under  $P^S$ .  $\tau = t/(H/V_1)$ . Except where indicated otherwise, the separation between divisions on the abscissa is the same for all graphs on a particular figure and is indicated in the upper left graph. The long-time divergent behavior is characteristic of the response function for a single generalized transmission path. The total perturbation response is obtained by adding the compressional and shear components with the appropriate time delay. The resultant function approaches a constant in the long-time limit. Convolution with a source function which has no static component produces a function which tends to zero in the long-time limit.

In Figure 5 the perturbation functions are featureless except for the discontinuity. The discontinuity develops into a sharp spike as  $\theta_{pp}$  approaches the critical angle. The asymptotic theory predicts that the discontinuity approaches infinity as  $\theta_{pp} \rightarrow \theta_c$  and that right on the critical cone the initial behavior is given by  $(\tau - \tau_{pp})^{-3/4}$ .

The condition for the existence of a Stoneley wave is not satisfied in Figure 6. The strong phase at grazing incidence is a pseudo-interface wave. Waves of this type have



been studied extensively by Strick (1959), Phinney (1961) and Gilbert and Laster (1962). There are no terms in the asymptotic expansions for either high frequency or large horizontal distance which would reveal the existence of pseudo-interface waves. These waves are associated with zeros of the denominator in the generalized coefficients which lie on a lower (non-permissible) sheet of the Riemann surface. The pseudo-interface wave propagates with a velocity which exceeds the smallest body wave velocity and continually radiates energy into one or both of the adjacent media. The velocity of the true interface wave is always less than the minimum body wave velocity and there is no net flux of energy normal to the interface. In Figure 6 the velocity of the pseudo-interface wave is intermediate between the two shear velocities. Therefore, the pseudo-interface wave produces motion in medium one but there is no net flux of energy normal to the interface which is directed into medium one.

Amplitude and phase spectra have been computed for the perturbation functions of Figure 5. Individual frequency components ( $\eta = fH/V_1$ ) are plotted against the angle of incidence in Figures 7 and 8 for the compressional and shear components respectively. The pronounced minima exhibited by the higher frequency components occur at angles where the discontinuity goes through zero. As  $\eta$  decreases the minimum becomes

less pronounced and shifts to larger angles. The lower frequency components show very little dependence on  $\theta_{pp}$ . The higher frequencies increase in amplitude very rapidly as  $\theta_{pp}$  approaches the critical angle. Recall that asymptotic theory predicted a sharp peaking of the high frequency components on each critical cone.

The geometric term is represented by a delta function. Therefore, at each angle of incidence all frequencies have the same amplitude. The amplitude is indicated by the dashed curves in Figures 7 and 8. Spectral components which intersect a vertical line above the dashed curve are strongest in the perturbation term. A spectral component is the crossover frequency at that angle where it intersects the dashed curve. The crossover frequency sets a lower limit on the frequency range over which the use of geometric theory is justified. For the compressional component the crossover frequency lies between .25 and .50 over nearly the entire range of  $\theta_{pp}$ , while for the shear component the crossover frequency varies from about 1.0 to infinity. The reason for the difference is that the geometric term for shear goes to zero at normal incidence and just inside the critical angle while the geometric term for the compressional component does not go to zero. At angles where the geometric term vanishes, it is the discontinuity in the perturbation function which determines the high frequency behavior of the total response.

Let  $T$  be the duration of a source function and  $f_d$  its dominant frequency. Whether the perturbation term can be neglected in the interval  $T$  following the onset depends on the relation between the crossover frequency and  $f_d$ . When  $f_d$  is large compared to the crossover frequency, the perturbation term can be neglected. Outside the interval  $T$  following the onset the situation is more complicated. The perturbation term may contain additional phases (e.g., pseudo-interface waves) which do not overlap with the reflected phase. Although these phases are diminished in amplitude by increasing  $f_d$ , they probably cannot be neglected unless they interfere with larger amplitude geometric phases reflected from other interfaces or fall outside the dynamic range of the recording system.

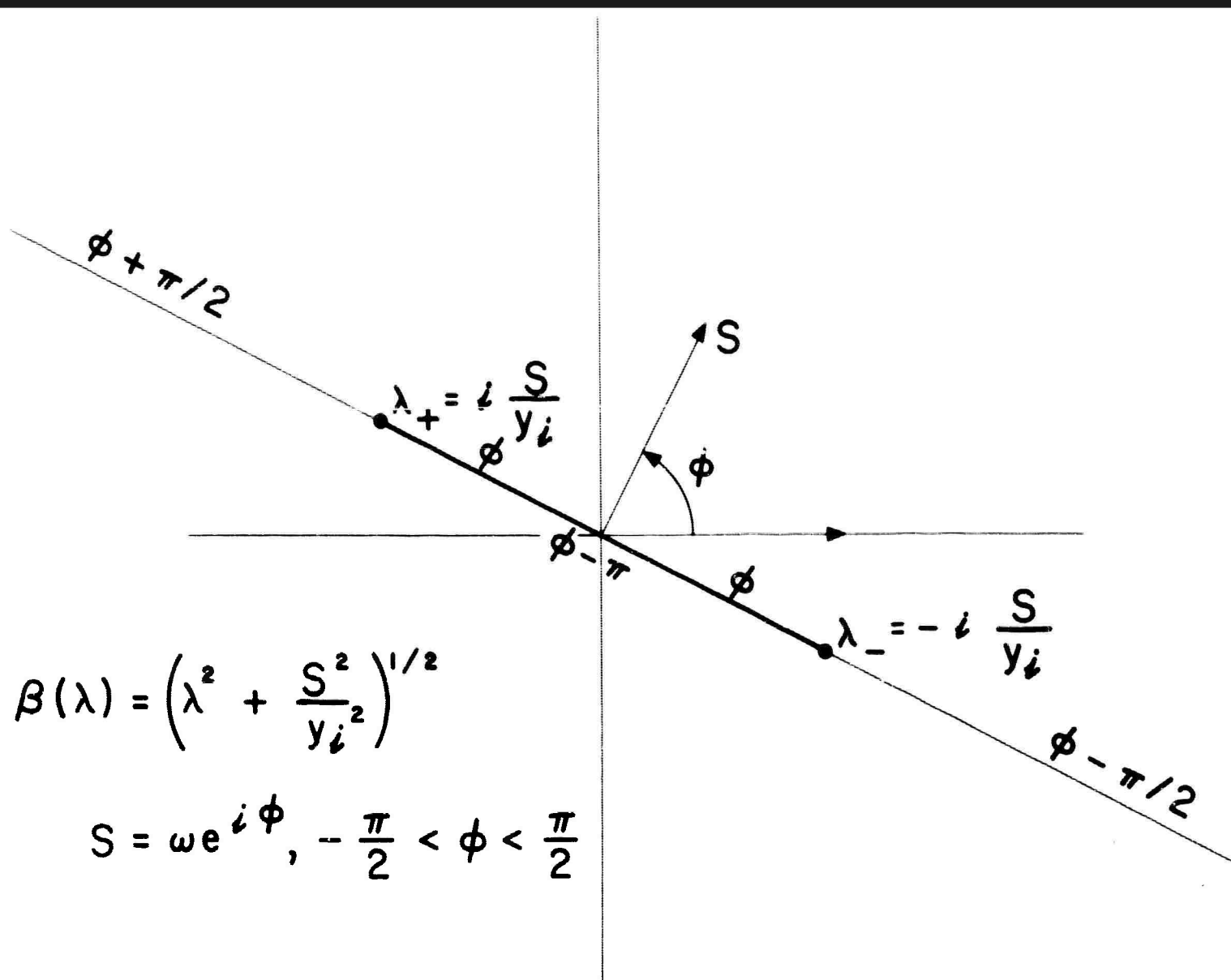


FIGURE 1

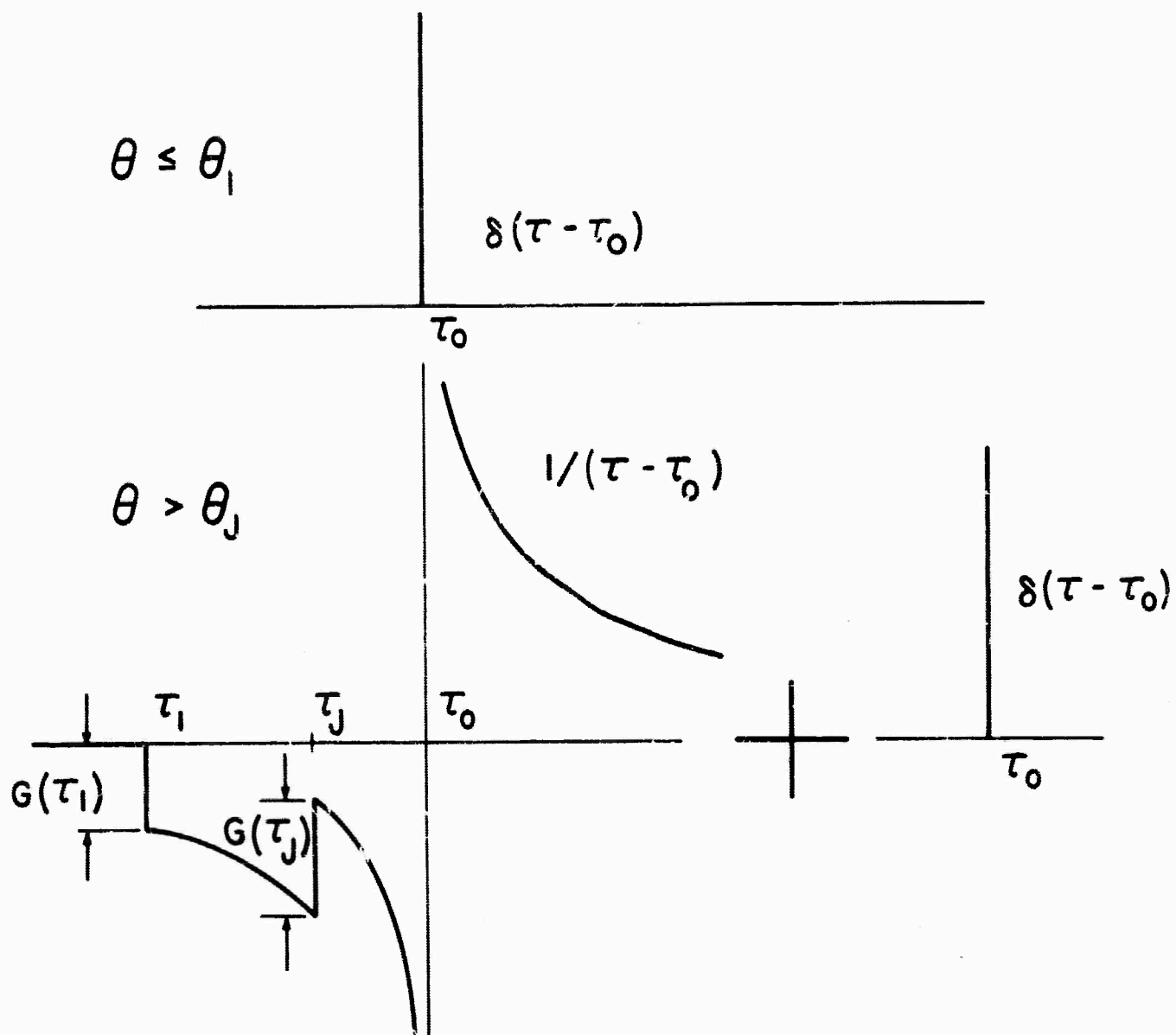
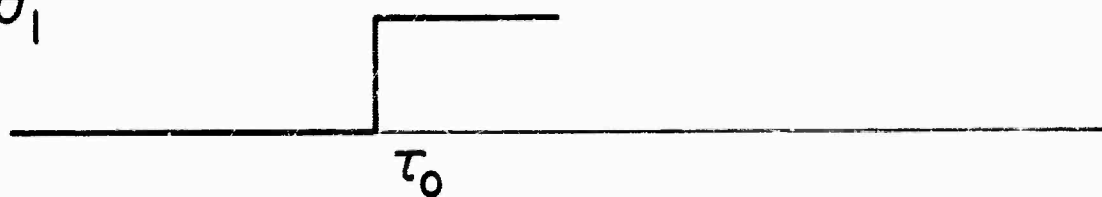
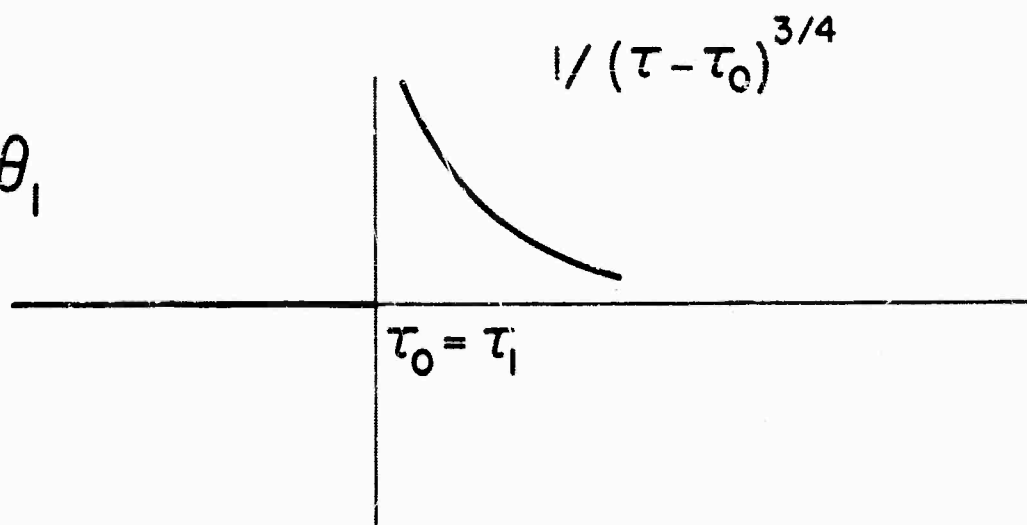


FIGURE 2

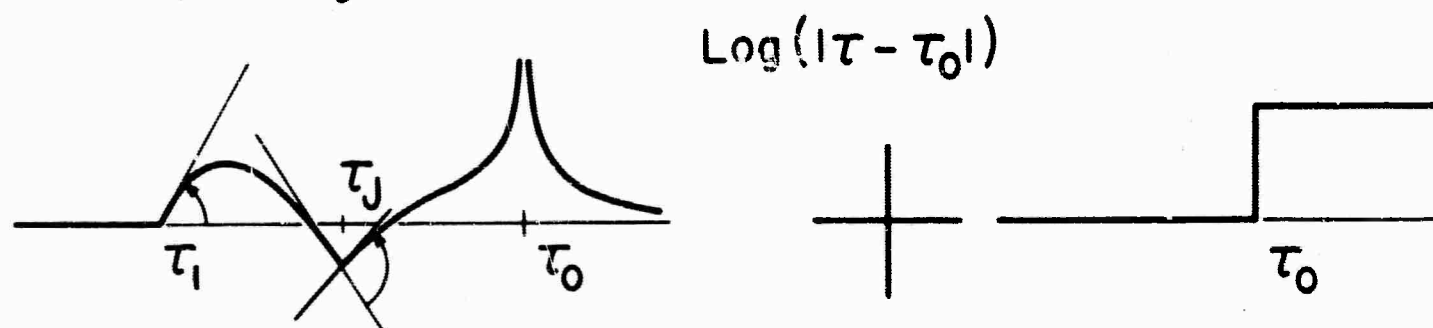
$$\theta < \theta_1$$



$$\theta = \theta_1$$



$$\theta > \theta_1, \theta \neq \theta_j$$



$$\theta > \theta_1, \theta = \theta_j$$

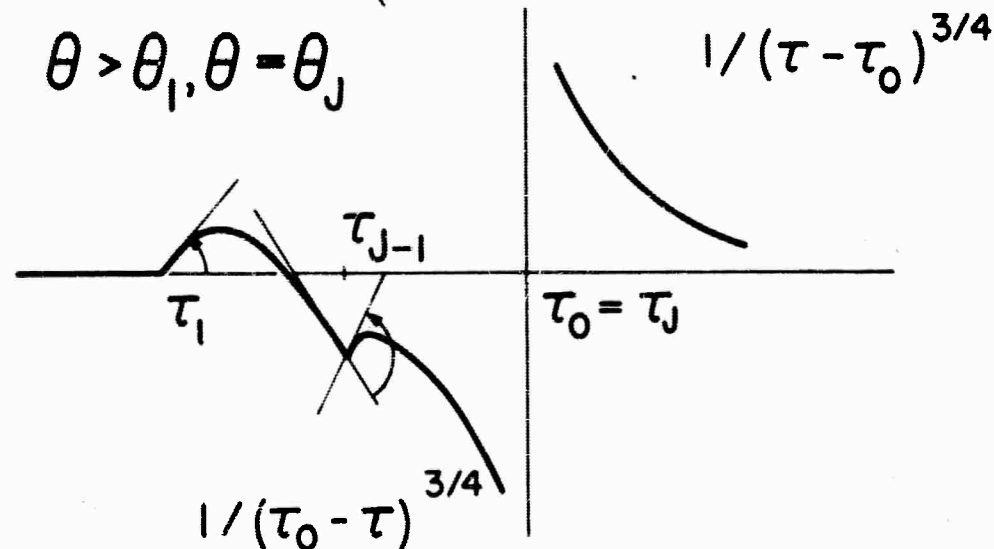


FIGURE 3

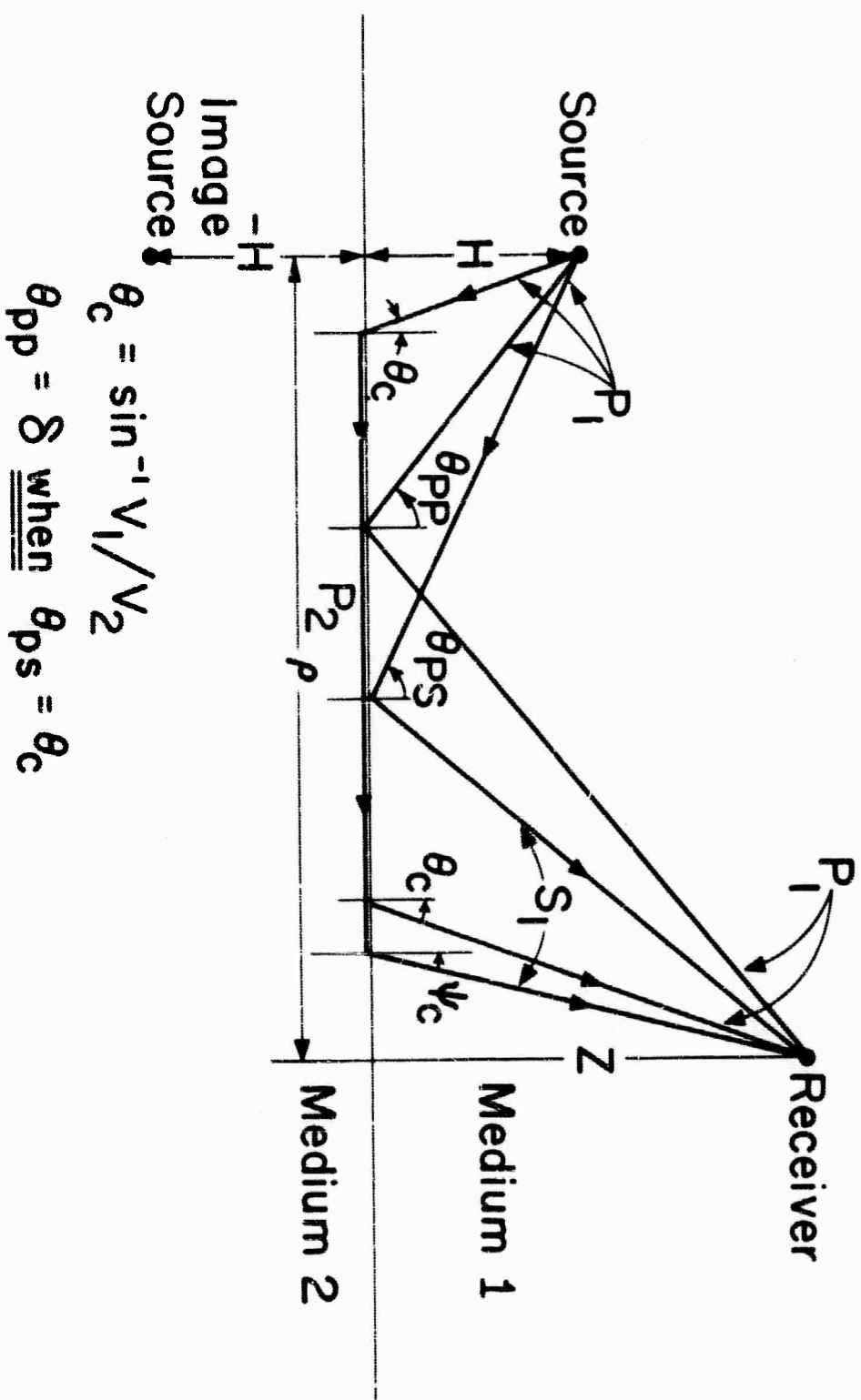
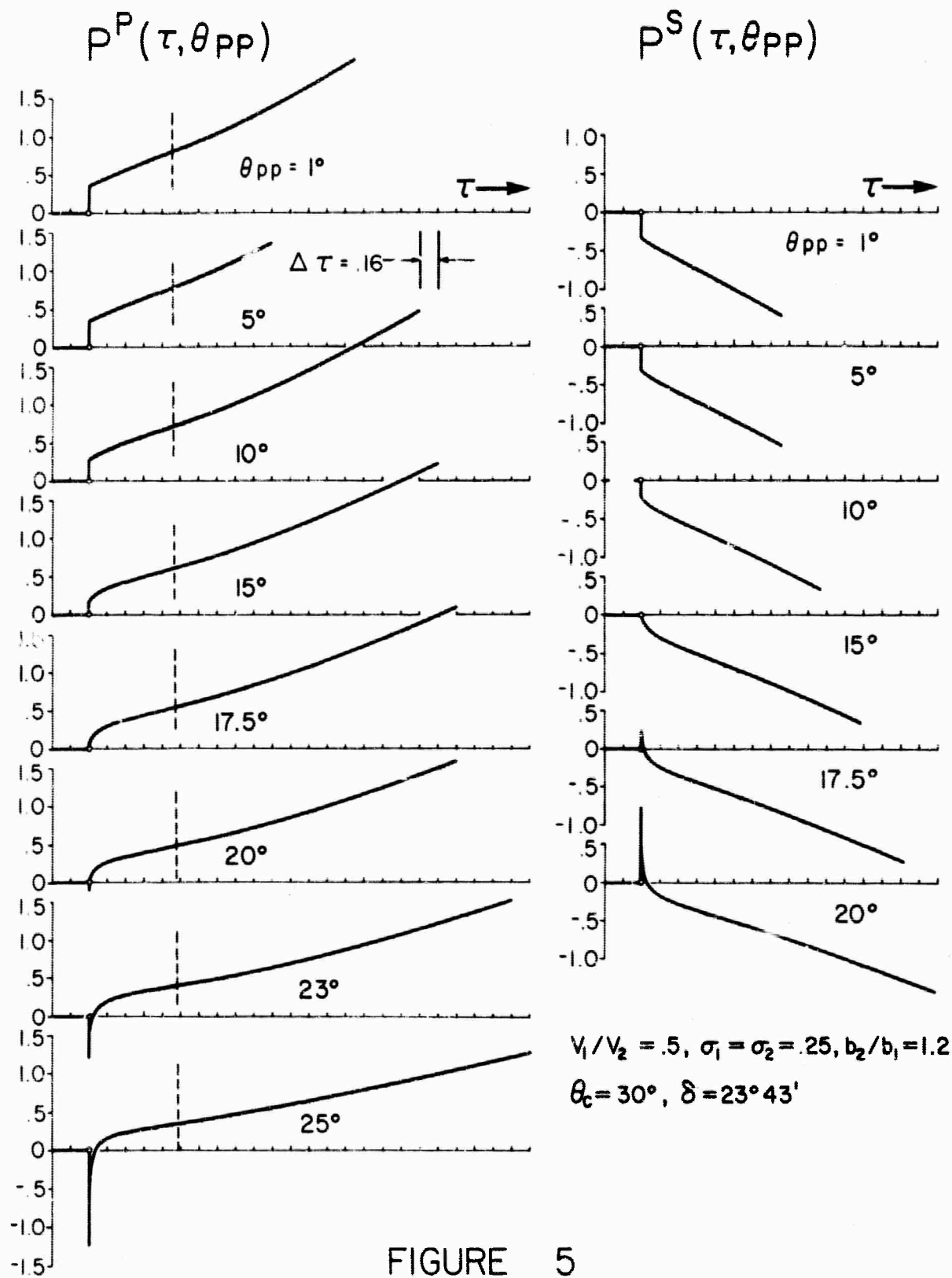
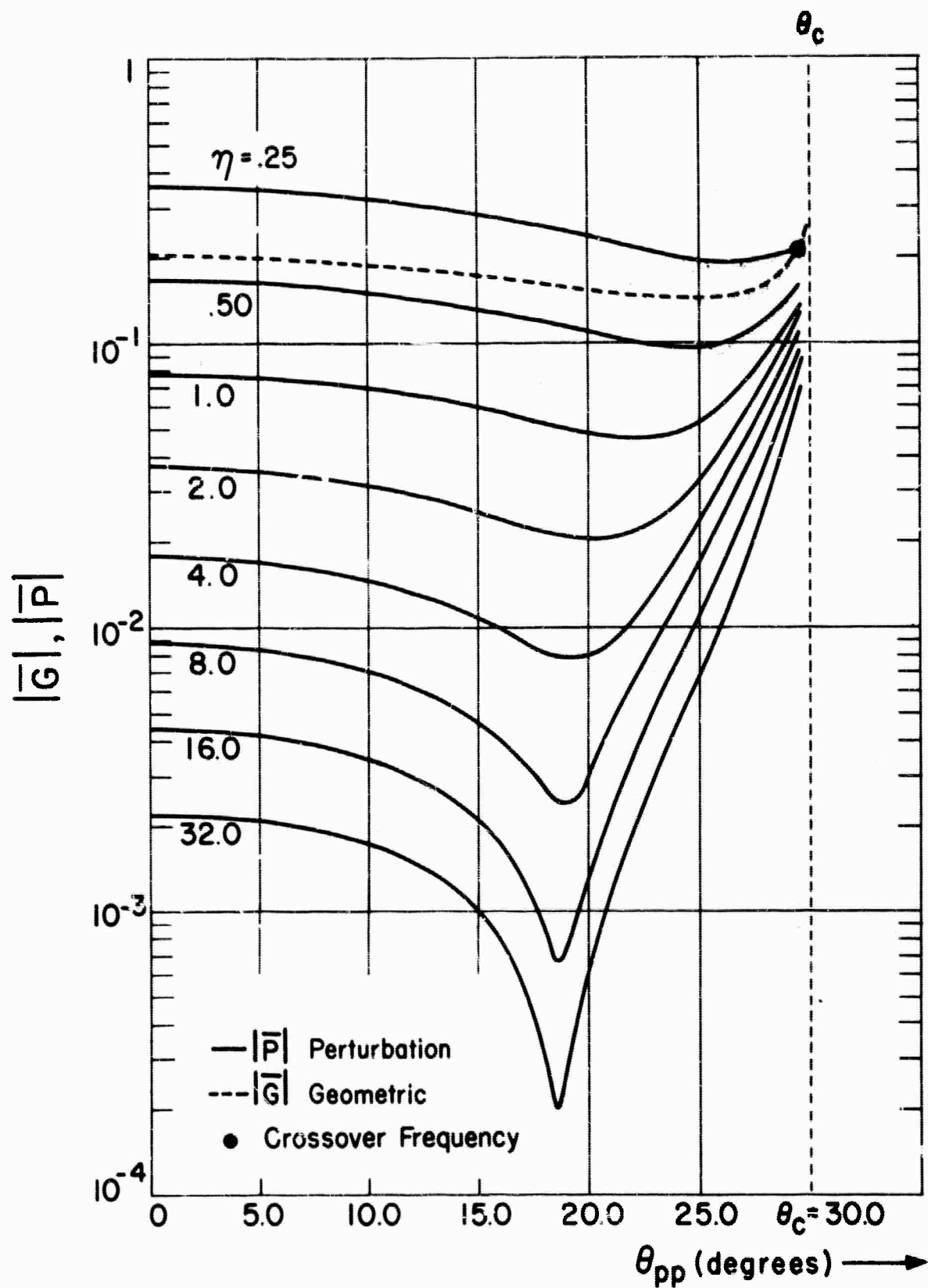


FIGURE 4



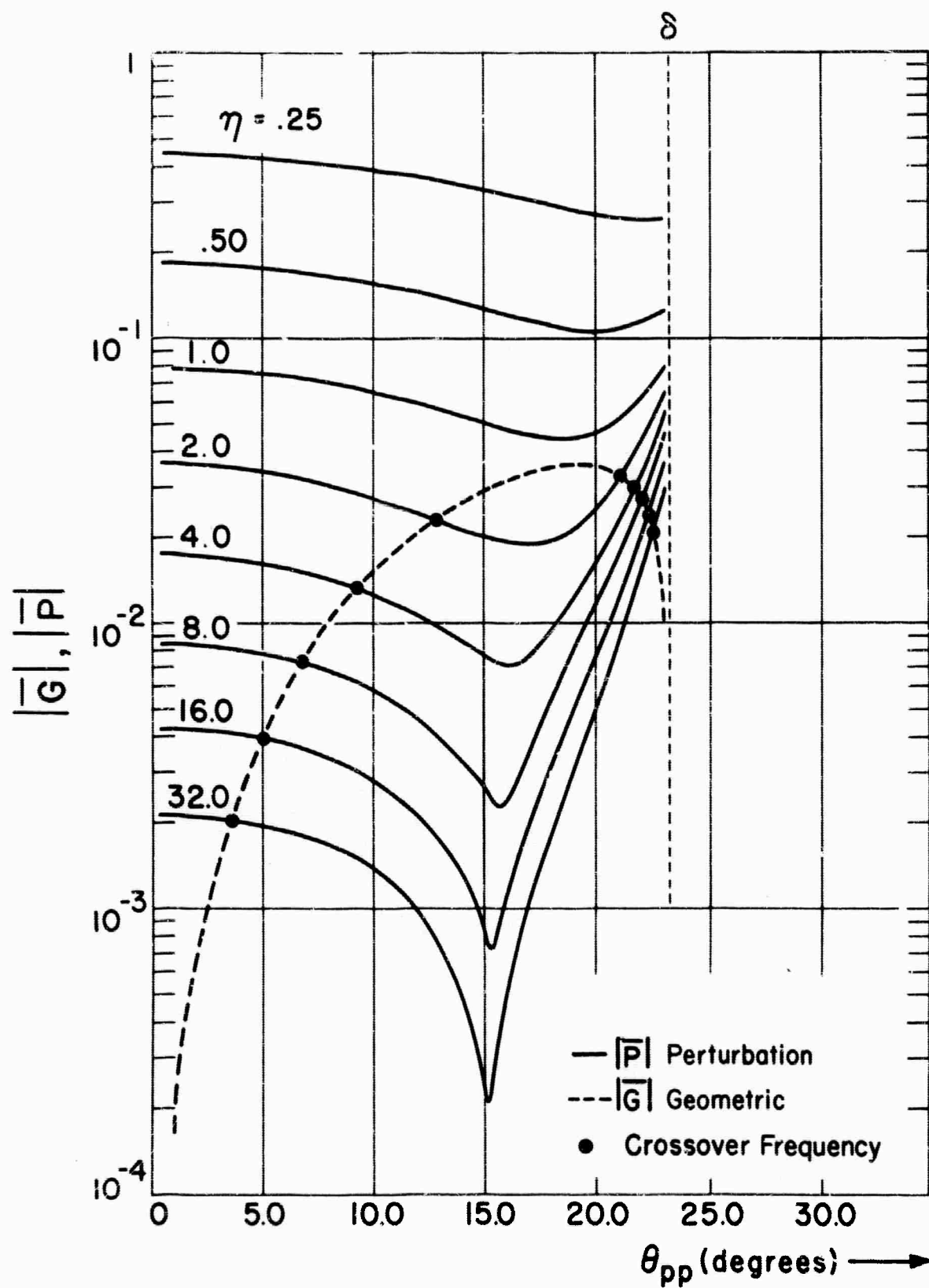






COMPRESSIONAL COM. JNENT  
 $V_1/V_2 = .5, \sigma_1 = \sigma_2 = .25, b_2/b_1 = 1.2$

FIGURE 7



SHEAR COMPONENT

$V_1/V_2 = .5, \sigma_1 = \sigma_2 = .25, b_2/b_1 = 1.2$

FIGURE 8

VI. ANALYSIS OF A PROGRAM FOR  
COMPUTING THEORETICAL SEISMOGRAMS  
FOR A MULTILAYERED MEDIA

The "matrix method" (Haskell, 1953) is in principle a method for the numerical computation of theoretical seismograms. The method is analyzed with the objective of determining the effect of source depth on the response of an elastic layered medium in the time interval preceding the arrival of the unattenuated normal modes. The mathematical model is based on an idealized physical model of a vacuum half-space overlying a set of liquid and solid elastic layers, with all liquid layers above the solid ones. The layers are homogeneous, isotropic, and perfectly coupled together at the interfaces. The point source and the point receiver may be located in any layer.

The mathematical technique is the common one of assuming that the stresses and displacements may be derived from a set of potential functions (one shear potential and one compressional potential for each layer), expressing these potentials in terms of their Fourier transforms and then using the matrix method to determine the transform of the response, i.e., the transforms of the stresses and displacements. In theory, the actual physical stresses and displacements may be found by inverting these transforms by double integration over the first quadrant of the plane of  $k$  (wave number) and  $w$  (circular frequency), the transform parameters. However, in general there

is a finite positive number  $C_0$  such that the transforms are singular for some curves in the region where  $\omega/k < C_0$  and regular for  $\omega/k > C_0$ .  $C_0$  is the maximum phase velocity for unattenuated normal mode propagation. In this work the integration is constrained to the regular region.

Other investigators have used a similar technique but have confined their attention to the location of the singular curves (dispersion curves) and the contribution to the total response of these singular curves, i.e., they have investigated the normal modes, which yield the most significant contributions to the response at large epicentral distances. Additionally, there are certain technical differences in the definitions in the matrix method itself, resulting in the fact that in our formulation the matrix which relates the stress-displacement vector at the bottom of a layer to the one at the top of the layer is real for all non-negative  $k$  and  $\omega$ . The point compressional source is also introduced here by real quantities, free of singularities.

The formulas were programmed in Fortran for the IBM 7094, with the exception that the complex subroutine was not used. Computation of the transformed response vector  $v$  for each  $k$  and  $\omega$  in the case of a vacuum over a solid half-space requires twenty milliseconds. Each additional solid layer

requires about five milliseconds. For each  $w$ ,  $v$  is computed for a set of equally spaced  $K$  values running from zero up to the cut-off value of  $w/C_0$ . The  $w$  values are also equally spaced, starting with  $w$  about ten.

The transformed response  $v$  for a vacuum over a solid half-space exhibits sharp peaking at the point  $K = w/\alpha$  ( $\alpha$  is the compressional velocity). In an interval of the  $K$  values of  $10^{-3}$ , one component rises from zero to 6500. Since these values are to be integrated, very fine sampling of the  $v$  functions is necessary in the  $K$  direction. Because it is desirable that the source pulse be sharp, a wide range of  $w$  values is also required, necessitating sampling the  $v$  functions at over a million points in the  $(K, w)$ -plane. This sampling alone would require five and one-half hours on the computer, not including the double integration which must follow.

Certain difficulties occur even during the computation of  $v$ . Elements of the matrices involve quantities such as  $\exp(h\sqrt{K^2 - (w/\alpha)^2})$ , where  $h$  is the thickness of a layer or combination of layers. This number is frequently outside the range of the computer (with the standard floating point subroutine) for many, indeed, most, problems of seismological interest. Also, expressions such as

$$\cosh \sqrt{K^2 - (w/\alpha)^2} h - \cosh \sqrt{K^2 - (w/\beta)^2} h$$

appear, which lead to large round-off errors for large  $h$  or  $K$ .

These problems have been experienced by others, who have circumvented

them by using the very low  $w$  values and the small  $k$  values which are more applicable in the normal mode theory. These problems of number size and round off can, of course, be solved by increasing the word length of the computer, either mechanically or by special programming.

The effect of restricting the  $w$  and  $k$  values to the region of regularity  $w/k > C_0$  was partially investigated by examining the effect of such a truncation on the potential function for a point compressional source in an infinite homogeneous isotropic medium. It was discovered that the distortion caused in this potential by eliminating the region  $w/k < C_0$  was not great if the receiver was on the same horizontal as the source, but was much greater if the receiver was on the same vertical as the source. Because of this distortion, it would be difficult to determine in the seismogram what role was played by the layering in the system and what role was played by the placing of the receiver.

It was concluded that though the matrix method is conceptually a simple numerical method for solving this complex problem, in practice too much computation is required to realize even the result distorted by truncation, which would be difficult to interpret. Certainly, the expense is currently too great to justify use of this method.

The matrix method has some value as a theoretical tool here, particularly regarding location of the curves of singularities. The following conclusions were reached by a simple examination of the appropriate mathematical expressions:

1) The only branch points of  $v$  in the case of the point compressional source are those involving the compressional and shear velocities in the last layer (the lower half-space), and this is true for any intermixed system of liquid and solid layers. Jardetzky (1953) proved this for solid layers.

2) If all layers are liquid with compressional velocities  $\alpha_j$ , then the phase velocity  $C$  of any unattenuated normal mode satisfies  $\min_{1 \leq j \leq n} \alpha_j \leq C \leq \alpha_n$ , where  $\alpha_n$  is the compressional velocity of the half-space. In particular, if  $\min_{1 \leq j \leq n} \alpha_j = \alpha_n$ , there are no unattenuated normal modes.

3) In the case of liquid layers over a solid half-space, if  $\min_{1 \leq j \leq n-1} \alpha_j > \alpha_n^*$ , where  $\alpha_n^*$  is the Rayleigh velocity of the half-space, there is at least one unattenuated normal mode with a phase velocity smaller than  $\alpha_n^*$ .



## VII. THE REFRACTED ARRIVAL FROM A LAYER

High-frequency geometric ray theory is used to investigate the refracted arrival from a high-speed layer embedded in an infinite medium. The geometric parameters are indicated in Figure 1. The top of the layer is at a depth  $H$  below the source and at a depth  $Z$  below the receiver. The  $Z$  axis passes through the source and is normal to the interface. The plane  $Z=0$  coincides with the top of the layer. The radiation field is axially symmetric about the  $Z$  axis.  $E$  is the layer thickness and  $\rho$  is the range.  $V$  is the compressional velocity,  $\nu$  is the shear velocity, and  $b$  is the density. Subscript 1 refers to the infinite medium and subscript 2 refers to the layer.

Refraction along a layer is considerably more complicated than refraction along an interface between two semi-infinite media. To demonstrate this, let  $T$  be the duration of the refracted arrival from a semi-infinite medium and let  $t_r$  be the travel time. Note that  $t_r$  is independent of layer thickness. The results for a semi-infinite medium are not valid if waves which are multiply reflected within the layer or other wave types arrive in the interval  $t_r \leq t \leq t_r + T$ . Multiple reflections distort the refracted arrival when  $T$  is large, the layer is thin, or the offset is large. When any of these conditions is satisfied, the individual phases are not completely resolved and the character and amplitude of the refracted arrival are determined by the way in which the individual phases interfere with one another.

When we attempt to take into account all the waves which are multiply reflected within the layer, we immediately encounter the problem of degeneracy. The simplest case of degeneracy arises when the ray crosses the layer once in the compressional (P) mode and once in the shear (S) mode. In Figure 1 we see that there are two such rays which arrive at exactly the same time and are therefore degenerate. These two rays differ in the sequence in which the P and S legs of the path are traversed. This type of degeneracy is entirely different from the accidental degeneracy which can occur when the velocities and the layer thickness are suitably related. It is a consequence of the fact that two different types of propagation occur in an elastic medium. Degeneracy occurs only for rays which cross the layer in both modes.

To reduce this idea to quantitative terms, we introduce the following notation:

$n$  = number of crossings in the P mode,

$m$  = number of crossings in the S mode.

Specifying  $n$  and  $m$  does not determine a particular ray but rather a family of degenerate rays. The number of rays in the family (i.e., the degeneracy) is

$$D_{nm} = \frac{(n+m)!}{n!m!} \quad (1)$$

Even for small  $n$  and  $m$ , the degeneracy can be quite large. If highly degenerate events are truly significant, a way must be found for removing the degeneracy--otherwise the ray theory becomes extremely inefficient from a computational standpoint. Also, because all the degenerate waves arrive at the same time, only the composite event has physical significance.

For the problem of an embedded layer, a simple method has been found for removing degeneracy. This method permits us to express the total amplitude of a degenerate event ( $A_{nm}$ ) in terms of a simple series which contains either  $m$  or  $n+1$  terms (whichever is smaller). Effectively we replace the computation of the amplitudes of  $D_{nm}$  individual rays by the evaluation of  $m$  or  $n+1$  terms in a series. Furthermore, the use of the series avoids the complicated bookkeeping required to insure that all members of the degenerate family have been included.

We study the refracted arrival produced by a source which radiates a spherically symmetric compressional wave. The vertical component of the particle velocity in the direct wave is

$$U_o = \left( \frac{P_o a}{b_1} \right) \left( \frac{t_d}{a/V_1} \right)^{-1/2} \frac{1}{r V_1} \left( \frac{Z-H}{r} \right) \left\{ \chi(\tau) + \frac{t_d V_1}{r} \int_0^\tau \chi(\xi) d\xi \right\}, \quad \tau = \frac{t - r/V_1}{t_d}. \quad (2)$$

$r$  is the distance between the source and receiver. The source function,  $\chi$ , is time-limited and merely expands or contracts with  $t_d$  but does not change shape. The amplitude spectrum of  $\chi$

is assumed to peak at a dominant frequency  $f_d = 1/t_d$ . At distances which are large compared with the dominant wavelength, the direct wave propagates without change of shape and the shape is determined by the source function  $\chi(\tau)$ .  $a$  is the radius of the assumed spherical cavity at the source and  $P_0$  is the peak pressure applied to the cavity wall. The factor  $(t_d/(a/V_1))^{-1/2}$  is introduced to make the total energy input independent of  $t_d$ .

Beyond a certain minimum range which depends on the time interval of interest, the only reflected waves which can contribute to the refracted arrival are those whose phase velocities approach the compressional velocity in the layer at large distances. According to geometric ray theory, the only reflected waves which satisfy this condition are those which cross the layer at least once in the compressional mode ( $n \geq 1$ ). The high-frequency asymptotic representation for the composite reflection when  $n \geq 1$  is

$$\left(\frac{H}{a}\right)^{3/2} \left(\frac{b_1 V_1}{P_0}\right) U_{nm}^r = R_{nm}^r \left(\frac{t}{H/V_1}, \frac{t_d}{H/V_1}, \frac{P}{H}, \frac{E}{H}, \frac{Z}{H}\right) - \frac{G_{nm}}{\left(\frac{t_d}{H/V_1}\right)^{1/2}} A_{nm} \chi\left(\frac{\frac{t}{H/V_1} - \tau_{nm}}{\frac{t_d}{H/V_1}}\right), \quad (3)$$

$n \geq 1.$

$A_{nm}$  is just the sum of products of the plane wave reflection and transmission coefficients and  $\tau_{nm}$  is the normalized travel time. The time variation in each reflected wave which contributes to the refracted arrival is determined by the source function  $\chi$ .  $G_{nm}$  determines the reduction in amplitude produced by geometric

spreading and is

$$G_{nm} = \left[ \left( \frac{\sin \theta_{nm}}{\rho/H} \right) / \left\{ \frac{1 + \frac{Z}{H}}{(1 - \sin^2 \theta_{nm})^{3/2}} + \frac{n \frac{E}{H} \frac{V_1^2}{V_2^2}}{\left( \frac{V_1^2}{V_2^2} - \sin^2 \theta_{nm} \right)^{3/2}} + \frac{m \frac{E}{H} \frac{V_1^2}{V_2^2}}{\left( \frac{V_1^2}{V_2^2} - \sin^2 \theta_{nm} \right)^{3/2}} \right\} \right] \quad (4)$$

where  $\theta_{nm}$  is the angle of incidence at the upper interface of rays which cross the layer  $n$  times in the compressional mode and  $m$  times in the shear mode. For  $n \geq 1$ ,  $\theta_{nm} < \theta_c = \sin^{-1} V_1/V_2$ .

The reflected waves that do not cross the layer in the compressional mode ( $n=0$ ) generate head waves. The head waves that propagate with a phase velocity  $V_2$  contribute to the refracted arrival. The direct P wave generates the ordinary head wave indicated by the segment ED in the upper diagram in Figure 2. It also generates a transmitted compressional wave ( $P_1 P_2$ ) and a transmitted shear wave ( $P_1 S_2$ ). The transmitted wavefronts intersect at the interface as long as the phase velocity in the direct wave exceeds  $V_2$ . When the phase velocity in the direct wave drops below  $V_2$ , the wavefronts separate. In this process an internal head wave is generated (BD). This wave travels in the direction normal to BD with the velocity  $V_2$ .

The lower diagram demonstrates what happens when the transmitted shear wave and the head wave reflect off the base of the layer. BQ is the reflected part of the head wave. The incident shear wave (PC) generates a reflected compressional wave (QF) and a reflected shear wave (PBA). These two reflected wavefronts begin to separate at a point on the lower interface where the phase

velocity in the incident shear wave drops below  $V_2$ . A new head wave is generated whose wavefront coincides with BQ. Each time the unconverted shear wave ( $n=0$ ) is reflected back into the layer, a new head wave is generated whose wavefront coincides with the wavefront of head waves generated by earlier shear reflections.

The high-frequency asymptotic representation for head waves which propagate with a phase velocity  $V_2$  is

$$\left(\frac{H}{a}\right)^{3/2} \left(\frac{bV_1}{P_0}\right) U_m^f = R_m^f\left(\frac{t}{H/V_1}, \frac{t_d}{H/V_1}, \frac{\rho}{H}, \frac{E}{H}, \frac{Z}{H}\right) = \left(\frac{t_d}{H/V_1}\right)^{1/2} \frac{\mu_m}{\left(\frac{\rho}{H}\right)^2 \left(1 - \frac{\rho_m}{\rho}\right)^{3/2}} \chi_I\left(\frac{\frac{t}{H/V_1} - \tau_m}{\frac{t_d}{H/V_1}}\right), \quad (5)$$

where

$$\chi_I(\tau) = \int_0^\tau \chi(\xi) d\xi.$$

$$(m = 0, 2, 4, \dots),$$

The time variation is determined by the integral of the source function. At large offsets the amplitude decays like  $(\rho/H)^{-2}$ , and the relative amplitudes are determined by the  $\mu_m$ . The  $\mu_m$  depend on the compressional velocity ratio, the density ratio, and the Poisson's ratios. The wavefront of each head wave is tangent to the reflected wave which generated it at the critical distance  $\rho_m$ .  $\tau_m$  is the normalized travel time. The head wave phases are separated by equal time intervals

$$\frac{2T_d}{H/V_1} = \tau_{m+2} - \tau_m = 2 \frac{E}{H} \left( \frac{V_1^2}{V_2^2} - \frac{V_1^2}{V_2^2} \right)^{1/2} \quad (6)$$

which do not depend on offset. This fact suggests that if the refracted arrival consisted of head waves alone, the condition  $t_d = 2T_A$  would lead to constructive interference when the  $\mu_m$  all have the same polarity.

Comparison of (3) and (5) shows that in the high frequency limit the reflected waves predominate over the head waves. The complete expression for the refracted arrival is

$$\left(\frac{H}{Q}\right)^{3/2} \left(\frac{b_1 V_1}{P_0}\right) U = R_Z \left( \frac{t}{H/V_1}, \frac{t_d}{H/V_1}, \frac{\rho}{H}, \frac{E}{H}, \frac{Z}{H} \right) = \sum_{m=0} \sum_{n=1} R_{nm}^r + \sum_{m=0,2,\dots} R_m^f, \quad t < t_{co}. \quad (7)$$

$t_{co}$  is the travel time of the earliest arriving reflected wave which is incident beyond the critical angle ( $\theta_c$ ). The minimum range at which (7) can be applied is determined by

$$t_{co} - t_r = \Delta T,$$

where  $\Delta T$  is the time interval of interest. Equation (7) indicates that except for the factor  $(H/Q)^{3/2} (b_1 V_1 / P_0)$ , the response expressed as a function of  $t/(H/V_1)$  depends on the three geometric parameters  $\rho/H$ ,  $E/H$  and  $Z/H$ , and on the dominant wavelength-to-thickness ratio through the parameter

$$\frac{t_d}{H/V_1} = \frac{\lambda_d}{H} = \left( \frac{\lambda_d}{E} \right) \left( \frac{E}{H} \right).$$

For high frequencies the multiply-reflected waves determine the characteristics of the refracted arrival. The travel-time curves for reflected waves for which  $m = 0, 1, 2$  are plotted in Figure 3. The difference in travel-time between the reflected wave and the refracted arrival is plotted along the ordinate. The range is plotted on a logarithmic scale to emphasize the fact that

all the travel-time curves for a particular  $m$  value approach the same asymptote at large ranges regardless of the  $n$  values. The travel-time difference between waves which have different  $m$  values approaches a finite value at large offsets which is a multiple of  $T_{\Delta}$ .  $T_{\Delta}$  is defined in (6), where it is shown that  $2T_{\Delta}$  is the time interval between head wave arrivals.

This clustering of the travel-time curves leads us to refer to waves with the same  $m$  value as a particular order. If the significant amplitudes in each order are confined to a limited range of  $n$  values, and if  $T$  (source duration) is less than  $T_{\Delta}$ , the refracted arrival at large ranges consists of a sequence of events. Each event is associated with a particular  $m$  value and propagates with a phase velocity which is very near the compressional velocity in the layer. The amplitude of each event is obtained by summing the amplitudes of all rays which have the same  $m$  value as follows:

$$A_m = - \sum_n G_{nm} A_{nm}.$$

A study of many cases reveals that for  $\rho/H > 20$  and  $E/H < .1$ ,

$$A_m = \gamma_m \left( \frac{\rho}{H} \right)^{-3/2} \left( \frac{E}{H} \right)^{1/2}. \quad (8)$$

At large ranges the head wave contributions decay like  $(\rho/H)^{-2}$ . This means that the reflected waves determine the character of the refracted arrival at large distances.



The  $\gamma_m$  determine the relative amplitudes of the events associated with the different  $m$  values. The  $\gamma_m$  depend on the compressional velocity ratio, the density ratio, and the Poisson's ratios. A study of many cases reveals that the higher orders ( $m \geq 1$ ) have amplitudes which are at least ten per cent of the amplitude for  $m = 0$  when either the compressional velocity contrast is large, the Poisson's ratio in the layer is near 0.25, or the Poisson's ratio in the infinite medium approaches 0.5.

Equation (8) cannot be used when the individual wavelets (corresponding to the different  $n$  values) are wholly or partially resolved. The degree of resolution increases as the offset decreases, the layer gets thicker, or the dominant frequency increases. In Figure 4, the amplitude of each wave is plotted along the ordinate and the difference between the arrival time of the reflected wave and the onset of the refracted arrival along the abscissa. Here we consider only multiples which do not cross the layer in the shear mode ( $m=0$ ). Each curve is drawn for a particular offset. The leftmost dot on each curve gives the amplitude and time difference for the wave which crosses the layer twice in the compressional mode ( $n=2$ ). As we move along each curve from left to right,  $n$  increases in increments of two.

The information displayed in Figure 4 predicts the phenomenon of shingling. This effect is generally explained in terms of normal mode propagation in which the phase velocity exceeds the group velocity. As the range increases, peaks and troughs move forward through the envelope which defines the refracted arrival. In this process, the amplitude of the first extremum decreases and is eventually lost in the noise. At this offset, a later extremum is selected to define the time-distance curve. At each offset where an extremum is lost, there is a discontinuity in the time-distance curve and a new shingle is added corresponding to a later, larger amplitude extremum. In Figure 4, we note that as the range increases, the time delay decreases for each  $\eta$  value. The wavelet associated with each reflection moves forward in time with respect to the onset and the amplitudes of the earliest arrivals ( $\eta=2$  and  $4$ ) decrease. As the range increases the amplitudes of the later arrivals increase (the open dot indicates this effect for  $\eta=8$ ), and the number of arrivals within a fixed time interval increases. When the wavelets are partially resolved, this causes additional wiggles to appear on the tail of the first event. The movement of each wavelet forward toward the onset, the decrease in amplitude of the early extrema (associated with small  $\eta$  values) and the appearance and increase in amplitude of the later extrema (associated with large  $\eta$  values)

act to create the shingling effect. Clearly, in shingling the duration of the individual wavelets must not be so short that they appear as discrete events. On the other hand, the duration must not be so long that all resolution is lost.

The reflected waves and head waves superpose to form the refracted arrival. The actual response function is obtained by (a) convolving the source function with the sequence of impulses which represent the reflected waves and (b) convolving the integral of the source function with the sequence of impulses which represent the head waves (as indicated in Equations (3), (5) and (7)). The choice of the source function is not completely arbitrary. It must be chosen so that if the medium which contains the source were infinite, each point would return to its original state a finite time after the arrival of the direct wave. This requires that the static components of the stress and strain be finite. The Laplace transform of the radial stress in a spherically symmetric compressional wave is

$$\overline{T}_{rr} = -P_0 a \overline{\chi} \frac{e^{-sr/v_1}}{r} \left\{ 1 + 4 \frac{v_1^2}{v_1^2} \left( \frac{v_1}{sr} \right) + 4 \frac{v_1^2}{v_1^2} \left( \frac{v_1}{sr} \right)^2 \right\}.$$

In order for the static component to be finite

$$\lim_{s \rightarrow 0} \overline{\chi} = A s^\lambda, \lambda \geq 2. \quad (9)$$

As a consequence of (9),  $\chi$  must have at least two axis crossings. We also require that the particle velocity and acceleration be

continuous. The function

$$\chi\left(\frac{t}{t_d}\right) = \left(\sin^2 \frac{\pi t}{K t_d}\right) \cos 2\pi \frac{t}{t_d}, \quad 0 \leq \frac{t}{t_d} \leq K, \quad K \geq 2,$$

satisfies all these requirements. The first factor determines the envelope. The duration of the function is  $T = K t_d$ . The condition  $K \geq 2$  forces the low-frequency behavior to satisfy (9). The source function and its integral are plotted in Figure 5 for  $K=4$ . The source function is symmetric about  $t/t_d = 2$ . The integral of the source function is antisymmetric about  $t/t_d = 2$ . Under certain conditions we can distinguish between reflected and head wave contributions to the refracted arrival on the basis of symmetry.

Figures 6-8 show how the character of the refracted arrival varies with the dominant frequency at three offsets. In each figure the dimensions are fixed. One division along the abscissa is equal to the dominant period. As we move down, the dominant period increases, the dominant wavelength increases, and  $E/\lambda_d$  decreases. Because the dominant period changes, the time scales cannot be compared directly.

The refracted arrival for an infinitely thick layer would have the antisymmetric form of the head wave and terminate at the fourth division on all traces. Figure 6 shows three distinct events on the traces designated  $E/\lambda_d = 7, 5$ , and  $4$ . These events correspond to  $m=0, 1$ , and  $2$ . As  $E/\lambda_d$  decreases, the later events move toward the first event, interfere with it, and become lost in it.

Changes in  $E/\lambda_d$  produce significant changes in character for  $\rho/H$  values of 3.5 and 10, but relatively minor changes for  $\rho/H=100$ . At large ranges the dominant frequency is not high enough to partially resolve the individual waves which contribute to the first event. At small ranges, the individual waves are separated by larger time intervals and the change in character is a consequence of interference.

Increasing the dominant period causes the individual waves to overlap to such an extent that only a single event is discernible and reduces the amplitude of the reflected waves relative to the head waves. This explains why the last trace on each figure approaches the antisymmetric shape associated with the head wave.

Each trace is normalized so that the maximum amplitude plots at the same value. The true maximum amplitude in the refracted wave train is plotted in Figure 9 as a function of the dominant-wavelength-to-thickness ratio. Each curve is drawn for a particular range. As the range increases, a relative maximum develops which migrates toward the vertical line marked  $t_d = T_\Delta$ . We have shown that at large ranges the waves arrive in groups which are associated with different  $m$  values and are separated by the time interval  $T_\Delta$ .  $t_d = T_\Delta$  is the condition for constructive interference between groups. The weak minimum and maximum at  $\rho/H=100$  are also a consequence of interference between the groups.

As the dominant frequency increases, the individual waves in the group begin to separate from one another, and the amplitude varies in a complex way. Destructive interference between individual waves produces the deep minimum. At sufficiently high frequencies, the individual waves are completely resolved, and each curve must approach an asymptote with slope  $-1/2$ . At very low frequencies the head wave is dominant, and each curve must approach an asymptote with slope  $1/2$ . The increase in amplitude at low frequencies is indicative of the failure of the high-frequency theory. If this increase were continued to very low frequency, the energy in the refracted arrival would exceed the total energy radiated into the system. We do not attach significance to dominant-wavelength-to-thickness ratios greater than unity. Consequently our analysis is restricted to thick, high velocity zones.

Figures 10-12 illustrate the effect of range for  $E/\lambda_d = 10, 7$  and  $4$ . On each figure,  $E/\lambda_d$  is fixed and the dominant period does not change from trace to trace. Each trace is normalized so that the maximum amplitude plots at the same value. The normalized range ( $\rho/H$ ) changes in increments of  $0.5$ . The group of lines that start in the upper left corner of Figure 10 shows how individual peaks and troughs move forward with respect to the onset and decrease in amplitude as the range increases. The decrease in amplitude would be considerably more pronounced if true

amplitudes had been plotted. The second group of lines shows how additional peaks and troughs appear on the tail of the first event as the offset increases. These phases are associated with the later arriving, higher  $N$  values which increase in amplitude with range. The third group of lines shows that the second event ( $m=1$ ) also exhibits shingling.

In Figure 11, the phase velocity is slightly greater for the third peak than it is for the earlier extrema. Shingling is exhibited only over a limited range. The second trough and third peak on the first trace can be correlated across the entire record, but the phase velocity difference disappears for  $\rho/H > 7$ . In Figure 12, there is no shingling. These observations indicate that shingling is range-limited. The maximum range decreases as the dominant period increases, and for sufficiently long dominant periods, shingling does not occur. When shingling is observed, it indicates that the high velocity zone is thick. Increasing the layer thickness, decreasing the dominant period, and decreasing the layer depth all act to increase the effective time interval between wavelets (i.e., the degree of resolution) and thereby extend the maximum range over which shingling can occur. Range-limited shingling is distinctly different from the range-independent shingling associated with normal mode propagation. The importance of shingling lies in its potential to determine layer thickness.

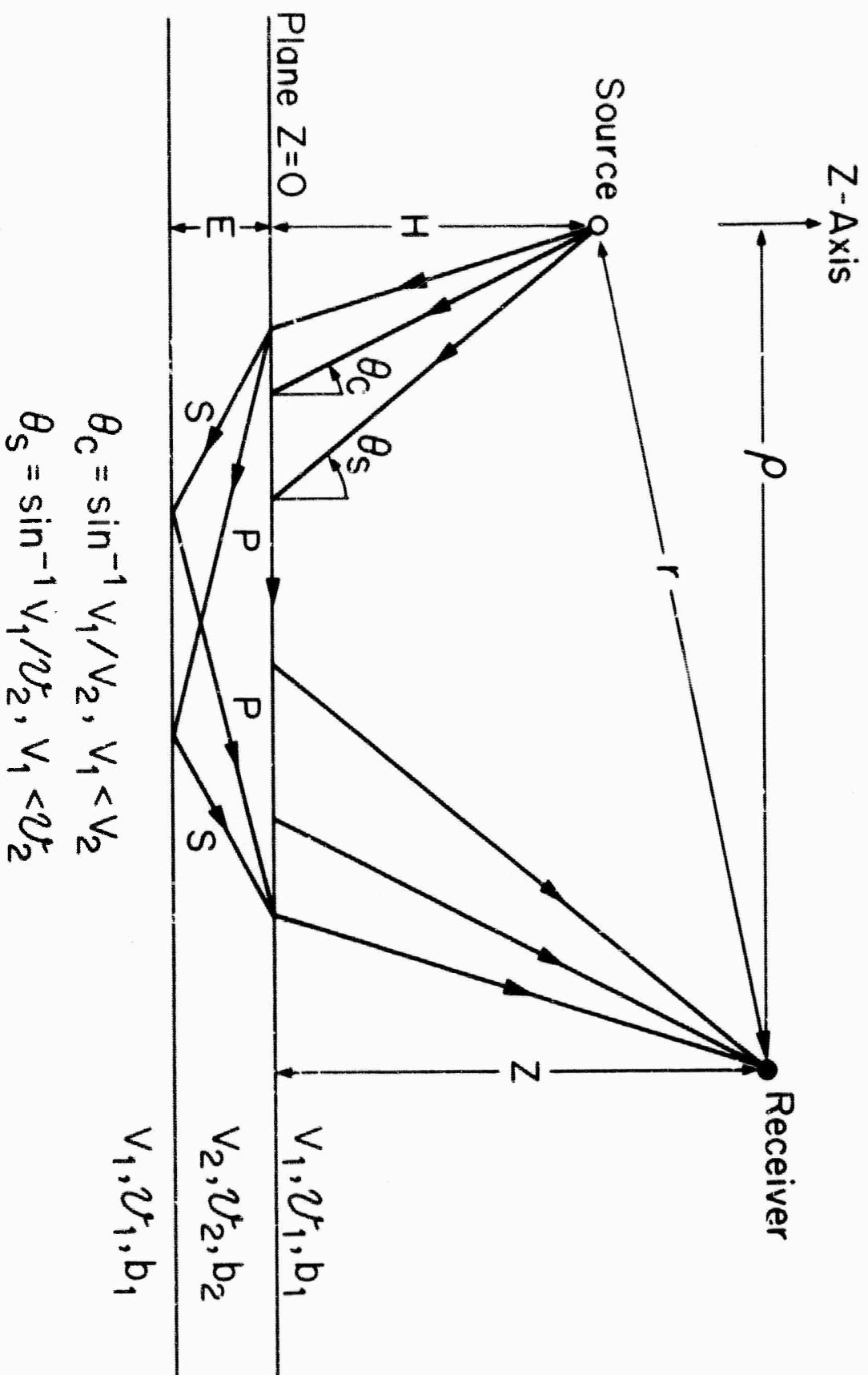


FIGURE 1



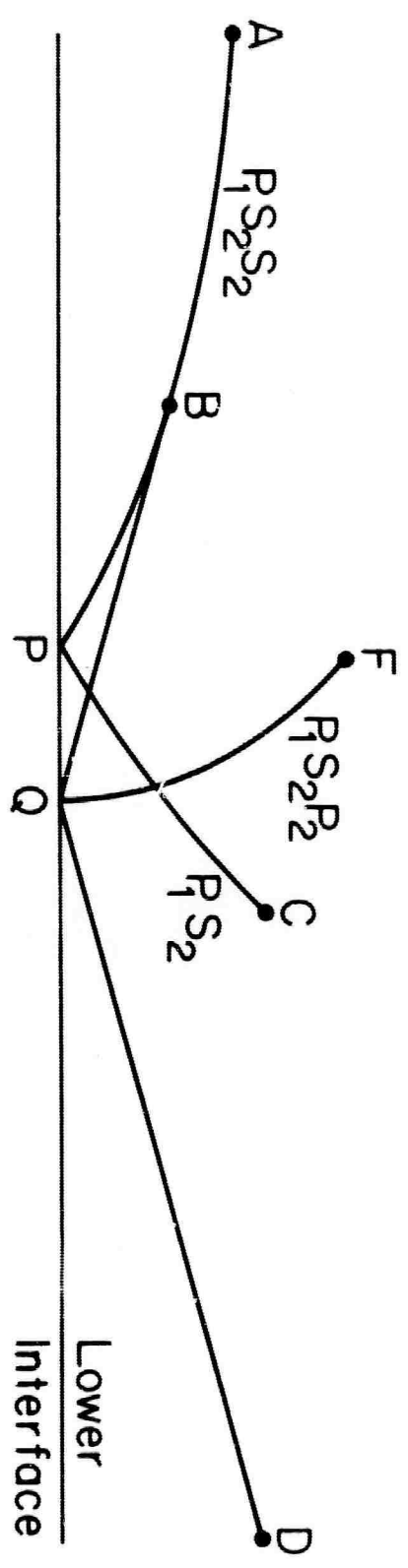
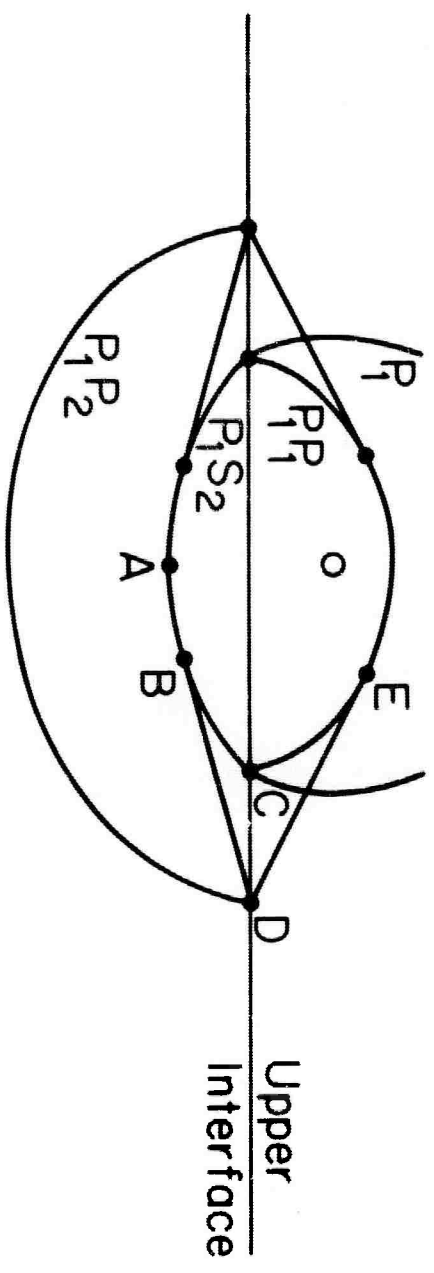


FIGURE 2

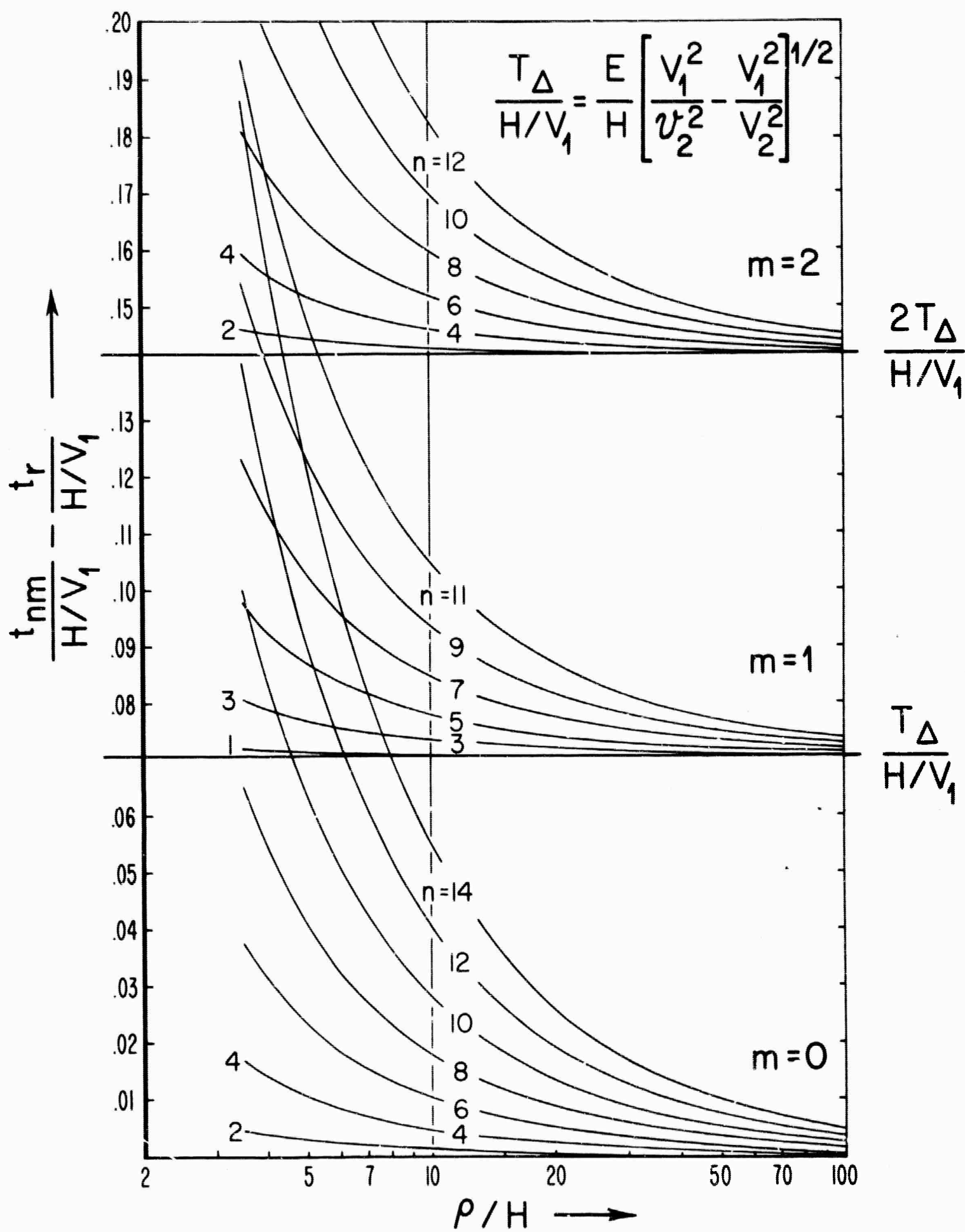


FIGURE 3

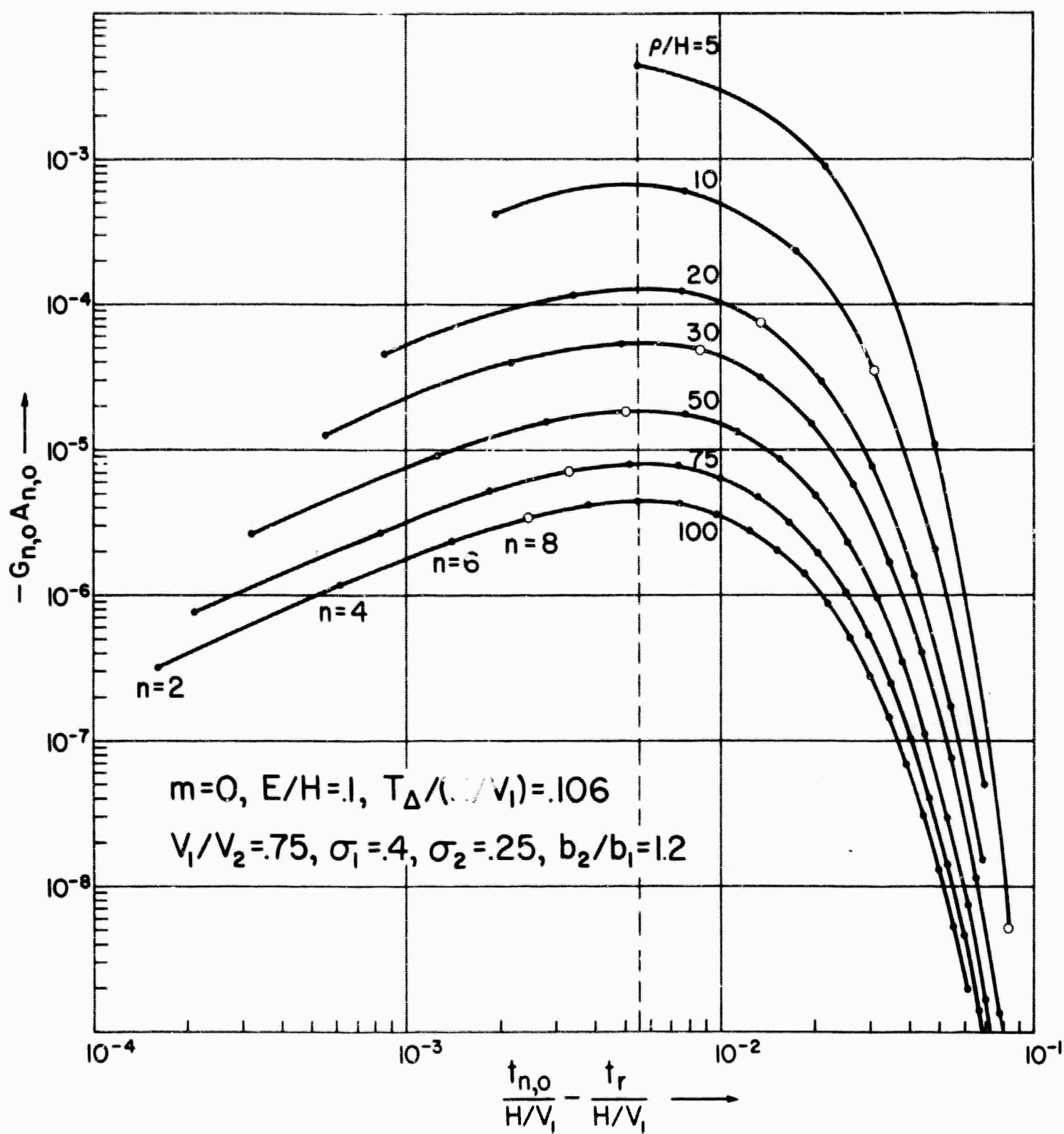


FIGURE 4

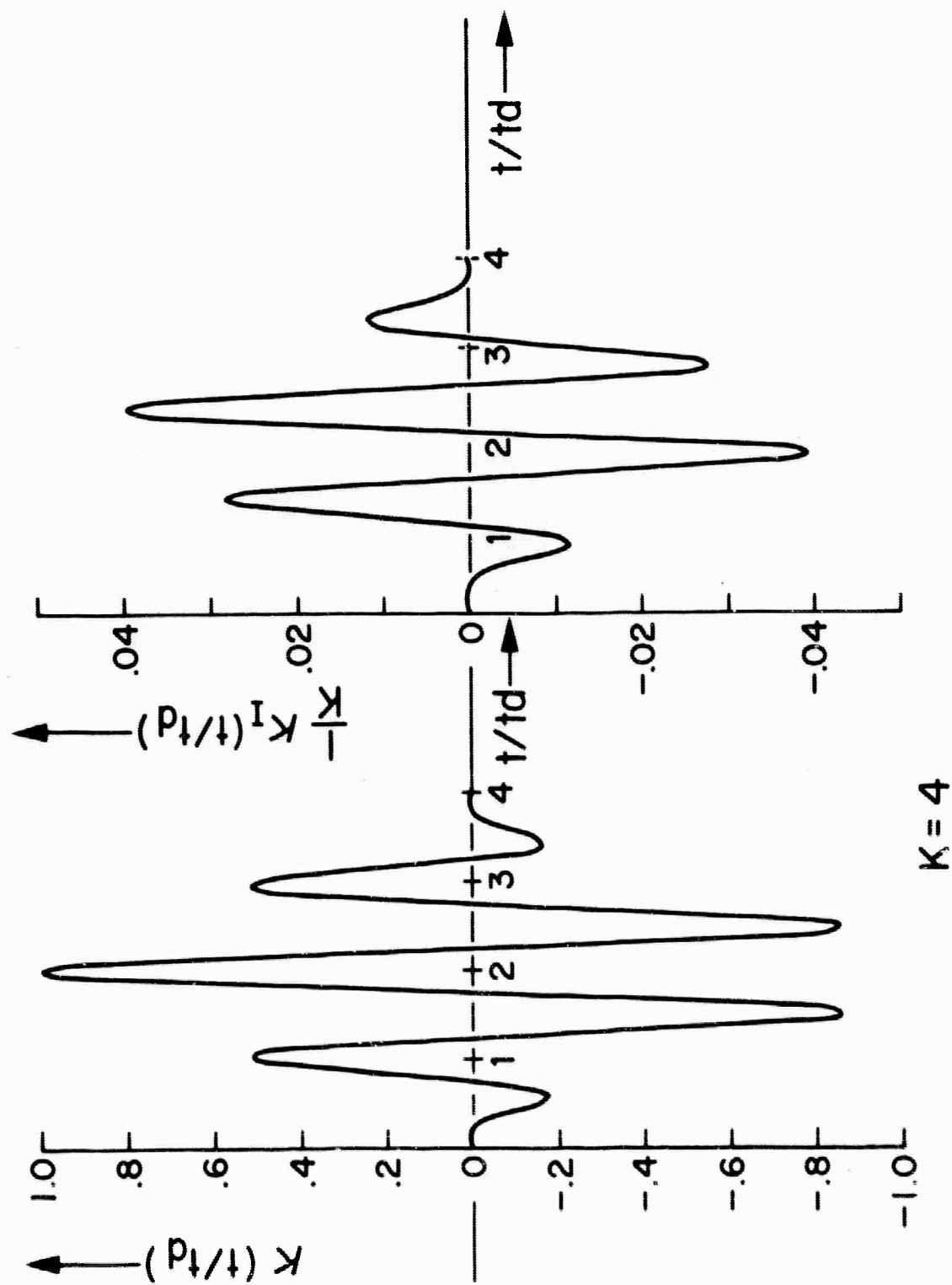


FIGURE 5

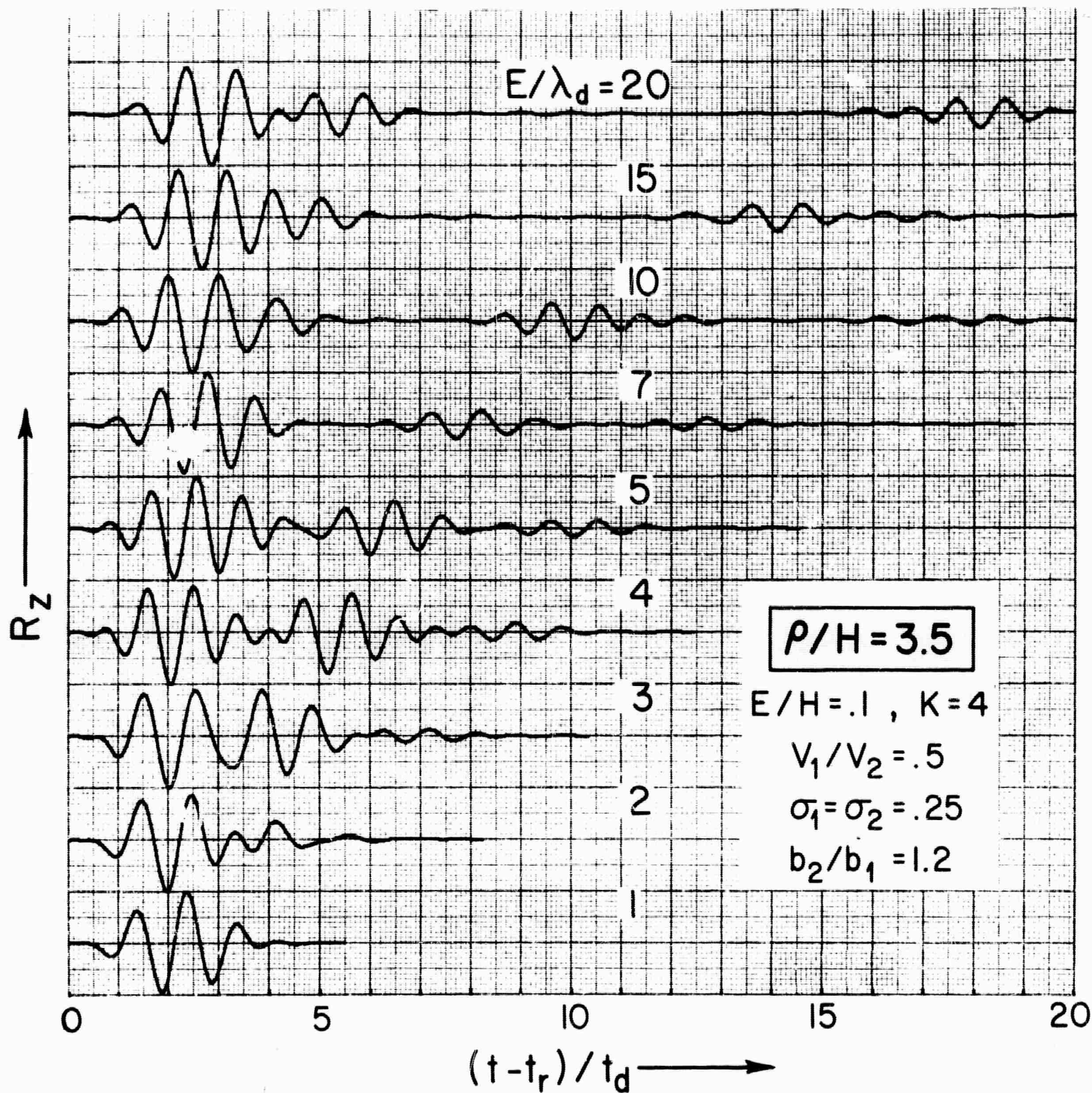


FIGURE 6



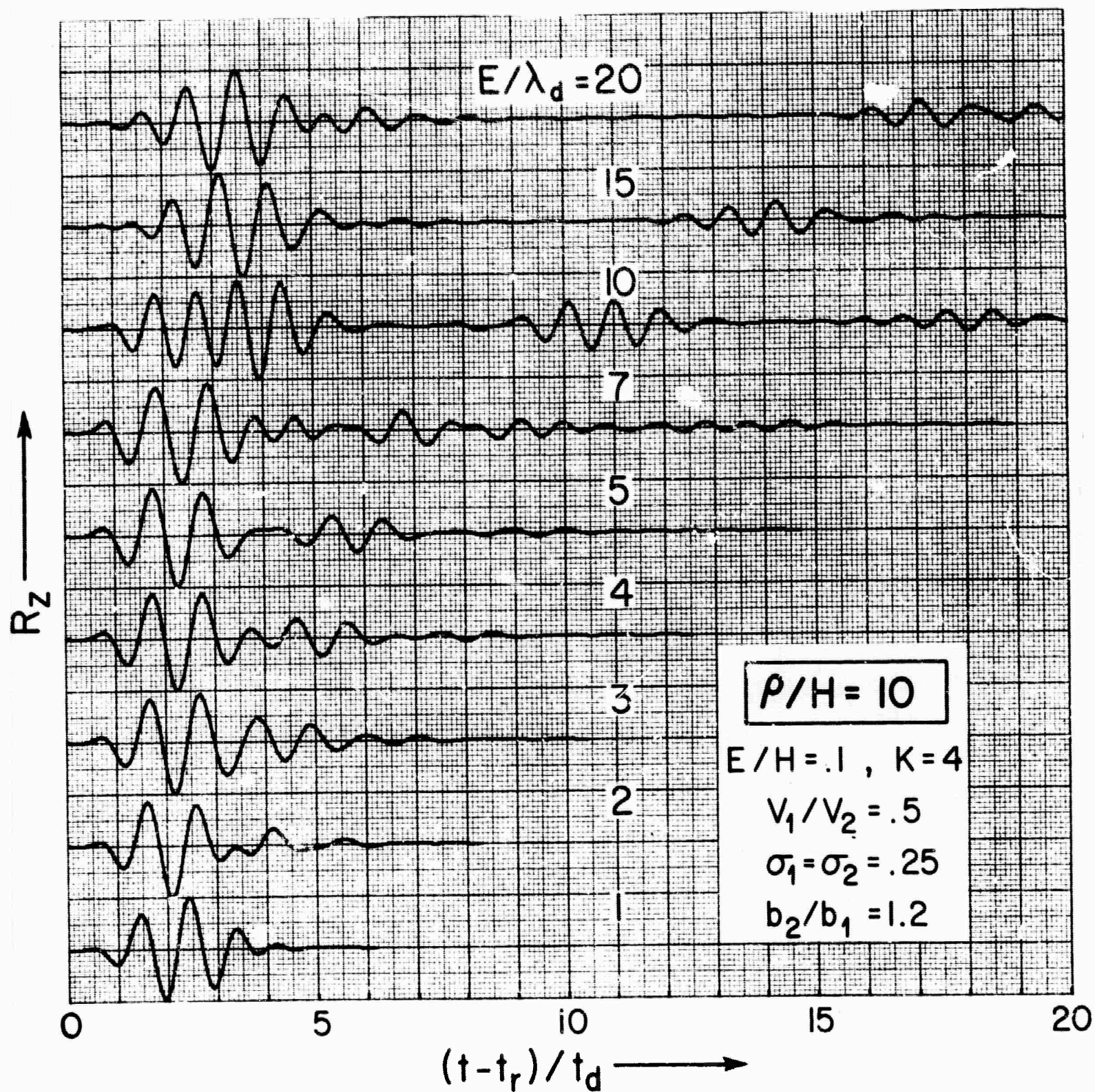


FIGURE 7

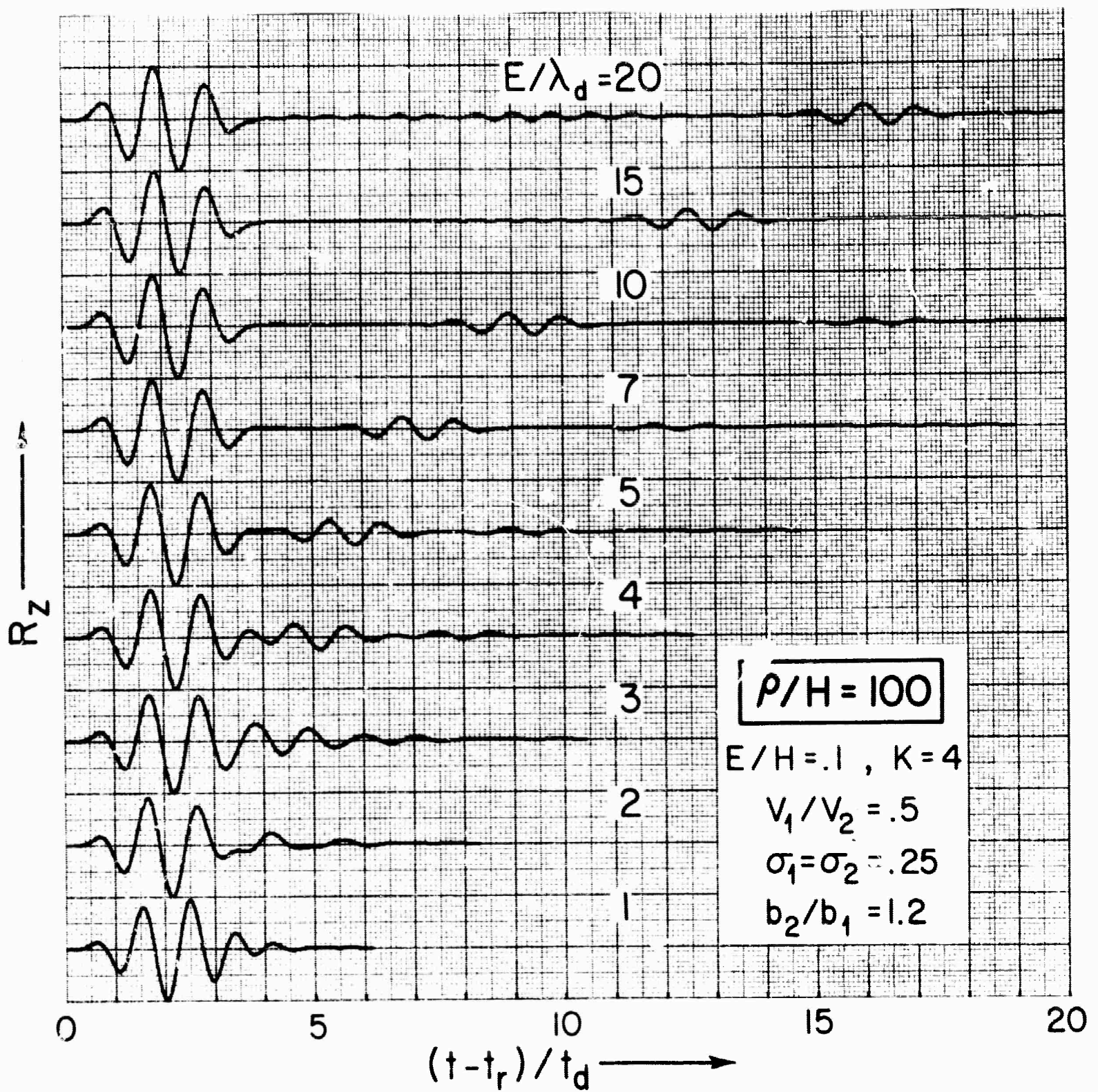
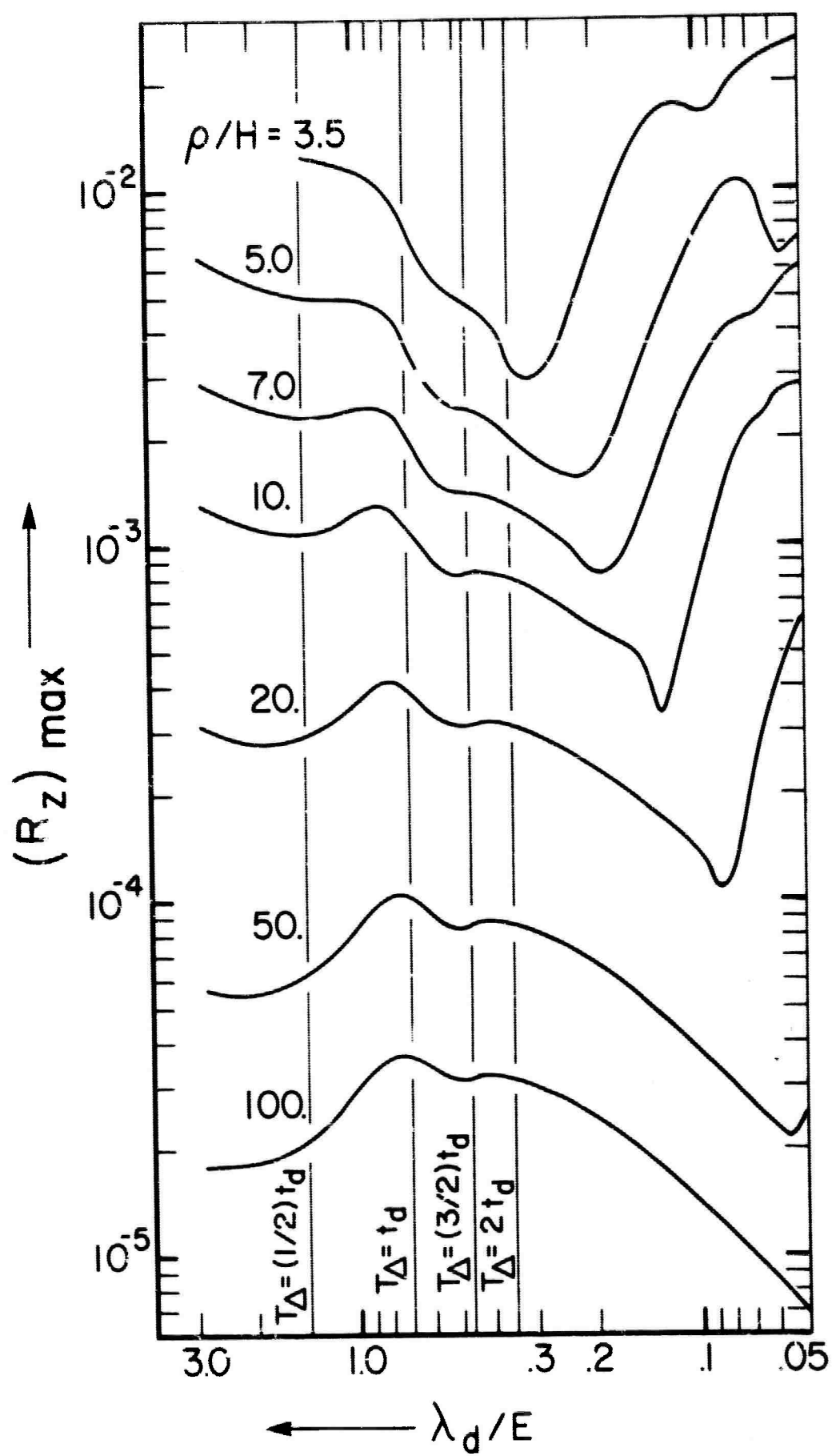


FIGURE 8



$E/H = .1, K = 4$

$V_1/V_2 = .5, \sigma_1 = \sigma_2 = .25, b_2/b_1 = 1.2$

FIGURE 9

LC44-372



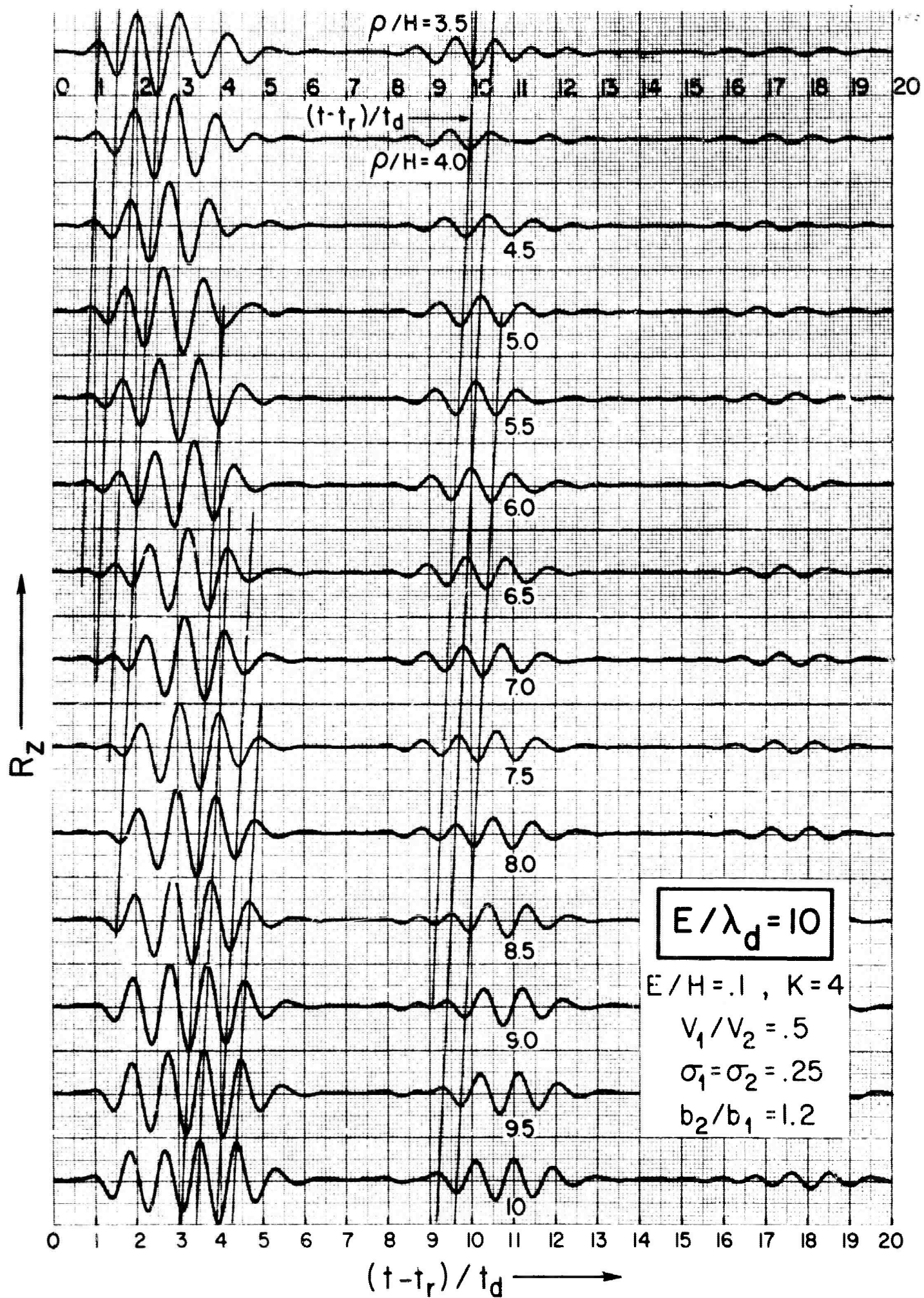


FIGURE 10

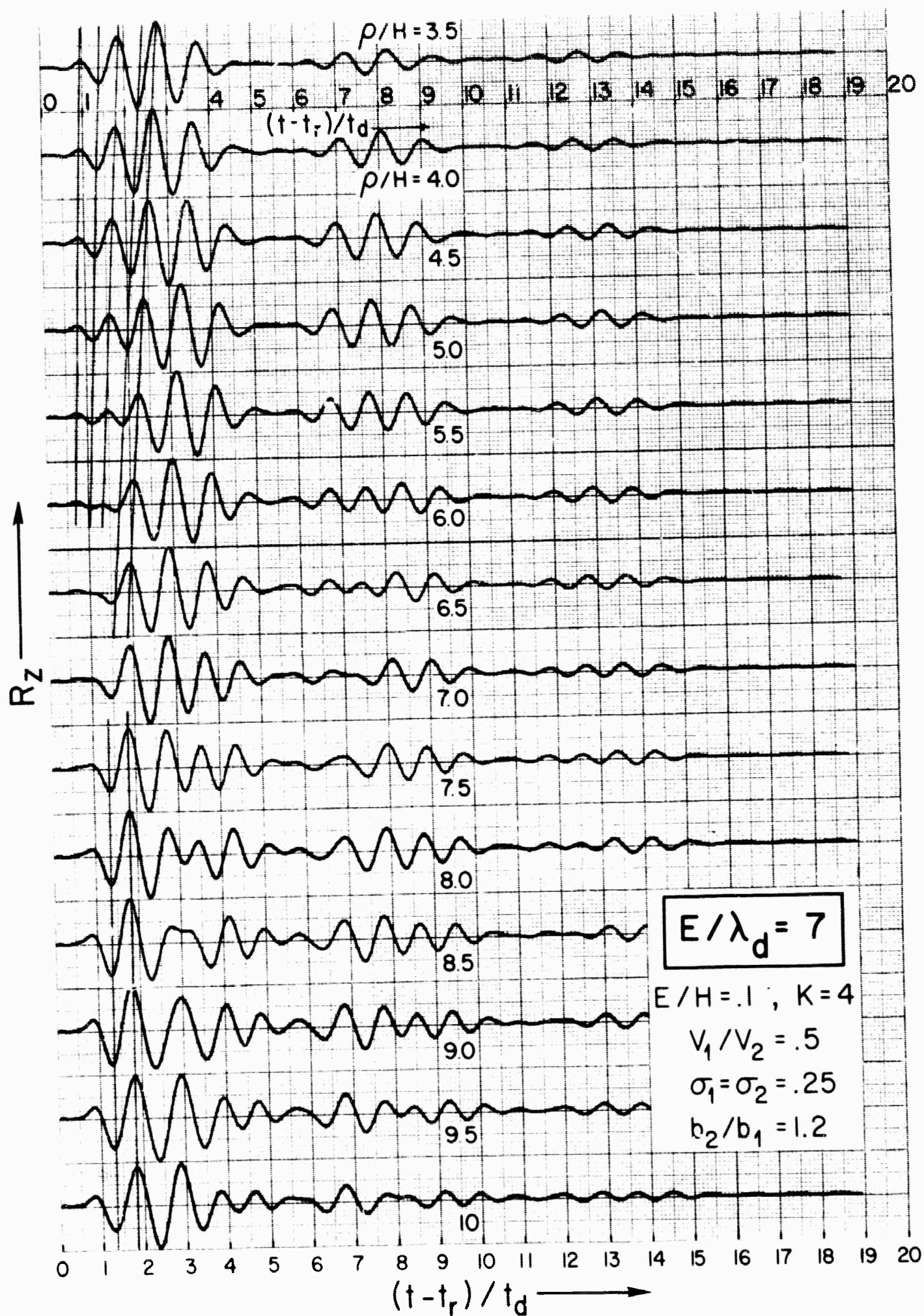


FIGURE 11



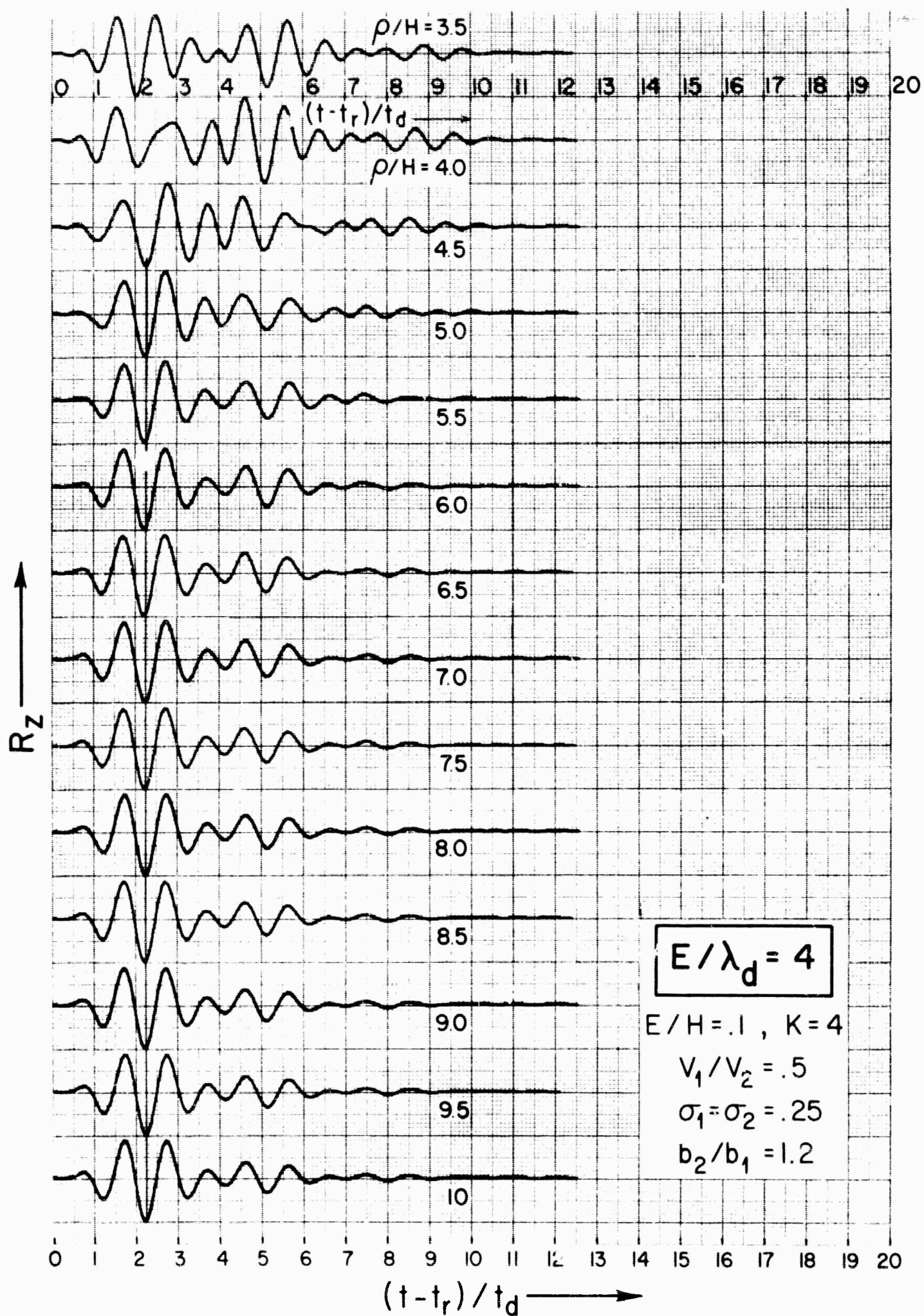


FIGURE 12

### VIII. REFLECTION AND TRANSMISSION OF PLANE COMPRESSIONAL WAVES

The reflection and transmission of a plane, monochromatic, compressional (P) wave at a plane interface between two semi-infinite media is studied in great detail in Vela Scientific Report No. 4 (AFCRL 64-205). That report contains extensive tables of the energy flux ratio in the vertical direction and of the relative phase of the vertical displacement for each of the reflected and transmitted waves. Our purpose in treating this problem is three-fold:

1. To provide the scientific community with a comprehensive set of data which demonstrates the effect of systematically varying the compressional velocity ratio, the density ratio, and the Poisson's ratios over a wide enough range to include cases of interest in geophysical applications, seismic modeling, and velocity measurements.
2. To arrive at certain general conclusions about the effect of the parameters on the partition of the incident flux among the different waves and on the angular dependence of the flux in each wave.
3. To clarify the physical significance of Knott's equation when the angle of incidence exceeds the critical angle.

The four parameters which we select to describe the media are the compressional velocity ratio  $V_{21}$ , the density ratio  $R_{021}$ , and the Poisson's ratios  $SIG1$  and  $SIG2$ . The incident P wave approaches the interface through medium 1 and is transmitted into medium 2. The notation  $V_{21}$  is used to represent the ratio of the compressional velocity in medium 2 to the compressional velocity in medium 1. Similarly  $R_{021}$  represents the density ratio.

The following range of parameters has been investigated:

$V_{21}$ --0.25, 0.50, 0.75, 1.00, 1.50, 2.0, 3.0 and 4.0;

$R_{021}$ --0.33, 0.50, 0.80, 0.90, 1.00, 1.10, 1.20, 1.50,  
2.0 and 3.0;

$SIG1$ --0.10, 0.20, 0.25, 0.30, 0.40 and 0.50;

$SIG2$ --0.10, 0.20, 0.25, 0.30, 0.40 and 0.50.

A material with a Poisson's ratio of 0.50 is a fluid. The flux ratios and phase angles have been tabulated for all combinations of the above parameters except where the fluid velocity is higher than the P wave velocity of the adjacent solid or where the fluid density is greater than that of the solid. In addition, we have studied the cases where  $V_{21}=0.10$ ,  $R_{021}=0.0005$ ,  $SIG2=0.5$  and  $SIG1$  varies from 0.10 to 0.50 as given above. These cases describe a wave which is incident upon an air boundary from a solid or liquid. And conversely, we have treated the air wave which is incident upon a solid or liquid boundary. Here  $V_{21}=10$ ,  $R_{021}=2000$ ,  $SIG1=0.5$  and  $SIG2$  varies over the range given above.

For each of some two thousand different combinations of parameters, the energy flux ratios and the relative phases of the vertical displacement have been computed at five degree intervals for angles of incidence ranging from 0 to 85 degrees. When a critical angle is present, these quantities are also computed at the critical angle and at one degree intervals within five degrees of the critical angle.

The computations indicate that when one medium is a fluid (or air), a large amount of shear (S) energy is generated in the solid medium. In many cases this conversion has an efficiency of better than 50 per cent over some tens of degrees of the angle of incidence.

Analytical expressions are presented for the reflection and transmission coefficients for the vertical component of the particle displacement. Each coefficient can be put in the form  $Q=A(\theta) e^{i\phi(\theta)}$ , where  $\theta$  is the angle of incidence.  $\phi(\theta)$  determines the phase shift between the incident and reflected (or transmitted) waves and is listed in the tables. When  $\theta$  is less than the critical angle, all the coefficients are real ( $\phi=0$  or  $\pi$ ), and  $Q$  determines the ratio of the vertical displacement in the reflected (or transmitted) wave to the vertical displacement in the incident wave. When  $\theta$  is greater than the critical angle, all the coefficients are in general complex, the

incident and reflected (and transmitted) waves are not in phase, and  $Q$  no longer measures the ratio of the vertical displacements (for the ratio is time-dependent).

Some interesting relations are obtained by evaluating the analytical expressions for the coefficients at the critical angles. At the critical angle for the transmitted P wave ( $\theta_p = \sin^{-1} v_1/v_2$ ), the vertical displacement in the transmitted P wave vanishes and the condition for perfect reflection with no conversion and no transmission is

$$\frac{v_1^2}{v_2^2} - \frac{\rho_2}{\rho_1} \frac{v_2^2}{v_2^2} = \frac{1}{2} \left( 1 - \frac{\rho_2}{\rho_1} \right). \quad (1)$$

$v_1$ ,  $v_1$ , and  $\rho_1$  are respectively the compressional velocity, shear velocity, and density in the  $i^{\text{th}}$  medium. When this condition is satisfied, all the energy in the incident P wave goes into the reflected P wave and the vertical displacement undergoes a  $180^\circ$  phase change. At the critical angle for the transmitted S wave ( $\theta_s = \sin^{-1} v_1/v_2$ ), the condition for perfect reflection is satisfied if either

$$\frac{v_1^2}{v_2^2} = \frac{1}{2} \frac{\rho_2}{\rho_1} \quad (2)$$

or

$$\frac{v_1^2}{v_2^2} = \frac{1}{2} \left( \frac{\rho_2}{\rho_1} - 1 \right). \quad (3)$$

Each of these conditions insures that no energy goes into the reflected S wave. At and beyond the critical angle for S, the net flux (the instantaneous flux integrated over a period) in each of the transmitted waves vanishes. There may be an instantaneous flux in the transmitted P and/or S wave, but when integrated over a period, it averages to zero. Therefore, (2) or (3) insures that the reflected P wave is the only wave which carries a net flux of energy away from the interface. On the other hand, (1) insures perfect reflection of both the instantaneous and net fluxes. This distinction between the instantaneous and net fluxes is basic in the discussion of the requirements for continuity of the normal component of flux across the interface.

The instantaneous value of the normal component of flux in each wave can be expressed in terms of the  $A$  and  $\phi$  associated with that wave. Inside the critical angle ( $\theta_p$ ), the vertical and horizontal components of displacement in each wave are either in phase or  $180^\circ$  out of phase, the particle motion is linear, and the direction (but not the magnitude) of the energy flux is independent of the time. If the "transmitted" P wave is studied for  $\theta > \theta_p$  or the "transmitted" S wave is studied for  $\theta > \theta_s$ , we find that the vertical and horizontal displacements are out of phase by  $90^\circ$ , the particle motion is elliptical and the direction (and magnitude) of the energy flux oscillates with time. Actually, at each point the flux direction reverses every



quarter cycle, and at each instant the flux direction reverses every quarter wavelength along the interface. Therefore, beyond the critical angle for a transmitted wave, the net flux in that wave vanishes and the energy is cycled back and forth between the two media.

Inside the critical angle,  $\theta_p$ , the conditions for the continuity of the normal component of the instantaneous flux and of the normal component of the net flux are identical and are expressed by Knott's equation. This equation contains the  $A^2$  associated with each wave. Beyond the critical angle, Knott's equation, by itself, is not sufficient to insure continuity of the instantaneous flux--actually three equations are required. The first is obtained from Knott's equation by setting the  $A$  for the transmitted P wave equal to zero when  $\theta > \theta_p$  (or the  $A$ 's for both the transmitted P and S waves equal to zero when  $\theta > \theta_s$ ). This modified Knott's equation guarantees the continuity of the net flux. The other two equations are just the real and imaginary parts of the complex equation obtained by substituting  $Ae^{i\phi}$  for  $A$  in Knott's equation. Inside the critical angle the terms in Knott's equation may be interpreted as either instantaneous or net flux ratios. Beyond the critical angle the terms in Knott's modified equation can be interpreted only as net flux ratios.

## IX. SOME EXPERIMENTS ON INVERSE FILTERING OF SEISMIC RECORDS

Our original research proposal tentatively suggested an investigation of the application of inverse filtering to the determination of seismic energy source depth. This was intended to be an offshoot of our own geophysical exploration research program, which has for several years included a study of general filtering problems together with the limitations imposed by background noise. Inverse filtering, which has also been called inverse convolution or deconvolution, is in fact very intimately linked with concepts of optimum filtering, such as those introduced by Norbert Wiener (1949). In recent years there have been many communications pertinent to the subject, including the tutorial article by G. L. Turin (1960) and those by R. B. Rice (1962), G. Kunetz (1961), M. M. Backus (1961), J. d'Hoerane (1962), M. R. Foster, et al (1962), and E. A. Robinson (1957).

The possible application of inverse filtering to the detection and identification problem is perhaps best visualized with the aid of the schematic diagram in Figure 1. It is quite similar to the general problem posed by G. L. Turin (1960) in his Figure 3. In the problem of interest here it is considered that the design of the processing filter is such that, when combined with the conventional receiver filter, it forms a composite

optimum inverse filter. This composite filter should be aimed at yielding an output which is a best possible representation of the seismic source conditions. It should ideally be a true inverse filter for the transmission characteristic of the earth, but in practice it must be optimized in some sense to take into account the estimated signal-to-noise ratio. The concept of such an optimum inverse filter is fairly straightforward, but in order to design it well, it is evidently necessary to know the relevant transmission characteristic of the earth in considerable detail. In fact, it is lack of detailed knowledge of this transmission characteristic that mainly hinders the application of inverse filtering to the detection and identification problem. Some earth transmission characteristics which have become reasonably well known in recent years are the low frequency phase dispersions of the first modes of the Love and Rayleigh surface waves. At large ranges these dispersions are very considerable. Hence it is not surprising to find that inverse filtering has already been applied to such surface waves by K. Aki (1960), J. N. Brune, et al (1960), and Y. Sato (1955, 1956). Further research into this application of inverse filtering to surface wave data is currently being directed by Professors M. Ewing and F. Press under Project VELA contracts. We have not attempted to perform such investigations at Calresearch as there would seem to be little point in mainly duplicating the efforts at the Lamont Geological Observatory and the California Institute of Technology.

Some detailed knowledge of long range, or third zone, direct body wave transmission through the earth has recently been obtained by the United Kingdom group using their Pole Mountain array. The Russian nuclear event of February 2, 1962, was recorded with a reasonable signal-to-noise ratio in the 0.7 to 1.7 cps band. The main significant arrival was a "lonesome P" pulse. A reproduction of this direct P pulse, as recorded by one of the "quietest" Pole Mountain seismometers, is shown in Figure 2A. The pulse is extremely simple in character. In fact, if it is assumed that the time behavior of the source function is fairly accurately known, then it may be considered that the recording in Figure 2a effectively specifies the composite filter of the Willmore seismometer and the  $89^\circ$  path between the location of the Russian bomb and Pole Mountain. On this basis, it might at first sight seem reasonable to design an inverse to this composite filter. This inverse filter could then be applied to some other direct P event, following a similar path of about  $89^\circ$ , in order to yield its approximate source function. There is at least one strong argument against such a course of action. It is evident from the simple pulse shape of Figure 2a that the composite transmission path and seismometer filter is essentially band-pass in nature with relatively slight phase distortion. It is this simplicity, of course, which makes third zone detection schemes look so attractive. An optimum inverse filter might well

narrow the direct P pulse in Figure 2a, but practical signal-to-noise limitations will normally prevent a dramatic shortening and simplification of the pulse. Nevertheless, the importance of the identification problem is such that even a marginal improvement in the over-all filtering system may be worth striving for.

Following reasoning somewhat analogous to this, but oriented more towards emphasizing first breaks, J. W. Birtill of the United Kingdom Atomic Energy Authority conducted some relevant analog inverse filtering experiments (private communication). In order to supplement J. W. Birtill's analog experiments, some digital studies were later instigated by us, using a slightly modified version of a Calresearch 7090 program. It must be emphasized that these studies were far from exhaustive, the lack of detailed data on signal-to-noise ratios of the records being a major restriction. Further research on this topic should definitely include a more detailed knowledge of realistic signal-to-noise ratios and would possibly be pursued more rapidly by personnel with more immediate access to contemporary data from seismic arrays.

In our simple investigation we assumed that the effective source function for the Russian bomb was doublet in displacement (see Figure 2b). The basis for this was our belief that,

at a large range from a detonation within an infinite medium, the displacement would be approximately impulsive. We considered that the presence of the free surface immediately above the detonation would generate a subsequent impulse of the same strength but with reversed polarity. If the actual surface stresses lie in a grossly non-linear region, this concept of a doublet source function may be substantially incorrect and this possibility should not be forgotten.

The approximate power spectra of the hypothesized doublet source and the Russian bomb event of Figure 2 are shown in Figures 3 and 4 respectively. The ratio of their amplitude spectra is shown in Figure 5 and the difference between their phase spectra is given in Figure 6.

By definition the amplitude and phase characteristics in Figures 5 and 6 specify the inverse filter which is required to change the Russian bomb event (Figure 2a) into the idealized doublet source function (Figure 2b). In the construction of this inverse filter, however, it is only sensible to note the following: although Figure 4 specifies a spectrum for the Russian bomb event between 0.0 and 3.0 cps, it is evident that, in all probability, there is a poor signal-to-noise ratio outside the region of, say, 0.3 to 2.0 cps.\* This means that the filter

---

\*Much of the noise is undoubtedly digitizing noise. Unfortunately, the ratio of signal-to-ambient ground motion has not been reliably estimated.

of Figure 5, which has a very strong transmission of high frequencies, will mainly pass noise when applied to the Russian event. It would be illogical to utilize such an inverse filter and, as we noted earlier, the estimated signal-to-noise ratio should be taken into account in optimizing this filter. However, because we had no reliable estimate of the signal-to-noise ratio, it was decided to modify the spectrum of Figure 5 by merely truncating it outside some pass band whose high- and low-cut frequencies can be specified arbitrarily. Approximate impulse responses of some resulting inverse filters are shown in Figures 7-10, together with their truncation frequencies.

The effect of applying these inverse filters to the Russian bomb event is shown in Figure 11. Attention should be given only to those pulses synchronized in time with the original Russian event.\* It is fairly evident that the main effect of narrowing the pass band of the inverse filter is to increase the effective width of the main output pulse. The output pulse is, in each case, asymmetrical and is essentially a band limited approximation to the hypothesized doublet source.

---

\*The surrounding ripple is due to the extremely sharp high-frequency cut off of each inverse filter. The outer pulses are caused by undersampling the associated inverse filter characteristics with the digitizing rate of only 0.1 cps. This admittedly detracts from the study but it was not considered worthwhile to reprocess the data with a more rapid frequency sampling rate.

The result of applying the inverse filters of the Russian bomb to the French bomb of May 1, 1962, (fortunately also at an epicentral range of  $89^\circ$ ) is shown in Figure 12. It is perhaps significant to note that the signal-to-noise ratio was poorer for the French bomb. This may account for the rather large oscillations of about 2.0 cps introduced with the 0.3 to 2.0 cps inverse filter. In any case it should be noted that our practical inverse filters do not cause gross instabilities when applied to the French bomb record.

As a final step the inverse filters were applied to an earthquake from the Ionian sea (April 10, 1962). The results are reproduced in Figure 13 and do not exhibit any particularly significant features. What originally looked like a seismogram still continued to look like a seismogram after the inverse filtering operations.

In conclusions, then, we have reported on the very simple inverse filtering experiments that we have applied to bomb and earthquake data. The results are very much as expected and are neither dramatic nor dismaying. We do not plan to continue with this phase of research. It is to be emphasized that any future research on this topic should incorporate reliable estimations of signal-to-noise ratios and would possibly best be performed by organizations with more immediate access to contemporary data from seismic arrays.



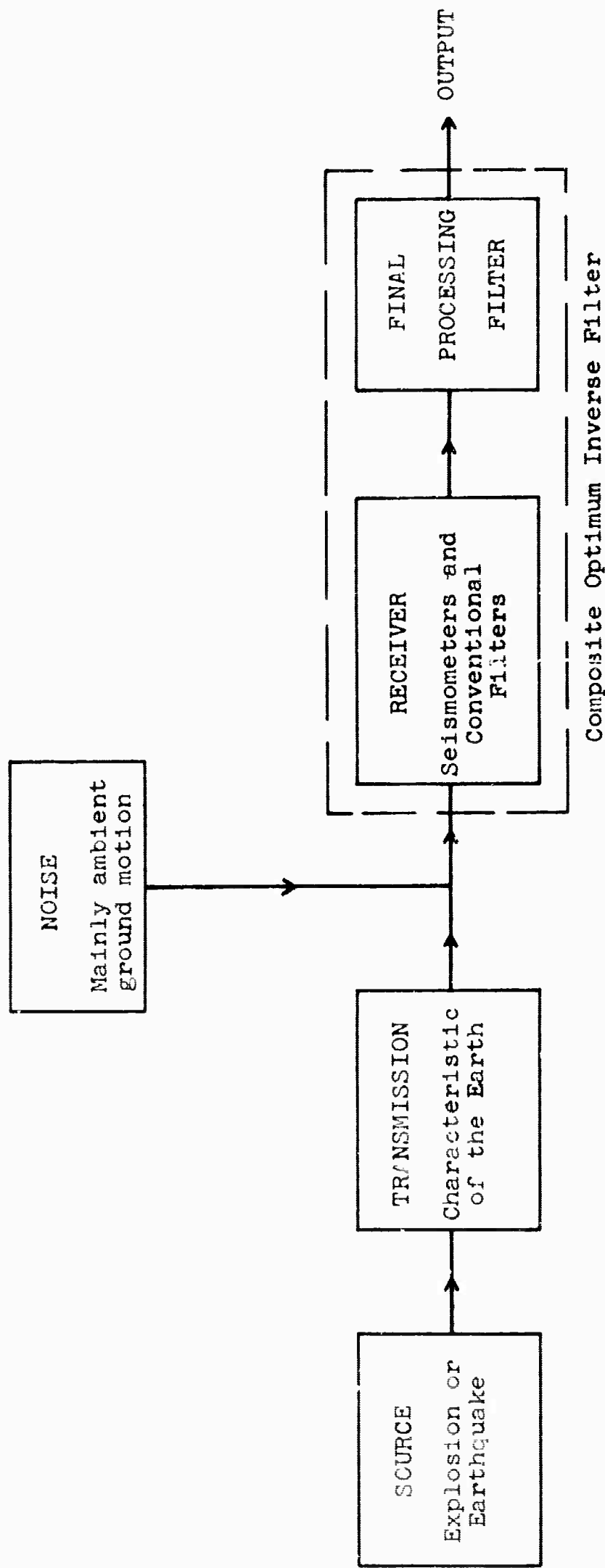
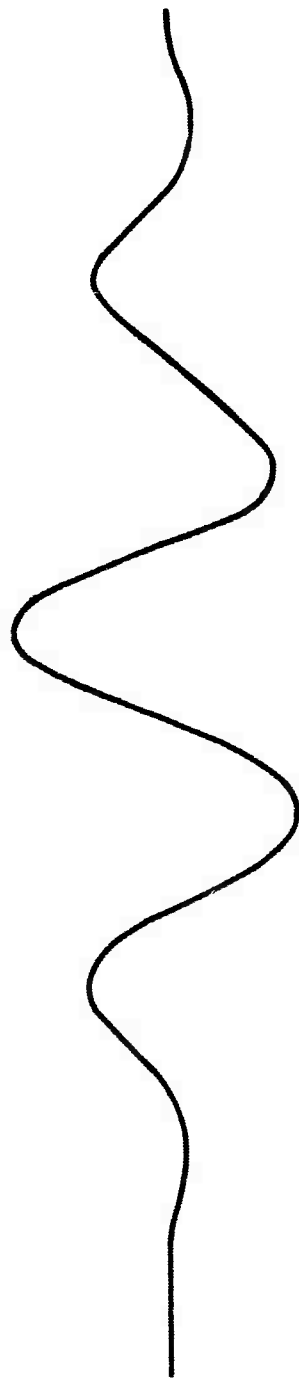
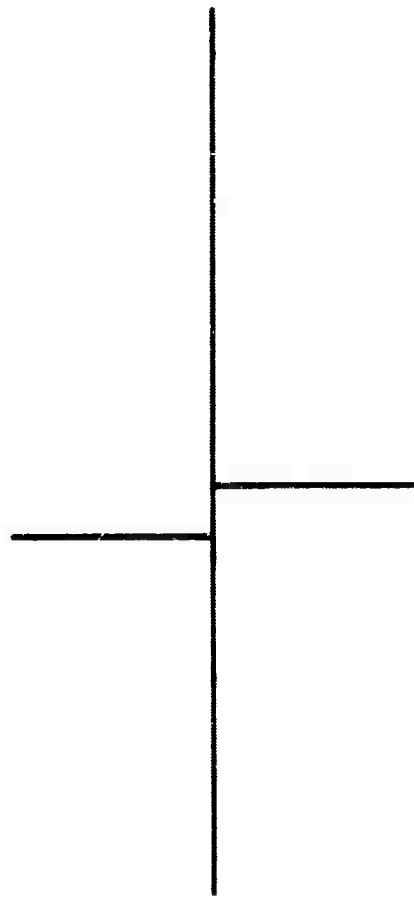


Figure 1. Schematic diagram of main factors in the detection problem.

1 second



a. Pole Mountain recording of direct P event from the Russian bomb of February 2, 1962.



b. Hypothetical doublet source function.

Figure 2.

VELAP. ASSUMES DOUBLET SOURCE AND FROM POLE MT. P EVENT OF RUSSIAN BOMB  
2.2.62 CALCULATES INVERSE FILTER FOR EARTH AND INSTRUMENTAL FILTERING.  
COMPENSATES RUSSIAN, FRENCH (5.1.62) BCMBS AND IUNIAN EARTHQUAKE (4.10.62)

DESIRED POWER SPECTRUM OF A TRACE 1

A = 0. C = 0.500000E 00

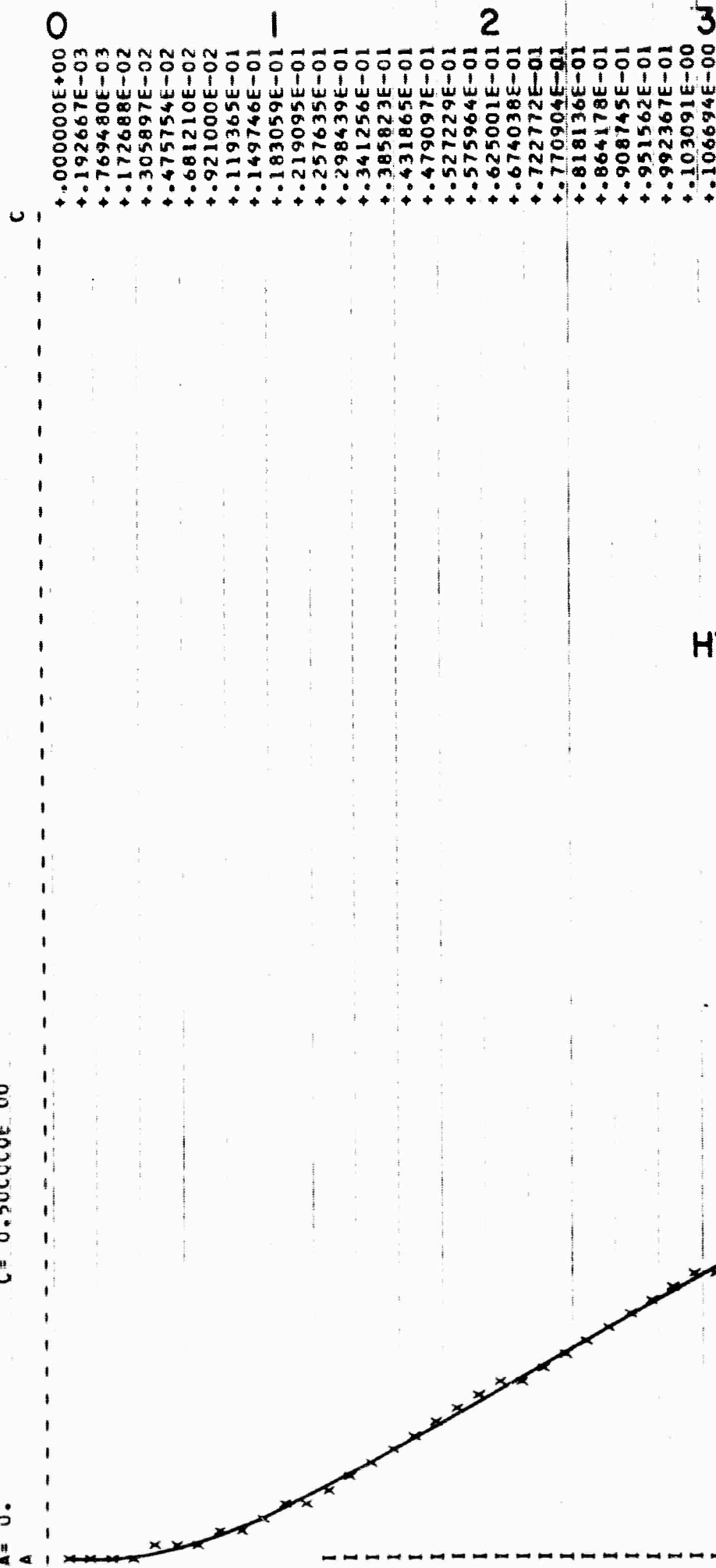


FIGURE 3.  
POWER  
SPECTRUM  
OF THE  
HYPOTHETICAL  
DOUBLET  
SOURCE

DESIRED POWER SPECTRUM OF B TRACE 1

A = 0.  
A  
C = 0.500000E 00

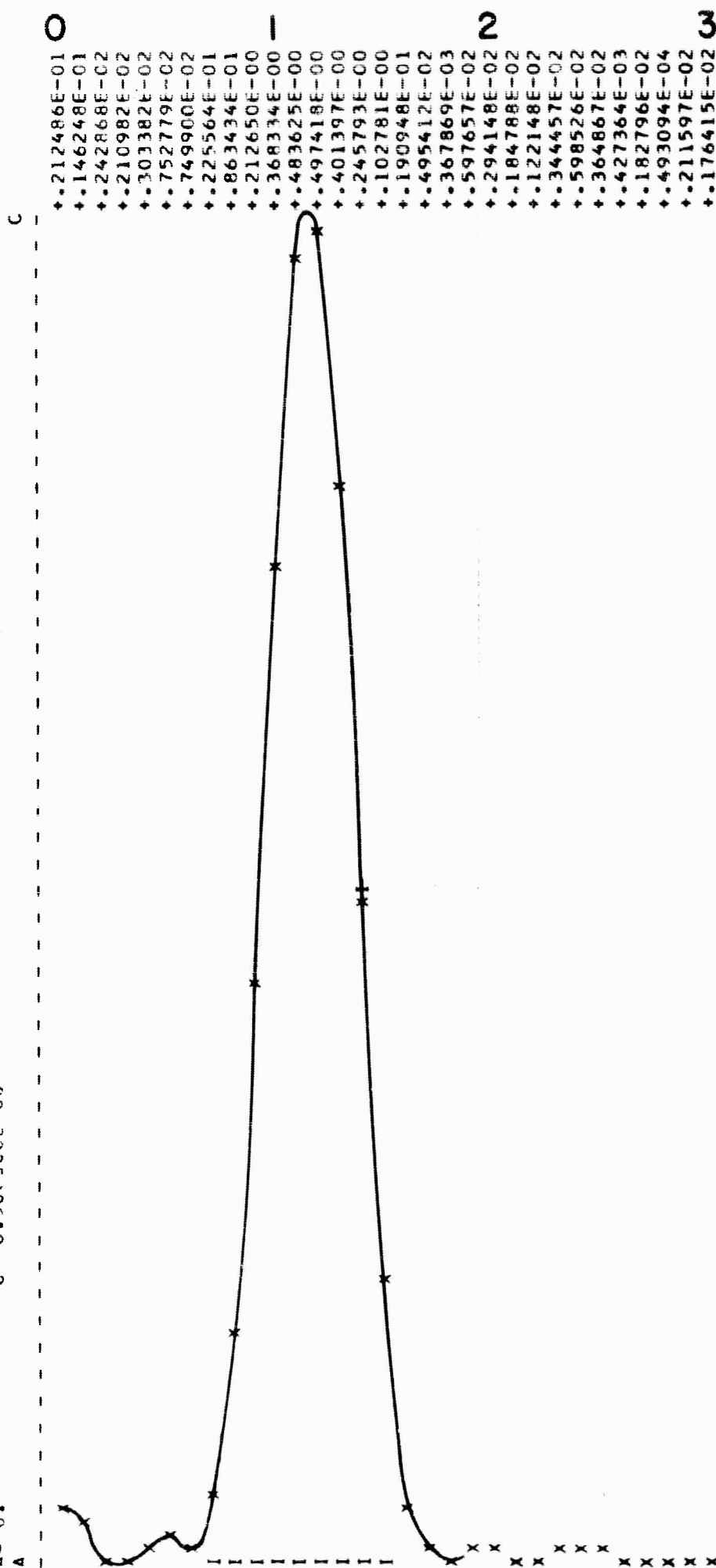


FIGURE 4.  
POWER  
SPECTRUM  
OF  
RUSSIAN  
BOMB  
EVENT

VELAP. ASSUMES DOUBLET SOURCE AND FROM POLE MT. P EVENT OF RUSSIAN BOMB  
2-2-62 CALCULATES INVERSE FILTER FOR EARTH AND INSTRUMENTAL FILTERING.  
COMPENSATES RUSSIAN, FRENCH (9.1.62) BOMBS AND IONIAN EARTHQUAKE (4.10.62)

RATIO OF AMPLITUDE SPECTRA OF TRACES A,B 1 1

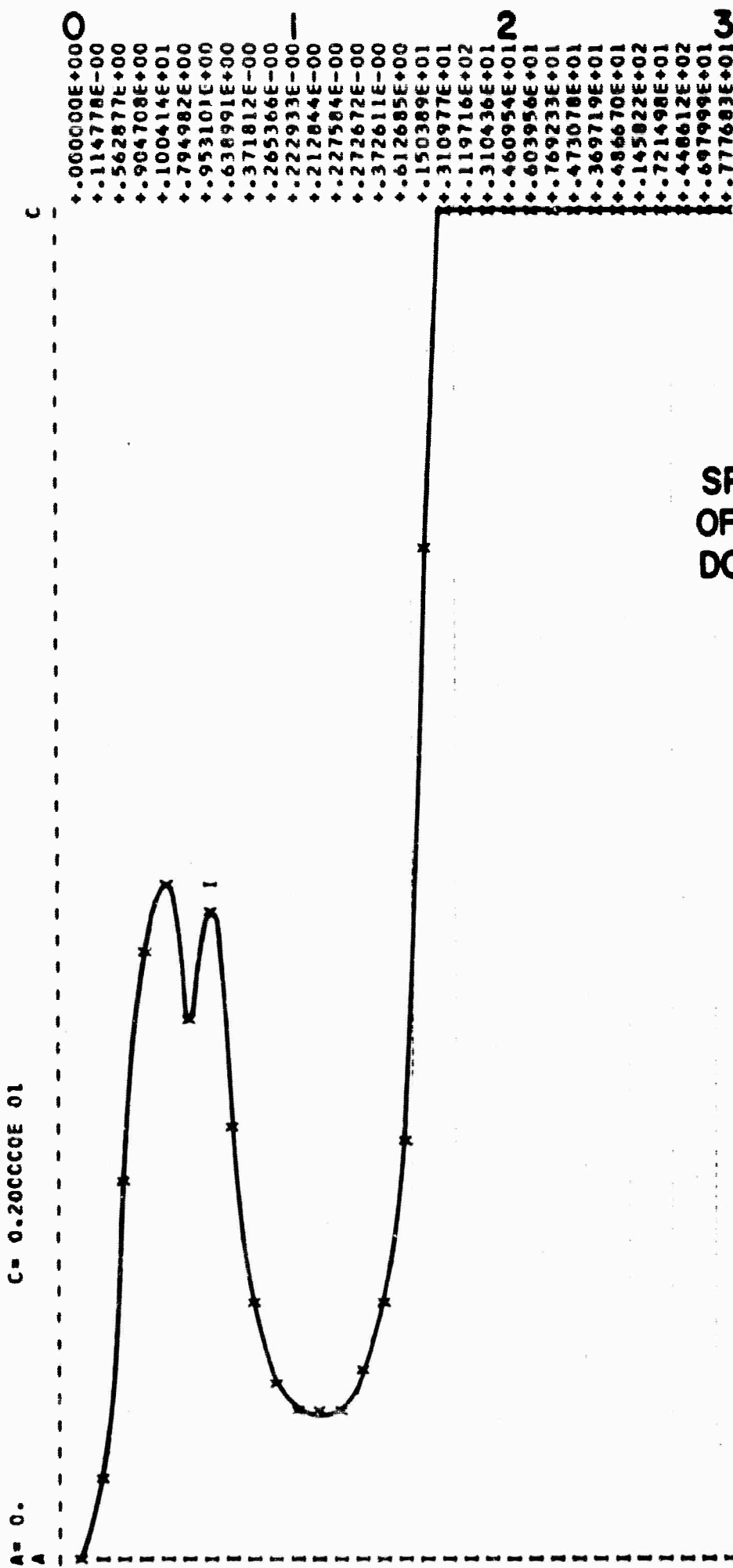


FIGURE 5.

AMPLITUDE  
SPECTRUM RATIO  
OF HYPOTHETICAL  
DOUBLET SOURCE  
TO RUSSIAN  
BOMB EVENT

PHASE CROSS SPECTRUM OF A TRACE 1 AND B TRACE 1

-  $\Pi$

A = -0.314159E 01

C = 0.314159E 01

+  $\Pi$  C

0	1	2	3	CPS
+000000E+00				
+159839E+01				
+163829E+01				
+168534E+01				
+156923E+01				
-391481E-00				
-736483E+00				
-804504E+00				
-844336E+00				
-867475E+00				
-874529E+00				
-866879E+00				
-846462E+00				
-815337E+00				
-775659E+00				
-732215E+00				
-700052E+00				
-862257E+00				
+307596E+01				
-305282E+01				
-181759E+01				
-587600E+00				
-129529E-00				
+314536E-00				
+781362E+00				
+116255E+01				
+143826E+01				
+175496E+01				
-215181E+01				
-169779E+01				
-154068E+01				

FIGURE 6.

DIFFERENCE BETWEEN  
PHASE SPECTRA OF  
HYPOTHETICAL DOUBLET  
SOURCE AND RUSSIAN  
BOMB EVENT

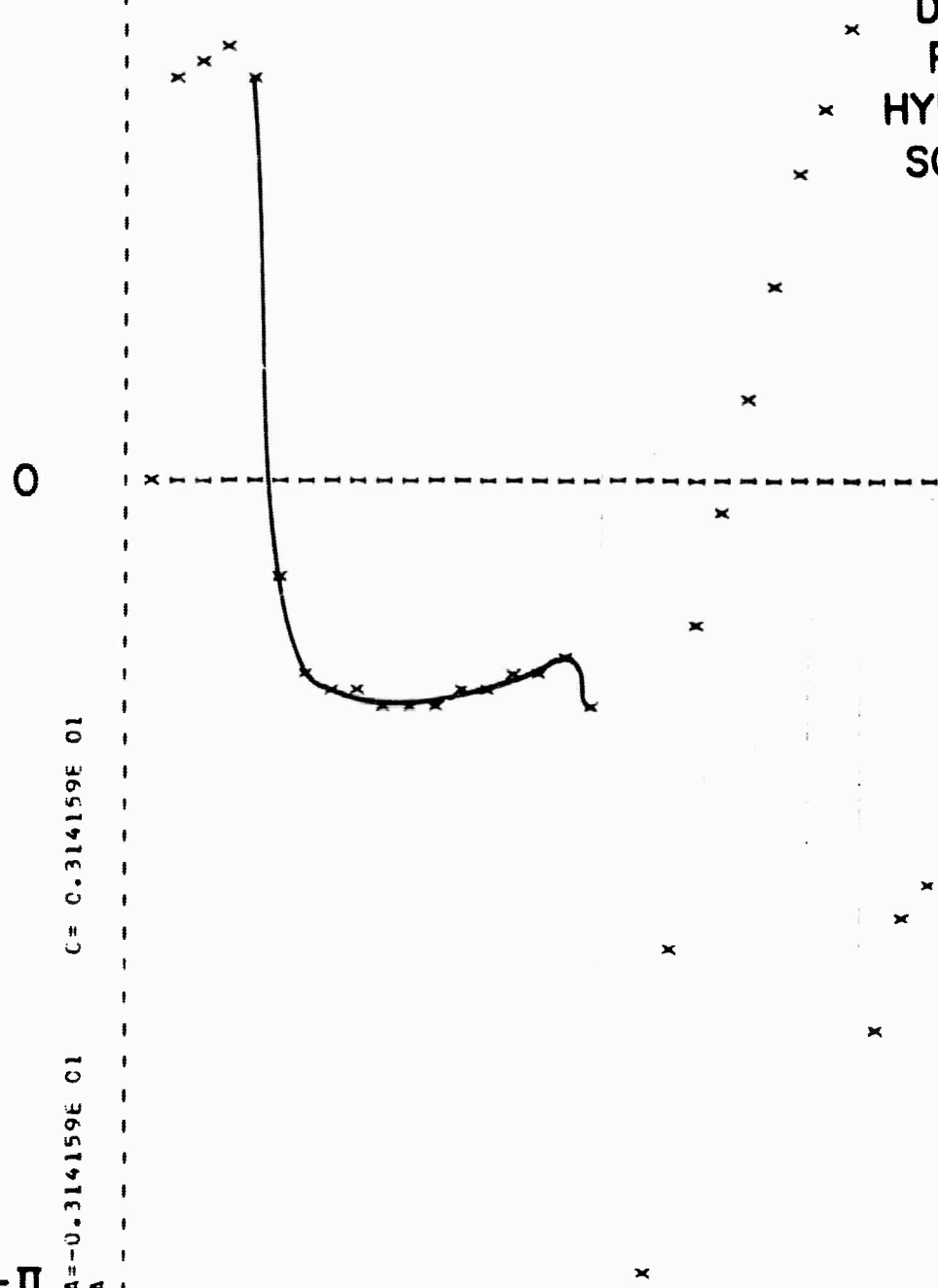
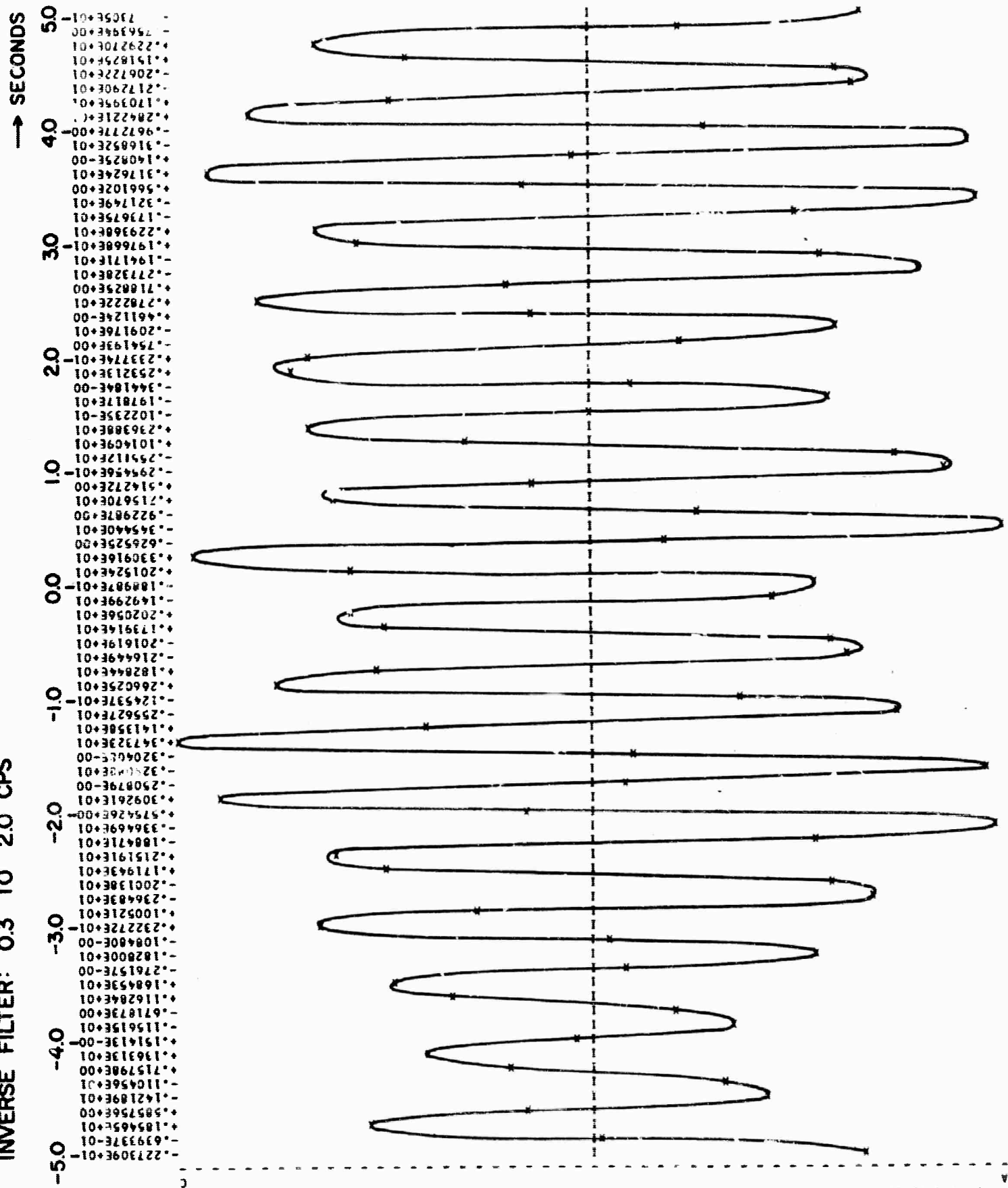


FIGURE 7.

INVERSE FILTER: 0.3 TO 2.0 CPS



VELAP, ASSUMES DOUBLET SOURCE AND FROM POLE MT. P EVENT OF RUSSIAN PCMB  
2.2.62 CALCULATES INVERSE FILTER FOR EARTH AND IONIAN EARTHQUAKE(4.10.62)  
COMPENSATES RUSSIAN/FRENCH (5.1.62) RECORDS AND IONIAN EARTHQUAKE(4.10.62)

FILTER OBTAINED FROM A,B TRACES 1 1

FIGURE 8.  
 INVERSE FILTER: 0.3 TO 1.9 CPS

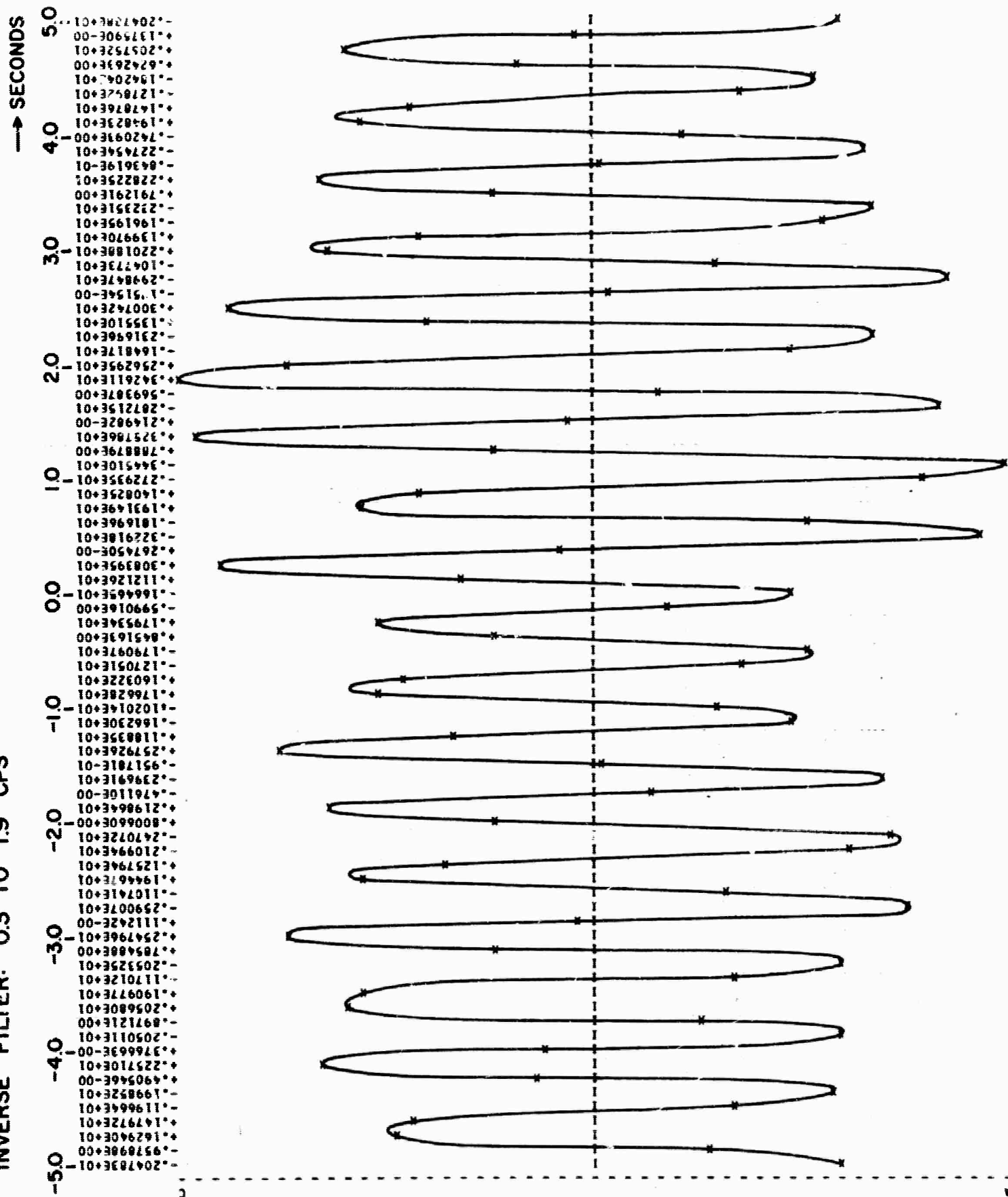
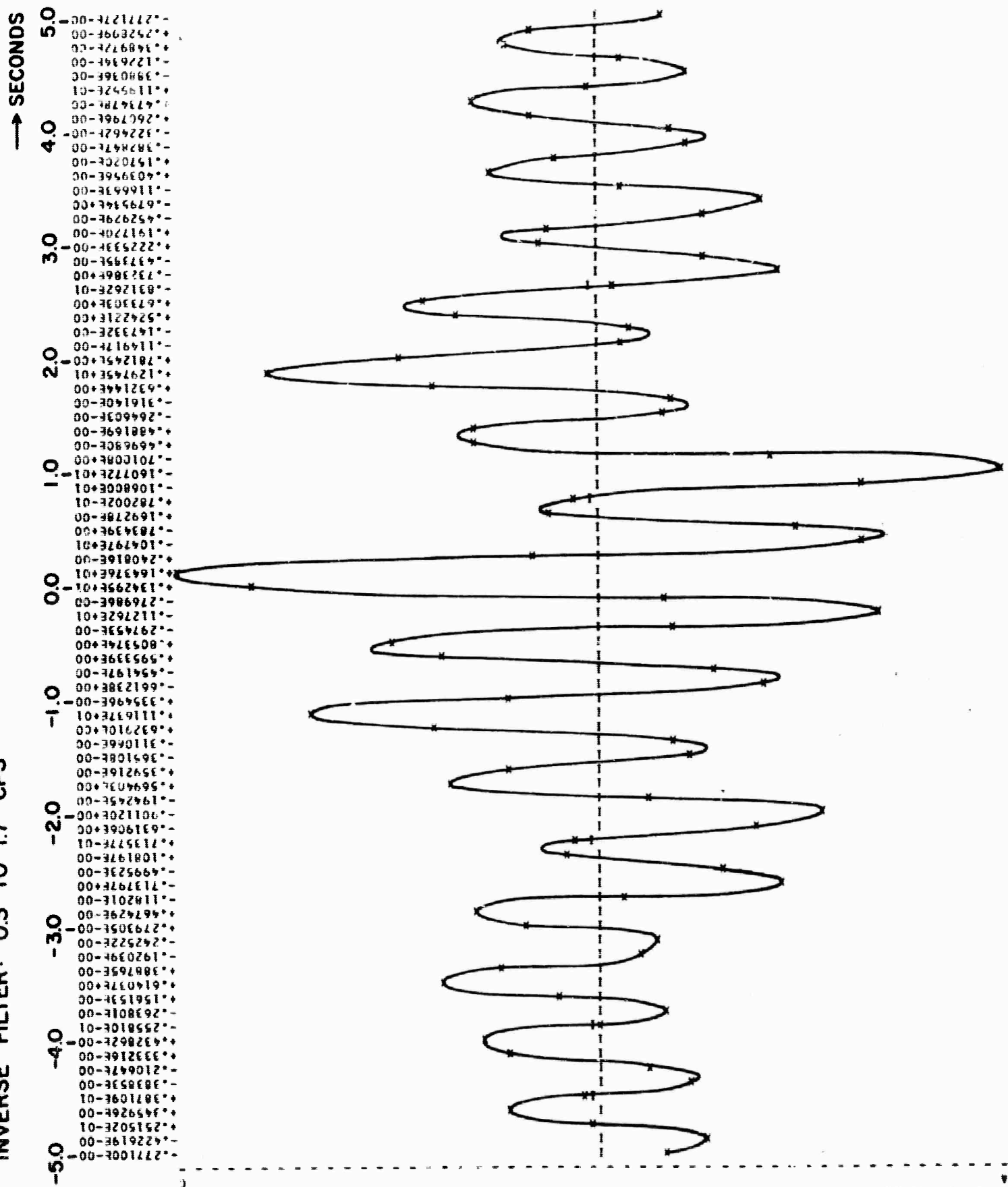




FIGURE 9.

INVERSE FILTER: 0.3 TO 1.7 CPS



WAPL, ASSUMES FOURIER SOURCE AND FROM POLE M1, P EVENT OF RUSSIAN BOMB  
CCPKSATES RUSSIAN/FRENCH (9.1.62) BOMB AND IONIAN FAIRHQUAKE(4.10.62)

FILTER OBTAINED FROM A/R TRACES 1 1

VLLAP, ASSUMES COUPLER SOURCE AND FROM POLE MT. P EVENT LF RUSSIAN BORN  
 2.2.62 CALCULATES INVERSE FILTER FOR EARTH AND INSTRUMENTAL FILTERING.  
 COMPENSATES RUSSIAN/FRENCH 19.1.62) BOMBS AND IONIAN EARTHQUAKE(14.10.62)

FILTER OBTAINED FROM A+B TRACES 1 1

A=-0.733510E 00 C=-0.834695E 00

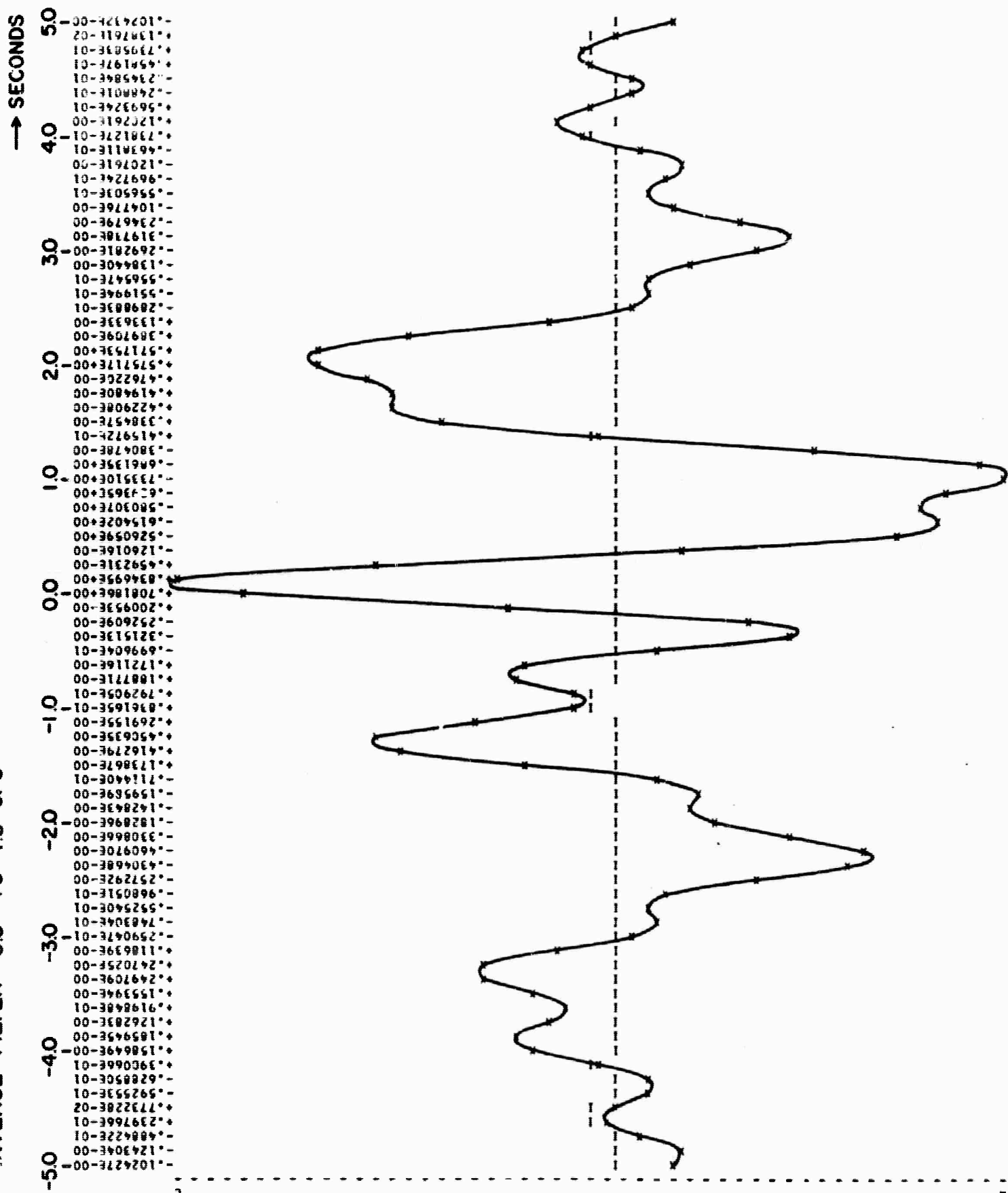


FIGURE 10.  
 INVERSE FILTER: 0.3 TO 1.5 CPS

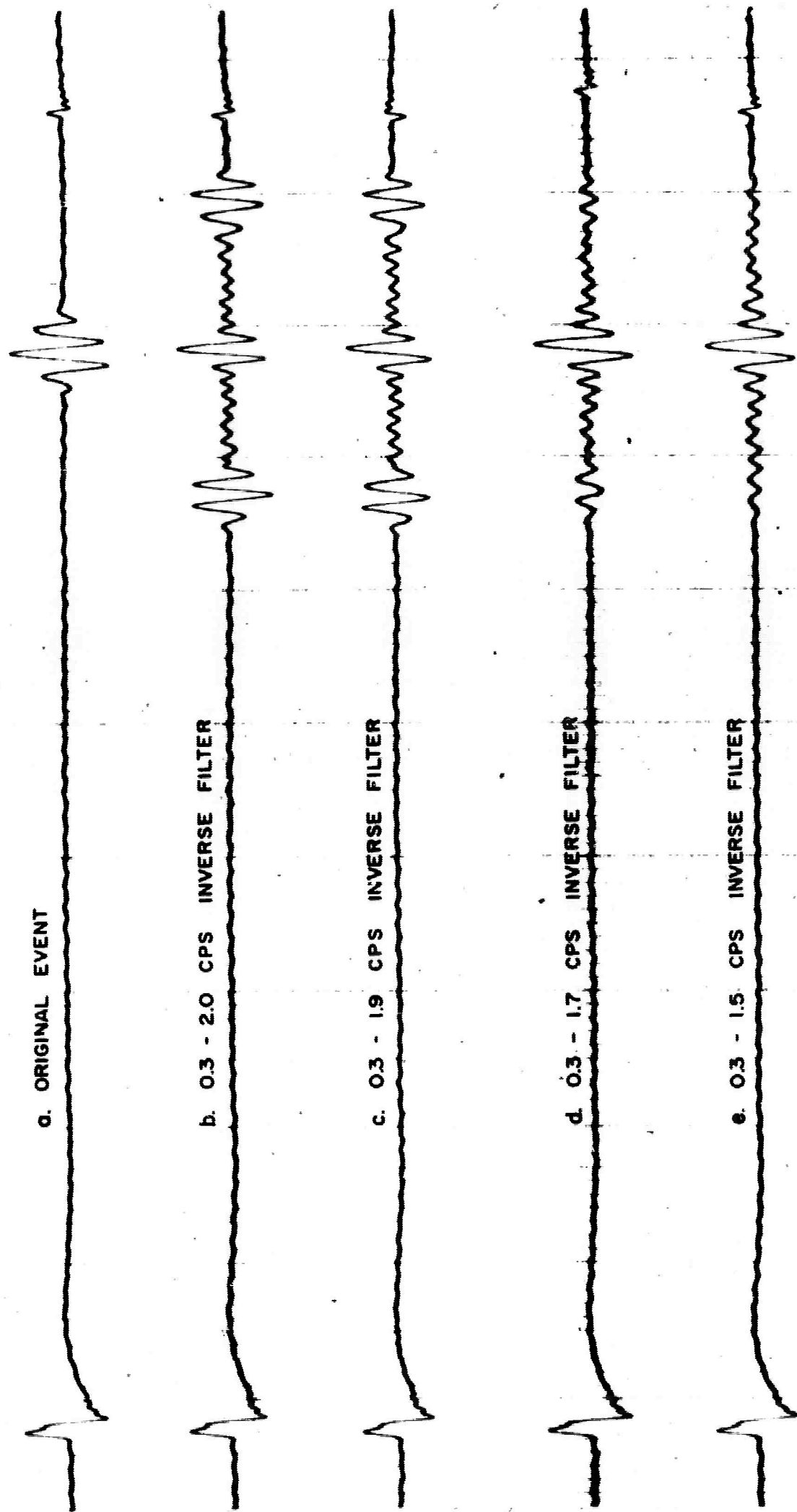


FIGURE II. INVERSE FILTERING OF RUSSIAN BOMB DIRECT P EVENT

1 SECOND INTERVALS

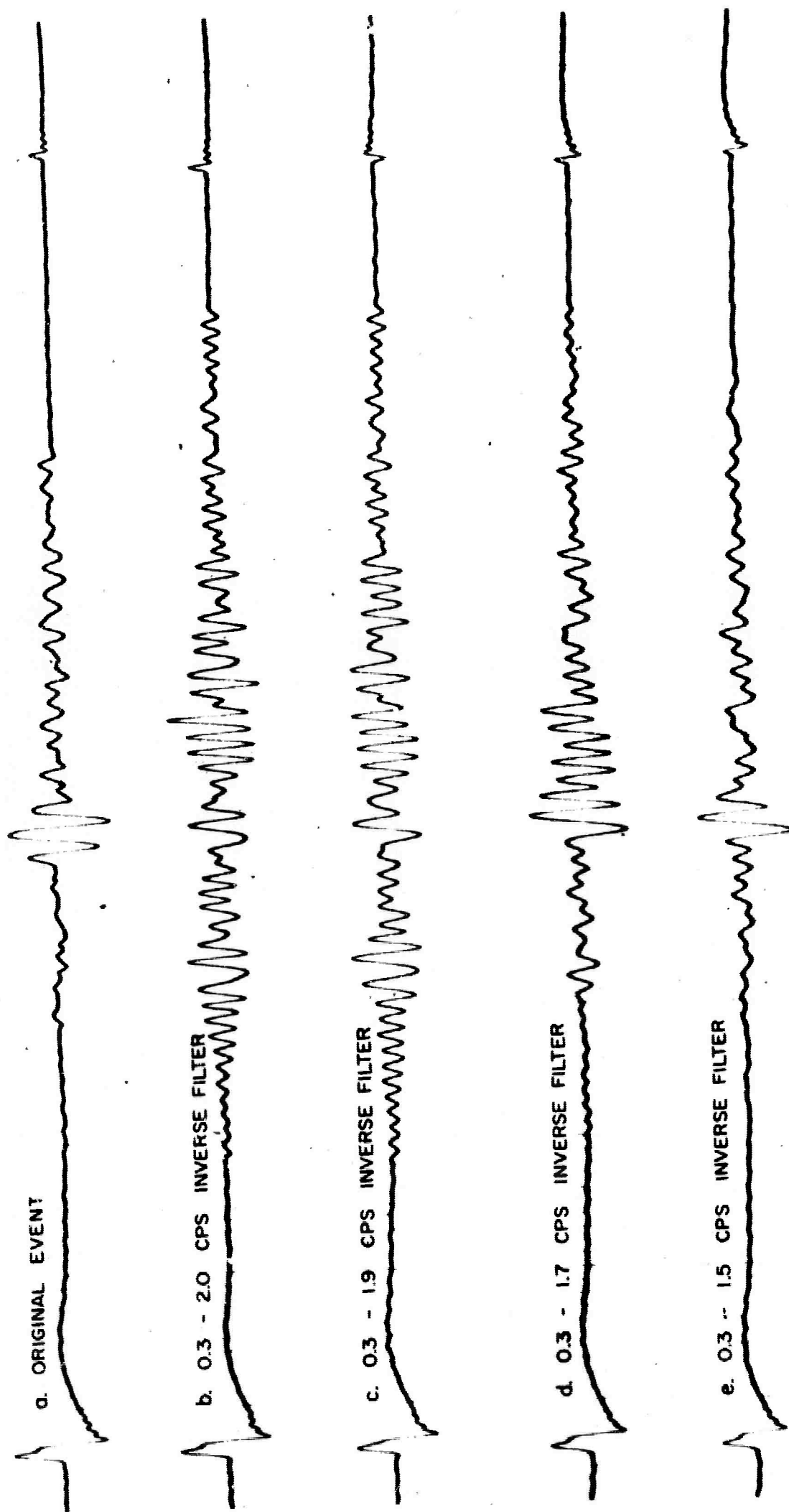


FIGURE 12. INVERSE FILTERING OF FRENCH BOMB P EVENT

1 SECOND INTERVALS

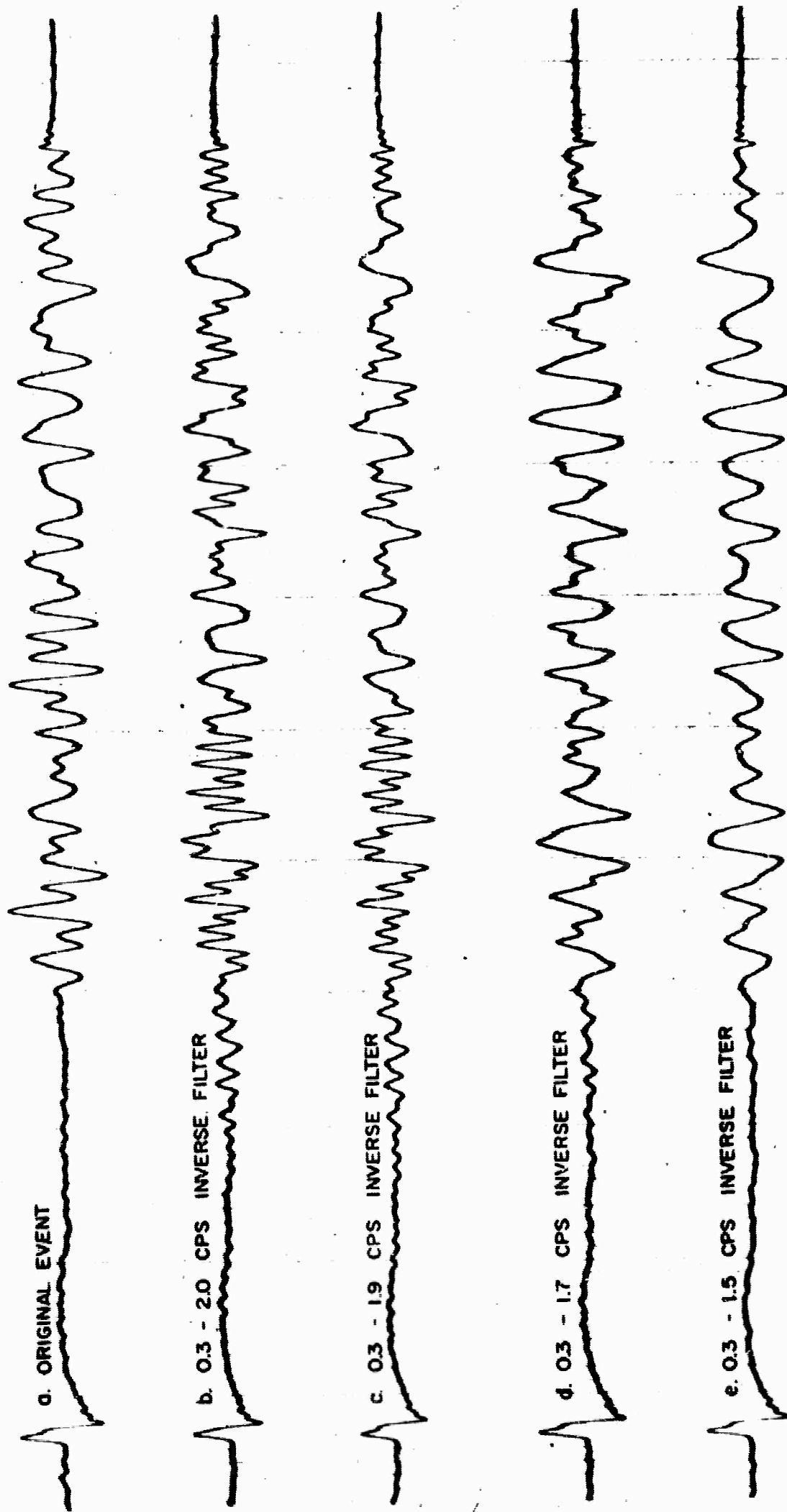


FIGURE 13. INVERSE FILTERING OF AN IONIAN SEA EARTHQUAKE ON APRIL 10, 1962

1 SECOND INTERVALS

REFERENCES

- Aki, K., 1960, Study of earthquake mechanism by a method of phase equalization applied to Rayleigh and Love waves: J. Geophys. Res., v. 65, p. 729.
- Angona, F. A., 1960, Two-dimensional modeling and its application to seismic problems: Geophysics, v. 25, p. 468-482.
- Arons, A. B., and Yennie, D. R., 1950, Phase distortion of acoustic pulses obliquely reflected from a medium of higher sound velocity: J. Acoust. Soc. Amer., v. 22, p. 231-237.
- Backus, M. M., 1961, Deconvolution and the one-dimensional reflection seismogram. Oral presentation at the Denver meeting of the Society of Exploration Geophysicists, on November 9, 1961.
- Brune, J. N., and Oliver, J., 1959, The seismic noise of the earth's surface: Bull. Seism. Soc. Amer., v. 49, p. 349.
- Brune, J. N., Nafe, J. E., and Oliver, J. E., 1960, A simplified method for the analysis and synthesis of dispersed wave trains: J. Geophys. Res., v. 65, p. 287-304.

- Cagniard, L., 1939, Reflexion et refraction des ondes seismiques progressives: Gauthier-Villars, Paris. Translation by Flinn, E. A., and Dix, C. H., 1962, McGraw-Hill, New York.
- Erdelyi, A. 1956, Asymptotic expansions: Dover Publications, New York, p. 26-56.
- Foster, M. R., Hicks, W. G., and Nipper, J. T., 1962, Optimum inverse filters which shorten the spacing of velocity logs: Geophysics, v. 27, p. 317-326.
- Gilbert, F., and Laster, S. J., 1962, Excitation and propagation of pulses on an interface: Bull. Seism. Soc. Amer., v. 52, p. 299.
- Gudzin, M. G., and Hamilton, J. H., 1961, Wichita Mountains Seismological Observatory: Geophysics, v. 26, p. 359.
- Haskell, N. A., 1953, The dispersion of surface waves in multi-layered media: Bull. Seism. Soc. Amer., v. 43, p. 17-34.
- Heelan, P. A., 1953, On the theory of head waves: Geophysics, v. 18, p. 871-893.
- d'Hoerane, J., 1962, Deconvolution de traces reelles: Geophys. Prospecting, v. 10, p. 68-83.

Hueter, T. F., and Bolt, R. H., 1955, Sonics: John Wiley and Sons, New York, p. 321.

Jardetzky, W. S., 1953, Period equation for an n-layered half-space and some related questions: Columbia Univ. Lamont Geol. Obs. Tech. Report Seismology, 29.  
Summarized by Ewing, M., Jardetzky, W. S., and Press, F., 1957, Elastic waves in layered media: McGraw-Hill, New York, p. 238-245.

Kunetz, G., 1961, Essai d'analyse de traces sismiques: Geophys. Prospecting, v. 9, p. 317-341.

Latter, A. L., Le Levier, R. E., Martinelli, E. A., and McMillan, W. G., 1961, A method of concealing underground nuclear explosions: J. Geophys. Res., v. 68, p. 943.

O'Brien, P. N. S., 1961, A discussion on the nature and magnitude of elastic absorption in seismic prospecting: Geophys. Prospecting, v. 9, p. 261.

Oliver, J., Press, F., and Ewing, M., 1954, Two-dimensional seismology: Geophysics, v. 19, p. 202-219.

Pekeris, C. L., 1948, Theory of propagation of explosive sound in shallow water: Geol. Soc. Amer., Memoir 27.



Pekeris, C. L., and Longmann, I. M., 1958, Ray theory solution of the problem of propagation of explosive sound in a layered liquid: J. Acoust. Soc. Amer., v. 51, p. 323-328.

Phinney, R. A., 1961, Propagation of leaking interface waves: Bull. Seism. Soc. Amer., v. 51, p. 527-555.

Press, F., and Ewing, M., 1954, An investigation of mantle Rayleigh waves: Bull. Seism. Soc. Amer., v. 44, p. 127.

Rayleigh, Lord, 1885, On waves propagated along the plane surface of an elastic solid: Proc. Lon. Math. Soc., v. 17, p. 4.

Rayleigh, Lord, 1945, Theory of sound: Dover Publications, New York.

Rice, R. B., 1962, Inverse convolution filters: Geophysics, v. 27, p. 4-18.

Robinson, E. A., 1957, Predictive decomposition of seismic traces: Geophysics, v. 22, p. 767-778.

Sato, Y., 1955, 1956, Analysis of dispersed surface waves I, II, III. Bull. Earthquake Research Institute, Tokyo Univ., v. 33, p. 33-48 and v. 34, p. 9-18.

- Sherwood, J. W. C., and Spencer, T. W., 1962, Signal-to-noise ratio and spectra of explosion-generated Rayleigh waves: Bull. Seism. Soc. Amer., v. 52, p. 573.
- Spencer, T. W., 1956, Reflection of an acoustical pressure pulse from a liquid-solid plane boundary: Geophysics, v. 21, p. 84-86.
- Spencer, T. W., 1960, The method of generalized reflection and transmission coefficients: Geophysics, v. 25, p. 625-641.
- Strick, E., 1959, Propagation of elastic wave motion from an impulsive source along a fluid/solid interface: Phil. Trans. Roy. Soc. London, (A), v. 251, p. 465-523.
- Turin, G. L., 1960, An introduction to matched filters: IRE Trans. Information Theory, IT-6, p. 311-329.
- Wiener, N., 1949, Extrapolation, interpolation and smoothing of time series: John Wiley and Sons, New York.

<p>California Research Corp., La Habra, Calif., THEORETICAL STUDIES RELATED TO THE DETERMINATION OF SEISMIC ENERGY SOURCE DEPTH, by T. W. Spencer, W. L. Baker, J. W. C. Sherwood, D. P. Squier, and R. D. Tooley. Air Force Cambridge Research Laboratories, Bedford, Mass. Final Report-Number AFCLR-64-750, 185 pages, July 15, 1964. Unclassified Report</p> <p>This report summarizes work on a number of dif- ferent but related topics as follows. The effect of seismic source depth on Rayleigh wave spectra is examined for a dissipative half space and for an elastic layer overlying an elastic half space. In the two layer earth model, the higher-mode amplitude spectra increase relative to the funda- mental as the source approaches the base of the crust. Two-dimensional model studies confirm this conclusion. Geometric ray theory is used to study the effects of layer thickness and range on the refracted arrival along a layer. When the layer is thick compared with the dominant wavelength, the refracted arrival exhibits range-limited shingling and may consist of two or more events separated by equal time intervals which depend only on the layer thickness.</p>	<ol style="list-style-type: none"> <li>1. Seismic Source Depth</li> <li>2. Rayleigh Spectra</li> <li>3. Modeling</li> <li>4. Ray Theory</li> <li>5. Matrix Method</li> <li>6. Refraction</li> <li>7. Reflection Coefficients</li> <li>8. Deconvolution</li> </ol>	<ol style="list-style-type: none"> <li>I. Project No. 8652 Task No. 865205 Contract AF19(604)-8344 T. W. Spencer, W. L. Baker, J. W. C. Sherwood, D. P. Squier, and R. D. Tooley. In DDC collection</li> <li>II.</li> <li>III.</li> <li>IV.</li> </ol>	<ol style="list-style-type: none"> <li>1. Seismic Source Depth</li> <li>2. Rayleigh Spectra</li> <li>3. Modeling</li> <li>4. Ray Theory</li> <li>5. Matrix Method</li> <li>6. Refraction</li> <li>7. Reflection Coefficients</li> <li>8. Deconvolution</li> </ol>	<ol style="list-style-type: none"> <li>I. Project No. 8652 Task No. 865205 Contract AF19(604)-8344 T. W. Spencer, W. L. Baker, J. W. C. Sherwood, D. P. Squier, and R. D. Tooley. In DDC collection</li> <li>II.</li> <li>III.</li> <li>IV.</li> </ol>
<p>California Research Corp., La Habra, Calif., THEORETICAL STUDIES RELATED TO THE DETERMINATION OF SEISMIC ENERGY SOURCE DEPTH, by T. W. Spencer, W. L. Baker, J. W. C. Sherwood, D. P. Squier, and R. D. Tooley. Air Force Cambridge Research Laboratories, Bedford, Mass. Final Report-Number AFCLR-64-750, 185 pages, July 15, 1964. Unclassified Report</p> <p>This report summarizes work on a number of dif- ferent but related topics as follows. The effect of seismic source depth on Rayleigh wave spectra is examined for a dissipative half space and for an elastic layer overlying an elastic half space. In the two layer earth model, the higher-mode amplitude spectra increase relative to the funda- mental as the source approaches the base of the crust. Two-dimensional model studies confirm this conclusion. Geometric ray theory is used to study the effects of layer thickness and range on the refracted arrival along a layer. When the layer is thick compared with the dominant wavelength, the refracted arrival exhibits range-limited shingling and may consist of two or more events separated by equal time intervals which depend only on the layer thickness.</p>	<ol style="list-style-type: none"> <li>1. Seismic Source Depth</li> <li>2. Rayleigh Spectra</li> <li>3. Modeling</li> <li>4. Ray Theory</li> <li>5. Matrix Method</li> <li>6. Refraction</li> <li>7. Reflection Coefficients</li> <li>8. Deconvolution</li> </ol>	<ol style="list-style-type: none"> <li>I. Project No. 8652 Task No. 865205 Contract AF19(604)-8344 T. W. Spencer, W. L. Baker, J. W. C. Sherwood, D. P. Squier, and R. D. Tooley. In DDC collection</li> <li>II.</li> <li>III.</li> <li>IV.</li> </ol>	<ol style="list-style-type: none"> <li>1. Seismic Source Depth</li> <li>2. Rayleigh Spectra</li> <li>3. Modeling</li> <li>4. Ray Theory</li> <li>5. Matrix Method</li> <li>6. Refraction</li> <li>7. Reflection Coefficients</li> <li>8. Deconvolution</li> </ol>	<ol style="list-style-type: none"> <li>I. Project No. 8652 Task No. 865205 Contract AF19(604)-8344 T. W. Spencer, W. L. Baker, J. W. C. Sherwood, D. P. Squier, and R. D. Tooley. In DDC collection</li> <li>II.</li> <li>III.</li> <li>IV.</li> </ol>